THE AGGREGATION OF IRON OXIDE NANOPARTICLES IN MAGNETIC FIELDS

by

PETER BRADFORD

A thesis submitted to
The University of Birmingham
for the degree of
DOCTOR OF PHILOSOPHY

UNIVERSITYOF
BIRMINGHAM

University of Birmingham Research Archive

e-theses repository

Abstract

The application of a magnetic field to a suspension of weakly magnetic nanoparticles should, based on previous work, increase the aggregation between particles. This is caused by the increase in the magnetic interaction in competition with repulsive forces due to the electric double layer.

This hypothesis was tested using suspensions of magnetite and hematite nanoparticles. Magnetite particles were used to characterise the aggregation behaviour of strongly magnetic particles, which then served as a basis of comparison with hematite particles in a magnetic field. The expectation was that applying the magnetic field to the suspensions of weakly magnetic hematite particles would alter their aggregation behaviour to be more like that of the strongly magnetic magnetite particles.

Experimental findings indicated this is not the case. No evidence was found indicating that the magnetic field affected particle interactions sufficiently to alter the aggregation. Aggregation behaviour was controlled by the chemical environment and shear forces. The magnetic field did influence the particles' motion. In static experiments hematite particles were separated from suspension, the efficiency of which was related to the degree of aggregation and thus to the aggregate size. In stirred systems the balance between shear and Lorentz forces affected aggregate formation.

Small aggregation increases were observed but once aggregates reach a certain size the magnetic field affects the movement of particles and does not change interactions.

ACKNOWLEDGEMENTS

CONTENTS

CHAPTER 1

INTRODUCTION

Magnetic treatment devices, used on fuel and water lines, are commonplace around the world. In fuel systems they are used to increase the fuel efficiency of motors, boilers and furnaces. In water systems they are used to prevent the build-up of scale as a result of calcium carbonate deposits in water systems. These effects are still controversial, particularly as the mechanisms which might be responsible for these effects are little understood. Explanations that have been put forward already include changes in the physical properties of the water or the fuel itself, changes in crystallisation of calcium carbonate deposits in water systems resulting in less scale, and the use of alternating versus static magnetic fields in both cases. Conclusive proof of these effects remains, however, elusive.

Suspended nanoparticles are occur naturally in water and fuel systems, as products of corrosion for example, and changes in their aggregation state could provide one possible mechanism for the action of magnetic treatment devices. Increased aggregation should prevent surface adhesion and fouling by nanoparticles, leading to better efficiency of heat exchangers.

Exploiting the role of the magnetic interaction in the aggregation of fine particles already has practical applications in minerals processing, where magnetic flocculation

is used to process slurries of mineral fines. This results in the improved separation of magnetic mineral fines and the recovery of greater amounts of mineral ores.

Magnetic nanoparticles are now used extensively in biological applications, such as MRI contrast agents, and thus understanding and being able to manipulate the particle interactions appropriately is essential. Magnetic iron oxide particles are often used for such applications and controlling the aggregation state of these particles is necessary in order to prevent the particles forming blockages in the body.

Theory and previous studies suggest that increasing the magnetic interaction through the application of a magnetic field should increase the aggregation of weakly magnetic particles due to the change in the particle interactions, in competition with the surface chemical repulsions caused by double layer forces. The application of a magnetic field is thus akin to increasing the contribution from the magnetic interaction in the total particle interactions. If this is true then the particle interactions should become more like the interactions expected from a system of strongly magnetic particles, and the aggregation of the weakly magnetic particles should become more like that of the strongly magnetic particles.

The aim of this work was to test this hypothesis experimentally. This was achieved by comparing how closely the aggregation behaviour of weakly magnetic hematite nanoparticles in an applied magnetic field matches the aggregation of strongly magnetic magnetite nanoparticles. This will be done in both static and stirred systems and the aggregation will be characterised in different chemical conditions of pH and electrolyte concentration. This allows the aggregation kinetics to be altered, through changing the collision efficiency and frequency between particles.

For the experiments three particle systems will be synthesised and characterised - magnetite, spherical hematite and ellipsoidal hematite. The different particle shapes of the weakly magnetic hematite will allow any difference due to particle shape to be also

observed.

This gives the following experimental outline which will be used for both a static system and a stirred system:

- Characterisation of the aggregation of magnetite nanoparticles

- Characterisation of the aggregation of spherical hematite particles with and without the applied magnetic field

- Characterisation of the aggregation of ellipsoidal hematite particles with and without the applied magnetic field

In order to monitor and characterise the aggregation of the particle systems static light scattering will be used, which allows data about both the size and structure of the aggregates to be obtained.

The comparison of the results will then allow the validity of the hypothesis about magnetic particle interactions to be tested.

The structure of this thesis is then as follows:

- Background concepts that are key to the understanding of the thesis are reviewed through the literature in chapter 2

- The aggregation of the particle systems are studied in static systems in chapters 4 (magnetite), 5 (spherical hematite) and 6 (ellipsoidal hematite)

- The aggregation of the particle systems in stirred systems are studied in chapters 7 (magnetite), 8 (spherical hematite) and 9 (ellipsoidal hematite)

- Finally conclusions are drawn and recommendations for further work are made in chapter 10.

CHAPTER 2

BACKGROUND

2.1   Iron oxides

Iron itself, uncombined with any other elements, occurs on the surface of the earth in very small quantities, but combined with other elements it is found in a number of ores which are so widely distributed that there are deposits of ores in all the continents (Silver, 1993). Many of these ores are iron oxides and magnetite and hematite are among the most common. For example, Mt. Whaleback in Australia is largely composed of magnetite and is now mined for this purpose. However, it used to be hazardous to aircraft as its large iron content affects magnetic navigation instruments from great distances, and it was not until the 1960s that this was discovered (Silver, 1993).

There are sixteen known iron oxides (oxides, hydroxides or oxide hydroxides), and these are listed in table 2.1.

Name	Chemical formula	Colour	Magnetic behaviour at room temperature
Goethite	$\alpha - FeOOH$	Yellow-brown	Antiferromagnetic
Lepidocrocite	$\beta - FeOOH$	Orange	Paramagnetic
Akaganeite	$\gamma - FeOOH$	Brown to bright yellow	Paramagnetic
	$\delta - FeOOH$	Red-brown	Ferrimagnetic
Feroxyhyte	$\delta' - FeOOH$	Red-brown	Superparamagnetic
	High pressure $FeOOH$		
Ferrihydrate	$Fe_5HO_8 \cdot 4H_2O$	Reddish brown	Superparamagnetic
Bernalite	$Fe(OH)_3$	Greenish	Weakly ferromagnetic
	$Fe(OH)_2$	White	
Schwertmannite	$Fe_{16}O_{16}(OH)_y(SO_4) \cdot nH_2O$	Yellow	Paramagnetic
Haematite	$\alpha - Fe_2O_3$	Red	Weakly ferromagnetic
Magnetite	Fe_3O_4	Black	Ferromagnetic
Maghemite	$\gamma - Fe_2O_3$	Dark brown	Ferrimagnetic
	$\beta - Fe_2O_3$		
	$\varepsilon - Fe_2O_3$		
Wustite	FeO	Black	Paramagnetic

Table 2.1: The sixteen known iron oxides (Cornell and Schwertmann, 1996).

Magnetite and hematite have been used as catalysts for a number of industrially important reactions (Cornell and Schwertmann, 1996; Uddin et al., 2008; Li et al., 2008), including the synthesis of NH_3 (the Haber process), the high temperature water gas shift reaction, and the desulfurization of natural gas. Other reactions include the dehydrogenation of ethyl benzene to styrene, the Fisher-Tropsch synthesis for hydrocarbons, the oxidation of alcohols, and the large scale manufacture of butadiene. Magnetite and hematite are semiconductors and can catalyze oxidation/reduction reactions (Kandalam et al., 2007; Jrgensen et al., 2007; Peterson et al., 1997). Hematite has also been used as a support material for gold in catalysts for the oxidation of carbon monoxide at low temperature (Zhong et al., 2007; Kozlova et al., 1998; Hutchings et al., 2006). Iron oxides can be used as acid/base catalysts (Shi et al., 2007) and to catalyze the degradation of

acrylnitrile-butadiene-styrene copolymer into fuel oil. Hematite has been used as photo-catalyst for the degradation of chlorophenol and azo dyes (Bandara et al., 2007), whereas maghemite and magnetite/carbon composites have been found useful for reducing the amount of undesirable N_2 in fuel oil (Brebu et al., 2001).

All three forms of magnetic iron oxide are commonly used in synthetic pigments in paints, ceramics, and porcelain (Cornell and Schwertmann, 1996). They possess a number of desirable attributes for these applications because they display a range of colors with pure hues and high tinting strength. They are also extremely stable and highly resistant to acids and alkalis. Pigments based on hematite are red, those based on maghemite are brown, and magnetite-based pigments are black (Lam et al., 2008). The transparent yellow pigments based on goethite can be transformed into the transparent red pigments of hematite by calcination at $400\text{-}500^{o}C$. These pigments are widely used in water-repellent stains for wood as they enable the wood grain to be seen while still providing protection against the damaging effects of sunlight. Pigments made from magnetite are also used in magnetic ink character recognition devices, and magnetic magnetite particles are used in metallography for detecting flaws in engines (Cornell and Schwertmann, 1996).

Magnetic iron oxide nanoparticles have been used *in vivo* as magnetic resonance imaging (MRI) contrast agents for molecular and cell imaging (Majewski and Thierry, 2007; Tartaj et al., 2003; Ai et al., 2005; Sadeghiani et al., 2005; Tartaj et al., 2005). Magnetite is used as the core in these agents which are used to differentiate between healthy and diseased tissue. The magnetic particles are generally coated with a polysaccharidic layer for colloidal stability (Babes et al., 1999). *In vivo* MRI cell tracking has been success-fully performed by Song and co-workers (Song et al., 2005). Magnetic particles with a polymer coating have been used in cell separation, protein purification (Tanyolac and Oz-dural, 2001), environment and food analyses, organic and biochemical syntheses (Avital et al., 2001), industrial water treatment (Cumbal et al., 2003) and biosciences (Kim et al.,

2003; Thunemann et al., 2006; Zhang et al., 2007). Encapsulation of magnetic nanoparticles with organic polymers is used to enhance their chemical stability, dispersability and functionality (Tartaj et al., 2005).

2.2 Nanoparticles

There has been a frenzy of activity in recent years into the investigation of nanoparticles and their possible applications, or as celebrated physicist and nobel laureate Richard Feynman put it "the problem of manipulating and controlling things on a small scale" (Feynman, 1960). The list of applications includes drug delivery, catalysis, food production, cosmetics and the many further applications of nanomaterials engineered with specific properties. The use of nanoparticles, however, goes back several millenia although those using this seemingly modern technology were unaware of it. There are examples of Roman glasswork over 2000 years old given their colour using glasses coloured with nanoparticles (Barber and Freestone, 1990; Wagner et al., 2000). Faraday (Faraday, 1857) presented his gold sols to the Royal Society in London over 150 years ago. Even the development of photography throughout the 19th century can be viewed as containing elements of nanotechnology and the use of nanoparticles (Hornyak et al., 2008).

2.2.1 The nanoscale, nanoscience and nanotechnology

Nanotechnology is generally defined as having one dimension between 1 and 100nm (Hornyak et al., 2008), although this is not a strict defintion as there are applications where the dimension of interest is less than 1nm or greater than 100nm. This scale is put into perspective in figure 2.1.
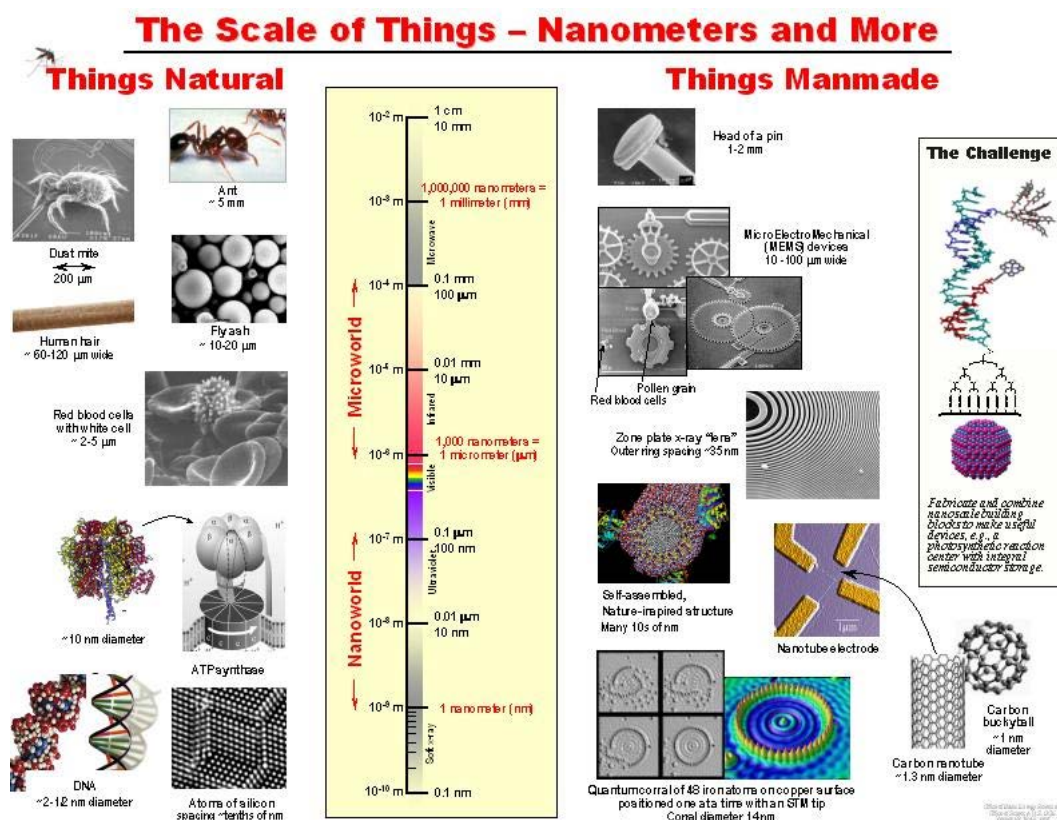
Figure 2.1: The nanoscale and natural and manmade objects for comparison (The Richard E Smalley Institute, Rice University).

The nanoscale is of such interest because it is the transition zone between atoms and bulk materials, and it is in this transition zone that significant deviation from the behaviour of the bulk material can be observed.

2.2.2 Nanothermodynamics

The concept of thermodynamics of small systems, now more commonly referred to as nanothermodynamics, goes back to the 1960s (Hill, 1962) and the consideration of colloidal systems, polymers and macromolecules. In his Faraday lecture Rowlinson (1983) stated that for particles less than a few nanometres "thermodynamics and statistical mechanics lose their meaning." Indeed, the material properties of nanoparticles can be as dependent

on the surrounding medium as on the particle size (Hill, 2001; Hill and Chamberlin, 2002).

An example of how things change at the nanoscale was provided by Wang et al (Wang et al., 2002). It was found that the second law of thermodynamics can be violated for small systems over short time scales. This was achieved by following the trajectory of a colloidal particle captured in an optical trap that was translated relative to surrounding water molecules. The system showed negative entropy over short time frames, but quickly returned to the normal positive entropy over longer time frames.

Another example is provided by Zhang et al. (2003). They found that water is able to drive the structural transformation of nanoparticles. It was reported that ZnS nanoparticles, of average diameter 3nm, exhibited stuctural changes as a function of the surface environment, the structure of the particles was significantly altered upon removal of the synthesis solvent (methanol) and immersion in water. It was thus concluded that the structure and reactivity of nanoparticles depend on both particle size and the surrounding environment.

2.2.3   Nanoparticle movement - Brownian motion

The seemingly random movement of particles suspended in a fluid is most commonly referred to as Brownian motion (or Brownian movement), and its discovery is attributed to the botanist Robert Brown who observed the motion in grains of pollen (Brown, 1828). Since then work by Einstein (1905), Perrin (1909, 1913) and Smoluchowski (1906, 1916a,b), among others, has advanced understanding of this phenomenon.

Many thousands of cases of Brownian motion have been examined, and suspended nanoparticles can be counted among these, and the same general properties of the motion have been found consistently (Mazo, 2002). The rapidity of the motions increases as the size of the suspended particles decreases. The motion is stable over time and persists as long as the particles remain suspended in the fluid. It is independent of most external

influences and thus electric fields, light, gravity and similar disturbances from the outside seem to have no effect on it. However, temperature does have a marked effect, which would be expected from the additional observation that the motion also depends on the viscosity of the medium.

2.2.4   Nanoparticle synthesis

There are two general approaches for making nanoparticles: (i) the top-down approach and (ii) the bottom-up approach. Top-down approaches start from bulk materials and break them down, whereas bottom-up approaches start from atoms or molecules and build them up.

Examples of both methods can be found in nature. Natural top-down methods of fabrication include erosion, volcanic activity (e.g. formation of fly ash), solar activity (radiation degeneration of bulk materials), biological decomposition and digestion. Biological bottom-up methods include protein synthesis (from amino acids), DNA and RNA synthesis (from sugars, phosphate and the nuclides adenosine, guanine, cytosine and thymine) and membrane synthesis (agglomeration of lipids and phospholipids to form organised membranes).

Laboratory and industrial top-down approaches include mechanical-energy methods such as ball milling and atomisation; thermal fabrication methods such as electrospinning; pyrolysis and combustion; and high-energy methods such as arc discharge, laser ablation and ultrasonication (Hornyak et al., 2008). Bottom-up approaches include gas-phase methods such as condensation and thermolysis; liquid-phase methods such as nucleation and sol-gel processes, supramolecular chemistry, and molecular self-assembly (Hornyak et al., 2008).

Some of the methods used for synthesising metal oxide particles are described in the following sections, with a particular emphasis on those methods that can be used to

produce magnetite and hematite.

2.2.4.1   Forced hydrolysis

Many metal oxide particles can be generated by heating the respective salt solution at moderately elevated temperatures (less than 100^oC). However, uniform particles only precipitate under a narrow set of conditions, which need to be determined experimentally. The process may take anywhere from several minutes to several hours or longer and low concentrations of electrolytes must be used to produce well-dispersed uniform particles (Matijevic and Sapieszko, 2000). This requirement is necessary to keep the ionic strength below a critical value in order to prevent coagulation of the precipitates (which consist almost without exception of charged particles).

The method can be used to produce monodisperse simple or internally composite particles, the latter of which are internally heterogenous. Another useful technique is the controlled double-jet precipitation process (CDJP) which can be used for a variety of uniform dispersions, including those of metal oxides of different modal sizes, ranging from several nanometers to several microns.

Hydolysis of FeCl$_3$ solutions   The aging of ferric chloride solutions can yield either colloidal akageneite (β-FeOOH) or hematite (α-Fe$_2$O$_3$). However, the two forms are closely related in the formation of the precipitates.

A variety of morphologies have been obtained by altering the experimental parameters over a small range of conditions. Thus, unifrom dispersions of hematite particles of spherical, ellipsoidal, rod-like, cubic, platelet-type, and other shapes have been produced.

	Fe^{3+} (mol dm^{-3})	Cl^- (mol dm^{-3})	Initial pH	Final pH	Temp. of aging (^{o}C)	Time of aging
(a)	0.018	0.104	1.30	1.10	100	24 h
(b)	0.315	0.995	2.00	1.00	100	9 days
(c)	0.090	0.280	1.65	1.88	100	24 h
(d)	0.090	0.280	1.65	1.70	150	6 h

Table 2.2: Conditions for particles obtained in solutions of FeCl$_3$ + HCl: (a) ellipsoidal hematite, (b) spherical hematite, (c) cubic hematite, (d) rod-like akageneite (Matijevic and Sapieszko, 2000).

There are some other conditions that affect the appearance of hematite. For example, ellipsoidal particles of various anisometries were obtained by the addition of small amounts of phosphate ions into the aging FeCl$_3$ solutions.

2.2.4.2 Gel-sol synthesis

In the 'gel-sol' method, highly viscous condensed gels are used as a solid precursor to the formation of particles. The solid precursor in the form of a gel protects the product particles against coagulation by fixing them on the gel network and, at the same time, works as a reservoir of metal ions to be dissolved and released in metal ions by degrees. If a solid precursor itself does not form a gel structure, some substance such as a lyophobic polymer or a surfactants is used as a subsidiary additive to form a gel-like structure. This idea is based on an earlier finding of selective formation of monodisperse particles on a precursory gel-like solid precipitated from a homogenous dilute solution (Sugimoto, 2000).

Dilute systems Sugimoto and Matijevic (1980) prepared uniform spherical particles of magnetite by partial oxidation of ferrous hydroxide gel with nitrate. The uniform magnetite particles were obtained at a slight excess of Fe^{2+}, and the mean size critically depended on the excess concentration of Fe^{2+} or pH.

Precipitation of ferric oxide gel was also observed in the preparation of spindle-like hematite particles in a dilute ferric chloride solution in the presence of phosphate (Ozaki

et al., 1984). Hamada and Matijevic (1982) prepared uniform particles of pseudocubic hematite by hydrolysis of ferric chloride in aqueous solutions of alcohol (10-50%) at 100^oC for several days.

Condensed systems In most cases, monodisperse particles are synthesized in dilute systems (concentrations of 10^{-4} to 10^{-2} mol dm^{-3}) in order to overcome the essential problem of coagulation. As low concentrations mean low particle productivity, it may be the most serious problem for general monodispersed particles to be used as an industrial products in spite of their ideally controlled properties. To resolve this fundamental problem, the 'gel-sol' method was invented. This method is based on the use of an extremely condensed precursor gel as a matrix of the subsequently generated product particles as well as a reservoir of the metal ions. It may be possible to prevent the coagulation of the particles by fixing them in the gel matrix even at high concentrations of electrolyte and keep them growing without renucleation at a moderate supersaturation by the constant release of the metal ions.

Uniform pseudocubic hematite particles were successfully obtained from a highly condensed ferric hydroxide gel (Sugimoto and Sakata, 1992; Sugimoto et al., 1993c). In a typical procedure, 5.4 dm^{-3} NaOH was added to the same volume of 2.0 dm^{-3} FeCl$_3$ in 10 min at room temperature under agitation, and the resulting highly viscous Fe(OH)$_3$ gel (pH $\approx$ 2.0) was aged in an oven preheated at 100^oC for 8 days. The shape of the hematite particles is drastically changed from pseudocubic to an ellipsoid or peanut-like shape by addition of sulphate or phosphate ions to the Fe(OH)$_3$ gel (Sugimoto et al., 1998, 1993a; Sug, 1993; Sugimoto et al., 1993b).

2.2.4.3 Aerosol synthesis

This method is based on chemical reactions on aerosols. Droplets of a reactant flowing in an inert carrier gas are contacted with the vapour of a coreactant, resulting (as a rule) in

spherical solid particles. If the latter are internally chemically mixed, their composition is determined by the contents of the reactants in the original droplets, since each of the latter acts as a separate 'reaction container'. The technique is also applicable to organic dispersion, and for making coated particles in a continuous process in which cores are formed first, following by encasing them in layers of different compositions and thicknesses (Matijevic and Partch, 2000).

The method described here is limited to the interactions of droplets with surrounding gases. However, other aerosol methods include dispersing aqueous dispersions of particles (e.g. of latex) and evaporating water and nebulising solutions of electrolytes or other substances, which on removal of the liquid result in solid particles, dispersed in the carrier gas. It is also possible to produce aerosols by vaporisation of solids and subsequent condensation.

Description of the aerosol method The essential steps of the method are:

1. Generation of droplets containing one or more reactive liquids.

2. Use of evaporation and nucleation phenomena to narrow the size distribution of the droplets.

3. Exposure of the droplets to a coreactant vapour.

4. Reaction of the liquids in the droplets with the surrounding vapour.

2.2.4.4   Gas phase synthesis

Formation methods of particles through the process of condensation of evaporated atoms or molecules are called gas evaporation methods. Gas evaporation methods are classified depending on the heating method used, such as resistance heating, induction heating, arc heating and laser heating. When a piece of metal is heated and evaporated in a mixture of inert gas containing oxygen, metal oxide particles are obtained. To heat the metal,

resistance or arc heating can be used. The former has problems due to a reaction between the molten metal and the heating device and oxidation of the heating device itself. In the latter, the electrode itself is evaporated, so it does not have the problems that occur in resistance heating (Oda, 2000).

A second method produces metal particles by evaporating metals in an inert gas atmosphere and transfering them to the region where oxidation occurs. This method was developed for monodisperse metal oxide particles in cases where the original metal can be evaporated by an induction heating and oxidation reaction can generate enough heat to recrystallise metal oxide particles.

A third method involves oxide melting followed by evaporation. A laser is the only heating method that evaporates the oxide itself to form particles.

2.2.5 Nanoparticle characterisation

There are many methods of characterising nanoparticles and many more recent methods have helped advance the science of nanotechnology (Hornyak et al., 2008). Typical particle sizing methods include dynamic light scattering (DLS); small angle x-ray scattering (SAXS), which can also be used for surface analysis; transmission or scanning electron microscopy (TEM and SEM respectively), which are also used for particle imaging. Advanced techniques such as atomic force microscopy (AFM) and surface tunnelling microscopy (STM) allow topological and surface structure characterisation with atomic scale resolution. Many techniques from chemistry are also used to characterise crystal structures and particle surfaces, which can also have adsorbed molecules, as well as chemical properties of particles. These techniques include x-ray diffraction (XRD); small angle neutron scattering (SANS); surface enhanced Raman spectroscopy (SERS); atomic absorption spectroscopy (AAS); and many more. A more extensive list and description of these techniques can be found in Hornyak et al. (2008) and further information can be

found in the various monographs on individual techniques, e.g. Berne and Pecora (1976) for DLS and Silver and Hunter (1993) for electron microscopy.

2.2.6 Natural nanoparticles

Nanoparticles occur naturally in the environment and can have important influences on natural processes. Atmospheric aerosols, for example, directly and indirectly affect the radiative balance of the Earth's atmosphere (Wang et al., 2010). A sample of natural nanoparticles from a site in Ireland (O'Dowd et al., 2004) found particles comprised of sea salt, sulphates and miscellaneous organic chemicals most likely having their origin in plankton near the sea's surface. Studies on tap water (Senftle et al., 2007; Barkatt et al., 2009) found magnetic iron nanoparticles present, most likely as products of corrosion, which could also serve as sites for the adsorption of contaminants such as lead, copper and arsenic. Atmospheric measurements carried out in city centres, isolated islands and forests, and the remote troposphere have never failed to encounter periods characterised by concentrations of up to 10^6 nanoparticles/cm^3 (Smith, 2009), which, particularly when produced from polluting processes, could cause health problems (Bang and Murr, 2002).

2.2.6.1 Biomineralization

It is well known that crystals nucleate and grow from saturated solutions. And so they do *in vitro*, but not necessarily *in vivo*. Biology has chosen another pathway; crystals are grown from an unstable solid colloidal phase, almost devoid of water (Weiner, 2008). The identification of this unexpected strategy has its origins in a much overlooked paper by Towe and Lowenstam (1967) showed for the first time that in the mineralized teeth of the chiton, a segmented mollusk, the initially formed mineral phase is not the same as the mature form, but transforms into the more stable mature phase.

The crystallization process normally follows from a supersaturated salt solution to the formation of nucleates and then crystallization. However, the natural process of

biomineralization does not follow this scheme and cells have developed a different route to produce minerals. This involves the formation of a precursor, an unstable colloidal phase, where little water is present, before the mature crystal phase is formed. In the example of Chiton teeth (Towe and Lowenstam, 1967) this gives a ferrihydrate phase before the formation of crystalline magnetite. It should be noted that the site of the precursor is not well known (Weiner, 2008).

The disorder in the precursor can also be partially observed in the final crystal, which Gueta (2003) termed a sort of 'memory' of how the crystal was formed. The criteria to assess the origin of magnetite are of prime importance because of their significance as biomarkers for extraterrestrial life and paleoenvironmental indicators. It is still unclear if morphology and magnetic properties of crystals do quantitatively allow the differentiation of abiotic from biotic magnetite crystals of nanometre size(Faivre and Zuddas, 2006). The extensive debate about a possible biogenic origin of nano-sized magnetite crystals in the Martian meteorite ALH84001 emphasized that bacterial magnetite cannot always be obviously differentiated from inorganic magnetite (Bradley et al., 1997; Becker et al., 1999; Kirschvink et al., 1997; McKay et al., 1996; Thomas-Keprta et al., 2000; Treiman and Romanek, 1998; Devouard et al., 1998).

Since the discovery of magnetic bacteria, the nanobiomineral inclusions synthesized within the cell, termed magnetosomes, have prompted considerable interest. Magnetotactic bacteria are ubiquitous Gram-negative prokaryotes that respond to a magnetic field. They are found in fresh and saltwater sediments. Although some strains can be grown under aerobic conditions, magnetosome synthesis only occurs under microaerobic conditions. Magnetic bacteria biomineralize magnetite (and less commonly greigite) crystals within lipid vesicles arranged in chains along the cell (typically 2040 particles long), which are responsible for the magnetotaxis. The magnetosomes are highly consistent with respect to size and morphology defined for each strain, which suggests a large degree of genetic

control over the synthetic process. The bacteria have a sensitive iron-uptake system that can concentrate large quantities of iron within the cell to biomineralize magnetosomes, and it is this biomineralization process that has attracted the most biological and materials science interest(Staniland et al., 2007; Amemiya et al., 2007; Staniland et al., 2008; Tanaka et al., 2010; Staniland et al., 2010).

Magnetosomes produced by magnetotactic bacteria are of great interest for understanding bacterial biomineralization along with sedimentary magnetism and environmental magnetism. One of the most intriguing species, *Magnetobacterium bavaricum* can synthesize hundreds of bullet-shaped magnetite magnetosomes per cell, which contribute significantly to magnetic properties of sediments (Li et al., 2010).

Recently, magnetosomes have attracted much attention because

1. they serve as an ideal system to understand the biomineralization process and the magnetite-based magnetoreception;

2. fossil magnetosomes (also called magnetofossils) could be suitable biomarkers for searching early terrestrial or extraterrestrial life and as potential proxies for reconstructing paleoenvironment;

3. and functionalized magnetosomes have potential applications as novel magnetic nano-biomaterials in biomedical and biotechnological fields.

2.3 Magnetism

Magnetism originates from the movement of electrons, such as in atoms, and each atom represents a tiny permanent magnet in its own right. The electron orbits the nucleus of an atom and produces its own orbital magnetic moment. There is also a spin magnetic moment because the electron itself spins on its own axis (figure 2.2 below) like the earth as it orbits the sun. In most materials these magnetic moments cancel each other out,

and there is no overall magnetisation.
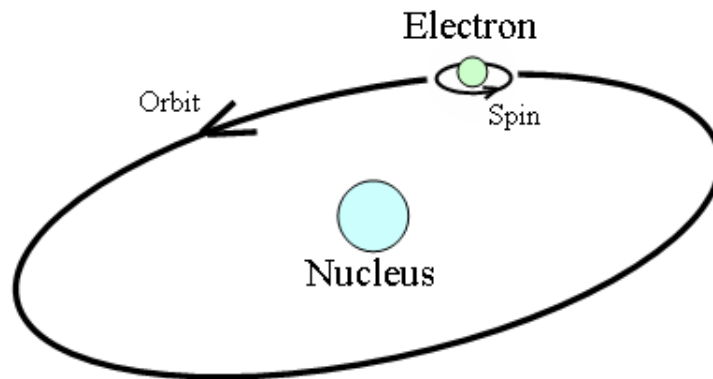
Figure 2.2: The orbit of a spinning electron about the nucleus of an atom (Magnetic Materials Group, University of Birmingham).

2.3.1 Magnetic behaviour

All materials can be classified in terms of their magnetic behaviour. The two most common types of magnetic behaviour are diamagnetism and paramagnetism. These account for the magnetic properties of most of the elements in the periodic table at room temperature (see figure 2.3). These elements are usually referred to as non-magnetic, and those which are usually referred to as magnetic are actually classified as ferromagnetic.

Figure 2.3: Periodic table showing the type of magnetic behaviour of each element at room temperature (Magnetic Materials Group, University of Birmingham).

The only other type of magnetism observed in pure elements at room temperature is antiferromagnetism. Finally, magnetic materials can also be classified as ferrimagnetic although this is not observed in any pure element but can only be found in compounds, such as the mixed oxides, known as ferrites, from which ferrimagnetism derives its name.

2.3.1.1 Diamagnetism

The orbital motion of electrons (see figure 2.2) creates tiny atomic current loops, which produce magnetic fields. When an external magnetic field is applied to a material, these current loops will tend to align in such a way as to oppose the applied field. This may be viewed as an atomic version of Lenz's law: induced magnetic fields tend to oppose the change which created them. Materials in which this effect is the only magnetic response are called diamagnetic. All materials are inherently diamagnetic, but if the atoms have some net magnetic moment as in paramagnetic materials, or if there is long-range ordering of atomic magnetic moments as in ferromagnetic materials, these stronger effects are always

dominant. Diamagnetism is the residual magnetic behaviour when materials are neither paramagnetic nor ferromagnetic.

Any conductor will show a strong diamagnetic effect in the presence of changing magnetic fields because circulating currents will be generated in the conductor to oppose the magnetic field changes. A superconductor will be a perfect diamagnet since there is no resistance to the forming of the current loops.

2.3.1.2 Paramagnetism

Several theories of paramagnetism exist, and these theories are valid for specific types of material. For example, the Langevin model states that each atom has a magnetic moment which is randomly oriented as a result of thermal agitation. The application of a magnetic field creates a slight alignment of these moments and hence a low magnetisation in the same direction as the applied field. As the temperature increases, so does the thermal agitation and it becomes more and more difficult for the atomic magnetic moments to align and thus the susceptibility will then decrease. This type of behaviour is known as the Curie law. It is represented mathematically in equation 1, shown below, where C is a material constant known as the Curie constant

$$\chi = \frac{C}{T}. \tag{1}$$

The materials that obey this law are materials in which the magnetic moments are localised at atomic or ionic sites and where there is no interaction between neighbouring magnetic moments. The hydrated salts of the transition metals, e.g. $CuSO_4 \cdot 5H_2O$, are examples of materials that exhibit this type of behaviour. The transition metal ions, which themselves have a magnetic moment, are surrounded by a number of non-magnetic ions or atoms, which then inhibit any interaction between neighbouring magnetic moments.

It was discovered, though, that the Curie law was in fact a special case of the more

general Curie-Weiss law (shown in equation 2). This incorporates a temperature constant, θ, and is derived from Weiss' theory that incorporates the interaction between magnetic moments

$$\chi = \frac{C}{T - \theta}. \tag{2}$$

The values of θ in equation 2 can either be positive, negative or zero. When $\theta = 0$ then the Curie-Weiss law simply equates to the Curie law in equation 1. When θ is non-zero then there is an interaction between neighbouring magnetic moments and the material is only paramagnetic above a certain temperature. If θ is positive then the material is ferromagnetic below this temperature and the value of θ corresponds to a transition temperature known as the Curie temperature, T_C. If θ is negative then the material is antiferromagnetic below the this temperature, and it is then known as the Néel temperature, T_N. It is important to note that this equation is only valid when the material is in a paramagnetic state. It is also not valid for many metals as the electrons contributing to the magnetic moment are not localised, but it is valid for metals such as the rare-earths, as the electrons that create the magnetic moment are closely bound.

Another model of paramagnetism is the Pauli model. This represents materials where the electrons can interact to form a conduction band, and is valid for most paramagnetic metals. The conduction electrons are considered to be free, and under an applied field an imbalance between electrons with opposite spin is established leading to a low magnetisation in the same direction as the applied field. The susceptibility is independent of temperature. But the electronic band structure may be affected by temperature, and this will in turn have an effect on the susceptibility.

2.3.1.3 Ferromagnetism

Ferromagnetism is only possible when atoms are arranged in a lattice and the atomic magnetic moments can interact to align parallel to each other. This effect is explained

in classical theory by the presence of a molecular field within the ferromagnetic material, which was first postulated by Weiss in 1907. This field is sufficient to magnetise the material to saturation. In quantum mechanics, the Heisenberg model of ferromagnetism describes the parallel alignment of magnetic moments in terms of an exchange interaction between neighbouring moments.

Weiss postulated the presence of magnetic 'domains' within the material, regions where the atomic magnetic moments are aligned. The movement of these domains determines how the material responds to a magnetic field and as a consequence the susceptibility is a function of applied magnetic field. Therefore, ferromagnetic materials are usually compared in terms of saturation magnetisation (magnetisation when all domains are aligned) and not in terms of susceptibility.

The only elements to exhibit ferromagnetism at room temperature and above are iron (Fe), cobalt (Co) and nickel (Ni). As the temperature increases, so does the thermal agitation of the atoms, and thus the degree of alignment of the atomic magnetic moments decreases. This results in a decrease in the saturation magnetisation. When the thermal agitation is large enough then the material becomes paramagnetic. As mentioned above in section 2.3.1.2, the temperature of this transition is the Curie temperature, T_C (the Curie temperatures for the ferromagnetic elements are: for Fe, $T_C = 770^oC$; for Co, $T_C = 1131^oC$; for Ni, $T_C = 358^oC$).

2.3.1.4   Antiferromagnetism

In the periodic table the only element exhibiting antiferromagnetism at room temperature is chromium. Antiferromagnetic materials are very similar to ferromagnetic materials but the exchange interaction between neighbouring atoms leads to the anti-parallel alignment of the atomic magnetic moments. Therefore, the magnetic field cancels out and the material appears to behave in the same way as a paramagnetic material. Like ferromagnetic materials these materials become paramagnetic above a transition temperature, known

as the Néel temperature, T_N. (e.g. for chromium, $T_N = 37^o$C).

2.3.1.5 Ferrimagnetism

Ferrimagnetism is only observed in compounds, which have more complex crystal structures than pure elements. Within these materials the exchange interactions lead to parallel alignment of atoms in some of the crystal sites and anti-parallel alignment of others. The material breaks down into magnetic domains, just like a ferromagnetic material and the magnetic behaviour is also very similar, although ferrimagnetic materials usually have lower saturation magnetisations. For example in barium ferrite (BaO·6Fe$_2$O$_3$) the unit cell contains 64 ions of which the barium and oxygen ions have no magnetic moment, 16 Fe^{3+} ions have moments aligned parallel and 8 Fe^{3+} aligned anti-parallel giving a net magnetisation parallel to the applied field, but with a relatively low magnitude as only 1/8 of the ions contribute to the magnetisation of the material.
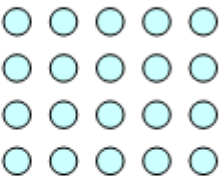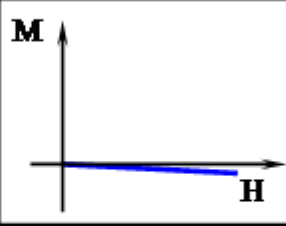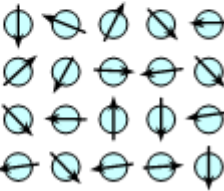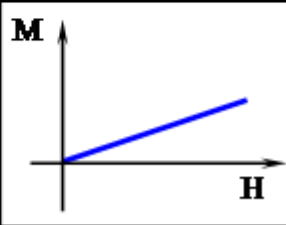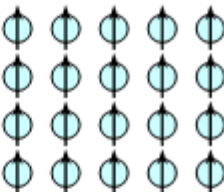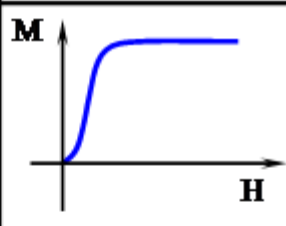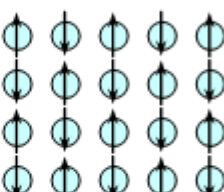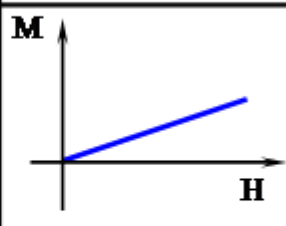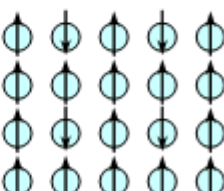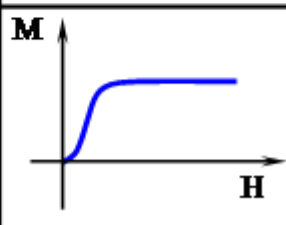
Type	Atomic / Magnetic Behaviour		
Dia-magnetism		Atoms have no magnetic moment	M vs H graph (slight negative slope)
Para-magnetism		Atoms have randomly oriented magnetic moments	M vs H graph (positive linear)
Ferro-magnetism		Atoms have parallel aligned magnetic moments	M vs H graph (saturating curve)
Antiferro-magnetism		Atoms have anti-parallel aligned magnetic moments	M vs H graph (positive linear)
Ferri-magnetism		Atoms have mixed parallel and anti-parallel aligned magnetic moments	M vs H graph (saturating curve)

Figure 2.4: Table summing up the different types of magnetic behaviour (Magnetic Materials Group, University of Birmingham).

2.3.2 Intrinsic Properties of Magnetic Materials

The intrinsic properties of a magnetic material are those properties that are characteristic of the material and are unaffected by the microstructure (e.g. grain size, crystal orientation of grains). These properties include the Curie temperature, the saturation magnetisation and the magnetocrystalline anisotropy.

2.3.2.1 Saturation Magnetisation

The saturation magnetisation (M_S) is a measure of the maximum amount of field that can be generated by a material. It will depend on the strength of the dipole moments on the atoms that make up the material and how densely they are packed together. The atomic dipole moment will be affected by the nature of the atom and the overall electronic structure within the compound. The packing density of the atomic moments will be determined by the crystal structure (i.e. the spacing of the moments) and the presence of any non-magnetic elements within the structure.

For ferromagnetic materials, at finite temperatures, M_S will also depend on how well these moments are aligned, as thermal vibration of the atoms causes misalignment of the moments and a reduction in M_S. For ferrimagnetic materials not all of the moments align parallel, even at zero Kelvin and hence M_S will depend on the relative alignment of the moments as well as the temperature.

The saturation magnetisation is also referred to as the spontaneous magnetisation, although this term is usually used to describe the magnetisation within a single magnetic domain.

2.3.2.2 Magnetic Anisotropy

In a crystalline magnetic material the magnetic properties will vary depending on the crystallographic direction in which the magnetic dipoles are aligned. Figure 2.5 demonstrates this effect for a single crystal of cobalt. The hexagonal crystal structure of Co can

be magnetised easily in the [0001] direction (i.e. along the c-axis), but has hard directions of magnetisation in the $< 10\bar{1}0 >$ type directions, which lie in the basal plane (90° from the easy direction).

A measure of the magnetocrystalline anisotropy in the easy direction of magnetisation is the anisotropy field, H_a (illustrated in figure 2.5), which is the field required to rotate all the moments by 90° as one unit in a saturated single crystal. The anisotropy is caused by a coupling of the electron orbitals to the lattice, and in the easy direction of magnetisation this coupling is such that these orbitals are in the lowest energy state.

The easy direction of magnetisation for a permanent magnet, based on ferrite or the rare earth alloys, must be uniaxial, however, it is also possible to have materials with multiple easy axes or where the easy direction can lie anywhere on a certain plane or on the surface of a cone. The fact that a permanent magnet has uniaxial anisotropy means that it is difficult to demagnetise as it is resistant to rotation of the direction of magnetisation.
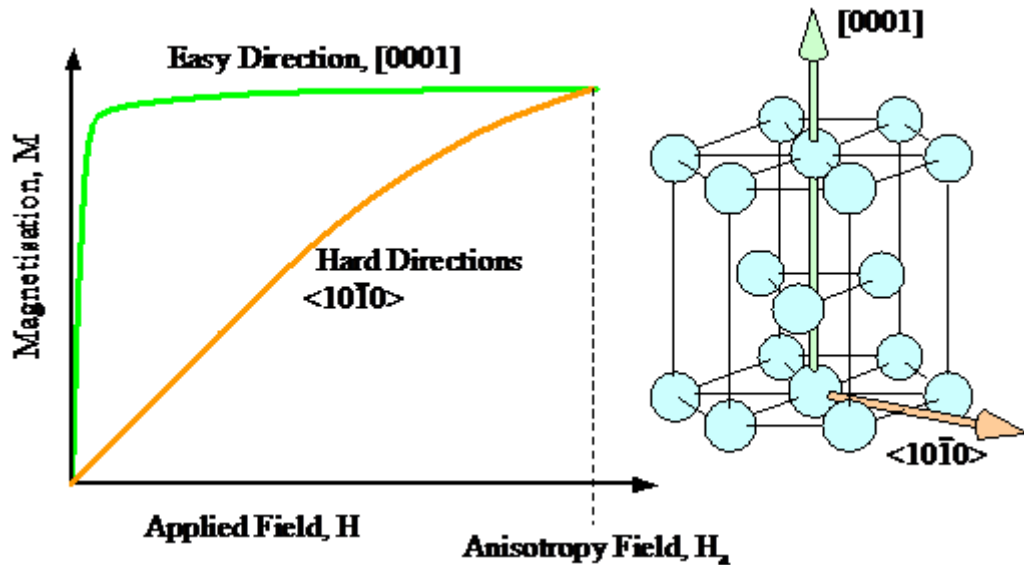
Figure 2.5: The magnetocrystalline anisotropy of cobalt.

2.3.2.3 Magnetic Hysteresis

Ferromagnetic and ferrimagnetic materials have non-linear initial magnetisation curves (i.e. the dotted lines in figure 2.6), as the changing magnetisation with applied field is due to a change in the magnetic domain structure. These materials also show hysteresis and the magnetisation does not return to zero after the application of a magnetic field. Figure 2.6 shows a typical hysteresis loop; the two loops represent the same data, however the red loop is the polarisation ($J = \mu_0 M = B - \mu_0 H$) and the blue loop the induction, both plotted against the applied field.

Illustrated in the first quadrant of the loop is the initial magnetisation curve (dotted line), which shows the increase in polarisation (and induction) on the application of a field to an unmagnetised sample. In the first quadrant the polarisation and applied field are both positive, i.e. they are in the same direction. The polarisation increases initially by the growth of favourably oriented domains, which will be magnetised in the easy direction of the crystal. When the polarisation can increase no further by the growth of domains then the direction of magnetisation of the domains will rotate away from the easy axis to align with the field. When all of the domains have fully aligned with the applied field then saturation is reached and the polarisation can increase no further.
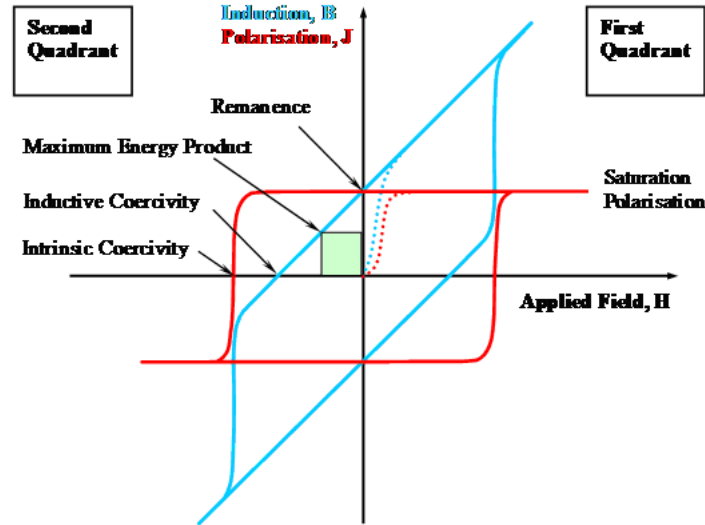
Figure 2.6: A typical hysteresis loop for a ferromagnetic or ferrimagnetic material.

If the field is removed then the polarisation returns along the solid red line to the y-axis (i.e. $H = 0$), and the domains will return to their easy direction of magnetisation, resulting in a decrease in polarisation. In figure 2.6, the line from the saturation point to the y-axis is horizontal, which is representative of a well aligned material, where the domains are magnetised in the easy direction of the crystal at the saturation point.

If the direction of applied field is reversed (i.e. to the negative direction) then the polarisation will follow the red line into the second quadrant. The hysteresis means that the polarisation lags behind the applied field and will not immediately switch direction into the third quadrant (i.e. negative polarisation). The polarisation will only decrease after a sufficiently high field is applied to nucleate and grow domains favourably oriented with respect to the applied field or to rotate the direction of magnetisation of the domains towards the applied field. After applying a high enough field saturation polarisation will be achieved in the negative direction. If the applied field is then decreased and again applied in the positive direction then the full hysteresis loop is plotted.

If the field is repeatedly switched from positive to negative directions and is of sufficient

magnitude then the polarisation and induction will cycle around the hysteresis loop in an anti-clockwise direction. The area contained within the loop indicates the amount of energy absorbed by the material during each cycle of the hysteresis loop.

2.3.3 Magnetic nanoparticles

Magnetic nanoparticles can be found everywhere, and they are found in the strangest of places: the human brain contains over 108 magnetic nanoparticles of magnetite-maghemite per gram of tissue that may be responsible for a variety of biological effects (Kirschvink et al., 1992).They are found as geomagnetic navigational aids in bacteria, eukaryotic algae, and the bodies of higher animals (Kirschvink et al., 1985; Kirschvink, 1989; Wiltschko and Wiltschko, 1995) such as homing pigeons (Hanzlik et al., 2000), migratory birds, ants, bees, salmon, tuna, sharks, rays, salamanders, newts, mice, cetaceans, etc., as the ferrihydrite-like mineral cores of the most common iron storage protein ferritin (Mann et al., 1989), present in almost every cell of plants and animals including humans, as key-stone crystals in the cells of hornet combs (Stokroos et al., 2001), as bacterial micro-fossils (Kirschvink et al., 1985; Petersen et al., 1986), precipitated to bacterial cell walls (Fortin et al., 1997; Watson et al., 2000), etc. In medical diagnosis magnetic nanoparticles are used as magnetic resonance imaging (MRI) contrast agents (Grttner and Teller, 1999; Roch et al., 1999; Bonnemain, 1998).

2.3.4 Magnetic properties and particle size

The magnetic properties of magnetic materials can change significantly with decreasing particle size.

2.3.4.1 Magnetic domains

The concept of magnetic domains was proposed by Weiss who built on earlier work carried out by Ampre, Weber and Ewing, suggesting their existence. The findings of this work

revealed that, within a domain, large numbers of atomic moments are aligned, typically $10^{12} - 10^{18}$, over a much larger volume than was previously suspected (Magnetic Materials Group, University of Birmingham). The magnetisation within the domain is saturated and will always lie in the easy direction of magnetisation when there is no externally applied field. The direction of the domain alignment across a large volume of material is more or less random and hence the magnetisation of a specimen can be zero.

In order to explain the fact that ferromagnetic materials with spontaneous magnetisation could exist in the demagnetised state, Weiss proposed the concept of magnetic domains, building on earlier work carried out by Ampre, Weber and Ewing, that suggested their existence. The findings of this work revealed that within a domain large numbers of atomic moments are aligned, typically 10^{12} - 10^{18}, over a much larger volume than was previously suspected. The magnetisation within the domain is saturated and will always lie in the easy direction of magnetisation when there is no externally applied field. The direction of the domain alignment across a large volume of material is more or less random and hence the magnetisation of a specimen can be zero.
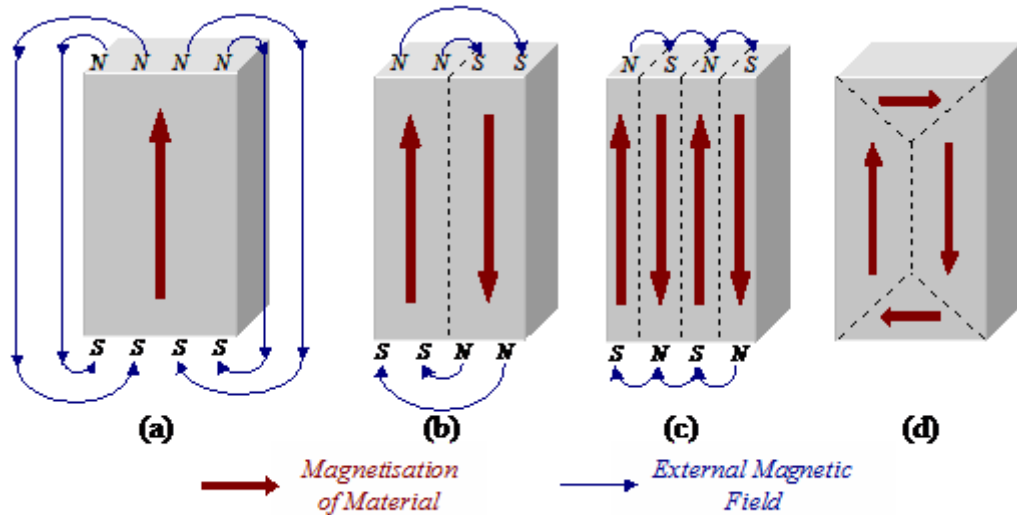
Figure 2.7: Schematic illustration of the break up of magnetisation into domains (a) single domain, (b) two domains, (c) four domains and (d) closure domains.

31

Magnetic domains exist in order to reduce the energy of the system. A uniformly magnetised specimen as shown in figure 2.7(a) has a large magnetostatic energy associated with it. This is the result of the presence of magnetic free poles at the surface of the specimen generating a demagnetising field, H_d. From the convention adopted for the definition of the magnetic moment for a magnetic dipole the magnetisation within the specimen points from the south pole to the north pole, while the direction of the magnetic field points from north to south. Therefore, the demagnetising field is in opposition to the magnetisation of the specimen. The magnitude of H_d is dependent on the geometry and magnetisation of the specimen. In general if the sample has a high length to diameter ratio (and is magnetised in the long axis) then the demagnetising field and the magnetostatic energy will be low.

The break up of the magnetisation into two domains as illustrated in Figure 5(b) reduces the magnetostatic energy by half. In fact if the magnet breaks down into N domains then the magnetostatic energy is reduced by a factor of $1/N$, hence figure 2.7(c) has a quarter of the magnetostatic energy of figure 2.7(a). Figure 2.7(d) shows a closure domain structure where the magnetostatic energy is zero, however, this is only possible for materials that do not have a strong uniaxial anisotropy, and the neighbouring domains do not have to be at 180° to each other.

Although the magnetostatic energy decreases as the number of domains increases, the material will not continue to split into more and more domains because the introduction of a domain wall also raises the overall energy of the system. This is because the domain wall has an energy associated with it, proportional to its area. The schematic representation of the domain wall, shown in figure 2.8, illustrates that the dipole moments of the atoms within the wall are not pointing in the easy direction of magnetisation and hence are in a higher energy state. In addition, the atomic dipoles within the wall are not at 180° to each other and so the exchange energy is also raised within the wall. Therefore,

the domain wall energy is an intrinsic property of a material depending on the degree of magnetocrystalline anisotropy and the strength of the exchange interaction between neighbouring atoms. The thickness of the wall will also vary in relation to these parameters, as a strong magnetocrystalline anisotropy will favour a narrow wall, whereas a strong exchange interaction will favour a wider wall.

A minimum energy can therefore be achieved with a specific number of domains within a specimen. This number of domains will depend on the size and shape of the sample (which will affect the magnetostatic energy) and the intrinsic magnetic properties of the material (which will affect the magnetostatic energy and the domain wall energy).
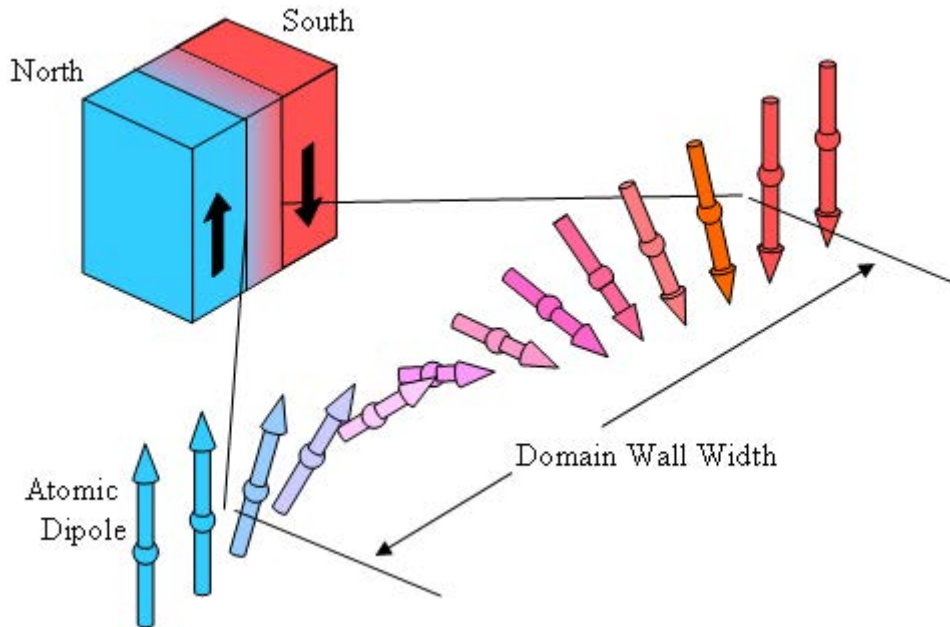
Figure 2.8: Schematic representation of a 180° domain wall.

A bulk single crystal is made up of many magnetic domains but as the particle size decreases it becomes closer to the equilibrium domain size of the bulk material (10^6 to 1 nm depending on the intrinsic material properties (Rancourt, 2001)).

At this size the particle changes from being a multi-domain bulk crystal to a single-

domain particle. This is an important boundary that dramatically affects the particle's magnetic properties (Stoner and Wohlfarth, 1948). Goya et al. (2003) have studied the evolution of this transition using spherical magnetite nanoparticles.

2.3.4.2 Superparamagnetism

Superparamagnetism is a phenomenon by which magnetic materials may exhibit behaviour similar to paramagnatism even when at temperatures below the Curie or the Neel temperature.

In sufficiently small nanoparticles ($\approx$ 1-10 nm), magnetization can randomly flip direction under the influence of temperature. The typical time between two flips is called the Neel relaxation time. In the absence of external magnetic field, when the time used to measure the magnetization of the nanoparticles is much longer than the Neel relaxation time, their magnetization appears to be in average zero: they are said to be in the superparamagnetic state.

In this state, an external magnetic field is able to magnetize the nanoparticles, similarly to a paramagnet (see 2.9). In this case even when the temperature is below the Curie or Neel temperature (and hence the thermal energy is not sufficient to overcome the coupling forces between neighbouring atoms), the thermal energy is sufficient to change the direction of magnetization of the entire crystallite. The resulting fluctuations in the direction of magnetization cause the magnetic field to average to zero.
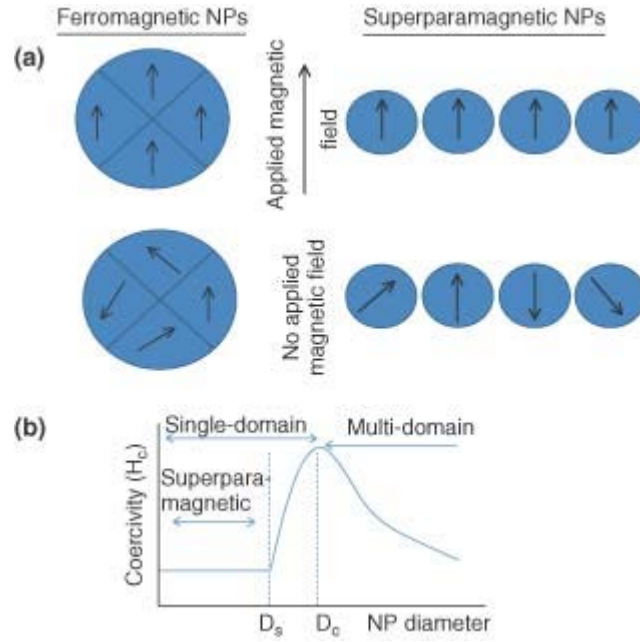
Figure 2.9: Illustration of superparamagnetism and the magnetism of superparamagnetic particles.

Thus the material behaves in a manner similar to paramagnetism, except that instead of each individual atom being independently influenced by an external magnetic field, the magnetic moment of the entire crystallite tends to align with the magnetic field.

2.4   Colloidal stability

Aggregation occurs because a net attractive force exists between particles. These forces vary in type but also in range of action, being significant only over certain distances and a thorough summary of all types of intermolecular and surface forces was compiled by Israelachvili (1991).

2.4.1   DLVO Theory

The DLVO theory, developed independently by Derjaguin and Landau (1945) and Verwey and Overbeek (1948), treats the stability of colloidal systems based on the energy changes

that take place when the particles approach one another. The total interaction energy of the particles can be estimated from the summation of estimations of the energy due to repulsion (from the overlap of electric double layers) and those due to attraction (London-van der Waals energy). This can be expressed simply by

$$V_T = V_A + V_R \tag{3}$$

where V_T is the total interaction energy, V_A is the attractive interaction energy and V_R is the repulsive interaction energy. The stability of the colloidal system can then be interpreted form the nature of the interaction energy-distance curve as illustrated in 2.10.
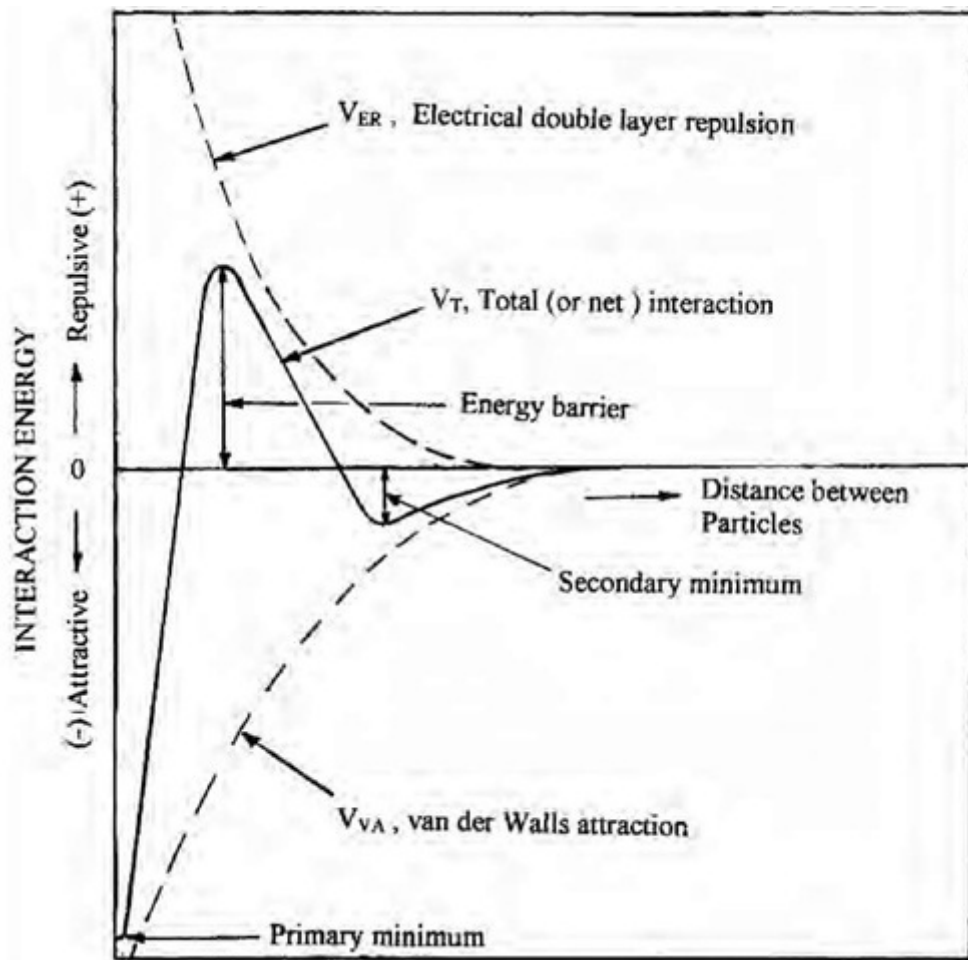
Figure 2.10: DLVO type interaction curves.

2.4.1.1 van der Waals interactions

The attractive forces, originally postulated by van der Waals to explain non-ideal gas behaviour, are dived into three types of intermolecular attraction (Shaw, 1992):

- Dipole-dipole interactions (also known as Keesom or orientation force) that result from the mutual orientation of molecules in such a way that there is a net attraction

- Dipole-induced dipole interactions (also known as Debye or induction force) that results in a net attraction due to dipolar molecules inducing dipoles in other molecules

37

- Induced dipole-induced dipole interactions (also known as London or dispersion force), first explained by London (1930) and are due to the polarisation of one molecule by fluctuations in the charge distribution in a second molecule, and vice versa.

Generally, unless the materials are highly polar, London dispersion forces account for nearly all of the resultant van der Waals attraction. This London dispersion force is very short range, however, and decays rapidly with the intermolecular distance. The dispersion forces for an assembly of molecules, such as a colloidal particle, can be estimated from the summation of the attractions between all molecule pairs. Such summations predict that the dispersion forces between colloidal particles do not decay as rapidly as the dispersion forces between individual molecules.

In the case of two identical spheres, van der Waals interaction between particles can be calculated (Garcia-Martinez et al., 2004) by

$$V_A = -\frac{A_{131}}{12}\left[\frac{1}{h} - \frac{5.32}{\lambda}\ln\left(\frac{\lambda}{5.32h}\right)\right] \tag{4}$$

where h is the interparticle distance, λ is the characteristic wavelength of the atoms and A is the Hamaker constant which may be obtained from Israelachvili (1991) as

$$A_{131} \approx \left(\sqrt{A_{11}} - \sqrt{A_{33}}\right)^2 \tag{5}$$

2.4.1.2 Electrostatic interactions

When in contact with a polar medium, such as water, most substances acquire a surface charge which then influences the distribution of nearby ions in the polar medium. Ions of opposite charge (counter-ions) are attracted towards the surface and ions of like charge (co-ions) are repelled. This leads to a distribution of nearby ions known as the electric

double layer, with an excess of counter-ions near the surface and a diffuse layer of counter-ions and co-ions moving further away from the surface. This is illustrated in figure 2.11.
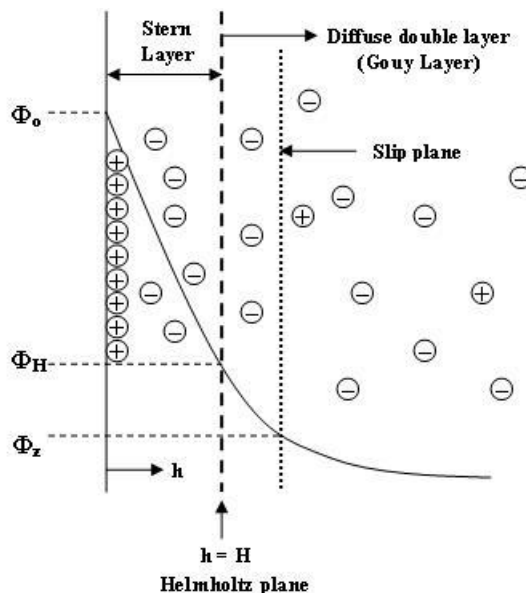
Figure 2.11: Illustration of the electric double layer.

The double layer consists of two layers, the Stern layer and the Gouy layer (also called diffuse double layer), and the two layers are separated by the Helmholtz plane. Between the solid surface and the Helmholtz plane is the Stern layer, where the electric potential drops linearly through the tightly bound layer of solvent and counter-ions. Beyond the Helmholtz plane until the counter ions reach average concentration in the solvent is the Gouy layer or diffuse double layer. In the Gouy layer, the counter ions diffuse freely and the electric potential does not reduce linearly.

Verwey and Overbeek (1948) obtained an approximated analytical expression for the electric double-layer interaction energy by integrating the contributions over the entire surface. In the case of two dissimilar particles with a low surface potential and a small electric double-layer thickness compared to the size of the particles, the approximation

for the electric double layer interaction was given by Hogg et al. (1966) as

$$V_R = \frac{\varepsilon a_1 a_2 \left(\psi_1^2 \psi_2^2\right)}{4 \left(a_1 a_2\right)} \left[\frac{2\psi_1 \psi_2}{\psi_1^2 + \psi_2^2} \ln \frac{1 + e^{-\kappa h}}{1 - e^{-\kappa h}} + \ln \left(1 - e^{-2\kappa h}\right) \right] \qquad (6)$$

where ε is the dielectric permittivity of the medium (in F m^{-1}), a_i is the particle radius (in m), ψ_i is the outer Helmholtz plane potential of particle i (in V), κ is the Debye length (in m) and h is the interparticle distance (in m).

2.4.2 Extended DLVO Theory

Interest in the use of magnetic fields to separate mineral fines resulted in an extension of the DLVO theory to consider the magnetic interaction between the particles (Svoboda, 1981; van Kleef et al., 1983). The extended DLVO theory considers the total potential energy of interaction between magnetic particles in surrounding media as the sum of the attractive (van der Waals), repulsive (electrostatic) and magnetic interaction energies of the particles, thus

$$V_T = V_A + V_R + V_M \qquad (7)$$

where V_T, V_A and V_R are the same as defined above and V_M is the magnetic interaction energy.

2.4.2.1 Magnetic interactions

Materials can be classified by their response to an applied magnetic field resulting in the magnetic behaviours, as described in section 1.3.1. This is important as the magnetic interaction between ferromagnetic particles is different from that between paramagnetic particles, and an applied magnetic field will alter the interactions differently depending on the material's magnetic behaviour. Equations for the estimation of the magnetic interaction can be found in the review by Garcia-Martinez et al. (2004), for example, for

ferromagnetic particles the interaction energy can be defined as

$$V_{M,ferromagnetic} = \frac{\mu_1 \mu_2}{r^3} - \frac{3(\mu_1 r)(\mu_2 r)}{r^5} \tag{8}$$

where μ_i is the magnetic dipole moment of particle i (in A m^{-1}) and r is the separation between particle centres (in m). The magnetic interaction for paramagnetic particles can be defined as

$$V_{M,paramagnetic} = \frac{4\pi a^6 \chi^2 B_0^2}{\mu_0 (2a + h)^2} \tag{9}$$

where μ_0 is the magnetic permeability of a vacuum (in H m^{-1}), a_i is the radius of particle i, χ is the magnetic susceptibility, B_0 is the magnetic induction (in T), h is the interparticle separation (in m).

2.5 Fractals and fractal aggregates

2.5.1 Fractal geometry

Classical Euclidean geometry is based on objects that exist in integer dimensions. We imagine the world to be made up of objects which exist in integer dimensions - single dimensional points, one dimensional lines and curves, two dimension plane figures like circles and squares, and three dimensional solid objects such as spheres and cubes. However, many things in nature do not conform to these ideal forms. Clouds, mountain ranges, coastlines, trees; all are best described with a dimension somewhere between two whole numbers. While a straight line has a dimension of exactly one, a fractal curve will have a dimension between one and two, depending on how much space it takes up as it curves and twists. The more a fractal fills up a plane, the closer it approaches two dimensions. In the same manner of thinking, a wavy fractal scene will cover a dimension somewhere between two and three. Hence, a fractal landscape which consists of a hill covered with tiny bumps would be closer to two dimensions, while a landscape composed of a rough

surface with many average sized hills would be much closer to three dimensions.
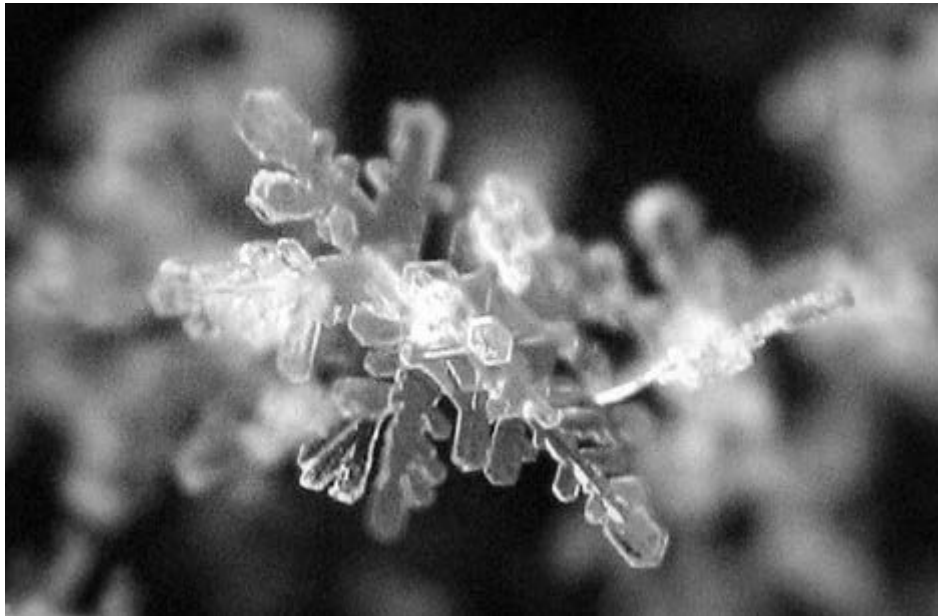
Figure 2.12: Examples of fractals in nature - a snowflake.

Figure 2.13: Examples of fractals in nature - Tibet from space.

Figure 2.14: Examples of fractals in nature - leaf veins.

The concept of fractal geometry came about in the 1970s, and gained notoriety with the publication of Benoit Mandelbrot's seminal work, *Les Objets Fractals: forme, hazard et dimension* (Mandelbrot, 1975). The book brought together observations from areas as diverse as coastline measurements, Brownian motion and a host of "monstrous" mathematical sets.

2.5.2 Aggregate structures

The relationship which embodies the whole concept of the fractal structure of aggregates is very simple:

$$M \propto R^{D_f} \tag{10}$$

where M is the mass of the aggregate, R is a linear measure of size an D_f is the fractal dimension.

This equation can take on two subtly different meanings without losing its validity.

43

The first meaning is the scaling in terms of the mass (number of particles) contained within aggregates of different sizes within a cluster polydisperse aggregating system. As a consequence of the fractal structure of the aggregates, the mass of each aggregate is related to its linear size by the above equation. The second meaning is in terms of the structure of within any individual aggregate. If an arbitrary particle within an aggregate is picked and an imaginary sphere centred upon it, the number of other particles enclosed within the imaginary sphere is related to the linear size of the sphere, R, by the above equation. This relationship is only asymptotically correct in the limit of large aggregates and is quite inaccurate for aggregates of only a few particles.

The fractal dimension cannot take on just any value. Although a set of disconnected points such as a Cantor dust can have a fractal dimension of less than one, for an object to remain a single connected entity its fractal dimension must be at least one because a line is the simplest possible way of connecting points. Likewise the fractal dimension must be less than or equal to the dimension of the space in which the fractal exists, or else the space cannot "contain" the fractal. Any object we can find in a natural or industrial process must therefore have a mass fractal dimension $1 \leqslant D_f \leqslant 3$. This idea is illustrated in figure 2.15.
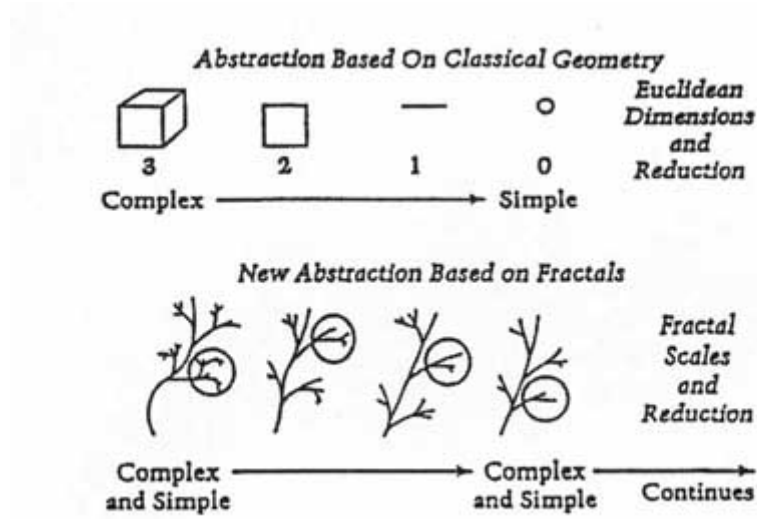
Figure 2.15: Illustrating the fractal dimension - contrasting Euclidean dimensions of form and reduction with fractal dimensions (Shearer, 1997).

2.5.3 Aggregation regimes

Real processes that form natural fractals probably impose even more strict limitations on the range of possible fractal dimensions. A simple computer simulation of colloidal aggregation that has been extensively studied (Meakin, 1988) is the cluster-cluster aggregation model. This type of simulation allows particles and clusters to diffuse according to a specified trajectory (usually Brownian or linear) and stick irreversibly with no restructuring at their point of contact. This type of simulation imposes natural limits on the resulting fractal dimensions such that $\approx 1.8 \leqslant Df \leqslant \approx 2.1$. The lower value comes about when a collision between clusters always results in the formation of a bond. This is known as the diffusion limited cluster aggregation, or DLCA, limit and produces quite tenuous, wispy structures. The higher value is a result of collisions almost never forming bonds, so that all physically possible conformations between clusters have an equal chance of forming a new bond and thus a new aggregate. This is known as the reaction limited cluster aggregation, or RLCA, limit and produces structures that are still quite tenuous

and rugged but noticeably more compact and stronger-looking than DLCA aggregates. Despite the simplistic algorithm, there is good evidence that this type of model describes quite accurately a range of colloidal aggregates that can be observed in the laboratory, Thouy and Jullien (1996) reported that their cluster-cluster aggregation model could not produce structures with a fractal dimension higher than about 2.55 in three dimensional space because the geometry of the clusters prevented them being placed close enough together to produce higher fractal dimensions.

Although the formation process determines the fractal dimension, the fractal dimension is not sufficient to characterise the process. This is stressed by Meakin and Julien (Meakin, 1988; Jullien and Meakin, 1989) who show that DLCA with a simple restructuring algorithm produces structures with the same fractal dimension as the RLCA processes.

2.6   Light scattering

The principle of radiation scattering as a particle characterisation tool is that irradiated matter emits secondary or sympathetic radiation. If that scattered radiation is then measured as a function of the scattering angle then information about the structure of the matter as a function of the length scale can be determined. Varying the scattering angle can be likened to varying the magnification of a structural probe. The actual type of radiation used is of secondary importance to this feature.

X-rays (Axelos et al., 1986; Amal et al., 1994; Moonen et al., 1989), neutrons (Kjems et al., 1986; Foret et al., 1992) and light (Sorensen et al., 1995; Cai et al., 1993; Cametti et al., 1987, 1989; Sorensen et al., 1992; Zhou and Chu, 1991; Lin et al., 1989; Jung et al., 1995) have all been used in the characterisation of colloidal particles and, in particular, of fractal aggregates. Of these techniques, light scattering perhaps is the fastest, easiest and least expensive. The wavelength of light is much longer than either x-rays or neutrons, making it suitable for probing structures of the order of microns in size. X-rays and

neutrons are generally only useful for probing structures much smaller than a micron. The disadvantage of using light scattering is that the interpretation of the scattered intensity pattern is complicated by the strong interaction of light and matter. Different, sometimes complicated theories of scattering are required to accurately predict light scattering for particles of different sizes and optical properties. In contrast, x-rays and neutrons interact comparatively weakly with matter so that in practice a simple scattering theory such as Rayleigh-Gans-Debye can always be used.

The polarisation of the incident and scattered light is often described as having vertical and horizontal components with respect to a horizontal plane. The horizontal plane is defined as the plane in which the scattered light is measured as a function of angle.

2.6.1 Scattering theories

There are several scattering theories that can be used for the interpretation of the scattering intensity pattern. More details and the mathematical derivation of these theories can be found in van de Hulst (1981). The relationship between the size of the particle and the wavelength of the incident light usually determines which theory can be applied. Rayleigh theory and the Rayleigh-Gans-Debye (RGD) approximation both assume that the scattering particle is smaller than the wavelength of the incident light. Rayleigh scattering of sunlight in the clear atmosphere is the main reason why the sky is blue. Rayleigh and cloud-mediated scattering contribute to diffuse light (direct light being sunrays). Fraunhofer diffraction assumes the scattering particle is much larger than the wavelength of the incident light. In between small particles (where the Rayleigh and Rayleigh-Gans-Debye approximations are appropriate) and large particles (where Fraunhofer diffraction is appropriate), there is a range where none of these theories are accurate. When the scattering particles have a size of the order of the wavelength of the incident light, exact solutions are required.

Exact solutions to scattering problems require the full formal solution of Maxwell's equations of electromagnetism (van de Hulst, 1981). The first solution of this kind was the full solution for scattering of an incident plane wave by a sphere, generally attributed to Gustav Mie in 1908 (Mie, 1908). The Mie solution represents the outgoing spherical scattered wave as an infinite series of spherical Bessel functions, and like all scattering problems framed in terms of Maxwell's equations, requires numerical solution. Equivalent solutions have been derived for exact solutions for cylinders (Bohren and Hufman, 1981) and spheroids (Asano and Yamamoto, 1975).

Another way of calculating scattering from any arbitrarily shaped body is the discrete dipole approximation (DDA). As the name suggests, the body is described as an array of dipole scatterers. The difference between this and the RGD approximation is that interaction between dipoles is accounted for. This, of course, requires an iterative and hence numerical solution, as do other approaches.

2.6.2   Interpretation of scattering data

The scattered intensity can be interpreted in several ways to give properties of interest about the system under observation. Perhaps the most common usage is that of determining particle size distributions of suspended particles and emulsions, especially in industry where the technique can be used as an online control system. The scattered intensity's angular dependence can reveal structural information and can be used to determine the fractal dimensions of aggregated matter, and also information about polymer and protein conformation. The relative molecular mass of particles can also be calculated using light scattering in appropriate conditions (Shaw, 1992).

A typical scattering graph of fractal aggregates is shown in figure 2.16. The axes represent the normalised scattered intensity on the y-axis and the wave vector q, which is a function of the scattering angle, on the x-axis. Logarithmic axes are used to plot this type

of graph. The slope of the fractal regime can be used to calculate the fractal dimension of the aggregates, thus yielding useful information about the aggregate structure. The technique of quantifying the structure of aggregates from their fractal dimensions should be employed with caution, however, as many aggregates do not exhibit fractal characteristics (although this can be deduced from the scattering data).
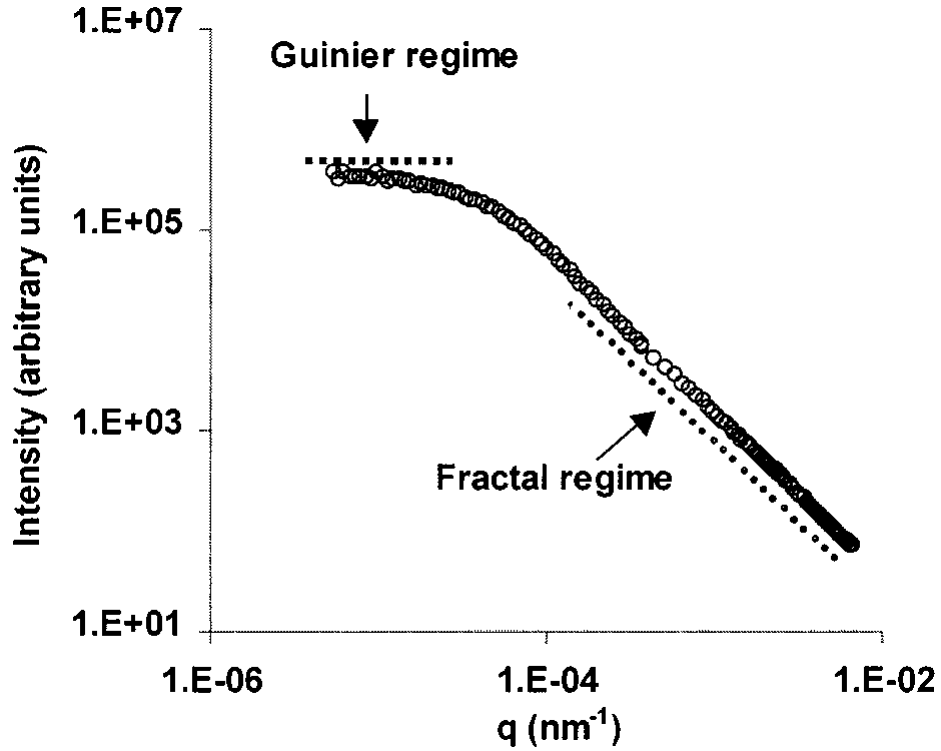
Figure 2.16: Typical I versus q plot of fractal aggregates (Selomulya et al., 2001).

In the Guinier regime, the scattered intensity is free from the effects of aggregate structure and is only a function of the linear measure of the aggregate size.

2.6.3 Dynamic light scattering

The discussion of light scattering has focused on static light scattering (also called laser diffraction). The technique has limitations at smaller length scales and it can be difficult to measure small particles accurately. However, there exists another light scattering

technique for the measurement of particles in this range. This is dynamic light scattering (DLS), also known as photon correlation spectroscopy and quasi-elastic light scattering.

2.6.3.1 Brownian motion

DLS measures Brownian motion and relates this to the size of the particles. Brownian motion is the random movement of particles due to the bombardment by the solvent molecules that surround them (see section 2.2.3). Normally DLS is concerned with measurement of particles suspended within a liquid.

The larger the particle, the slower the Brownian motion will be. Smaller particles are kicked further by the solvent molecules and move more rapidly. An accurately known temperature is necessary for DLS because knowledge of the viscosity is required (because the viscosity of a liquid is related to its temperature). The temperature also needs to be stable, otherwise convection currents in the sample will cause non-random movements that will ruin the correct interpretation of size.

The velocity of the Brownian motion is defined by a property known as the translational diffusion coefficient (usually given the symbol, D).

2.6.3.2 The hydrodynamic diameter

The size of a particle is calculated from the translational diffusion coefficient by using the Stokes-Einstein equation,

$$d\left(H\right) = \frac{kT}{3\pi\eta D} \tag{11}$$

where $d(H)$ is the hydrodynamic diameter, k is the Boltzmann constant, T is the temperature, η is the viscosity and D is the translational diffusion coefficient.

Note that the diameter that is measured in DLS is a value that refers to how a particle diffuses within a fluid so it is referred to as a hydrodynamic diameter. The diameter that is obtained by this technique is the diameter of a sphere that has the same translational

diffusion coefficient as the particle.
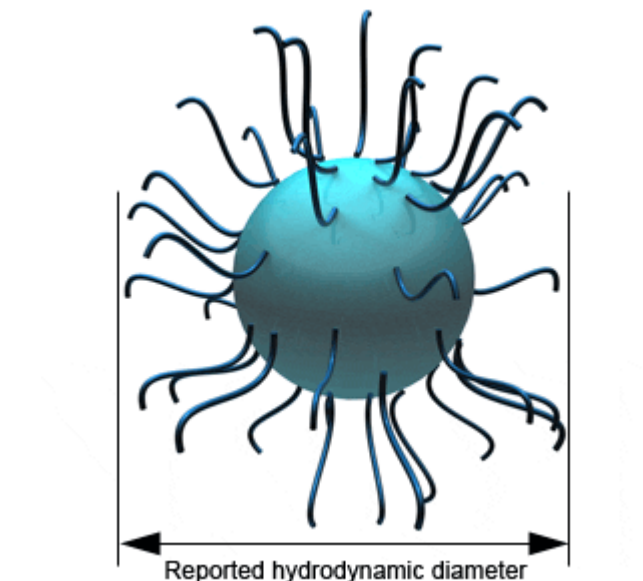
Figure 2.17: Illustration of the hydrodynamic diameter.

The translational diffusion coefficient will depend not only on the size of the particle "core", but also on any surface structure, as well as the concentration and type of ions in the medium. Factors that affect the diffusion speed of particles are discussed in the following sections.

2.6.3.3 Ionic strength of the medium

The ions in the medium and the total ionic concentration can affect the particle diffusion speed by changing the thickness of the electric double layer called the Debye length (κ^{-1}). Thus a low conductivity medium will produce an extended double layer of ions around the particle, reducing the diffusion speed and resulting in a larger, apparent hydrodynamic diameter. Conversely, higher conductivity media will suppress the electrical double layer and the measured hydrodynamic diameter.

The performance of a DLS instrument is normally verified by measurement of a suitable polystyrene latex standard. If the standard needs to be diluted prior to measurement,

then dilution in an appropriate medium is important. The International Standard on DLS (ISO13321 Part 8 1996) says that dilution of any polystyrene standard should be made in 10mM NaCl. This concentration of salt will suppress the electrical double layer and ensure that the hydrodynamic diameter reported will be the same as the hydrodynamic diameter on the certificate or the expected diameter.

2.6.3.4   Surface structure

Any change to the surface of a particle that affects the diffusion speed will correspondingly change the apparent size of the particle. An adsorbed polymer layer projecting out into the medium will reduce the diffusion speed more than if the polymer is lying flat on the surface. The nature of the surface and the polymer, as well as the ionic concentration of the medium can affect the polymer conformation, which in turn can change the apparent size by several nanometres.

2.6.3.5   Non-spherical particles

All particle-sizing techniques have an inherent problem in describing the size of non-spherical particles. The sphere is the only object whose size can be unambiguously described by a single figure.

Different techniques are sensitive to different properties of the particle, e.g. projected area, density, scattering intensity, and in general will produce different mean sizes and size distributions for any given sample. Even the size in a microscope image will depend on parameters set such as edge contrast etc. It is important to understand that none of these results are inherently "correct"

The hydrodynamic diameter of a non-spherical particle is the diameter of a sphere that has the same translational diffusion speed as the particle.

If the shape of a particle changes in a way that affects the diffusion speed, then the hydrodynamic size will change. For example, small changes in the length of a rod-shaped

particle will directly affect the size, whereas changes in the rods diameter, which will hardly affect the diffusion speed, will be difficult to detect.

The conformation of proteins and macromolecules are usually dependent on the exact nature of the dispersing medium. As conformational changes will usually affect the diffusion speed, DLS is a very sensitive technique for detecting these changes.

2.6.3.6 How DLS works

In dynamic light scattering, the speed at which the particles are diffusing due to Brownian motion is measured. This is done by measuring the rate at which the intensity of the scattered light fluctuates when detected using a suitable optical arrangement. How do these fluctuations in the intensity of scattered light arise?
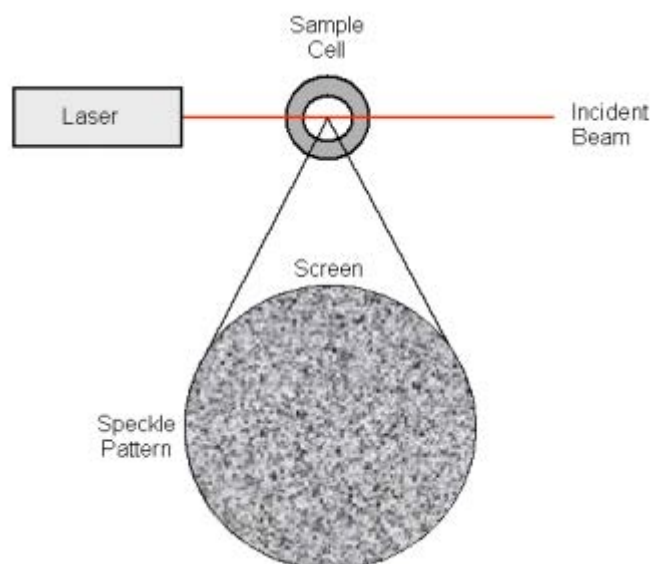
Figure 2.18: Schematic representation of a speckle pattern.

Imagine if a cuvette, containing particles which are stationary, is illuminated by a laser and a frosted glass screen is used to view the sample cell. A classical speckle pattern would be seen (figure 2.18). The speckle pattern will be stationary both in speckle size and position because the whole system is stationary. The dark spaces are where the phase

53

additions of the scattered light are mutually destructive and cancel each other out (figure 2.19A). The bright blobs of light in the speckle pattern are where the light scattered from the particles arrives with the same phase and interfere constructively to form a bright patch (figure 2.19B).
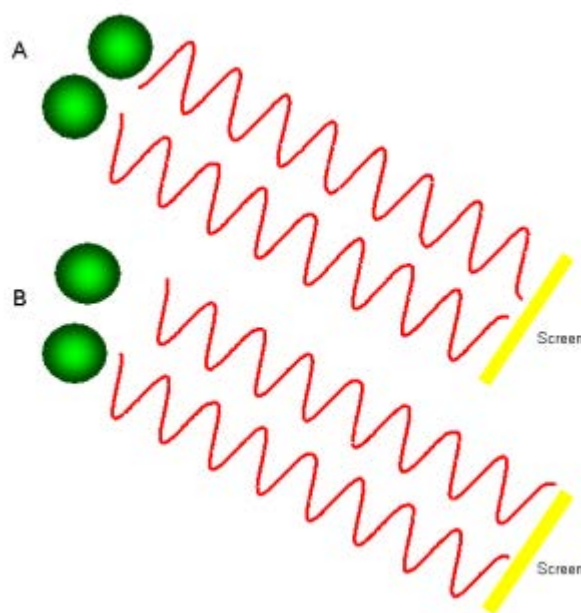
Figure 2.19: The observed signal depends on the phase addition of the scattered light falling on the detector. In example A, two beams interfere and 'cancel each other out' resulting in a decreased intensity detected. In example B, two beams interfere and 'enhance each other' resulting in an increased intensity detected.

For a system of particles undergoing Brownian motion, a speckle pattern is observed where the position of each speckle is seen to be in constant motion. This is because the phase addition from the moving particles is constantly evolving and forming new patterns. The rate at which these intensity fluctuations occur will depend on the size of the particles. Figure 2.20 schematically illustrates typical intensity fluctuations arising from a dispersion of large particles and a dispersion of small particles. The small particles cause the intensity to fluctuate more rapidly than the large ones.
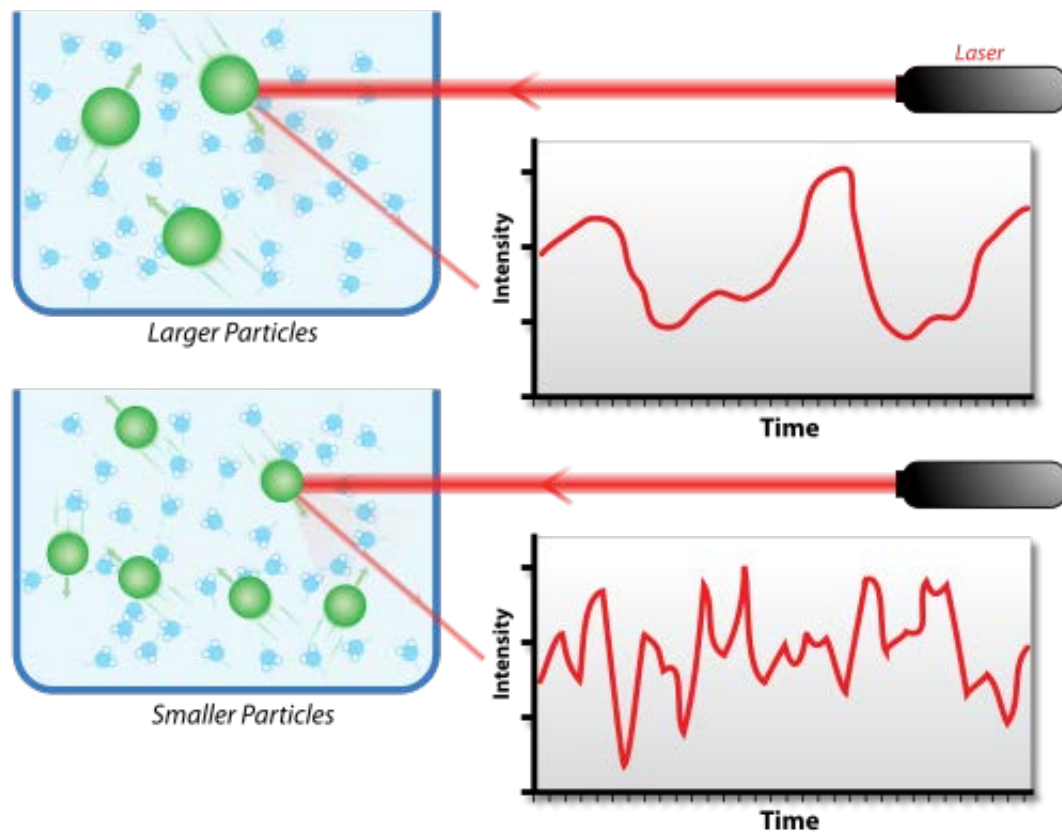
Figure 2.20: Typical intensity fluctuations for large and small particles.

It is possible to directly measure the spectrum of frequencies contained in the intensity fluctuations arising from the Brownian motion of particles, but it is inefficient to do so. The best way is to use a device called a digital auto correlator.

2.6.3.7 How a correlator works

A correlator is basically a signal comparator. It is designed to measure the degree of similarity between two signals, or one signal with itself at varying time intervals.

If the intensity of a signal is compared with itself at a particular point in time and a time much later, then for a randomly fluctuating signal it is obvious that the intensities are not going to be related in any way, i.e. there will be no correlation between the two signals (figure 2.21). Knowledge of the initial signal intensity will not allow the signal

intensity at time $t = $ infinity to be predicted. This will be true of any random process such as diffusion.
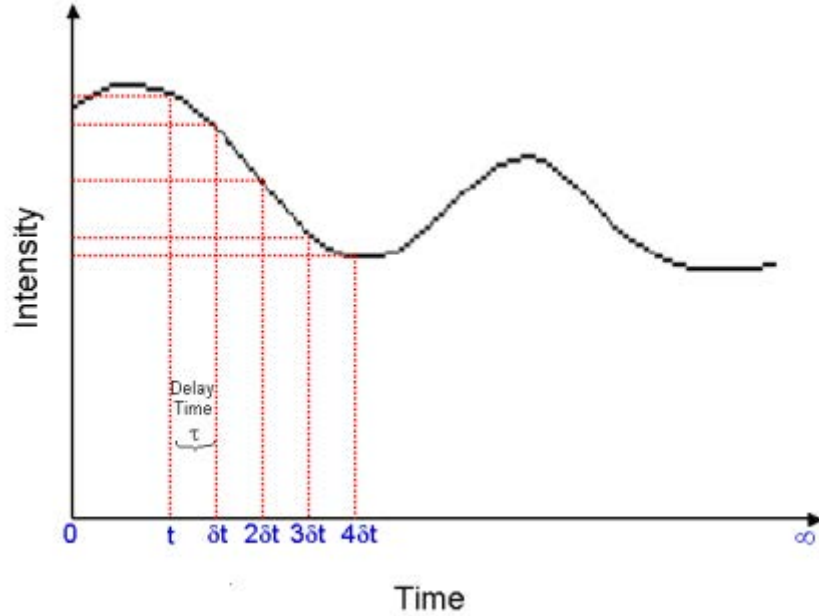
Figure 2.21: Schematic showing the fluctuation in the intensity of scattered light as a function of time.

However, if the intensity of signal at time $= t$ is compared to the intensity a very small time later $(t + \delta t)$, there will be a strong relationship or correlation between the intensities of two signals. The two signals are strongly or well correlated.

If the signal, derived from a random process such as Brownian motion, at t is compared to the signal at $t + 2\delta t$, there will still be a reasonable comparison or correlation between the two signals, but it will not be as good as the comparison at t and $t + \delta t$. The correlation is reducing with time. The period of time δt is usually very small, maybe nanoseconds or microseconds and is called the sample time of the correlator. $t = \infty$ maybe of the order of a millisecond or tens of milliseconds.

If the signal intensity at t is compared with itself then there is perfect correlation as the signals are identical. Perfect correlation is indicated by unity (1.00) and no correlation

56

is indicated by zero (0.00).

If the signals at $t + 2\delta t$, $t + 3\delta t$, $t + 4\delta t$ etc. are compared with the signal at t, the correlation of a signal arriving from a random source will decrease with time until at some time, effectively $t = \infty$, there will be no correlation.

If the particles are large the signal will be changing slowly and the correlation will persist for a long time (figure 2.22). If the particles are small and moving rapidly then correlation will reduce more quickly (figure 2.23).
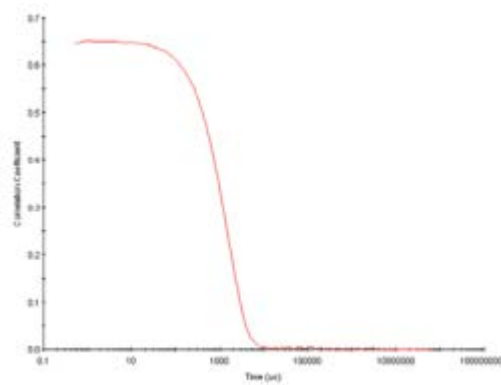
Figure 2.22: Typical correlogram from a sample containing large particles in which the correlation of the signal takes a long time to decay.
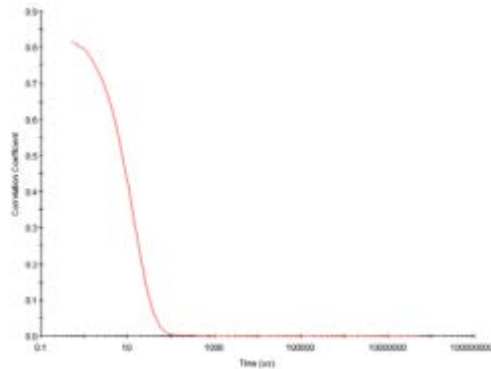
Figure 2.23: Typical correlogram from a sample containing small particles in which the correlation of the signal decays more rapidly.

Viewing the correlogram from a measurement can give a lot of information about the

sample. The time at which the correlation starts to significantly decay is an indication of the mean size of the sample. The steeper the line, the more monodisperse the sample is. Conversely, the more extended the decay becomes, the greater the sample polydispersity.

2.6.3.8 The correlation function

It has been seen that particles in a dispersion are in a constant, random Brownian motion and that this causes the intensity of scattered light to fluctuate as a function of time. The correlator used in a PCS instrument will construct the correlation function $G(\tau)$ of the scattered intensity:

$$G(\tau) = \langle I(t).I(t+\tau)\rangle \tag{12}$$

where τ = the time difference (the sample time) of the correlator.

For a large number of monodisperse particles in Brownian motion, the correlation function (given the symbol $[G]$) is an exponential decaying function of the correlator time delay τ

$$G(\tau) = A\left[B + \exp(-2\Gamma\tau)\right] \tag{13}$$

where A is the baseline of the correlation function, B is the intercept of the correlation function, and Γ is given by the equation

$$\Gamma = Dq^2 \tag{14}$$

where D is translational diffusion coefficient, and q is given by the equation

$$q = \left(\frac{4\pi n}{\lambda_0}\right)\sin\left(\frac{\theta}{2}\right) \tag{15}$$

where n is refractive index of the dispersant, λ_0 is the wavelength of the laser, and θ is

the scattering angle.

For polydisperse samples, the equation can be written as

$$G(\tau) = A\left[B + g_1(\tau)^2\right] \tag{16}$$

where $g_1(\tau)$ is the sum of all the exponential decays contained in the correlation function.

2.6.3.9 Obtaining size information from the correlation function

Size is obtained from the correlation function by using various algorithms. There are two approaches that can be taken

1. fit a single exponential to the correlation function to obtain the mean size (z-average diameter) and an estimate of the width of the distribution (polydispersity index) (this is called the Cumulants analysis and is defined in ISO13321 Part 8), or

2. fit a single exponential to the correlation function to obtain the mean size (z-average diameter) and an estimate of the width of the distribution (polydispersity index) (this is called the Cumulants analysis and is defined in ISO13321 Part 8), or

The size distribution obtained is a plot of the relative intensity of light scattered by particles in various size classes and is therefore known as an intensity size distribution.

If the distribution by intensity is a single fairly smooth peak, then there is little point in doing the conversion to a volume distribution using the Mie theory. If the optical parameters are correct, this will just provide a slightly different shaped peak. However, if the plot shows a substantial tail, or more than one peak, then Mie theory can make use of the input parameter of sample refractive index to convert the intensity distribution to a volume distribution. This will then give a more realistic view of the importance of the tail or second peak present. In general terms it will be seen that

$$d(intensity) > d(volume) > d(number) \tag{17}$$

A very simple way of describing the difference between intensity, volume and number distributions is to consider 2 populations of spherical particles of diameter 5nm and 50nm present in equal numbers (figure 2.24). If a number distribution of these 2 particle populations is plotted, a plot consisting of 2 peaks (positioned at 5 and 50nm) of a 1 to 1 ratio would be obtained. If this number distribution was converted into volume, then the 2 peaks would change to a 1:1000 ratio (because the volume of a sphere is equal to $4/3\pi(d/2)^3$. If this was further converted into an intensity distribution, a 1:1000000 ratio between the 2 peaks would be obtained (because the intensity of scattering is proportional to d^6 (from Rayleighs approximation)). Remember that in DLS, the distribution obtained from a measurement is based on intensity.
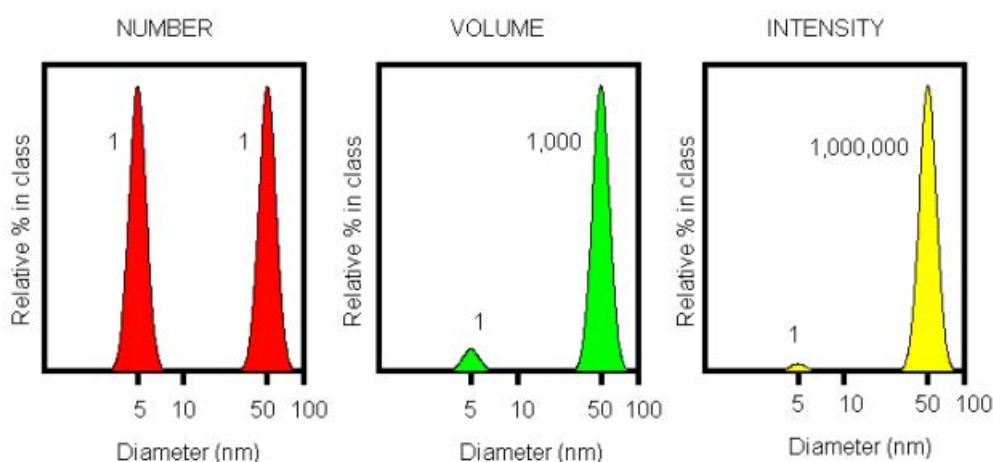
Figure 2.24: Number, volume and intensity distributions of a bimodal mixture of 5 and 50nm lattices present in equal numbers.

More information about dynamic light scattering, including in depth information about the mathematical approaches, is available in Berne and Pecora (1976); Johnson and Gabriel (1981); Dahneke (1983).

2.7   Applications

2.7.1   Magnetic separation of minerals

In 1792 a patent was filed by William Fullarton describing the separation of iron minerals with a magnet and the field of magnetic separations was born (Gunther, 1909; Parker, 1977). The early applications relied on the intrinsic magnetic properties of sediments for separation. In 1852, magnetite was separated from apatite by a New York company on a conveyor belt separator (Gunther, 1909). Later, a new line of separators were introduced for separation of iron from brass fillings, turnings, metallic iron from furnace products and magnetite from plain gangue.

Magnetic separation technology has also been used in kaolin benefication, the steel industry, power plants, water treatment and coal purification (Gerber and Birss, 1983). It has also found increasing use in biotechnology, being employed in cell separation (Melville et al., 1975; Safarik and Safarikova, 1999), protein and DNA purification (Safarik and Safarikova, 2004), drug delivery (Goodwin et al., 1999; Alexiou et al., 2000, 2005) and biocatalysis (Gao et al., 2003; Yang et al., 2004).

2.7.2   Magnetic fluids

Magnetic fluids, or ferrofluids, are an important class of magnetic nanomaterials. Ferrofluids are colloidal dispersions of magnetic particles in an appropriate carrier fluid. They were first synthesised in the mid-1960s giving rise to materials with novel physical, physio-chemical and hydrodynamic properties in the presence of a magnetic field. Since then a number of practical applications have been realised - examples include magnetofluidic seals, oscillation dampers, fluid bearings and magnetic lubricants, new sensors and elements for automation systems, magnetogravimetric analysers and separators, thermomagnetic converters of energy, magnetic guided drug delivery systems (Blums et al.,

1997).

The particles are usually made from magnetite and are around 10nm in size. The dispersions are stabilised by addition of an appropriate surfactant which coats the particles to prevent coagulation. The behaviour of such fluids is then determined by its magnetic properties. This can be surprising as there is an increase in initial magnetic susceptibility of a factor of $\approx 10^2$ in contrast to paramagnetic salt solutions. This means that the fluid can be controlled by weak magnets, of the order of 50 mT (Odenbach, 2003).

Internal structures also arise in magnetic fluids, the origin of which is generally recognised to be the dipolar interactions between magnetic grains (Odenbach, 2002). The effects of these interactions were outlined in the work of de Gennes and Pincus (1970) who foresaw the two possible consequences of magnetic interparticle interactions. These were the *phase separation* and the *association phenomenon*. Below a certain critical temperature, a magnetic fluid separates into the dilute vapour and condensed liquid phases (the phase separation), which is analogous to the case of simple fluids. In the presence of high external magnetic fields the dipoles align along the direction of the field and tend to form chains (the association phenomenon). Thus, the two interactions differ on the scale of their effects. The condensation is a macroscopic phenomenon whereas the grain association manifests itself as a microscopic phenomenon. De Gennes and Pincus also discussed chain-like structures appearing in the absence of an applied field, although the link between the two phenomena remained unclear.

2.7.3   Magnetic treatments

2.7.3.1   Magnetic therapies

Magnetic devices that are claimed to be therapeutic include magnetic bracelets, insoles, wrist and knee bands, back and neck braces, and even pillows and mattresses. These devices are used in complentary and alternative medicine but the effects of such devices

are controversial and an editorial in the British Medical Journal (Finegold and Flamm, 2006) claimed that there are no proven benefits, although they still generate sales of a billion dollars (US) annually (Finegold and Flamm, 2006).

However, magnetic therapies used clinically include transcranial magnetic stimulation (TMS) (Fitzgerald et al., 2006; Strafella et al., 2006) for the treatment of various neurological conditions (e.g. migraine, stroke, Parkinson's disease, dystonia, tinnitus) and psychiatric conditions (e.g. major depression, auditory hallucinations). Magnetic resonance imaging (MRI) is also now a common diagnostic tool which images the body by using a powerful magnetic field to align the nuclear magnetization of (usually) hydrogen atoms in water in the body (Haacke et al., 1999).

2.7.3.2   Magnetic nanoparticles in medicine

Magnetic nanoparticles for biological use usually have a size range from 1 to 100nm which puts them on a comparable size to biological macromolecules such as antibodies, receptors, nucleic acids and proteins.

Diagnostics   Diagnostic uses of magnetic nanoparticles include magnetic cell separation, MRI contrast agents, drug delivery systems, and photodynamic therapy (quantum dot).

One partilcuar use of magnetic nanoparticles is in hyperthermia therapy for the treatment of cancer. Hyperthermia treatment involves heating the tumour cells which are less resistant to heat than healthy cells. To do this, magnetic nanoparticles with surface molecules that allow them to bind to the tumour cells are guided using a magnetic field to the tumour. Heating is then induced via an AC magnetic which causes the nanoparticles to vibrate and produce heat. The advantage is that this process is local and targets the area of the tumour rather than more brute force treatments such as chemotherapy (Zhang et al., 2007; Laurent et al., 2011; Tietze et al., 2012).

Sufficient particle size is needed (80-150nm) to allow attraction from an external mag-

netic field as the magnetic force is dependent on particle size (proportional to r^3). The heating properties of magnetic particles are strongly dependent on composition. Failure of the colloidal stability could lead to thrombosis.

Iron oxide is tolerated by the body and ferrofluids are broken down metabolically in the liver and spleen as in physiological iron metabolism.

Theragnostics Magnetic particles can be used as carriers for active substances and can also be visualized and can thus serve as both a therapeutic and a diagnostic tool, termed 'theragnostics' in the growing field of nanomedicine (Tietze et al., 2012).

2.7.3.3   Magnetic water treatment

Many suggestions have been made about the influence of magnetic fields on scaling in water pipes but the effects are not well understood or even agreed upon (Powell, 1998). There is, however, some evidence that magnetic fields can affect the precipitation of certain substances in water and thus affect the scaling. Liburkin et al. (1986) found that magnets affected the structure of gypsum (calcium sulphate). The gypsum particles formed under a magnetic field were found to be larger and more regularly orientated than those formed in the absence of a magnetic field. Kronenberg (1985) reported that magnetic treatment changed the mode of calcium carbonate precipitation such that circular disc-shaped particles are formed rather than the dendritic (branching or treelike) particles observed in non-treated water. Fortin et al. (1997) found that the application of a magnetic field to hard water successfully prevents the growth and agglomeration of calcium carbonate as calcite, noting the importance of the magnetic field strength and direction. Donaldson and Grimes (1988) reported that a magnetic field altered the crystal nuclei of precipitating calcium carbonate causing the formation of larger crystals and altering the equilibrium between the fluid and the precipitate. Herzog et al. (1989) reported that magnetic treatment liberated Fe^{2+} ions which inhibited calcite growth and thus would reduce scaling.

Others, e.g., Chechel and Annenkov (1972), and Martynova et al. (1967) have also found that magnetic treatment affects the structure of subsequently precipitated solids.

2.7.3.4 Magnetic fuel treatment

As pointed out by Powell (1998) there is very little literature on magnetic fuel treatment despite the abundance of vendors claiming improvements of up to 20 per cent on fuel consumption. A more recent report by the RAND Corporation (Bernstein et al., 2007) commissioned to study the effects of magnetic devices fitted to automobiles also found that there is scant scientific literature on the subject. However, research conducted for the report (Tao and Xu, 2006) found that a magnetic field can cause a reversible change in the viscosity of crude oil. The report also highlighted the need for more understanding and more research of these effects.

There are several companies selling such magnetic devices, whether they are small devices for automobiles or larger more costly devices for oil pipelines or industrial boilers, and while some seem to have empirical evidence to support their claims there is still no satisfactory scientific explanation. This has also led to certain companies making deceptive claims about their devices, and in the US has resulted in legal action by the Federal Trade Commission (FTC) against one company (Federal Trade Commission, Press Release).

2.7.4 Magnetic fields and biological systems

The behaviour of magnetic fields and biological systems is generally referred to as *bio-electromagnetism* and can be divided into two areas, (i) the production of magnetic fields in biological systems, commonly termed *biomagnetism*, and (ii) the effects of applied magnetic fields on biological systems, commonly termed *magnetobiology*.

Research has shown that a magnetic field can have an effect on chemical reactions and thus can also influence metabolic processes (Wadas, 1991). Most organic molecules are

diamagnetic but the production of susceptible free radicals during reactions allows the magnetic field to exert an influence. The time frame for this influence is very small, of the order of 10^{-10}s, but is nonetheless sufficient to produce differences in reactions. Evidence has even been found that shows the growth of plants can be affected by a magnetic field (Dunlop and Schmidt, 1964, 1965; Wadas, 1991).

Possible physical causes for effects of magnetic fields on organisms are the action of a magnetic field on (Wadas, 1991):

- uncompensated electron spins, present in free radicals and molecules containing cations of transition group elements, e.g. active centres in enzyme molecules, myoglobin and hemoglobin;

- diamagnetic substances, including biological liquid crystals;

- moving charges, which occurs primarily in the nervous system.

More recent research by Hashimoto et al. (2007) has found that static magnetic fields affect cell migration. Gerardi et al. (2008) studied the effects of electromagnetic fields of low frequency and low intensity on rat metabolism and found evidence that long term exposure to electromagnetic fields with a well defined frequency may have relevant effects on parameters such as body weight, blood glucose and fatty acid metabolism. There is also a current investigation commissioned by the Home Office looking into the effects of electromagnetic fields on mice (Science, Research and Statistics, Home Office).

2.8   Summary

Nanoparticles are found throughout the environment as the result of natural processes. Many properties of nanoparticles are related to their size, and this includes their magnetic properties. Static light scattering has previously been shown to be a successful technique for monitoring the aggregation of particles and the concepts of fractal geometry can be

used to describe the structure of aggregates. The aggregation behaviour of particles in magnetic fields could thus provide one possible mechanism for the effects seen in magnetic treatments.

Chapter 3

Population balance modelling

3.1 Previous work

The aggregation of small particles to form low density clusters and networks, such as flocs or gels, is a common phenomenon. It is important in many areas of science and has important applications in areas such as air pollution, water pollution and purification, the nuclear winter scenario, the formation of high performance ceramics and rheology control in paints, other coating systems and foods.

The modelling of colloidal aggregation generally follows one of two approaches: the microscopic approach or the macroscopic approach (Thomas et al., 1999; Taboada-Serrano et al., 2005). The macroscopic model, often referred to as the classical approach, is derived from Smoluchowski's coagulation equation, which is basically a mathematical expression of the rate of successful collisions between discrete particles (Thomas et al., 1999). The microscopic, or molecular, approach avoids assumptions and approximations that are typical of the macroscopic approach but has the disadvantage of the complexity associated with the extrapolation of results to the macroscopic scale (Taboada-Serrano et al., 2005). Models have then progressively been extended to include magnetic interaction (Tsouris and Scott, 1995), floc structural variation (Selomulya et al., 2003), breakup of aggregates

(Chin et al., 1998), magnetic chain aggregates (Mendelev and Ivanov, 2005) and heteroaggregation (Rolli et al., 2009), amongst other effects. The review by Taboada-Serrano et al. (2005) gives more details and examples about the various effects and interactions that have been added to models over the years.

Tsouris and Scott (1995) used a Brownian flocculation model, in which hydrodynamic, van der Waals, double-layer, and magnetic forces were incorporated. A population balance was employed in conjunction with the flocculation model to predict the evolution of the particle state with time. The effects of such parameters as strength of magnetic field, magnetic susceptibility of particles, particle size and zeta potential were investigated. The results showed that the particle size and magnetic susceptibility each play an important role in the selective flocculation of particles of different properties.

Chin et al. (1998) investigated flocculation kinetics in a stirred tank under turbulent shear flow using colloidal polystyrene and paramagnetic particles consisting of mixtures of polystyrene and magnetite. A trajectory model applicable for shear-flow systems was formulated to describe particle flocculation in stirred tanks. Results suggested that the flocculation rate was enhanced by increasing the agitation speed, even though the collision efficiency decreased at a higher agitation speed. It was also found that the collision rate increased and the collision efficiency decreased as the particle size ratio increased. Results also suggested that the breakup rate of aggregates in a turbulent shear flow could be significant and may need to be included in the population balance modelling to correctly predict the evolution of particle size distribution.

Ying et al. (2000) used a model combining trajectory analysis, a buildup model, and a bivariate population balance model applicable for Brownian flocculation, to predict magnetically seeded filtration. Results indicated that the effect of hydrodynamic resistance on the removal efficiency becomes important as the particle size and Reynolds number are increased or the magnetic field is decreased. From magnetically seeded filtration experi-

ments, it was found that the removal efficiency increases with an increase in the magnetic field strength and particle size and a decrease in the flow rate. The differences between modelling predictions and experimental results are possibly due to the accuracy of particle size and magnetic susceptibility distributions, as well as due to model limitations.

The purpose of this chapter is to combine the models of particles interactions with a population balance model which is inclusive of restructuring and breakage of the particles. This achieved by the combing the population balance model of Selomulya et al. (2003) with the particle interaction model described by Tsouris and Scott (1995). The effects of various parameters can then be explored to provide theoretical insight into the aggregation process with a magnetic field.

3.2   Theory

The classical coagulation equation was introduced in a 1916 paper by the Polish physicist Marian Smoluchowski, and describes the evolution of the number density of particles of size x at a time t. The discretised form of the equation is

$$\frac{\partial n(x_i, t)}{\partial t} = \frac{1}{2} \sum_{i \neq j}^{N} K(x_i - x_j, x_j) n(x_i - x_j, t) n(x_i, t)$$

$$- \sum_{0}^{\infty} K(x_i, x_j) n(x_i, t) n(x_j, t) \quad (1)$$

where t is time, i and j are section intervals, n is the number density and the operator K is known as the aggregation kernel and can take one of three simple forms, that is

$$K = 1, \ K = x + y \text{ or } K = xy$$

known as the constant, additive, and multiplicative kernels respectively. However, in most practical applications the kernel takes on a significantly more complex form, for example

the free-molecular kernel which describes collisions in a dilute gas-phase system

$$K = \sqrt{\frac{\pi k_B T}{2}} \left(\frac{1}{m(x)} + \frac{1}{m(y)} \right)^{\frac{1}{2}} (d(x) + d(y))^2 \tag{2}$$

Generally the coagulation equations which result from such physically realistic kernels are intractable, and as such, it is necessary to appeal to numerical methods. There exist well-established deterministic methods that can be used when there is only one particle property, x, of interest, the two principal ones being the method of moments and sectional methods.

The Smoluchowski equation is based on several assumptions about the particles and their aggregation. These include:

- every collision is successful

- the system is mondisperse

- binary collisions

- spherical particles

- laminar fluid motion

- no breakup of aggregates.

Modifications to this equation have been performed in the past to make it more relevant to real systems. For example, the presence of short range forces and fluid between particles could prevent an attachment or bond being formed with every collision, and thus the efficiency of collisions would be therefore much less than previously assumed.

3.3 Population Balance Model

The lumped discretised form of a popualtion balance model, based on $v_{i+1} = 2v_i$, which descibes the rate of change of the number concentration, can be written as

$$\frac{dN_i}{dt} = \sum_{j=1}^{i=2} 2^{j-i+1} \alpha_{i-1,j} \beta_{i-1,j} N_{i-1} N_j + \frac{1}{2} \alpha_{i-1,i-1} \beta_{i-1,i-1} N_{i-1}^2$$
$$- N_i \sum_{j=1}^{i-1} 2^{j-i} \alpha_{i,j} \beta_{i,j} N_j - N_i \sum_{j=i}^{max_1} \alpha_{i,j} \beta_{i,j} N_j$$
$$- S_i N_i + \sum_{j=i}^{max_2} \Gamma_{i,j} S_j N_j \quad (3)$$

where N_i is the number concentration of flocs containing 2^{i-1} particles (accordingly, N_i is the number concentration of singlets or primary particles).

The first two terms from the right hand side of equation (3) descibe the formation of aggregates in the interval i from the collisons of aggregates from smaller size ranges. The third and fourth terms represent the loss of aggregates in interval i by the agglomeration of aggregates from from section i with those from other size ranges. The fifth term accounts for the loss of aggregates in interval i via fragmentation, and the last term denotes the gain of aggregates in section i through the fragmentation of larger aggregates.

The parameters $\alpha_{i,j}$ and $\beta_{i,j}$ are, respectively, collision efficiency and frequency between aggregates in sections i and j. The parameter S_i is the fragmentation rate of aggregates in the interval i, whereas $\Gamma_{i,j}$ is the breakage distribution function for the breakup of aggregates in the interval j, which generates fragments of sizes that fall in the interval i. The number of intervals can be selected to sufficiently represent the overall size distribution, e.g. with 25 intervals the model covers sizes ranging from primary particles to aggregates comprising 2^{24} particles.

3.4   Model Parameters

The model used here is that developed by Selomulya et al. (2003) which incorporates the breakage and restructuring of aggregates. This model is altered, however, by adding the particle interactions expressed in the form of the collision efficiency as provided by Tsouris and Scott (1995).

3.4.1   Collison efficiency

The collision efficiency function α is obtained from the solution of the generalised Smoluchowski equation for the diffusing particles under the action of interparticle forces

$$\alpha_{ij} = \left[(1 + r_j/r_i) \int_{(1+r_j/r_i)}^{\infty} \left(\frac{D_\infty}{D_{i,j}} \right) \exp \left(\frac{V_T}{k_B T} \right) \right]^{-1} \tag{4}$$

where D_∞ is the diffusion coefficient in the absence of particle interactions, $D_{i,j}$ is the relative diffusion coefficient between particles in the intervals i and j, and the ratio $D_\infty / D_{i,j}$ incorporates the hydrodynamic interaction between the particles. The total particle interaction V_T is given by

$$V_T = V_A + V_R + V_M \tag{5}$$

where V_A is the van der Waals interaction, V_R is the electrostatic interaction and V_M is the magnetic interaction.

3.4.1.1   Hydrodynamic resistance

D_∞ is the diffusion coefficient in the absence of any interparticle forces given by

$$D_\infty = D_i + D_j = \frac{k_B T}{6\pi\mu} \frac{r_i + r_j}{r_i r_j} \tag{6}$$

where D_i and D_j are the diffusion coefficients of particles i and j respectively, k_B is the

Boltzmann constant, T is the temperature, μ is the viscosity of the medium and $D_{i,j}$ is the relative diffusion coefficient between particles i and j defined as

$$D_{i,j} = bk_BT \tag{7}$$

where b is the relative mobility of the particles, a function of particle separation. For two spheres moving along their centreline, the relative mobility b can be obtained from the exact solution of Stokes' equation (Spielman, 1970).

3.4.1.2   van der Waals interaction

Hamaker's formula for the London-van der Waals attractive interaction energy V_{vdw} between spherical particles is

$$\frac{V_{vdw}}{k_BT} = -\frac{A}{6k_BT}$$
$$\left[\frac{2r_ir_j}{r^2 - (r_i + r_j)^2} + \frac{2r_ir_j}{r^2 - (r_i - r_j)^2} + \log\left(\frac{r^2 - (r_i + r_j)^2}{r^2 - (r_i - r_j)^2} \right) \right] \tag{8}$$

where A is the Hamaker constant, k_B is the Boltzmann constant, T is the temperature and r is the interparticle distance.

3.4.1.3   Electrostatic interaction

In the case of thin double layers, symmetrical electrolytes and dimensionless interparticle separations κl greater than 4 (where κ is the inverse Debye-Huckel length, a measure of the double-layer thickness), the linear superposition approximation can be used

74

$$V_{el} = \varepsilon \left(\frac{k_B T}{e} \right)^2 Y_i Y_j \frac{r_i r_j}{r} \exp(-\kappa l), \qquad \text{for } \kappa l \geqslant 4 \tag{9}$$

$$Y_i = 4 \tanh\left(\frac{\psi_i}{4} \right), \quad \text{for } \kappa r \geqslant 10 \text{ and } \phi_i < 8 \tag{10}$$

$$\phi_i = z e \psi_{0i} / k_B T \tag{11}$$

where z represents the valence of the electrolyte dissociated in the solution, and ϕ_{0i} represents the surface potential of the particles i. It is assumed that the potential of one particle remains undisturbed in the presence of the others. The inverse Debye-Huckel length κ is given by

$$\kappa^{-1} \approx 2.8 \times 10^{-8} I^{-0.5} \tag{12}$$

where I is the ionic strength of the solution.

3.4.1.4 Magnetic interaction

The magnetic interaction is calculated using the formula provided by Chan et al. (1985)

$$\frac{V_{mag}}{k_B T} = s(x) \left(-\frac{x^2}{3} \frac{1}{1 + 7x^2/150} \right)$$
$$+ (1 - s(x)) \left[-2x + \log(6x^2) - \frac{2}{3x} - \frac{7}{9x^2} \right] \tag{13}$$

where

$$s(x) = \exp\left[-\log(2) \left(\frac{x}{2.4} \right)^8 \right] \tag{14}$$

and

$$x = \frac{1}{k_B T} \frac{\pi d_i^3 d_j^3 \chi_i \chi_j B^2}{144 \mu_0 r^3} \tag{15}$$

where μ_0 is the permeability of free space, χ is the magnetic susceptibility, B is the strength of the magnetic field, d is the particle diameter and r is the separation of the particles.

3.4.2 Collision frequency

The collision frequency β_{ij} for perikinetic flocculation is applicable if both of the colliding particles are small ($< 1 \mu m$). Differential settling prevails when one particle is considerably larger than the other, otherwise β_{ij} is strongly dependent on the fluid velocity gradient in addition to the particle size (orthokinetic flocculation).

The frequency of binary collisions between spherical particles, which are due to Brownian motion, can be estimated by (Smoluchowski, 1916a)

$$\beta_{ij,perikinetic} = \left(\frac{2k_B T}{3\mu} \right) \frac{(R_{ci} + R_{cj})^2}{R_{ci} R_{cj}} \tag{16}$$

whereas the collision frequency for orthokinetic coagulation in isotropic turbulence is equal to (Saffman and Turner 1956)

$$\beta_{ij,orthokinetic} = 1.294 \left(\frac{\varepsilon}{\nu} \right)^{\frac{1}{2}} (R_{ci} + R_{cj})^3. \tag{17}$$

For fractal aggregates the collision, or effective capture, radius is

$$R_{Ci} = r_0 \left(\frac{N_i}{k_c} \right)^{\frac{1}{D_f}} \tag{18}$$

where r_0 is the primary particle radius, k_c is a proportionality constant relating to the packing density, genarally assumed to be unity (Wiesner 1992), and D_f is the mass fractal

dimension. Thus, by substituting R_{Ci} for fractal aggrgeates in equations (16) and (17) the structural effect can be accounted for when approximating the aggregate collision rates (Jiang and Logan 1991).

The overall collision frequency can therefore be calculated as the sum of frequencies due to Brownian motion and shear (assuming the two mechanisms are independent of each other, and that collision due to differential settling are negligible when $\rho_{particle} \approx \rho_{water}$) (Wiesner 1992).

3.4.3 Fragmentation rate

The fragmentation rate can be written (which is equal to the breakage frequency) can be written as

$$S_i = \left(\frac{4}{15\pi}\right)^{\frac{1}{2}} \left(\frac{\varepsilon}{\nu}\right)^{\frac{1}{2}} \left(\frac{-\varepsilon_{bi}}{\varepsilon}\right) \qquad (19)$$

where ε_{bi} is the critical energy dissipation rate that causes breakup. The estimate of ε_{bi} can be related to floc size based on the relationship

$$\varepsilon_{bi} = \frac{B}{R_{Ci}} \qquad (20)$$

where B is ? coefficient and R_{Ci} is the effective captive radius. This basically states that the magnitude of energy dissipation rate required to induce breakage will be lower for larger aggregates.

3.4.4 Breakage distribution function

The breakage distribution function (Γ_{ij}) describes the distribution of fragments in i-interval from the break-up of flocs in j-interval. There are several forms of breakage distribution functions; e.g. binary breakage where the floc is split into two equal-sized aggregates, ternary breakage where the floc is broken into three daughter fragments, and

normal breakage where the fragments are normally distributed in the lower size ranges. The binary breakage function was selected by Selomulya et al (2003). The binary breakage distribution function (Γ_{ij}) is expressed as

$$\Gamma_{ij} = \frac{V_j}{V_i} for\, j = i + 1 \tag{21}$$

$$\Gamma_{ij} = 0 for\, j \neq i + 1 \tag{22}$$

3.4.5 Estimation of size

One assumption of the model is that the particles are all spherical, but this is generally not the case in experimental systems and so on basis of comparison is the volume mean diameter of the particles. This is also known as volume moment mean of the particle, and normally noted as $d[4, 3]$ (being a function of the diameter, d, to the fourth power over the diameter to the third power). In the model the number concentration of flocs in i-intervals (N_i) can be used to estimate the volume mean diameter, $d[4, 3]$ through the following equation (Kusters, 1991)

$$d[4, 3] = \frac{\sum N_i D_i^4}{\sum N_i D_i^3} \tag{23}$$

where

$$D_i = \left(2^{(i-1)/d_F}\right) d_0 \tag{24}$$

3.4.6 Structure variation

The coefficient AB is used to represent the compounded effect of the amount of floc formation and breakup, to underscore the impact of both mechanisms on floc compaction

$$AB = \sum_{i}^{i\ max} |\text{aggreagtion terms i}| \times |\text{fragmentation terms i}| \tag{25}$$

where

$$|\text{aggreagtion terms i}| = abs\left[\sum_{j=1}^{i-2} 2^{j-i+1}\alpha_{i-1,j}\beta_{i-1,j}N_{i-1}N_j + \frac{1}{2}\alpha_{i-1,i-1}\beta_{i-1,i-1}N_{i-1}^2\right]$$

$$+ abs\left[-N_i\sum_{j=1}^{i-1} 2^{j-i}\alpha_{i,j}\beta_{i,j}N_j - N_i\sum_{j=i}^{max_1}\alpha_{i,j}\beta_{i,j}N_j\right]$$

and

$$|\text{fragmentation terms i}| = abs\left[-S_iN_i + \sum_{j=i}^{max_2}\Gamma_{i,j}S_jN_j\right]$$

The following empirical function is therefore used to approximate the change in d_F with tim as a cumulative effect of floc size and aggregate formation/breakup

$$\frac{dd_F}{dt} = \left[c_1\left(\frac{d}{d_o}\right)^{c_2} + c_3AB\right] \times (d_{F,max} - d_F) \tag{26}$$

where c_1, c_2 and c_3 are fitting parameters that embody additional factors such as binding strength or other intrinsic properties.

3.5 Simulation method

A MATLAB routine was written using a numerical technique (ODE23 in the MATLAB library) to solve the population balance equation. The collision efficiency was calculated using the *quad* integral function in the MATLAB library. The MATLAB code for this routine can be found in the appendix.

3.6 Results

The effects of various parameters on the aggregation are explored in the model.

3.6.1 Particle interactions

The particle interactions as calculated for different values of the surface potential and with a magnetic field at surface potential values of 5 and 55mV are shown in figures 3.1, 3.2 and 3.3.
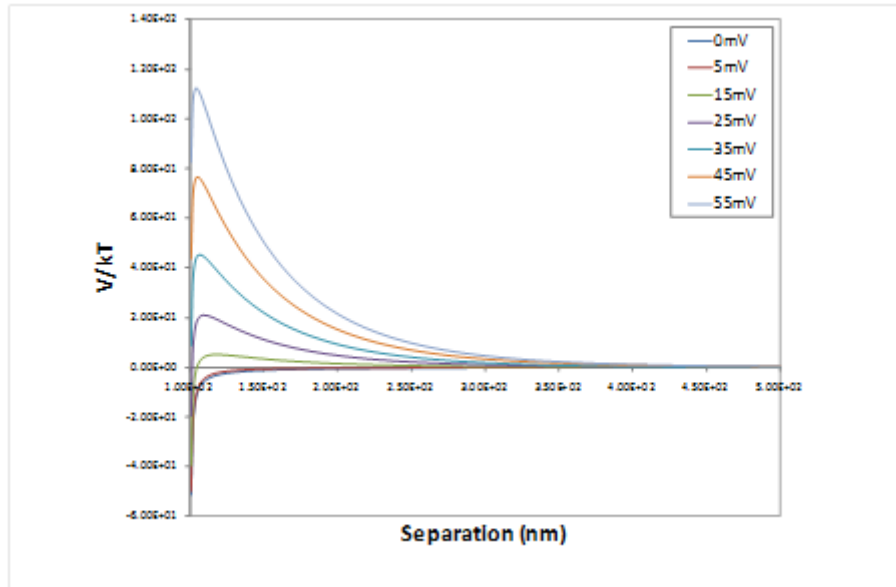
Figure 3.1: Interaction profiles at different zeta potentials.

Figure 3.2: Interaction profiles at different magnetic field strengths at 5mV.
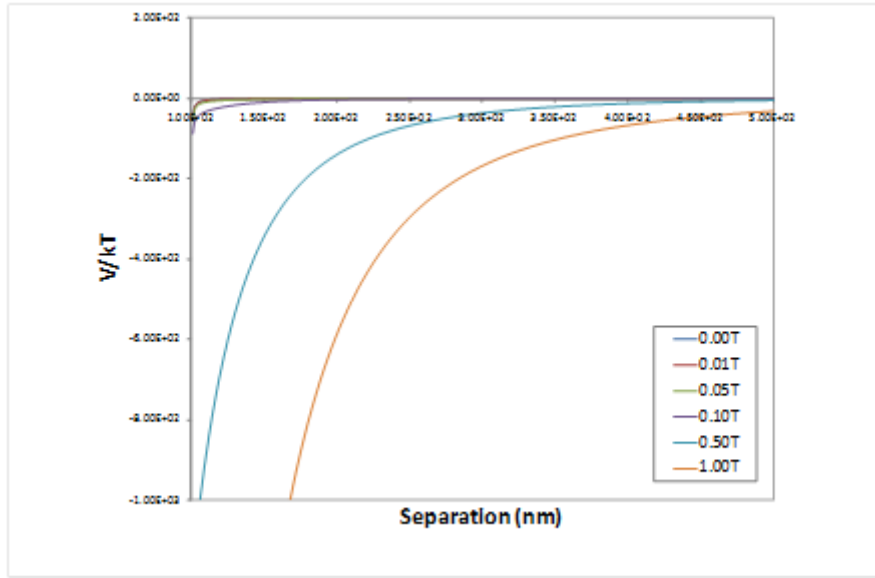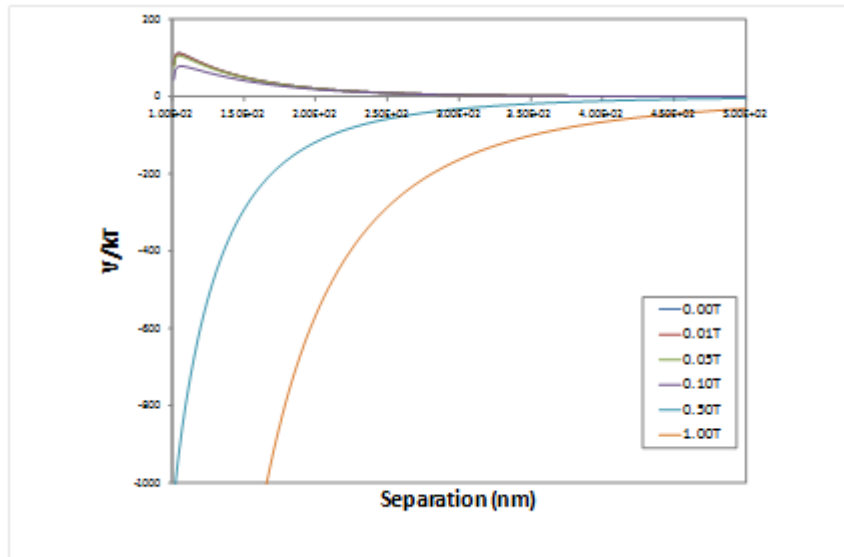

Figure 3.3: Interaction profiles at different magnetic field strengths at 55mV.

As can be seen in figure 3.1 an increasing amount of repulsion between the particles is calculated as the surface potential increases. At low values for the surface potential the overall interaction profile is attractive and thus provides favourable conditions for the

81

aggregation of particles. Changing the ionic strength does not alter the interactions in a significant way.

The applied magnetic field provides another source of attractive interactions which is reflected in the interaction profiles shown in figures 3.2 and 3.3. At small values for the applied magnetic field there is little difference but as it is increased the overall interaction profile becomes increasingly attractive, even at higher values of surface potential.

3.6.2 Collision efficiency

The effect of changing the surface potential in the model, akin to altering the pH in an experimental system, is to promote or prohibit aggregation as the value of the surface potential is increased. The evolution of the VMD is shown in figure 3.4. The number of size intervals used is 25 and the ionic strength is 0.1.

At high values, comparable to pH far from the isoelectric point of an experimental system, the VMD increases only slightly. At lower values of the surface potential, corresponding to values closer to the isoelectric point of the system, the VMD increases more as the value of the surface potential decreases. The evolution of the fractal dimension over time is shown if figure 3.5. The structure evolves more rapidly at lower values for the surface potential although it is unrealistic that there would be any fractal aggregates where there is little increase in the VMD and thus virtually no aggregation.
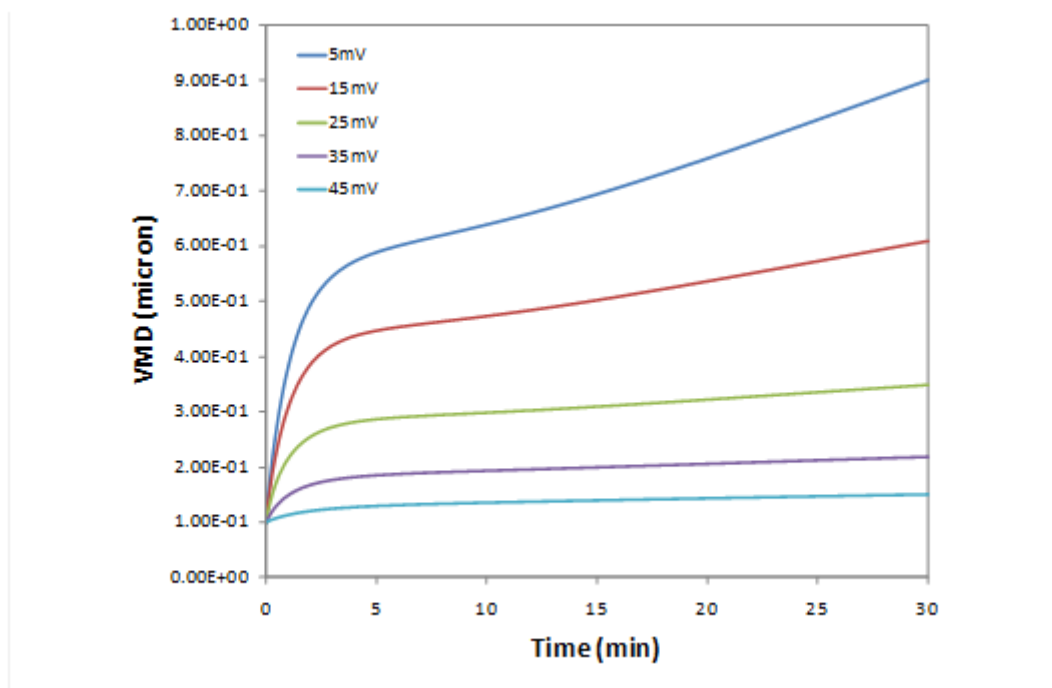
Figure 3.4: Evolution of VMD at different values of the surface potential.
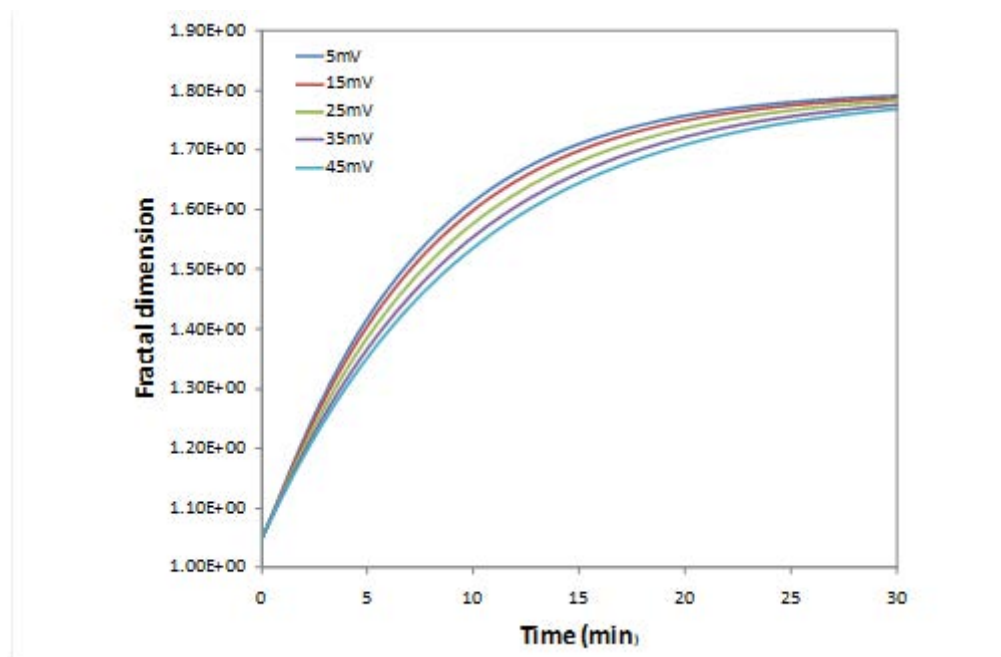
Figure 3.5: Evolution of VMD at different values of the surface potential.

Altering the value of the ionic strength, I, in the model is a way of simulating the electrolyte concentration in a suspension. The results of this are shown in figure 3.6 (VMD) and figure 3.7 (fractal dimension).
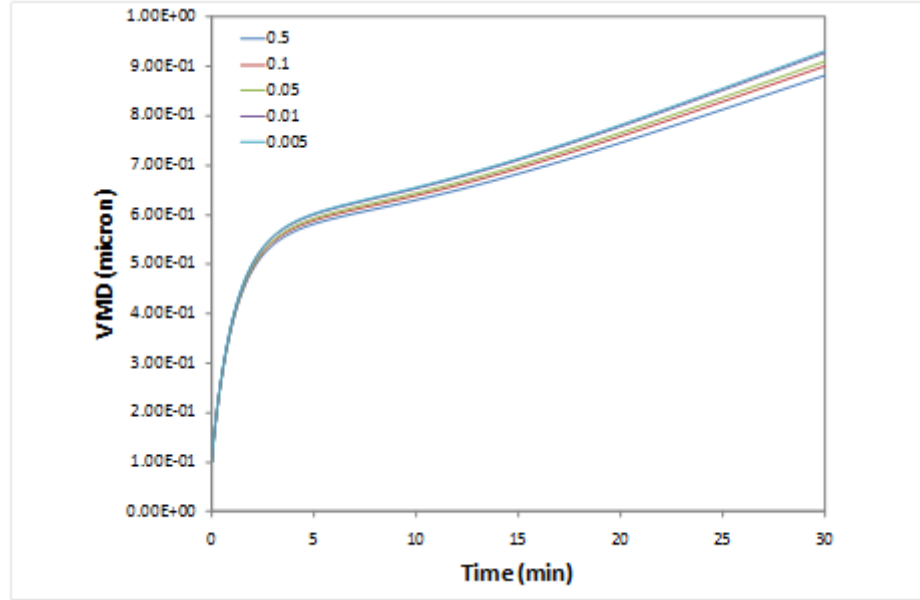
Figure 3.6: Evolution of VMD at different values of the ionic strength, I.
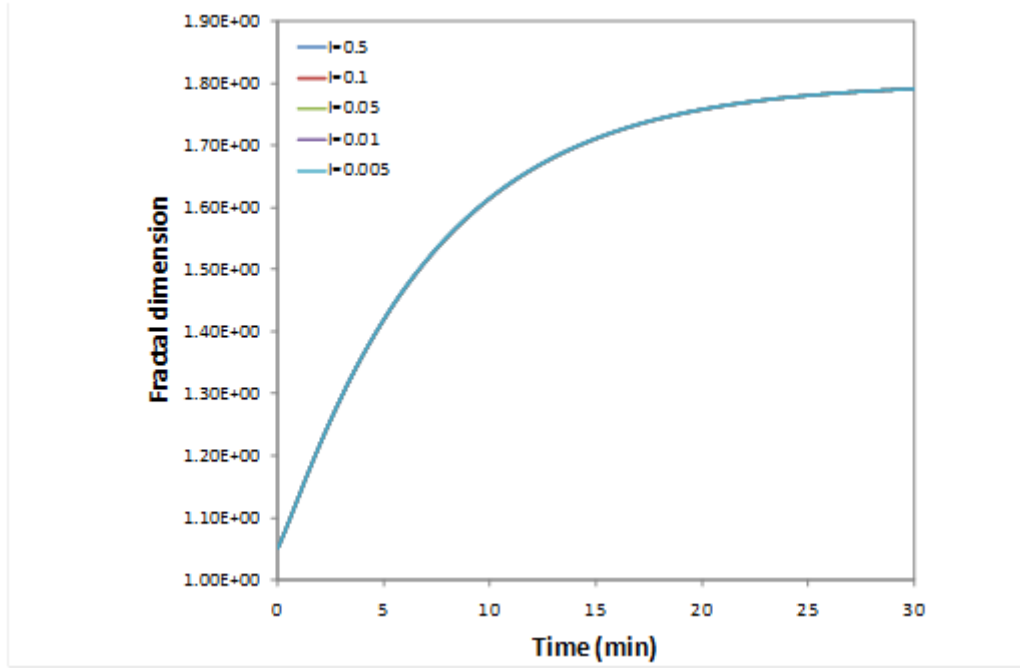
Figure 3.7: Evolution of the fractal dimension at different values for ionic strength, *I*.

There is little difference in the results at different values of the ionic strength, indicating that the ionic strength, and thus the electrolyte concentration, does not have a significant effect on the aggregation. Experimental observations do not agree with this, as the addition of electrolytes to colloidal suspensions has been shown to destabilise the suspensions causing the formation of large aggregate structures. The evolution of the fractal dimension is identical in each case (see figure 3.7), once again highlighting the virtual indifference of the model to changes in ionic strength.

3.6.3 Collision Frequency

The collision frequency is altered by changing the value of the shear rate, which until now has been at zero. Altering the shear rate does not alter the interactions between the particles and thus is independent of collision efficiency. However, as the particles collide more frequently there is a greater chance that there will be more successful collisions and

thus more aggregation.
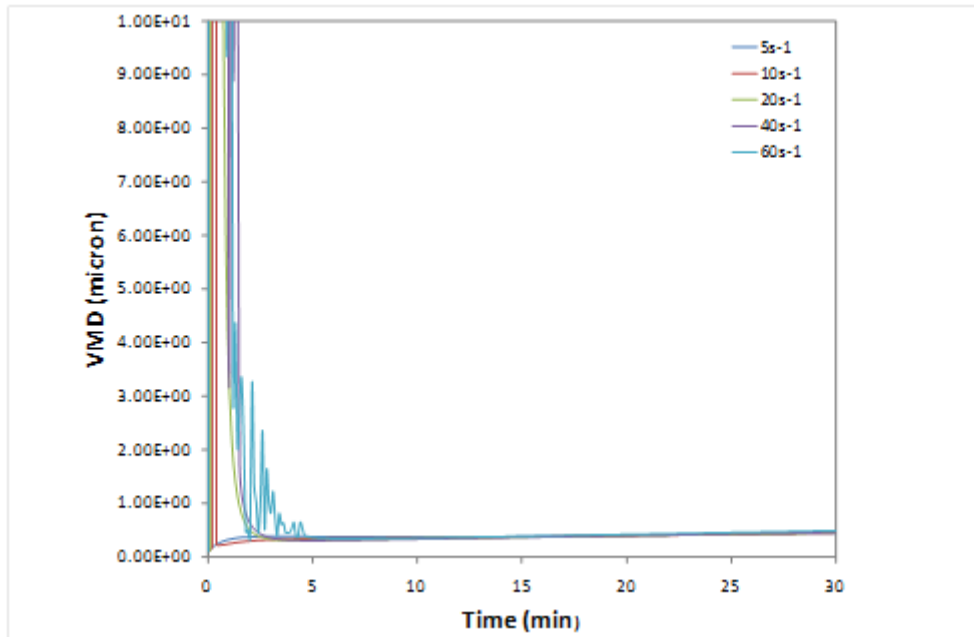
Figure 3.8: Evolution of the VMD for different values of shear rate.
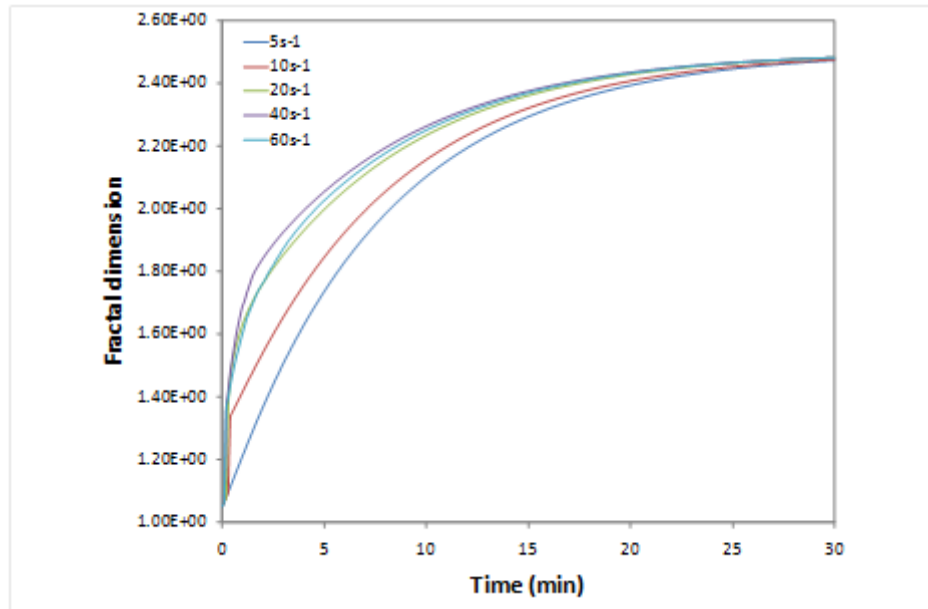
Figure 3.9: Evolution of the fractal dimension at different shear rates.

Figure 3.8 shows the evolution of the VMD and figure 3.9 the evolution of the fractal dimension over the time of the simulation for a surface potential of 5mV and an ionic strength of 0.1. As before the number of size intervals is 25.

A large overshoot can be seen once the shear rate reaches $10s^{-1}$ and greater. This is due to an initial rapid aggregation which, reflected in both the VMD and the fractal dimension. This large overshoot in the calculation causes the simulation routine to end prematurely and thus the constant volume constraint must be disabled to allow the simulation to run.

At higher shear values ($60s^{-1}$) the VMD can be seen to oscillate.

3.6.4 Magnetic field

The simulation was run with the magnetic field turned on, thus adding the effect of the magnetic interaction to the interparticle interactions. This caused various problems in running the code, due to the way the magnetic interaction affects the simulated aggregation process.

In the code there is a condition to keep the volume of particles almost constant. This allows not more than a one per cent change in total volume of particles between time steps. This condition is broken after a certain number of time steps when the magnetic field is turned on, thus terminating the simulation. In order to allow the calculation to finish this condition was suspended and the results shown in figure 3.10 come from this.
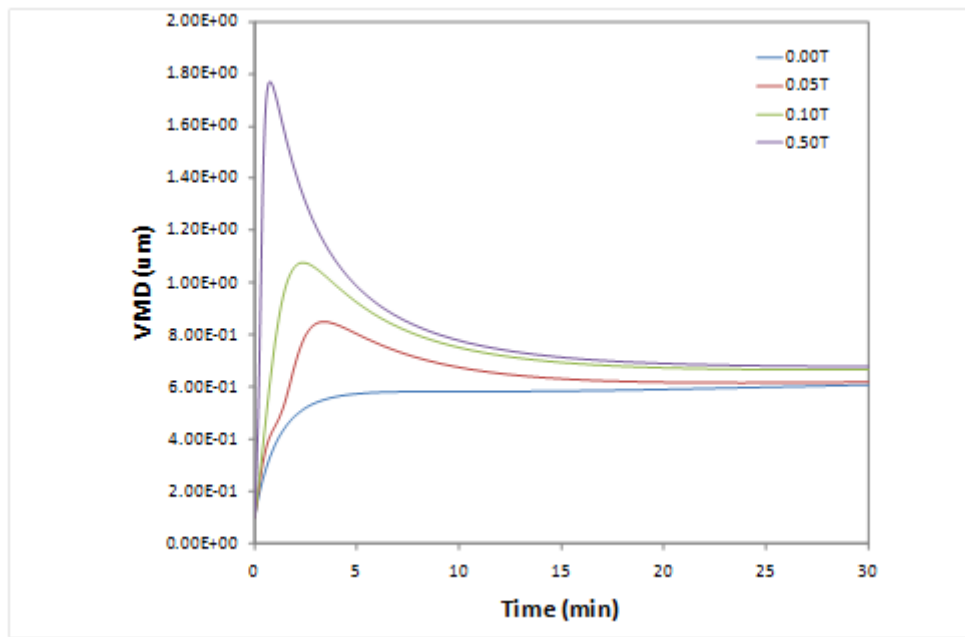
Figure 3.10: Evolution of the VMD at different values of the applied magnetic field.
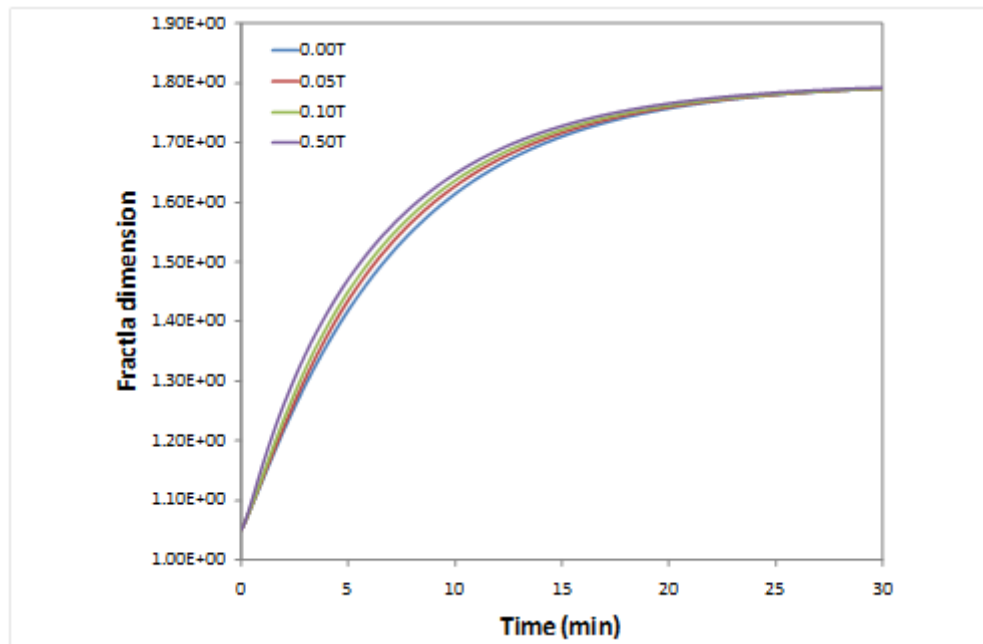
Figure 3.11: Evolution of the fractal dimension at different values of the applied magnetic field.

With the volume condition not in effect there is a loss in the total number concentration as the magnetic field is increased, interpretable physically by a loss of particles from the system.
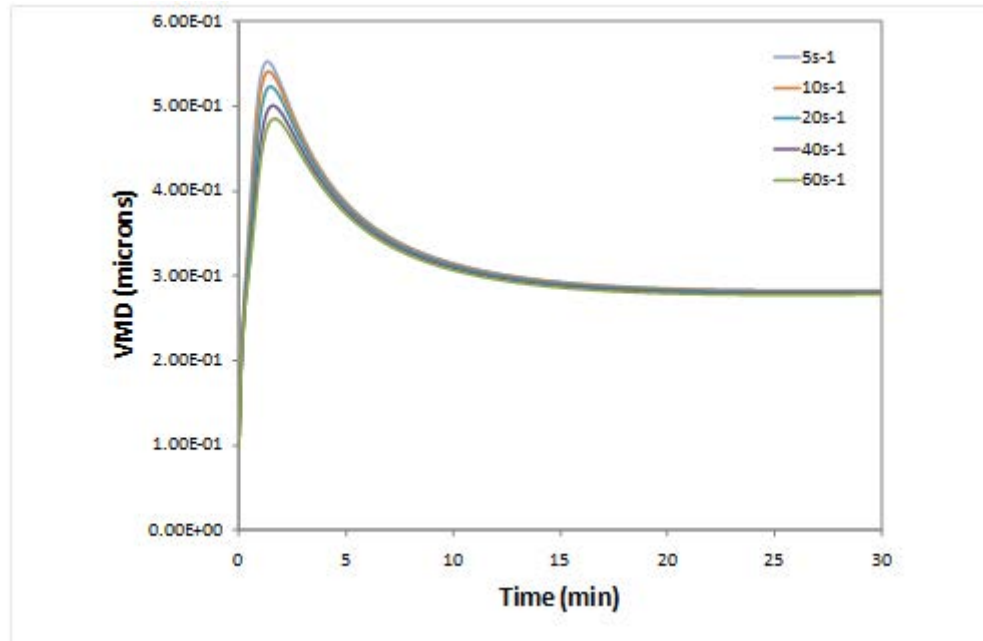
Figure 3.12: Evolution of the VMD at different values of shear rate with an applied magnetic field of 0.1T.
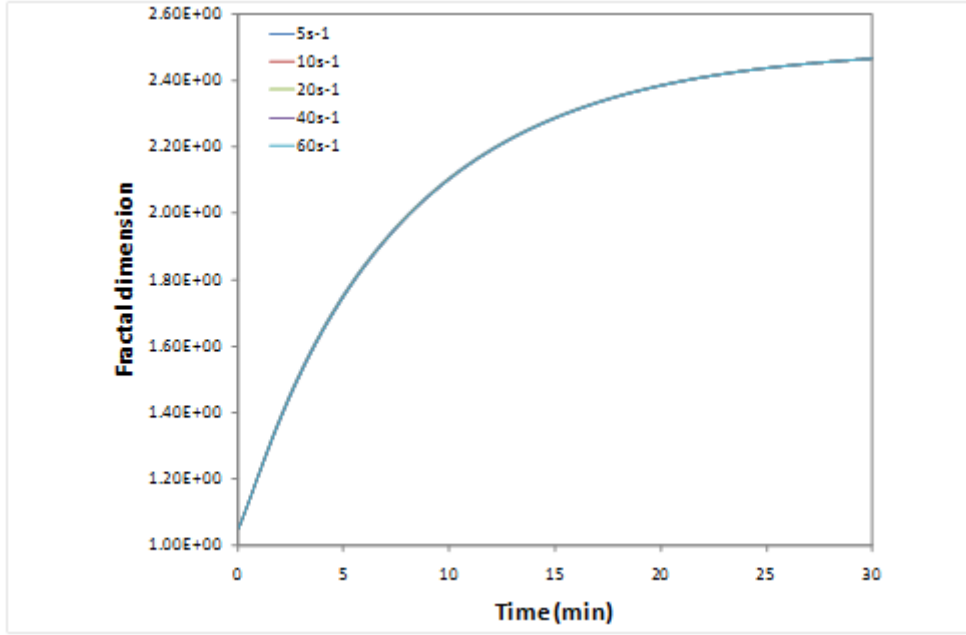
Figure 3.13: Evolution of the fractal dimension at different values of shear rate with an applied magnetic field of 0.1T.

Figure 3.12 shows the evolution of the VMD at different shear rates for a magnetic field of 0.1T. There is little difference caused by altering the shear rate, the magnetic field having a greater effect on the aggregation.

3.7   Discussion

From the calculated particle interaction profiles it can be seen that decreasing the surface potential makes the overall interaction less and less repulsive until the interaction becomes attractive at 5mV. When a magnetic field is added into this calculation the interaction becomes more and more attractive. For the profiles calculated at a surface potential value of 5mV all the profiles are attractive and a magnetic field seems only to add to this attractive interaction. For the profiles calculated at 55mV the profiles are weakly repulsive until the field strength reaches 0.5T, after which the interaction profiles are attractive.

Running the simulation, it can be seen that the VMD increases significantly as the surface potential decreases, which corresponds with the calculated particle interactions. However, the ionic strength seems to have virtually no effect in the simulation, the VMD curves virtually on top of each other. The values of the fractal dimension are set points in the simulation. The minimum value of 1 (for linear structures) was used as the starting point and a maximum value of 1.8 was set. Thus in the simulation the evolution of aggregate structures is represented by the evolution of this value.

The model has certain limitations in practice. Certain constraints have to be broken to allow the simulation to run when changing certain parameters but useful information can nonetheless be extracted from these calculations.

In terms of interactions, while altering the surface potential and the magnetic field can significantly alter the interaction profile, the ionic strength has little effect (see figure 3.6). This is unrealistic as the addition of electrolyte to a suspension of particles raises the ionic strength and destabilises the suspension.

The ability of the simulation to model the aggregation with the magnetic field is severely limited. This limitation is a result of the overwhelmingly net attractive interaction that is calculated with an applied magnetic field included resulting in large values for the collision efficiency, α. This highlights another problem in the method employed by Tsouris and Scott (1995) to calculate α. The calculation is based on the inverse of the stability ratio W and thus is not limited to values between 0 and 1 as might be expected for an efficiency factor.

The advantage of this approach is that is relatively quick (simulations can be run in only several minutes) and computationally inexpensive. However, certain limitations are inherited from the basis of the model and a slightly different solution, particularly as regards the calculation of the collision efficiency, would greatly improve the model and its usefulness.

Chapter 4

Aggregation of magnetite nanoparticles

Iron oxides are widespread in environmental systems as iron is the third most abundant element in the lithosphere (Cornell and Schwertmann, 1996), and magnetite, along with hematite, is one of the most common forms of commercial iron ore (Jorgenson, 2008). Magnetite nanoparticles have been and continue to be investigated extensively due to the large number of possible applications, particularly in paints and biomedical applications (Brigger et al., 2002; Ito et al., 2005). Often the surface of the magnetite nanoparticles is altered, either in order to stabilise the suspension, for example a surfactant in ferrofluids (Odenbach, 2003), or to functionalise the particle surface, for example with peptides, nucleic acids or antibodies (Shubayev et al., 2009). The attractiveness of such materials is in then being able to control them in their various applications using a magnetic field.

Early arguments by de Gennes and Pincus (1970) pointed to the existence of clusters and chains, which are due to the attractive parts of the dipolar magnetic interactions. Small chains (dimers, trimers) begin to form when the dipolar energy is greater than the thermal energy. By increasing the dipole moment (or lowering the temperature) the chains grow and reach an equilibrium state which consists of a distribution of chains, rings or

more complex structures of different lengths, breaking and reforming, with relative concentrations depending on density and temperature. Structure formation in suspensions of magnetic nanoparticles is highly dependent on the balance of attractive and repulsive forces, the dipolar magnetic interaction adding to the attractive force. The various interactions can be controlled by the particle size (or that of the magnetic core), thickness of the surfactant layer or the ionic strength of the solution in the case of electrostatically stabilized suspensions (Holm and Weis, 2005).

In investigating the fate of nanoparticles in natural systems Illes and Tombacz (2006) studied the effect of humic acid adsorption onto magnetite nanoparticles and its pH dependence. In this study they also investigated the pH dependent aggregation of magnetite nanoparticles by measuring the particle size using dynamic light scattering. It was found that the stable suspensions of clusters ($\approx$100nm compared to less than 10nm primary particle size, with the possibility that there are fractal aggregates also present, as commented by the authors) formed at pH away from the point of zero charge (PZC) and that large aggregates formed closer to the PZC. This type of pH dependence was also found by Pang et al. (2007), who also measured the particle size using dynamic light scattering and used a primary particle size of 6-12nm.

Previous static light scattering studies have determined various fractal dimensions for aggregates of magnetite nanoparticles. Shen et al. (2001) found a fractal dimension of 2.5 for an aqueous based ferrofluid with $\approx$10nm primary particles stabilised by a surfactant bilayer. Martinez-Pedrero et al. (2005) found fractal dimensions close to 1 for magnetite particles embedded in polystyrene. Bica et al. (2007) investigated various sterically stabilised magnetite particles, all with primary particle diameter less than 10nm, and found fractal dimensions of 1.47 and 1.58 depending on the surfactant used for stabilisation. It was also found that there were two scattering levels, the difference being attributed to there being one scattering level for clusters of several particles and another for the larger,

fractal aggregates composed of the smaller clusters.

The purpose of this chapter is to characterise the aggregation of a suspension with a large magnetic interaction which contributes to the agglomeration of the particles, and thus the characteristics of a magnetically aggregating suspension. Magnetite, being an iron oxide, also has similar surface chemistry to hematite, which is used later in this study to observe how its aggregation is affected by a magnetic field.

4.1 Synthesis and Characterisation

4.1.1 Synthesis

Cubic magnetite particles were prepared by the aging of a ferrous hydroxide gel under controlled conditions (Sugimoto and Matijevic, 1980). The gel was prepared by mixing an 80ml solution of $FeSO_4$ (prepared from 0.6948g of crystalline $FeSO_4 \cdot 7H_2O$ (CAS number 7782-63-0, supplied by ACS Chemicals) in 80ml of distilled water; the water was first deoxygenated by bubbling nitrogen gas through for an hour) with 10ml of 2 M KNO_3 solution (taken from a stock solution made by mixing 202.2064g of crystalline KNO_3 (CAS number 7757-79-1, supplied by ACS chemicals) in 1000ml of distilled water). Nitrogen gas was then bubbled through the mixture for 15 minute before adding 10ml of 1 M NaOH solution (taken from a stock solution made by mixing 39.9971g of crystalline NaOH (CAS number 1310-73-2, supplied by ACS chemicals) in 1000ml of distilled water) which caused the precipitation of the ferrous hydroxide gel. This was then aged in a water bath at 90^oC for two hours after which it was removed and allowed to cool. The particles were then separated using a magnet and then redispersed in distilled water.

4.1.2 Characterisation

4.1.2.1 TEM

Transmission electron microscopy was used to look at the size and shape of the particles after synthesis. The images were captured using a JEOL 1400 Microscope with a beam current of 100kV. A TEM mage of the synthesised magnetite nanoparticles is shown in figure 4.1, where the particles can be seen to be cubic in shape.
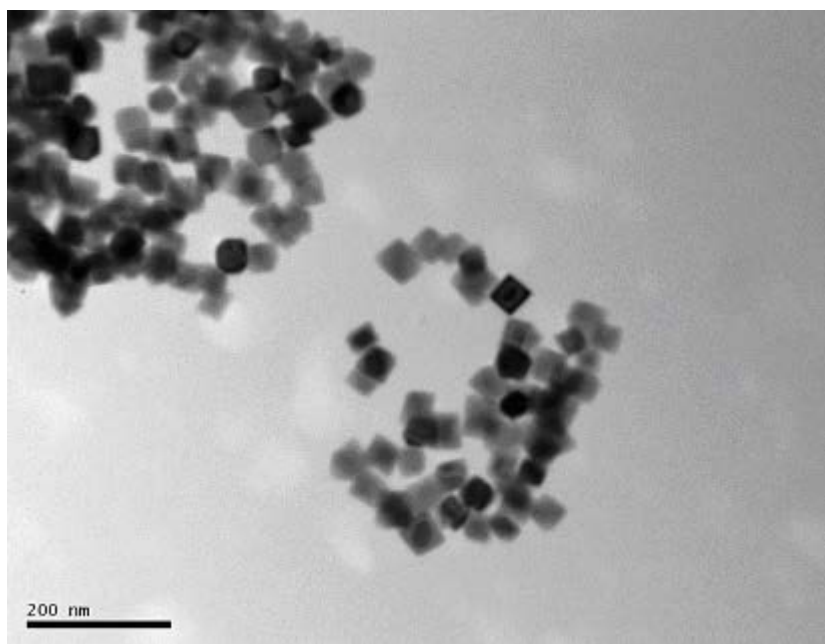
Figure 4.1: TEM image of the magnetite nanoparticles.

The average particle size from TEM images was calculated, using the ImageJ software package, to be 32.92 nm $\pm$ 4.58.

4.1.2.2 Dynamic Light Scattering

Dynamic light scattering (DLS) measurements were also performed using a Brookhaven ZetaPALS system, which uses a scattering angle of 90°. DLS measurements measure the hydrodynamic diameter, as opposed to the actual physical diameter as can be done from

a TEM image, and give an indication of the degree of aggregation in the suspension. The particles were first placed in an ultrasonic bath before being diluted in distilled water for the measurement. Extrapolating size data from a DLS measurement can be done based on one of two assumptions - (i) there is a single population of particles, or (ii) there are several populations of particles. In the first case this would mean the suspension is assumed to be monodisperse and could be represented by a single value. This is here called the effective diameter. In the second case polydispersity is assumed and the data is deconstructed and fitted to a size distribution.

The DLS measurement gave an effective diameter of 70.0nm ±7.8 for the magnetite particles. The intensity distribution obtained from DLS is shown in figure 4.2.
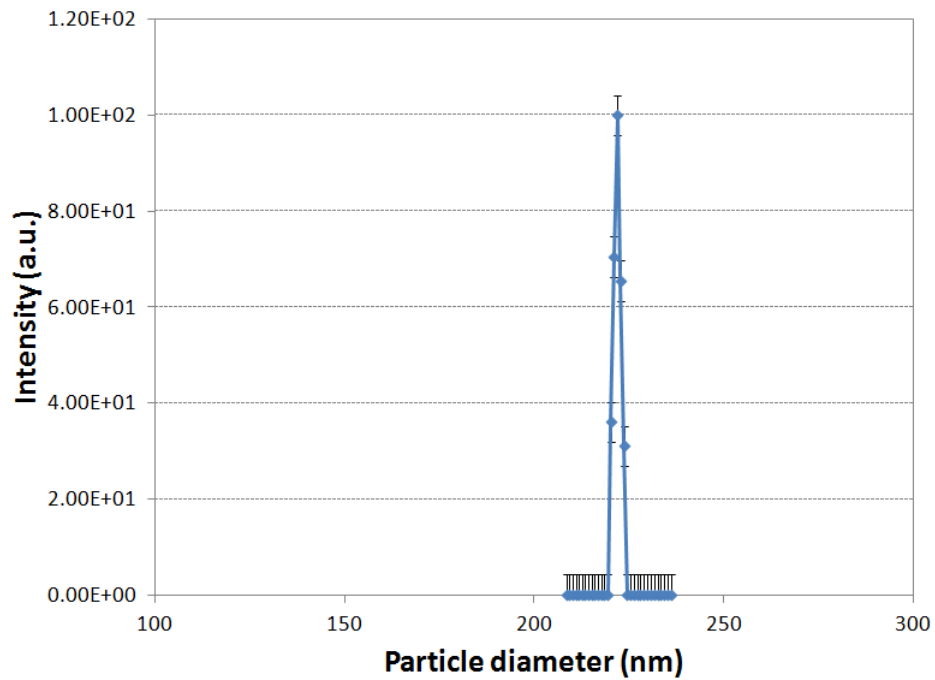
Figure 4.2: DLS size distribution for the magnetite nanoparticles. (Combined results from 3 sets of measurements.)

The intensity distribution shows a narrow peak, and also gives a larger size than the effective diameter. This, however, is misleading as it is merely a temporary state.

96

Magnetite nanoparticles aggregate rapidly to form large aggregates. After one hour the particles grow to micron size aggregates, and this is shown in figure 4.3, where the effective diameter is plotted against time. The polydispersity index is also shown to increase at the same time. The polydispersity index gives an indication of the validity of the assumption of a monodisperse population of particles. It is a measure of the difference between the measured data and the fitted data, with 0 indicating a good fit and 1 indicating no fit. Thus as the polydispersity index increases the monodisperse assumption loses its validity.
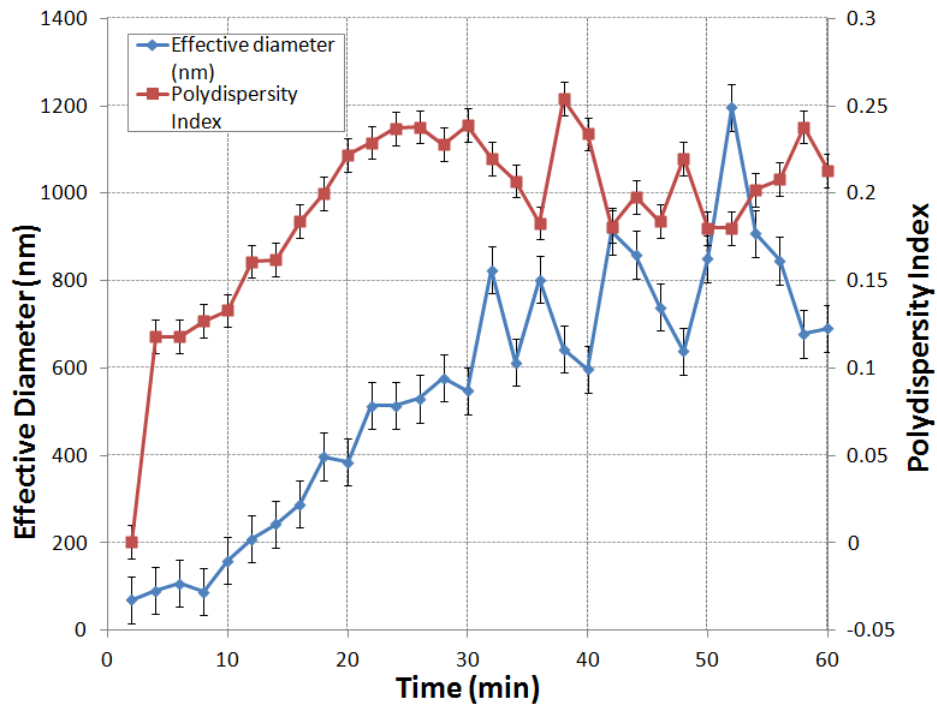
Figure 4.3: Evolution of the particle diameter (in nm) and the polydispersity index of magnetite particles over 1 hour. (Combined results from 3 sets of measurements.)

Thus measuring the particle size using DLS is difficult with an unstable suspension which is aggregating during the measurement. This is a well known problem and the colloidal stabilisation of magnetic nanoparticles is the subject of much current research due to their potential applications in medicine and nanobiotechnology.

4.1.2.3 Zeta Potential

The zeta potential of the particles was measured at various salt concentrations and pH values using a Brookhaven ZetaPALS system with a pH titrator. The salt used was potassium nitrate (KNO_3). The system uses phase analysis light scattering (PALS) to determine the zeta potential of the particles at the measured pH. The results of these measurements are shown in figure 4.4.
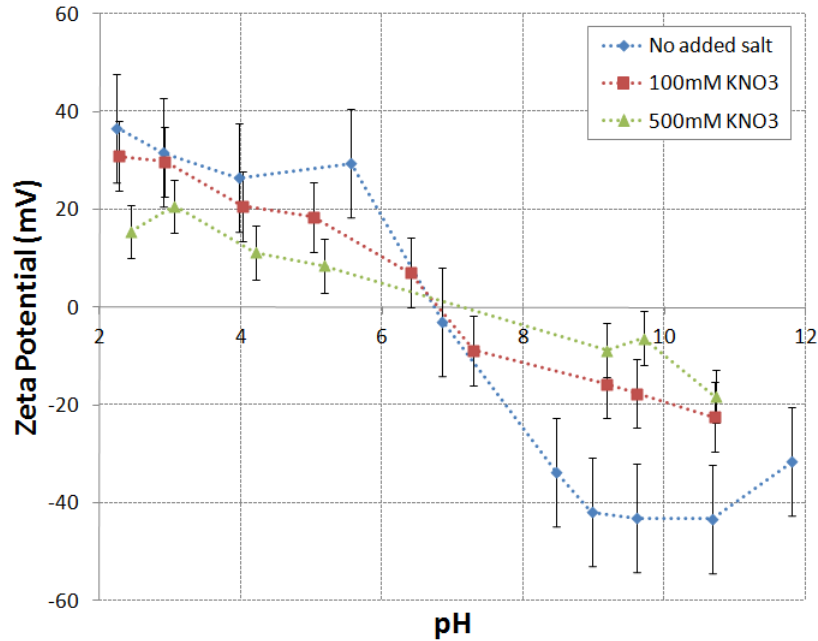
Figure 4.4: The zeta potential of the particles at various pH and salt concentrations. The salt used was potassium nitrate (KNO_3). (Combined results from 3 sets of measurements.)

The isoelectric point was determined to be at pH 6.7 for the magnetite particles when dispersed in distilled water. This is similar to the values around pH 7 reported by other investigators (Regazzoni et al., 1983; Perales-Perez et al., 2000; Gómez-Lopera et al., 2001; Pang et al., 2007). Illes and Tobacz (Illes and Tombacz, 2006) reported a slightly higher isoelectric point of pH 7.9 for their magnetite nanoparticles, and also noted as other authors have (Perales-Perez et al., 2000) the effect of electrolytes on the surface

charge of the particles due to specific adsorption of ions onto the particle surface.

4.1.2.4 Magnetic Behaviour

The magnetic behaviour of the particles was measured using a vibrating sample magnetometer (VSM). The particles were dried to give a powder which was used to perform the measurement at a temperature of 300K. This is shown in figure 4.5.
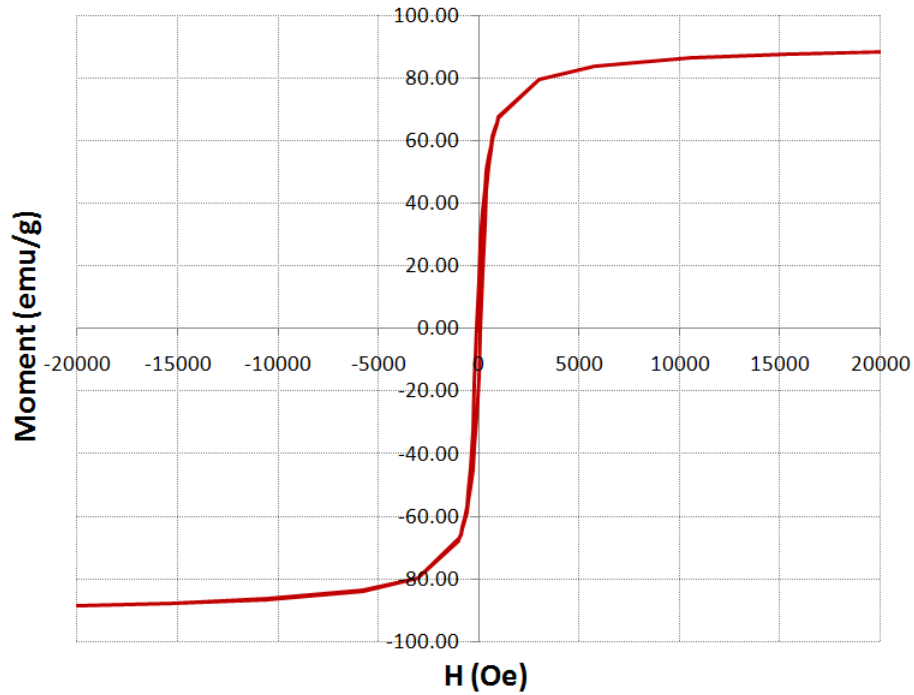
Figure 4.5: Plot of the magnetic behaviour of the spherical magnetite particles.

The magnetite particles have a magnetic saturation of 88.4 emu/g similar to values found by other researchers.

4.1.2.5 Concentration of Particles

The concentration of the suspended hematite nanoparticles was determined using atomic absorption spectroscopy. 1ml of the suspension was added to approximately 10-15ml of strong hydrochloric acid ($\approx$3M) in a 50ml flask. After several hours the hematite dissolved

to form a solution of Fe^{3+}. Distilled, deionised water was then added to make the volume up to 50ml. The solution prepared in this way was then diluted to a number of different concentrations and analysed using ICP.

The concentration of Fe was determined by this method to be 90.87 mg/l. Taking the molar mass of iron to be 55.84 g/mol and that of oxygen to be 15.99 g/mol that gives a concentration of Fe_3O_4 of 125.58 mg/l.

4.2 Experimental

4.2.1 Experimental setup

The aggregation process was monitored by small angle static light scattering using a Malvern Instruments Mastersizer S with the batch processing sample holder.

4.2.2 Experimental method

The stock suspension was sonicated and then 0.1ml was dispersed into 50ml of either 3.75mM HCl, distilled water or 3.75mM NaOH to give suspensions at pH 2.4, 7.0 and 11.5 respectively. The effect of added electrolyte was investigated in the same way by dispersion in 100mM potassium nitrate KNO_3. The aggregation was monitored over 1 hour and the experiments were repeated at least 3 times to ensure reproducibility.

4.2.2.1 Calculation of scattering exponents

The fractal dimension can be calculated from the gradient of the scattered intensity plot, but as fractal dimensions only take values from 1 to 3 (or 0 for points) this is referred to as the scattering exponent as the gradient could also be outside this range. If the scattering exponent is less than 1 this simply means that there are more likely to be small clusters (doublets, triplets, etc.) of particles as well as many single particles (which would theoretically have a scattering exponent of 0, being single points). The scattering

exponent was calculated from the scattering data using a Matlab routine (see Appendix A).

4.3 Results

As seen in the characterisation, magnetite nanoparticles aggregate rapidly to form large structures. However, in spite of this, the sedimentation of the particles was not observed during the timescale of the experiments.

4.3.1 Effect of pH

The aggregation can be affected by altering the pH and thus increasing or decreasing the electrostatic repulsion between the particles. The result of this is that aggregates of different size and also structure form at different pH.

At pH 2 and 11, which are further from the isoelectric point, the size distributions are similar and show large peaks at around 140um. The size distribution at pH 7, which is very near to the isoelectric point, is much broader and also shows the presence of very large aggregates. These size distributions are shown in figure 4.6.
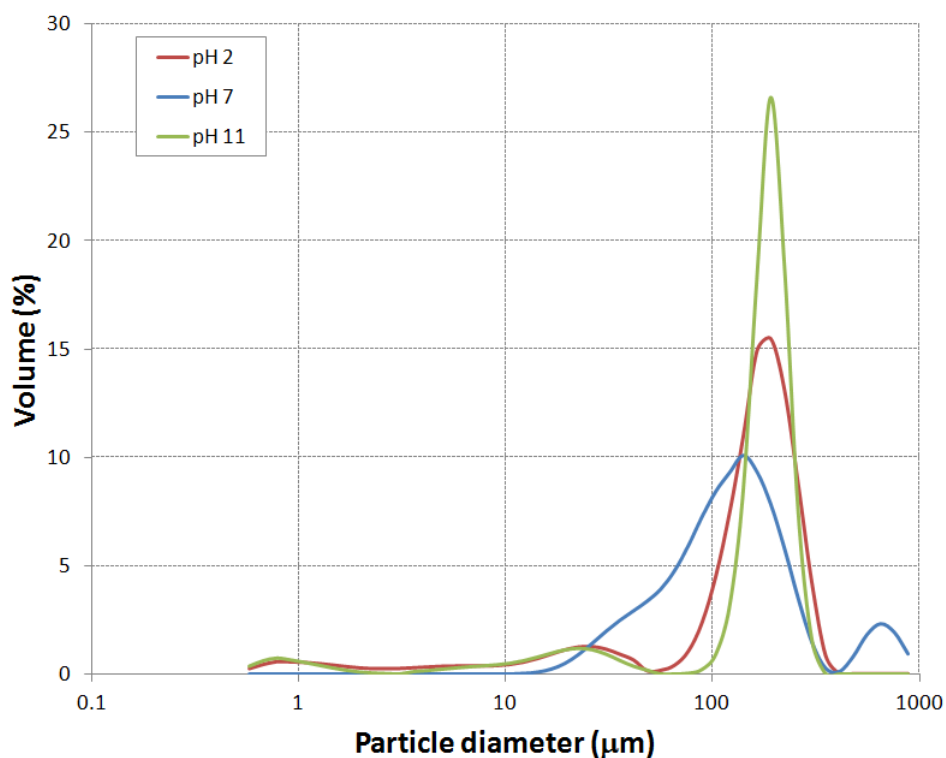
Figure 4.6: Size distributions of the magnetite particles at different pH after 1 hour.

This difference in aggregate size can also be seen in DLS measurements. The evolution of the effective diameter (size as calculated on the assumption of monodispersity, as discussed in the characterisation section 4.1.2.2) is similar at pH 2 and pH 11, but increases more rapidly when the suspension is closer to the isoelectric point at pH 7. This is shown in figure 4.7. The sizes derived from these DLS measurements are not accurate, especially as the population of particles aggregates into a more polydisperse suspension, but the effect of the pH on aggregate growth is apparent.
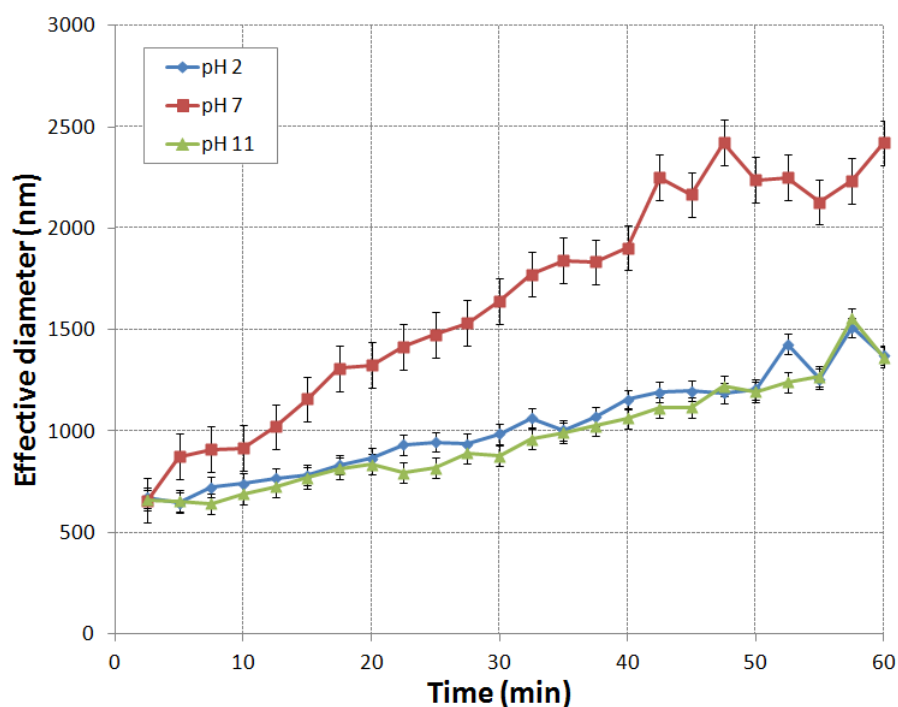
Figure 4.7: Effective diameter of magnetite particles over 1 hour as measured by dynamic light scattering.(Combined results from 3 sets of measurements.)

The structure of the aggregates changes with the pH as well as the size. The scattering exponents are similar at pH 2 and pH 11, with scattering exponents of 1.5, a value lower than that normally seen for diffusion limited aggregation (Meakin, 1983). There is also little change in the structure over time which is the case when aggregates grow fractally (the structure remains the same as the aggregate grows larger). At pH 7 the aggregates have scattering exponents closer to 2, thus implying a more compact structure. These differences in the size and structure of the aggregates at different pH can also be seen in TEM images. These are shown in figure 4.8, 4.9 and 4.10.
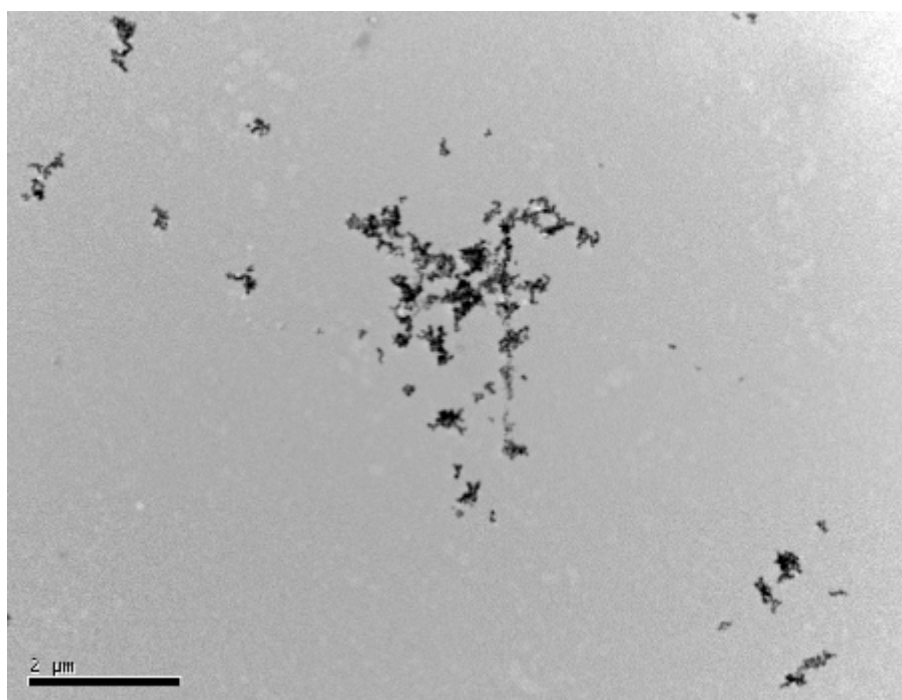
Figure 4.8: TEM image of the magnetite nanoparticles at pH 2.
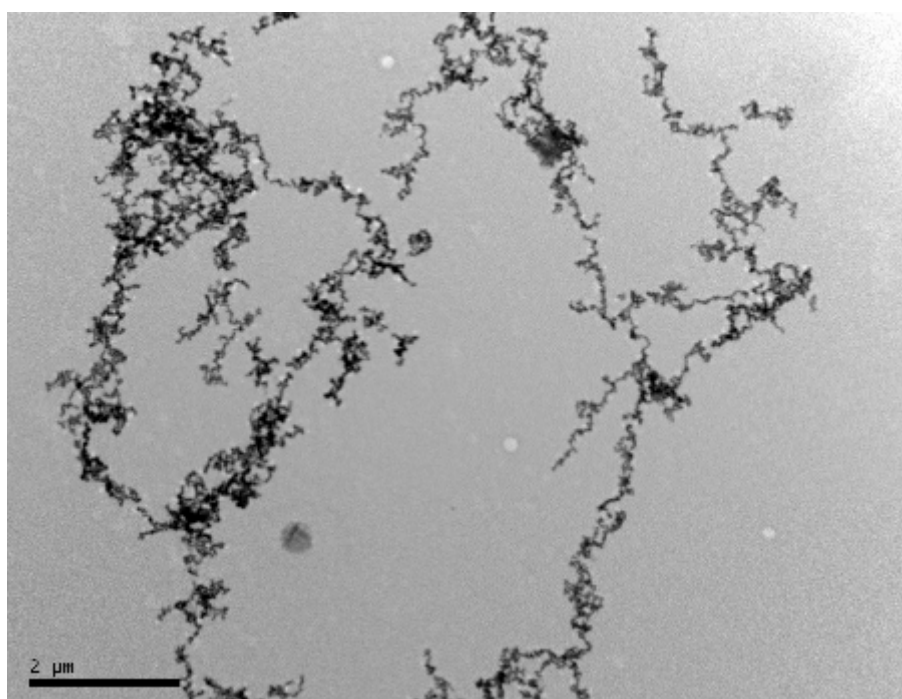
Figure 4.9: TEM image of the magnetite nanoparticles at pH 7.

104
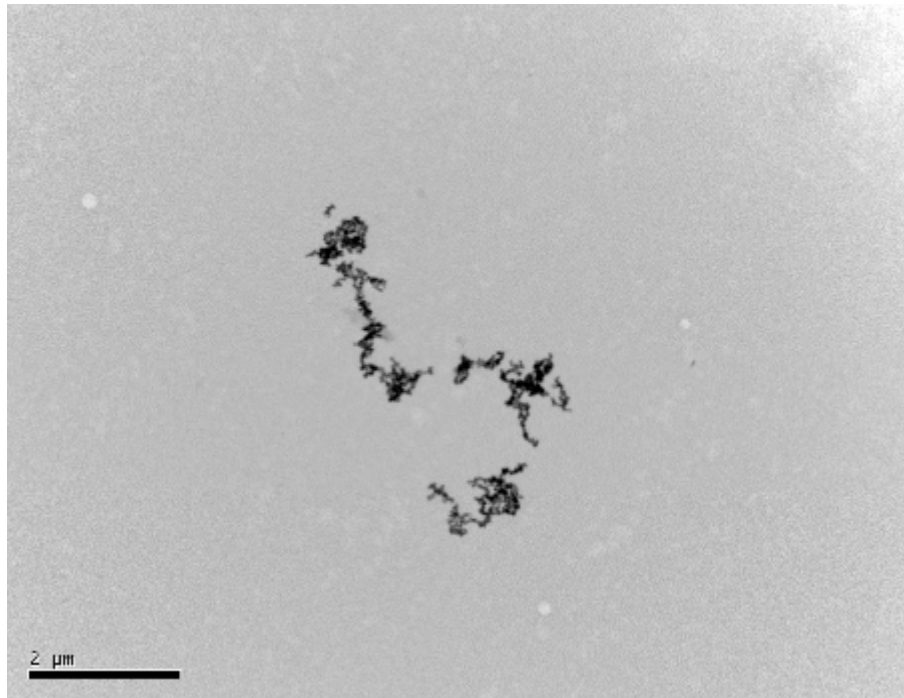
Figure 4.10: TEM image of the magnetite nanoparticles at pH 11.

However, at pH 7, the structure does not appear to be that typically expected from a more compact aggregate with a fractal dimension close to 2. This can be explained further by looking at the scattering data, shown in figure 4.11. Two slopes can be distinguished in the scattering data, which implies a variation in the structure of the aggregates with the length scale. The lower slope has a shallower gradient, indicative of more open, linear structures, and the upper slope has a steeper gradient, indicative of more compact aggregates.
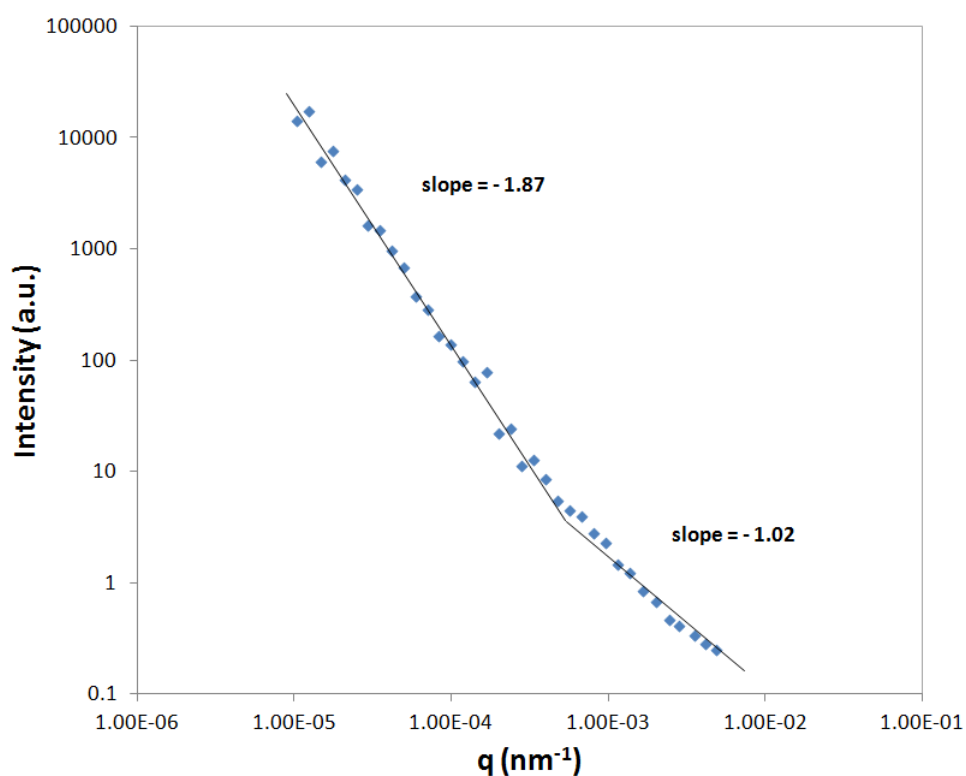
Figure 4.11: Scattering data for the magnetite nanoparticles at pH 7 after one hour.

This structural variation can also be better explained by looking at the TEM images. Large tenuous structures can be seen as well as more compact ones, which could account for the variations in the scattering exponents. However, at a greater magnification (figure 4.12) the aggregates can be seen to be composed of many chain type structures which could account for the low scattering exponents at shorter length scales.
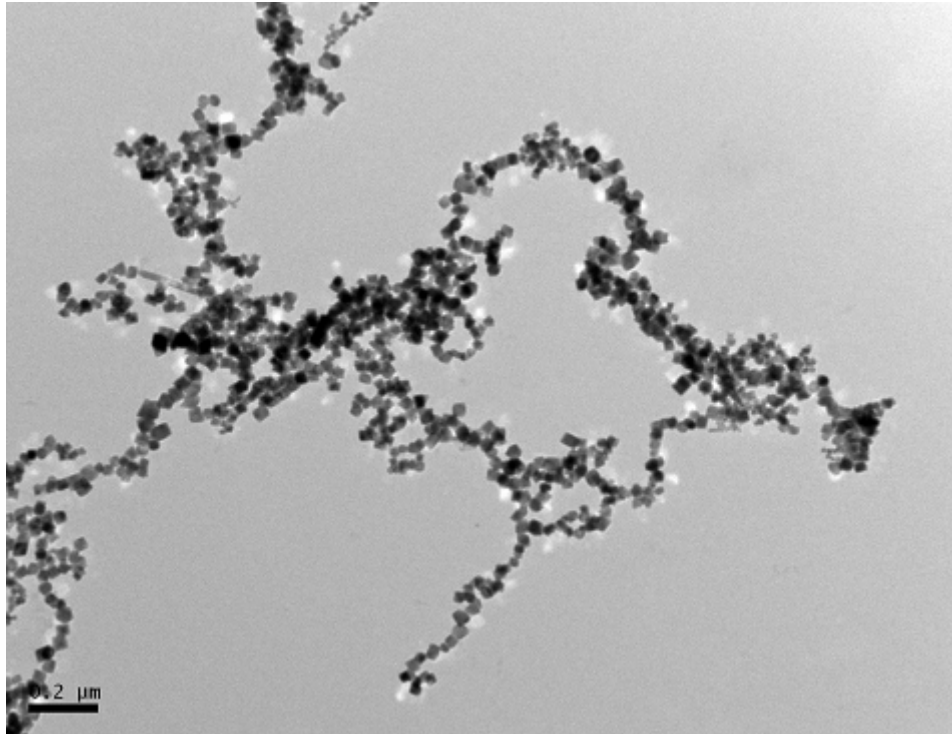
Figure 4.12: TEM image of the magnetite nanoparticles at pH 7.

This can also be seen by taking a closer look at the TEM images, such as that in figure 4.12. Linear, chain like structures and rings, such as those predicted by de Gennes and Pincus (1970) can be seen at small length scales, which could account for the shallow slope in the scattering data (figure 4.11).

At larger length scales, the structure is more compact as in figure 4.9, and as indicated by the upper slope of the scattering data (figure 4.11) which is much steeper.

4.3.2 Effect of electrolyte

The addition of electrolyte to the suspensions of magnetite particles reduces the effect of electrostatic repulsion through the suppression of the electric double layer, allowing the magnetic interaction an even greater influence on the aggregation process. The experiments were performed with suspensions at pH 7.

The size distributions for the magnetite particles with and without added electrolyte are shown in figure 4.13. The peaks are broader when electrolyte is added to the suspensions of magnetite particles, and the main peak is at a larger size as the amount of added electrolyte is increased.
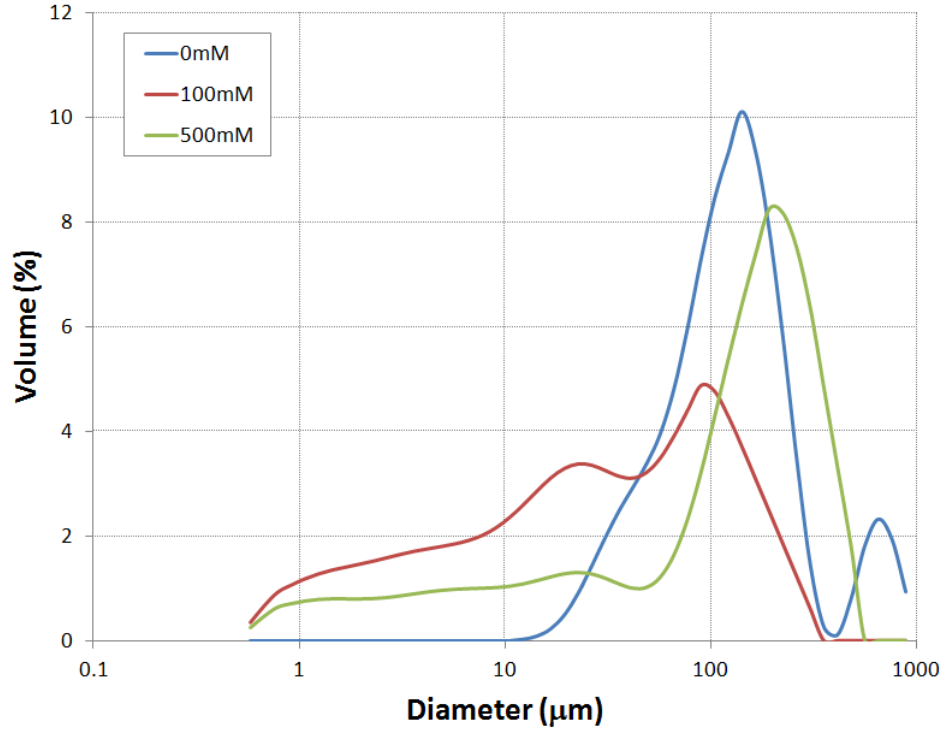
Figure 4.13: Size distributions of the magnetite particles at different concentrations of KNO_3 after 1 hour.

The structures of the aggregates, indicated by the scattering exponents, also vary with the concentration of electrolyte added. The scattering exponents calculated from the scattering data were 1.9 at 0mM, 1.5 at 100mM and 1.3 at 500mM. This trend implies that the aggregates grow into more open structures as the amount of electrolyte added to the system is increased. TEM images of the aggregates formed with added electrolyte are shown in figures 4.14, 4.15 and 4.16 (for 100mM KNO_3) and figures 4.17, 4.18 and 4.19 (for 500mM KNO_3).
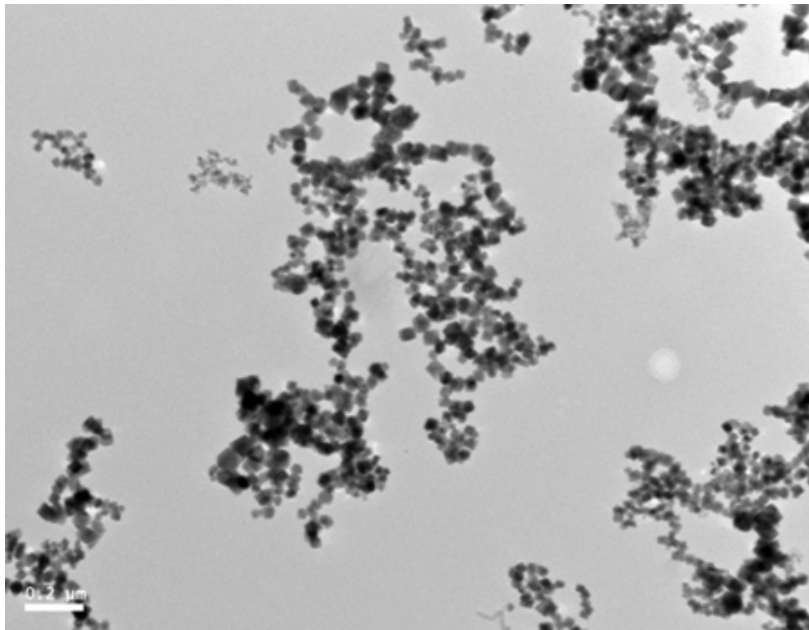
Figure 4.14: TEM image of magnetite particles after 1 hour, aggregated using 100mM KNO$_3$.
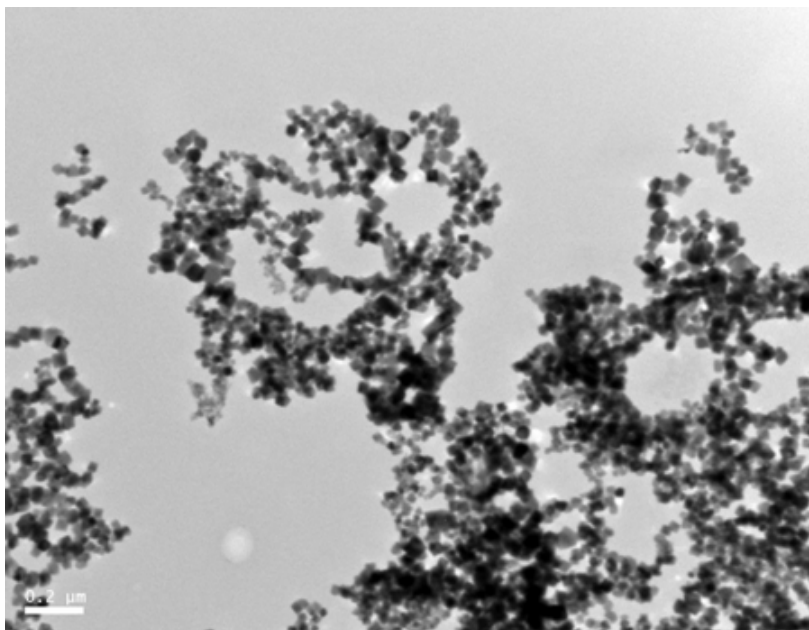
Figure 4.15: TEM image of magnetite particles after 1 hour, aggregated using 100mM KNO$_3$.
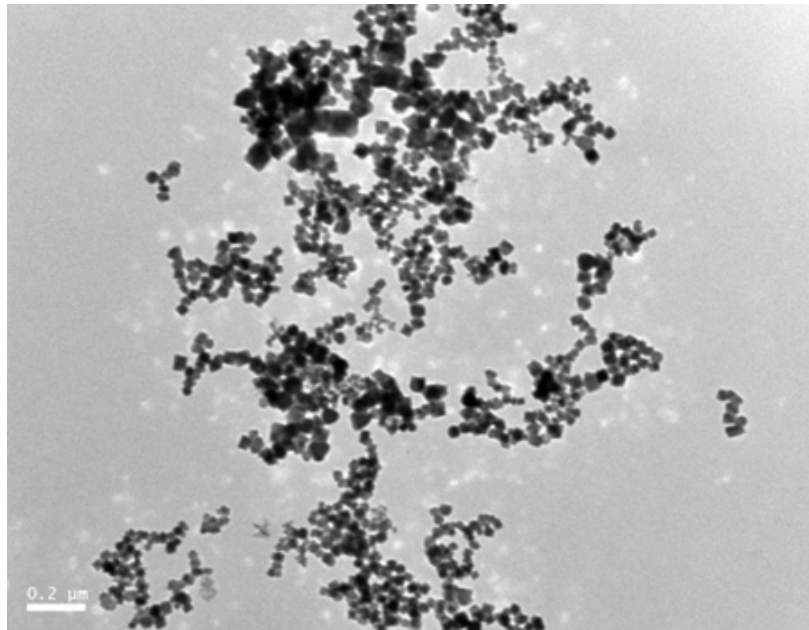
Figure 4.16: TEM image of magnetite particles after 1 hour, aggregated using 100mM KNO$_3$.
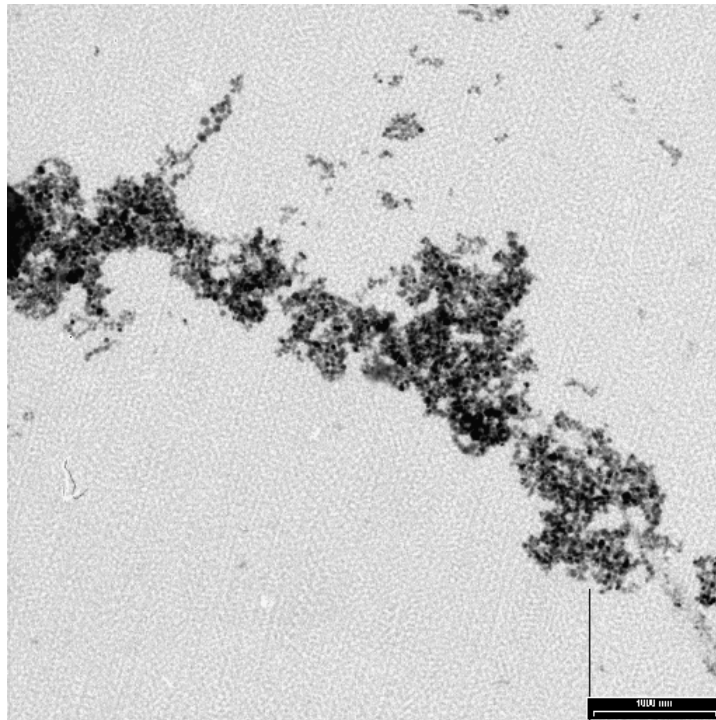
Figure 4.17: TEM image of magnetite particles after 1 hour, aggregated using 500mM KNO_3.
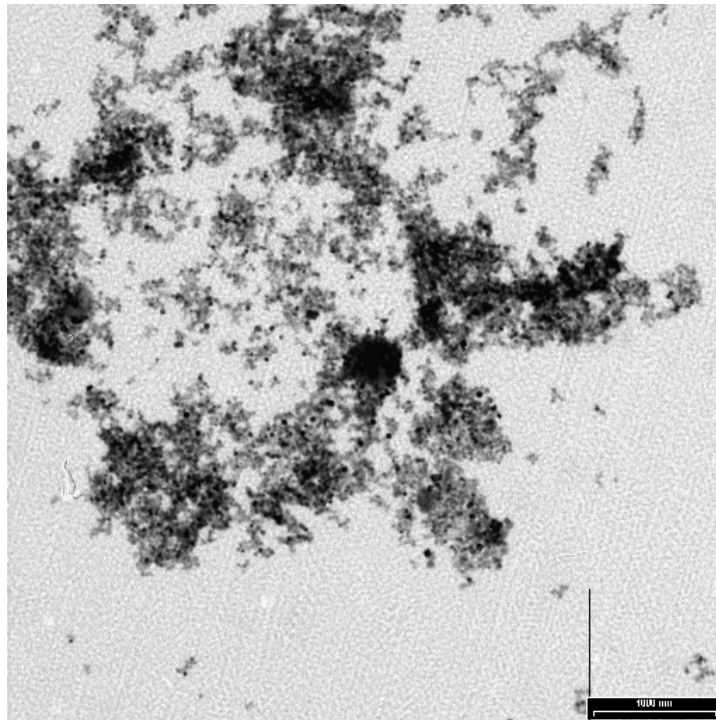
Figure 4.18: TEM image of magnetite particles after 1 hour, aggregated using 500mM KNO$_3$.
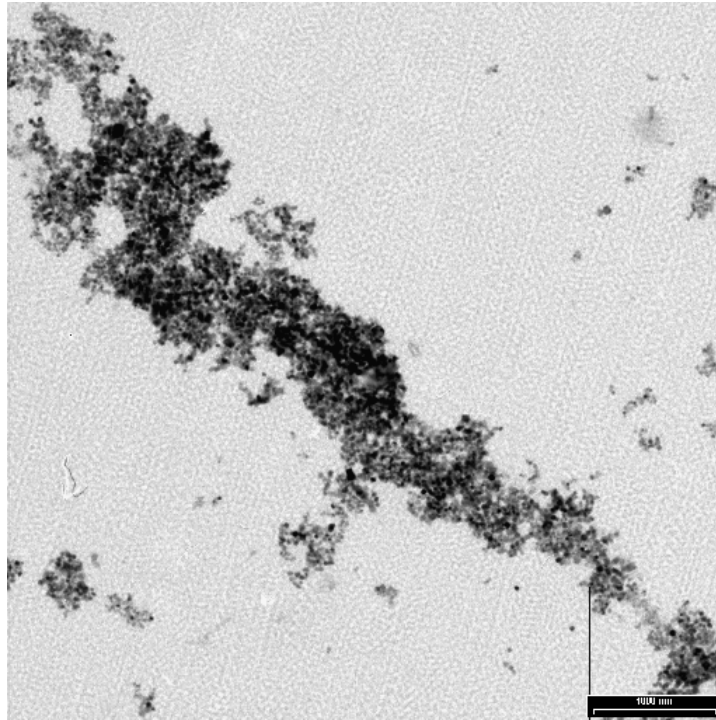
Figure 4.19: TEM image of magnetite particles after 1 hour, aggregated using 500mM KNO$_3$.

The structures seen in the TEM images are not in agreement with the type of structures expected from the corresponding scattering exponents. The aggregates appear to be denser than the type of structure seen without the addition of electrolyte (see figures 4.9 and 4.12). The structural variation seen in the scattering data without the addition of electrolyte is also not observed when electrolyte is added. In addition, while there is more variation of the scattering exponent as the particles aggregate without added electrolyte, this is not seen when the particles aggregate in the presence of the added electrolyte.

4.4 Discussion

The particles were synthesised following the method of Sugimoto and Matijevic (1980) and show the features of the magnetite particles produced (colour, shape and magnetic behaviour). However, equipment to perform x-ray diffraction (XRD) measurements on

the particles was not available and thus the crystal structure was not confirmed in this manner to be that of the iron oxide, magnetite (Fe_3O_4).

The magnetic interaction between the particles is of much greater importance in the interplay of interparticle forces in this system, and so the particles are easily separated from suspension by a magnetic field. The important contribution of the magnetic interaction is what is of interest in this chapter as it is an intrinsic property of the particle as opposed to an externally applied field (which is what becomes of interest in the next chapter on hematite).

The magnetic interaction is what accounts for the inherent instability of the particle system and its rapid aggregation characteristics. Contrary to most studies focusing on magnetite nanoparticles, the particles described here have no surfactant to stabilise the suspension and what is of interest is the aggregation behaviour of the bare particles which serves as a sort 'benchmark' for comparison with the hematite particles in the next chapter. No such comparable experimental study could be found in the literature at the time of writing to describe the aggregation of bare magnetite particles.

Comparison of TEM images, DLS results and static light scattering results show that the pH has a clear effect on the aggregation. In particular, the TEM images reveal the formation of long chains and ring structures close to the isoelectirc point at pH 7 (see figure 4.4) not seen further from the isoelectric point at pH 2 and pH 11. This can be explained using the DLVO paradigm in terms of changes in the overall interaction energy as the pH is altered. The extended DLVO theory includes three terms - the attractive forces, the repulsive forces and the magnetic forces. The attractive van der Waals forces are very short range and only really come into play when particles are close to each other (within a few nanometres). The repulsive forces are electrostatic and expressed through the electric double layer, which is directly affected by changing the pH. The magnetic interaction acts over a longer range. Thus the chemical environment, in this case the

electric double layer, acts to slow down aggregation of the particles but is not sufficient to prevent it. According to the DLVO theory, the addition of electrolyte compresses the electric double layer thus lowering the repulsion between particles. This can be seen in the change of aggregates from long chains and rings (see figure 4.12) to much more dense aggregates (see figures 4.14 to 4.19).

The aggregation of the magnetite particles is characterised by the rapid formation of large aggregate structures with low scattering exponents. The scattering exponents are mostly in the fractal range (from 1 to 3) and thus can be referred to as the fractal dimension. These low fractal dimensions mean that whilst the aggregates formed are large, they are very open structures and thus have low densities. The low density of the aggregates could also account for why no sedimentation occurred during the experiments, despite the large sizes the aggregates reached. The formation of these structures is affected by the suspension conditions showing that the influence of the magnetic interaction can be altered by the chemical conditions. However, the suspension was never observed to be stable and, generally, this is only achieved by using smaller particles (Holm and Weis, 2005) or through the alteration of the particle surface with surfactants (Khalafalla and Reimers, 1980) and is made even more difficult when trying to simulate biochemical conditions where much greater ionic strengths occur (Zhang and Zhang, 2005).

The pH of the suspension clearly influences the degree of aggregation, in particular the overall aggregate size and structure, as can be seen from the TEM images in figures 4.8, 4.9 and 4.10. This follows the trend observed by Illes and Tombacz (2006), although the suspensions synthesised in that study were much more stable. This is most likely due to the smaller size of the primary particles which have a greater thermal motion, as remarked by Holm and Weis (2005), which were less than 10nm as compared to $\approx$25nm in this study.

The structures formed at pH 7 are more typical of those originally predicted by

de Gennes and Pincus (1970) consisting of agglomerated clusters of chain and rings (figure 4.12). At pH 2 and 11 the structures appear to be composed of slightly more compact clusters, with much less formation of the chain type structures seen at pH 7, although the scattering exponents are similar to those found by Bica et al. (2007) for surfactant stabilised particles. From the scattering data, the aggregate structures were also observed to show structural variation at pH 7, as was also observed by Bica et al. (2007), according to the length scale considered. For example, at larger length scales at pH 7 the structures appear more compact, whereas at a shorter length scale the structures appear more open. This could be due to the predominance of chain-like structures at a small length scale whereas the overall structure at a larger length scale is indeed more compact.

Structural variation at different length scales has also previously been observed in aggregates of silica nanoparticles (Hermawan et al., 2003, 2004). The investigators found the inverse of the situation observed here - more compact short range structures and more open long range structures. Similar scattering data has also been observed in shear flows where aggregates restructure (Selomulya et al., 2001). In that case restructuring occurred more rapidly at larger length scales due to the greater influence of hydrodynamic forces, resulting in a similar situation to that here with more open structures at smaller length scales.

The addition of electrolyte causes the suppression of the electrical double layer, as can be seen from the zeta potential curves in figure 4.4, providing even less resistance to the aggregation of the particles. The addition of electrolyte also seems to encourage the formation of a more uniform structure that exhibits a greater degree of the self-similarity that is characteristic of fractal aggregates. The overall structure is also more open than that at pH 7 without added electrolyte according to the scattering exponents, and the TEM images show these structures to be more similar to those formed at pH 2 and 11. There is however some of the chain and ring type formation found at pH 7, although

not to same degree. Thus, with the added electrolyte the particles form large aggregates, similar in size to those observed at pH 7 without any added electrolyte, but with a more open overall structure.

The aggregation of magnetite nanoparticles is thus greatly influenced by the chemical conditions of the suspension, and the pH can be used to reduce aggregation but not prevent it. The large magnetic interaction between the particles provides an attractive force that results in rapid aggregation kinetics. The resulting aggregates are large and have open structures with low fractal dimensions.

CHAPTER 5

AGGREGATION OF HEMATITE

NANOPARTICLES IN A MAGNETIC FIELD

5.1 Previous work

Several studies have been done using hemtite as model particles for investigations of magnetic effects on colloidal stability. Hematite is an attractive model system because it is easily synthesised at low cost and has already been well characterised (Amal et al., 1990).

Tombacz et al. (1991) studied the effect of a static magnetic field on stationary and (turbulent) flowing systems of hematite nanoparticles. The investigators found that a significant change was found only when the magnetic field was applied to a flowing system with an optimum electrolyte concentration which was below that of the critical coagulation concentration. The scattered light intensity increased under these conditions which the authors attributed to an increase in particle aggregates. This was also supported by dynamic light scattering measurements showing an altered size distribution with an increase of aggregates. Changes in zeta potential were also observed under these conditions, with the zeta potential changing by up to 10 mV.

In the static system the scattered light intensity decreased, and in a flowing system without the applied magnetic field there was a slight increase, but no significant change was observed as with both flow and magnetic field. Changes in zeta potential were also small compared to the changes seen with flow and magnetic field.

The effects were attributed to magnetohydrodynamic effects by the authors, in particular the interaction between the magnetic field and the electrical double layer, although no definitive explanation could be offered. Similar observations were also made for suspensions of cholesterol (stabilised by sodium taurodeoxycholate) and polystyrene latex in NaCl solutions (Busch et al., 1996), and the authors suggest that the magnetic aggregation does not appear to involve direct interaction between the field and the solid phase, but interpreted it in terms of orthokinetic effects involving magnetohydrodynamic changes in the flow profile resulting from the presence of the transverse field.

Other authors have also seen increases in the size of aggregates of hematite nanoparticles when a magnetic field is applied. Kendall and Kosseva (2006) observed an increase in the size of small aggregates in a static system, which is not in accordance with the results of Tombacz et al. (1991). It was found that the increase in aggregation was sensitive to the pH of the suspension and had no effect at a pH where the suspension was essentially stable. However, increasing the pH caused the formation of clusters, observed via dynamic light scattering, which were then susceptible to the influence of the magnetic field.

Earlier studies by Ozaki et al. (1986, 1988) on larger, micron-sized hematite particles demonstrated the reversible agglomeration of the particles through the application of a weak magnetic field (≈ 100Oe). The aggregates formed by the action of the magnetic field were easily broken up with shear or by ultrasound. The authors also noted, through their calculations, the increasing importance of the electrolyte concentration as the particle size decreased, and also the importance of the particle size itself as the magnetic interaction (as calculated by Ozaki et al. (1986, 1988)) is proportional to the square of the particle

volume.

This purpose of this chapter is to study the changes in aggregation with an applied magnetic field at the larger length scale accessible using static light scattering, and also to gather information about changes in the aggregate structure, information that cannot be extracted using the dynamic light scattering technique.

5.2 Synthesis and Characterisation

5.2.1 Synthesis

Spherical hematite nanoparticles were synthesised by the forced hydrolysis of homogenous $FeCl_3$ solutions under controlled conditions (Matijevic and Scheiner, 1978; Amal et al., 1990). 2.43 g of $FeCl_3 \cdot 6H_2O$ (CAS number 10025-77-1 supplied by ACS Chemicals) was diluted in 12.5 ml of 3.75×10^{-3} M HCl and mixed with 487.5 ml of 3.75×10^{-3} M HCl preheated to 100^oC. Vigorous stirring was applied during addition to ensure a homogenous mixture. Growth of the hematite particles was achieved by incubating the mixture for 24hrs at 100^oC. The particles were then washed of excess chlorides by adding KCl to flocculate the particles and then separated by cenrifugation. The supernatant was then poured off and the particles were redispersed in water using an ultrasonic bath. This was repeated three times producing suspensions of particles at pH 3.

5.2.2 Characterisation

5.2.2.1 TEM

The particles are not perfect spheres, but rather are spheroidal in shape as can be seen in figure 5.1.
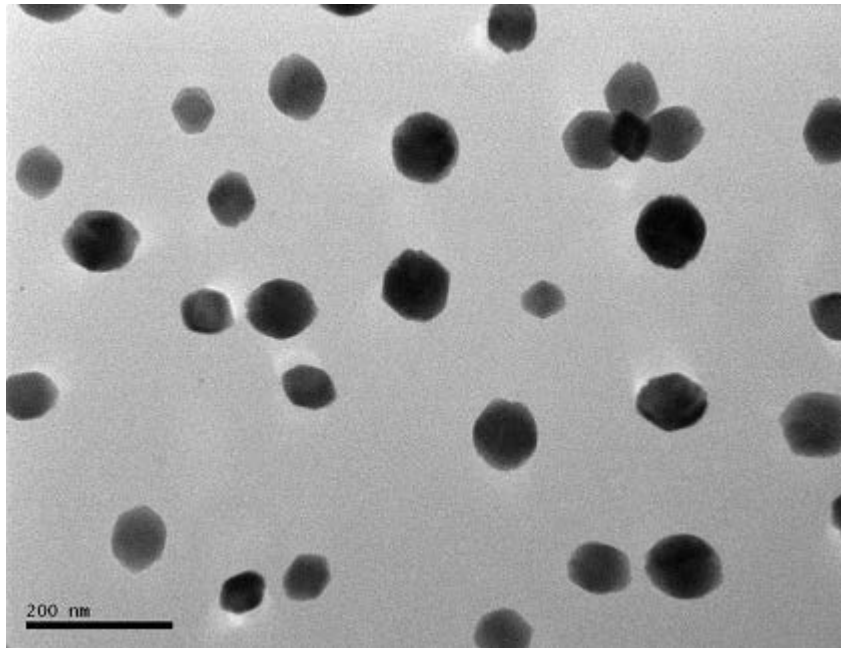
Figure 5.1: TEM image of the spherical hematite nanoparticles.

The average particle size from TEM images is 85.08 nm $\pm$ 13.63.

5.2.2.2 Dynamic Light Scattering

The DLS intensity size distribution is shown in figure 5.2.
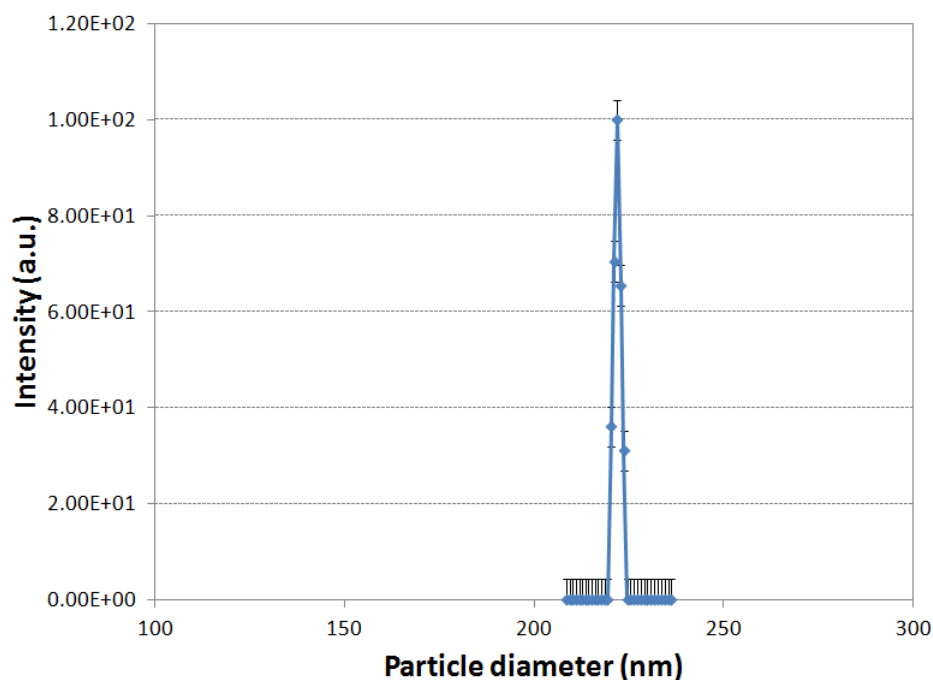
Figure 5.2: DLS intensity size distribution for the spherical hematite nanoparticles. (Combined results from 3 sets of measurements).

The DLS measurement gave an 'effective' diameter of 107.8 ± 36.7 for the particles, though the size distribution (figure 5.2) shows a peak at around 200nm. However, the method is very sensitive to larger particles which scatter light with more intensity than smaller particles, and thus can overemphasise the presence of small amounts of aggregates. Also, the particles are dispersed in distilled water which leads to a greater degree of aggregation as the pH of the suspension is close to the isoelectric point (IEP). The 'effective' diameter is in better agreement with the TEM images of the particles and thus is a more credible value than that shown by the size distribution.

5.2.2.3 Zeta Potential

The zeta potential titration measurements are shown in figure 5.3.
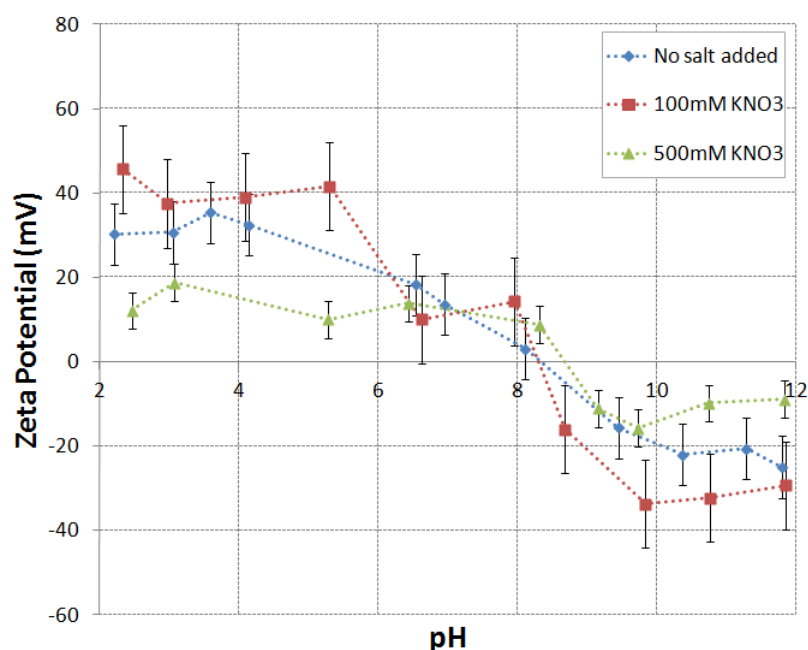
Figure 5.3: The zeta potential of the particles at various pH and salt concentrations. The salt used was potassium nitrate (KNO_3).(Combined results from 3 sets of measurements).

As can be seen, increasing the concentration of electrolyte reduces the variation of zeta potential with pH due to the suppression of the electrical double layer. The isoelectric point (IEP), is calculated by the instrument as the crossing point when the zeta potential changes signs. This is calculated as pH 8.33. This agrees with other IEP values found in the literature which vary from 7.2 to 9.5 (He et al., 2007) and are dependent on the method used for synthesising the particles and the experimental procedure used to determine the IEP (Kosmulski, 2002, 2004, 2006).

5.2.2.4 Magnetic Behaviour

The magnetic behaviour of the particles is shown in figure 5.4.
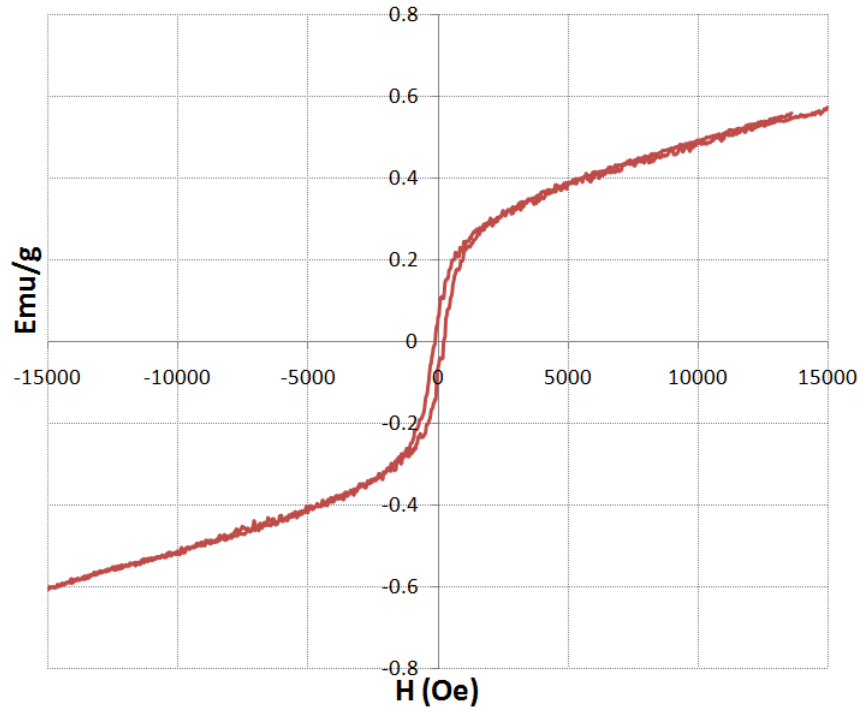
Figure 5.4: Plot of the magnetic behaviour of the particles.

The hysteresis phenomenon (see section 2.3.2.3) can easily be seen, as has been observed by other investigators of hematite nanoparticles (Shi et al., 2007; Cao et al., 2006; Jing and Wu, 2005). The particles have a remanent magnetisation of 0.06158 emu/g and a coercivity of 220 Oe, which are similar to other reported values for hematite nanoparticles.

5.2.2.5 Concentration of Particles

The concentration was determined using ICP as described in chapter 4. The concentration of Fe was determined to be 69.15 mg/l. Taking the molar mass of iron to be 55.84 g/mol and that of oxygen to be 15.99 g/mol that gives a concentration of Fe_2O_3 of 98.87mg/l

124

5.3 Experimental

5.3.1 Experimental Setup

The aggregation process was monitored by small-angle static light scattering using a Malvern Instruments Mastersizer S with the batch processing sample holder. A magnetic field was applied to the particles by placing magnets directly into the sample cell, creating a 'magnetic cell'. This arrangement is shown schematically in figure 5.5. Rare earth magnets ($Ne_2Fe_{14}B$) were used and had a remanence of around 1 Tesla (as provided by the manufacturer, AMF Magnetics).
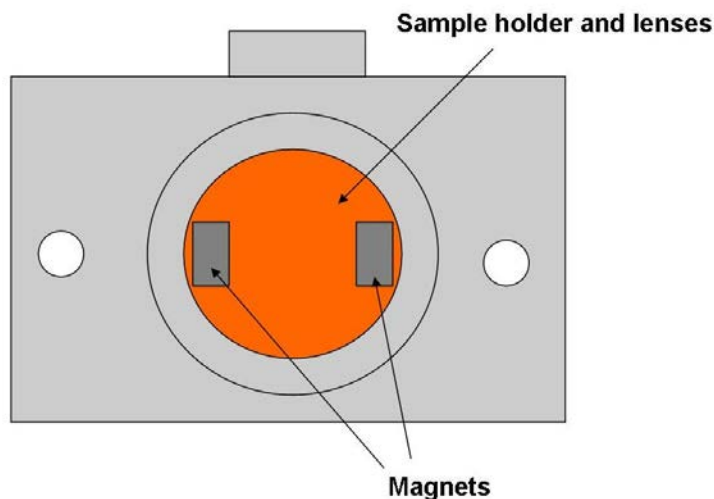
Figure 5.5: Schematic of the 'magnetic cell'.

5.3.2 Experimental Method

The stock suspension was sonicated and then 0.5ml was dispersed into 50ml of 3.75mM HCl, distilled water or 3.75mM NaOH to give suspensions at pH 2.4, 7.0 and 10.8 respectively. The effect of added electrolyte was investigated in the same way by dispersion in 100mM potassium nitrate KNO_3. The aggregation was monitored over 13 hours so

as to ensure sufficient time for the slow growth of aggregates and the appearance of any differences due to the presence of the magnetic field. The experiments were repeated at least 3 times to ensure reproducibility.

5.4 Results

5.4.1 The effect of pH

The stability of colloidal suspensions can be altered by changing the suspension pH. The suspension pH affects the zeta potential of the particles and thus alters the electrostatic repulsion between the particles. No significant growth of the particles at the different pH was measured. While there was some growth at pH 7, which was close to the particles isoelectirc point, resulting in the formation of small aggregates, there was no development of structures that could be considered fractal aggregates.

The application of the magnetic field caused no increase in the aggregation of the particles, and in fact the scattered intensity decreased throughout the experiment. The evolution of the scattered intensity in the Guinier regime is shown in figure 5.6.
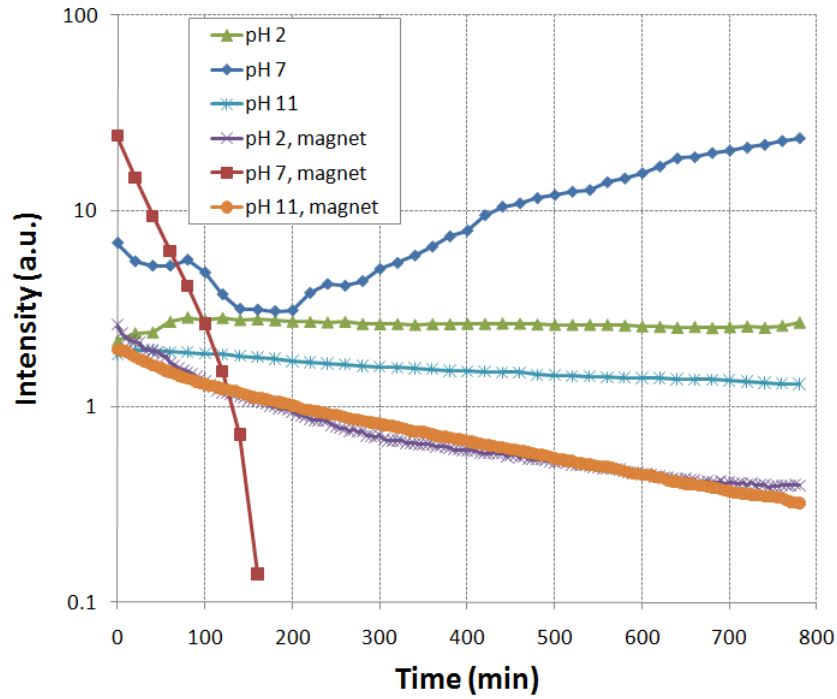
Figure 5.6: Evolution of the scattered intensity in the Guinier regime for the spherical particles.

This decrease in intensity is associated with a phase separation, as the particles are removed from suspension by the magnetic field. This was confirmed visually at the end of the experiment, when the separated particles were seen to have formed a film at the sides of the sample cell where the magnets were. The decrease in intensity with the magnetic field was fastest at pH 7 until the point where a useful measurement could not be performed. This is most likely due to the formation of aggregates which are then separated more easily by the magnetic field. The separation also occurred in what would normally be considered stable suspensions at pH 2 and 11, at a much slower rate. At these pH the suspension is considered monodisperse and thus the separation of the particles occurs at a much slower rate.

5.4.2 The effect of electrolyte

The addition of electrolyte suppresses the electric double layer around the particles and so reduces the electrostatic repulsion. This destabilisation encourages the growth of large, fractal aggregates (Amal et al., 1990) and should be more susceptible to the influence of the magnetic field.

The addition of the electrolyte to the suspension causes the growth of large aggregates, particularly as compared to the aggregation without the addition of electrolyte. This can be seen in the evolution of the size distributions over the length of the experiment shown in figure 5.7. The aggregation of the particles can be observed through growth of the peak at around 35um and the diminishing of the peak at around 1um as the primary particles and small clusters form larger aggregates.
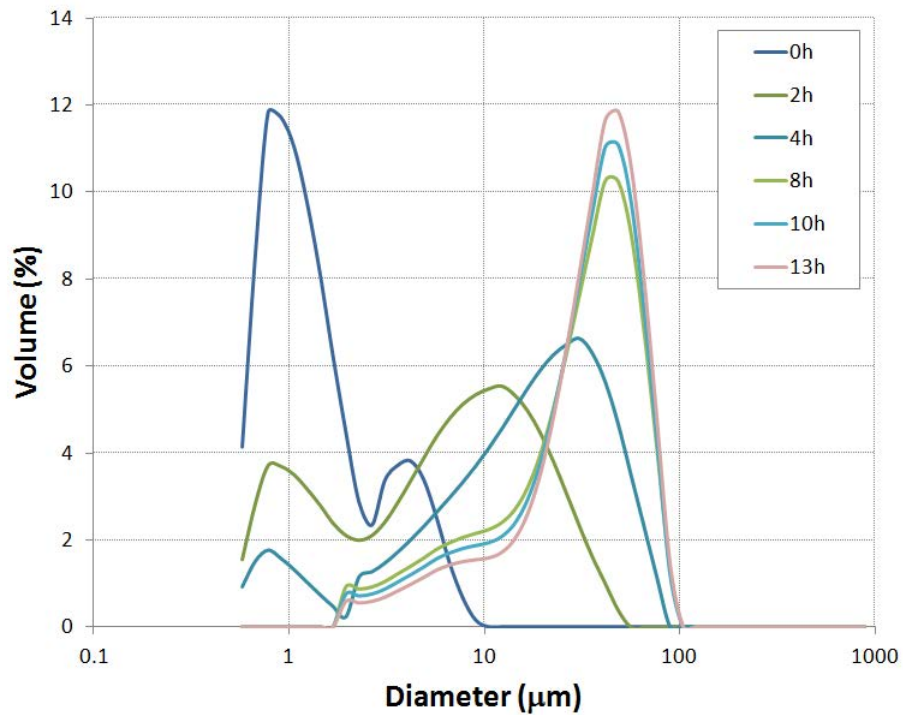
Figure 5.7: Size distributions of spherical hematite particles in 100mM KNO_3 **without** a magnetic field over 13 hours.

The evolution of the size distributions in the presence of a magnetic field is shown in figure 5.8. A similar pattern of aggregate growth is seen initially, but the particles form aggregates of around 5μm, significantly smaller size than without the magnetic field.
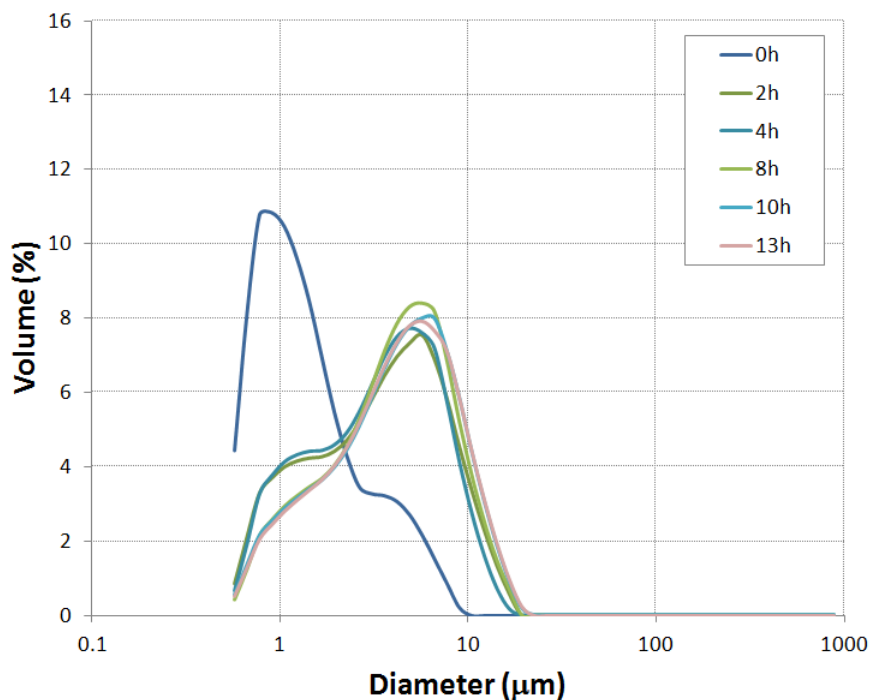
Figure 5.8: Size distributions of spherical hematite particles in 100mM KNO_3 over 13 hours **<u>with</u>** a magnetic field.

This difference in the sizes of the aggregates with and without a magnetic field, as seen by comparing figures 5.7 and 5.8, can be explained by the observation that the phase separation that was seen with the particles at different pH values with the magnetic field is once again observed here. This was again confirmed visually at the end of the experiment. The volume mean diameters (VMDs) of the particles over the length of the experiment are shown in figure 5.9 and show the similar initial growth of the aggregates. Without the magnetic field the particles continue to aggregate, while with the magnetic field the VMDs remains virtually constant.
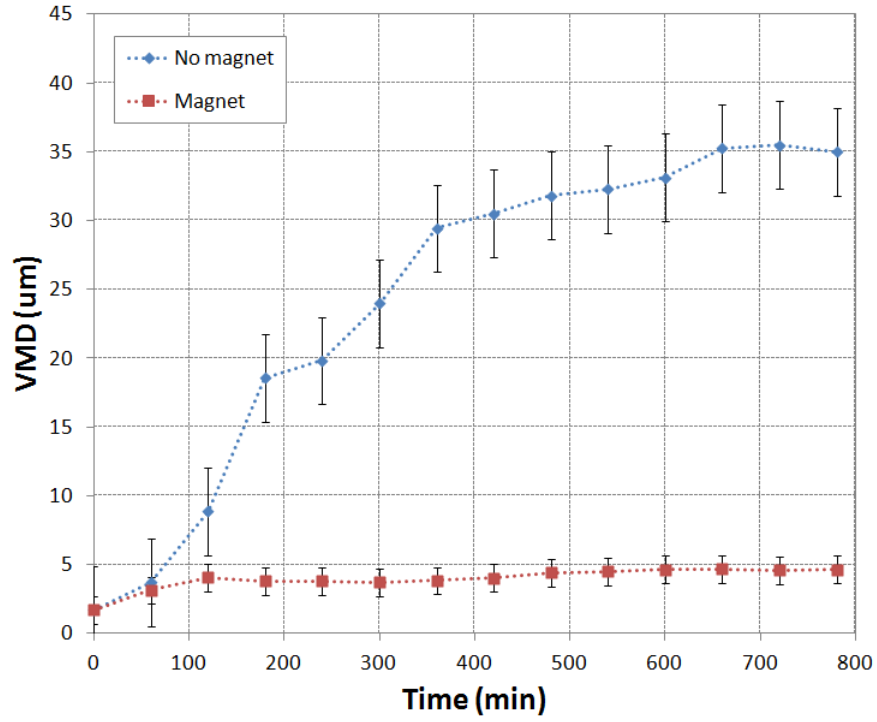
Figure 5.9: The evolution of the volume mean diameter (VMD) of spherical hematite particles in 100mM KNO$_3$ with and without the presence of a magnetic field. (Combined results from 3 sets of measurements).

The scattering exponents of the aggregates formed with a magnetic field are lower than those formed without a magnetic field. The evolution of the scattering exponents is shown in figure 5.10. The initial growth stage is similar with and without a magnetic field, but without a magnetic field the aggregates form into the large, more compact structures with scattering exponents of ≈ 1.8 typically expected of the diffusion limited aggregation (DLA) process whereas with the magnetic field the aggregates remain smaller with lower scattering exponents.
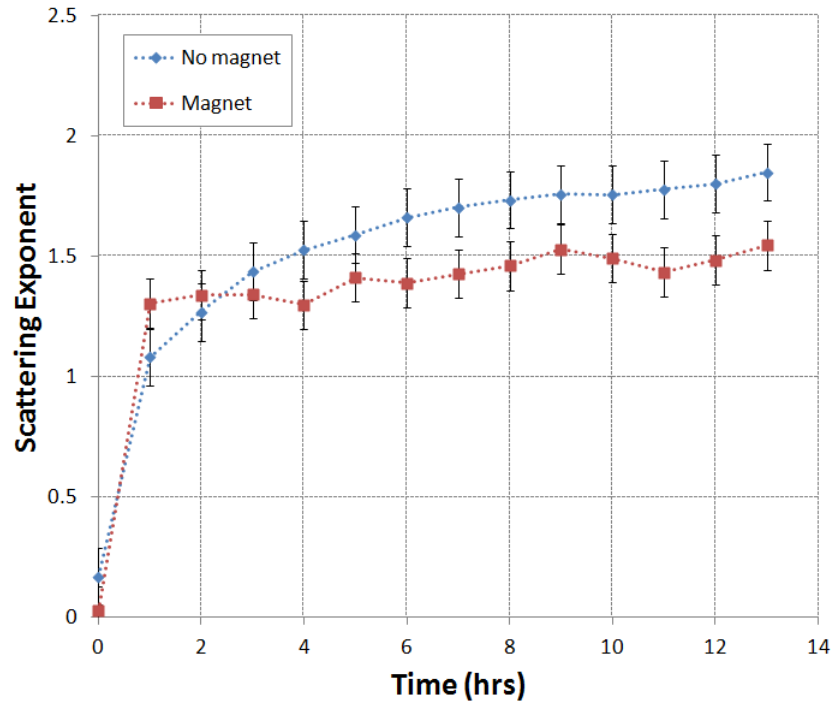
Figure 5.10: The evolution of the scattering exponent for the spherical hematite particles in 100mM KNO$_3$. (Combined results from 3 sets of measurements).

TEM images also show the particles to be similar in the earlier stages of aggregation with and without the magnetic field, as can be seen in figures 5.11 and 5.12.
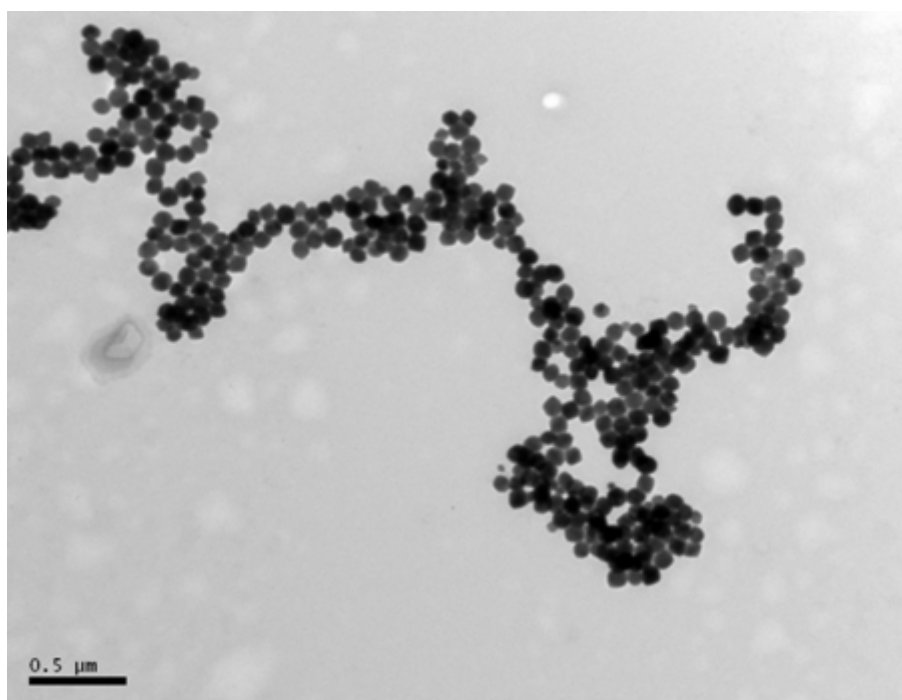
Figure 5.11: TEM image of hematite particles after 3 hours aggregated using 100mM KNO$_3$ **without** a magnetic field.
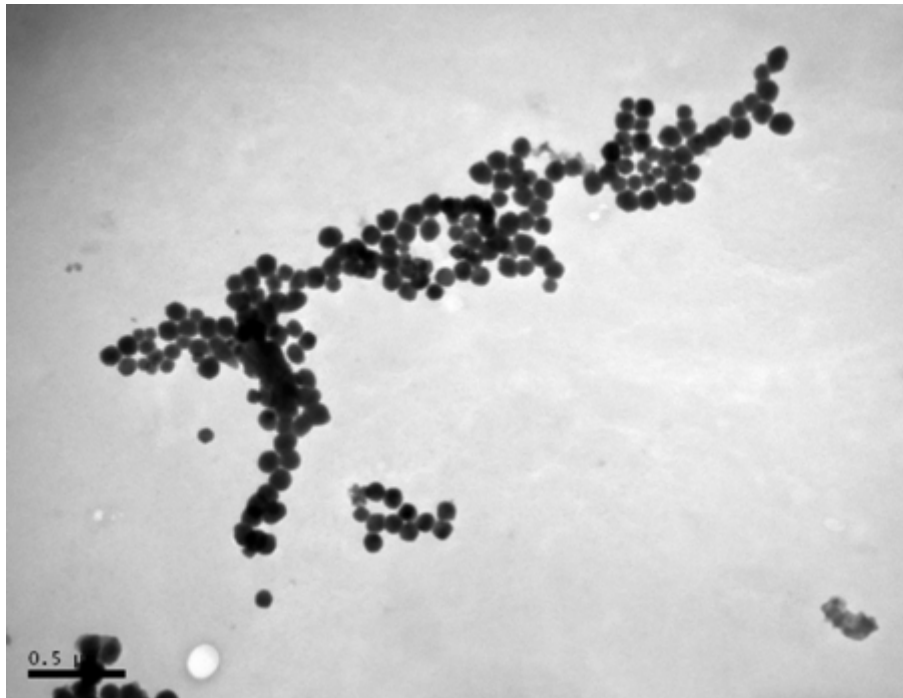
Figure 5.12: TEM image of hematite particles after 3 hours aggregated using 100mM KNO$_3$ **with** a magnetic field.

This can also be seen by comparing the scattered intensity from the Guinier scattering region, shown in figure 5.13. Initially the scattered intensity is similar but then decreases and remains constant with a magnetic field present while the intensity increases as the particles form larger aggregates without the magnetic field.
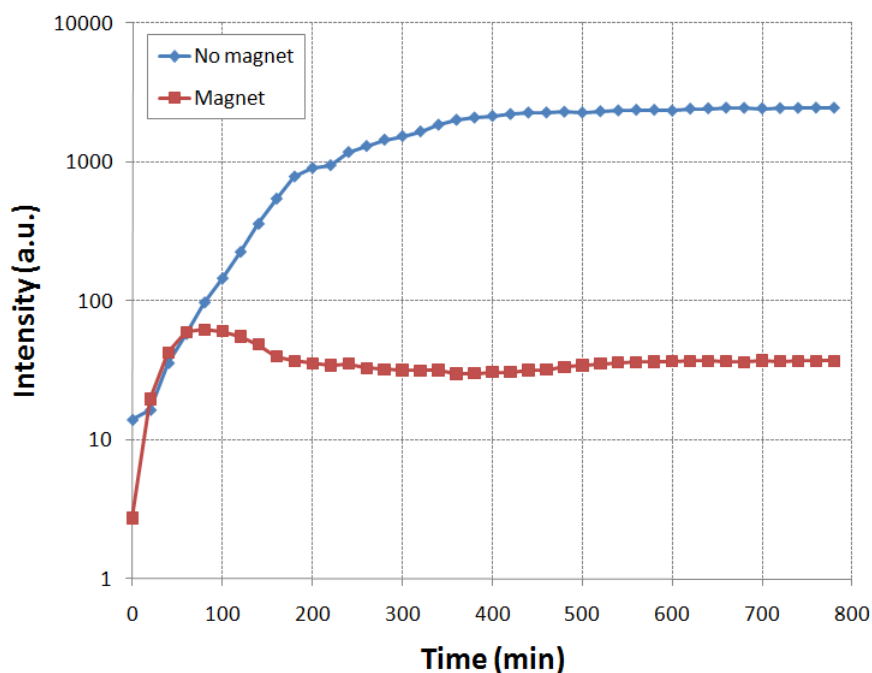
Figure 5.13: The evolution of the scattering in the Guinier region in 100mM KNO_3 with and without the presence of a magnetic field.

Thus the magnetic field is able to separate the particles from suspension, but does not seem to cause any significant difference in the aggregation behaviour.

5.5 Discussion

As in chapter 4, a method was followed for the synthesis of hematite particles but XRD measurements could not be performed. Thus, once again the particles exhibited the expected characteristics of hematite (colour, shape, magnetic properties) but the crystal structure could not be confirmed.

As explained in the introduction this work investigates the hypothesis that an externally applied magnetic field can contribute to the overall particle interaction to increase aggregation. Thus, in chapter 4 particles with an intrinsically high magnetic interaction were investigated as a basis for comparison.

134

The particularity of the magnetic field also needs consideration. The experimental setup produces a magnetic gradient with a low magnetic field strength at the point of observation. This is in keeping with the low field strengths used in previous work (Kendall et al., 2007) and also with the largest increase in aggregation found in a previous work by the author (Bradford, 2007).

The work of Ozaki et al. (1986) found that reversible chains of hematite could be formed using particles of approximately 1000nm. The pH affects the particle suspension as would be expected. The suspension is far away from the isoelectric point at pH 2 and pH 11 and thus, as discussed in the previous chapter 4 (see section 4.4) the electric double layer provides a repulsive force. The difference here is that the magnetic interaction between particles is relatively weak and thus the pH serves to effectively stabilise the suspension when it is far from the isoelectric point. However, close to the isoelectric point at pH 7 the particles aggregate steadily although much more slowly than the magnetite particles discussed in chapter 4.

With the magnetic field, the particles are separated from suspension at all pH values measured. The main difference is the rate of separation. At pH 7 where the repulsion from the electric double layer is lower, the particles are separated significantly more quickly than at pH 2 and 11 (see figure 5.6).

The separation of the particles from suspension due to the applied magnetic field demonstrates that the magnetic field is acting on the particles. A decreasing intensity in a static magnetic field was mentioned in an earlier work by Tombacz et al. (1991), although it was not mentioned if the particles were separated from suspension as was observed here. The results imply that there is no change in the aggregation of the particles as a result of applying the magnetic field. It is clear that the particles are affected by the magnetic field as they are physically removed from suspension, even in otherwise stable conditions (at pH far from the IEP without added electrolyte).

This could imply that the magnetic contribution to the overall interaction energy is too small here to cause any changes in the aggregation of the particles beyond that observed on smaller length scales by previous investigators (Tombacz et al., 1991; Tsouris and Scott, 1995; Kendall and Kosseva, 2006), who predominantly used dynamic light scattering. Or, it could mean that an applied magnetic field does not affect the interaction energy of weakly magnetic particles in the way that has previously been assumed. The magnetic field does act on the particles, as their phase separation demonstrates, and the chemical conditions have a clear influence on the kinetics of this separation.

The differences in the rate of the phase separation at different pH can be explained by considering the particle size when the magnetic field is present. The stable, monodisperse suspensions at pH 2 and 11 undergo a phase separation that takes a much greater amount of time. The Brownian diffusion is much more difficult to overcome for such small particles, although the phase separation is achieved. At pH 7 there is a noticeable degree of aggregation although there is no growth of the large aggregates seen when electrolyte is added. The particles are separated much more quickly in this condition, and this can be explained through the larger size of the aggregates, composed of several particles, as compared to the primary particles alone.

This preferential size separation can also help to explain the aggregation behaviour with addition of electrolyte. The addition of the electrolyte destabilises the suspension so that aggregation occurs more quickly and encourages the growth of fractal aggregates. The suspensions initially aggregate in the same manner as a result of the suppression of the electric double layers. However, when the magnetic field is present these large aggregates become separated whilst in the suspension without the magnetic field the aggregates continue to grow, as expected from previous work (Amal et al., 1990). After this initial growth stage it could be argued that the system achieves a sort of dynamic equilibrium between aggregate growth from primary particles or smaller aggregates and

136

the subsequent separation of the larger aggregates. The scattering data shows a decay of data at low q values with time, corresponding to the separation of the larger structures which can be seen initially. The size distributions also support this interpretation, showing a fairly consistent size distribution of larger aggregates but with a decreasing supply of smaller aggregates. The smaller aggregates and any remaining primary particles are separated from suspension more slowly, as seen in the suspensions at different pH, and thus aggregate due to the chemical environment, which destabilises the suspension.

The magnetic field also appears to be sufficient to overcome the random Brownian motion of the particles and move the particle toward the magnetic field, but the particle size, or rather the aggregate size, appears to have a significant influence on this behaviour. Future investigators using in situ magnetic fields with dynamic light scattering instruments, or other diffusion based instruments, may wish to consider this when interpreting results as the diffusion of weakly magnetic particles seems no longer to be strictly Brownian in the presence of a magnetic gradient, and thus could create errors for such measurements.

CHAPTER 6

AGGREGATION OF ELLIPSOIDAL

HEMATITE NANOPARTICLES IN A

MAGNETIC FIELD

6.1 Previous work

The aggregation behaviour of particles is affected by the properties of the aggregating particles. The size, shape and magnetic properties of particles can all contribute to make the aggregation behaviour different.

The size affects both the movement of the particles and the aggregation process. It is a characteristic of Brownian motion that the rapidity of the motions of the particles increase with decreasing particle size (Mazo, 2002), and it has been noted by previous authors that the particle size affects the aggregation. Kallay and Žalac (2002) showed that extremely small particles cannot be stabilized by an electrostatic repulsion barrier. The authors also pointed out that at the same mass concentration, nanoparticles aggregate more rapidly than ordinary colloidal particles due to their higher number concentration. He et al. (2007) found that at the same ionic strength and pH conditions, for hematite

nanoparticles, different particle sizes show a different tendency to aggregate.

The particle shape also affects the particles' Brownian motion, and thus their movement in suspension. In particular the rotational movement of rod-like or ellipsoidal particles will differ significantly from that of the spherical particles upon which most theory is based, including the classical theories of Smoluchowski (1906, 1916a,b), Einstein (1905) who gave some consideration to the rotational diffusion of particles, and Debye (1929) who produced the first theory of rotational diffusion in an external field based on the Smoluchoswki equation. The shape can also affect the surface chemistry of the particles and Ho and Ottewill (1998) have suggested that the distribution of surface charge on ellipsoidal particles is not uniform, which could have significant implications for particle aggregation.

The particle size also affects the magnetic properties as the magnetic moment of the particles is proportional to its size (Garcia-Martinez et al., 2004), and thus larger particles possess a higher magnetisation than do smaller ones. The particle shape also affects the magnetic properties, as has been postulated by other investigators. Usov et al. (2002) also predicted differences in the magnetisation of spheroidal and ellipsoidal particles due to differences in the orientations of the magnetic axes.

The particle shape also affects the fractal dimensions of the aggregates. The fractal aggregate models developed during the 1980s established the two aggregation regimes of DLA and RLA, but were based on the assumption of spherical particles. Typical fractal dimensions generated were ≈ 1.8 for DLA and ≈ 2.1 for RLA (Meakin, 1999). Mohraz et al. (2004) showed that the aspect ratio of rod-like particles determined the fractal dimension in the DLA regime due to the anisotropic interaction of the particles. Philipse and Wierenga (1998) discussed the density and structure formation in clusters and gels of colloidal rods and fibres and noted the lower fractal dimensions produced, for example, a fractal dimension of 1.95 for rod-like iron hydroxide particles in the RLA

regime (as measured by Brunner et al. (1995)). Mohraz and Solomon (2006) found that internal dynamics of fractal cluster gels of colloidal boehmite rods differed to that of polystyrene spheres, specifically in that the critical volume fractions of gelation were dependent on the aspect ratio and significantly lower for rods than for spheres, and also that the fractal cluster size of rod gels was not the determinant of the relaxation time of density fluctuations as is found in spherical particle gels.

A previous study on the magnetic agglomeration of hematite particles of different shape was performed by Ozaki et al. (1988). They observed the aggregation of cubic and spindle-like hematite particles in a metallurgical microscope, although these particles were much larger than what are now considered nanoparticles. It was found that the ordered agglomeration in dispersions of uniform colloidal hematite occurs under the influence of exceedingly weak magnetic fields without the addition of any electrolyte for the cubic particles. The addition of a minimum amount of electrolyte was necessary to observe similar effects in smaller cubic particles. It was also observed that the spindle-type particles aligned along the major axis perpendicular to the direction of the external magnetic field.

Considering the effects that the particle shape has on both the magnetic properties of the particles and the aggregation process itself, the purpose of this chapter is thus to investigate the aggregation of ellipsoidal hematite particles and how that aggregation is affected by the application of magnetic field (as used in chapter 5) and the differences apparent as compared to the spheroidal particles.

6.2 Synthesis and Characterisation

6.2.1 Synthesis

Needle shaped hematite particles were prepared by aging $2.00 \times 10^{-2} \, \mathrm{mol \, dm^{-3}}$ $FeCl_3$ (CAS number 10025-77-1 supplied by ACS Chemicals) containing $4.50 \times 10^{-4} \, \mathrm{mol \, dm^{-3}}$ KH_2PO_4

(CAS number 7778-77-0, supplied by ACS Chemicals) at 100°C (standard conditions) for 5 days (Ozaki et al., 1984; Sugimoto and Muramatsu, 1996). The particles were then washed by separating the particles by centrifugation, pouring off the supernatant and then redispersing the particles in distilled water. This was repeated three times to produce a suspension at pH 3.

6.2.2 Characterisation

6.2.2.1 TEM

The TEM image in figure 6.1 shows the particles to be ellipsoidal.
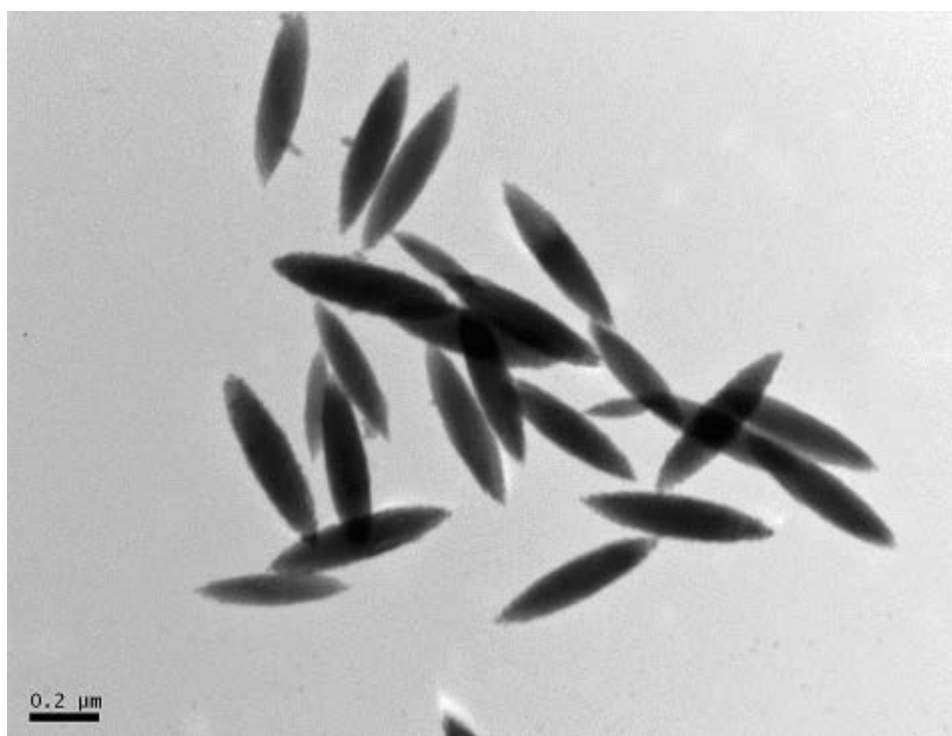
Figure 6.1: TEM image of the needle shaped hematite nanoparticles.

6.2.2.2 Dynamic Light Scattering

The DLS measurement gave an effective diameter of 85.1nm $\pm$0.8 for the needle shaped particles. The size distribution (figure 6.2) shows only a single peak, indicating the system

is fairly monodisperse. However, the particles can clearly be seen to be larger in the TEM image (figure 6.1).
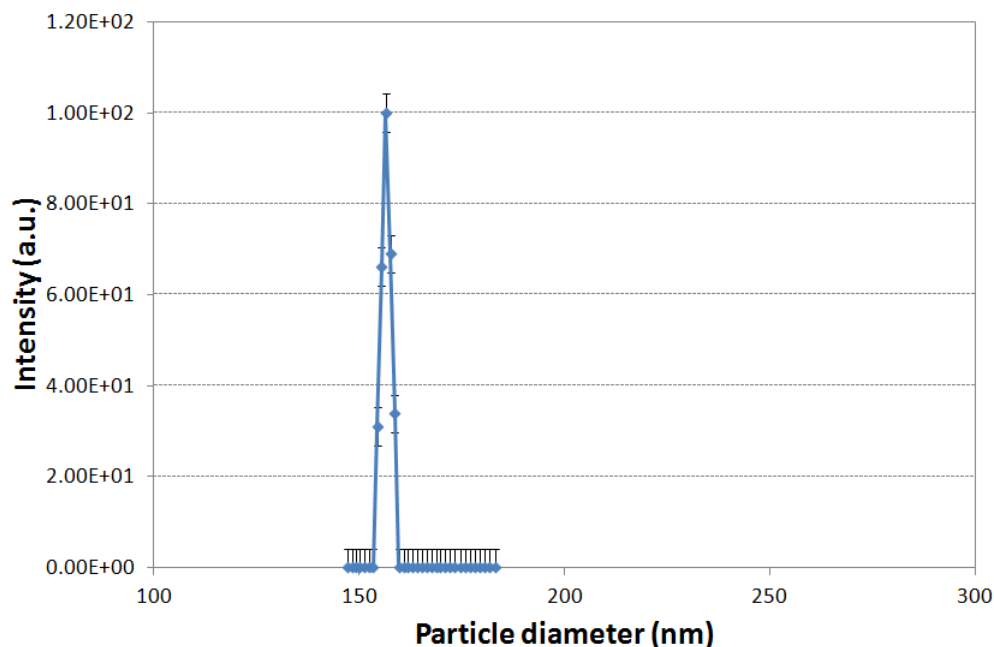
Figure 6.2: DLS size distribution for the needle shaped hematite nanoparticles. (Combined results from 3 sets of measurements).

Most dynamic light scattering instruments work on the assumption of spherical particles, and calculate a diameter using the Stokes-Einstein equation from the obtained diffusion coefficient, which is the translational diffusion coefficient (Tracy and Pecora, 1992). Other relations by Broersma (1960a,b) and Tirado and de la Torre (1979, 1980) exist for the translational and rotational diffusion coefficients of rigid rod-like particles, but measurement of the rotational diffusion coefficient is more difficult though it can be done via techniques such as depolarised DLS, electric dichroism decay and transient electric birefringence decay (TEB), and DLS-polarised photon correlation techniques. The dimensions of rodlike particles in dilute solution may be obtained by combining measurements of rotational and translational diffusion coefficients.

6.2.2.3 Zeta Potential

The zeta potential titration measurements are shown in figure 6.3.
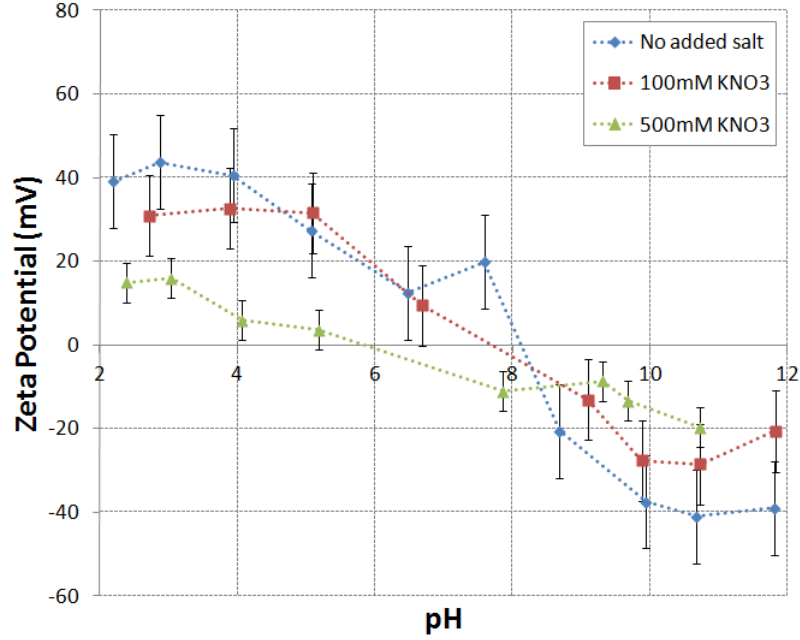
Figure 6.3: The zeta potential of the needle shaped particles at various pH and salt concentrations. The salt used was potassium nitrate (KNO_3). (Combined results from 3 sets of measurements).

6.2.2.4 Concentration of Particles

The concentration was determined using ICP as described in chapter 4. The concentration of Fe was determined to be 38.28 mg/l. Taking the molar mass of iron to be 55.84 g/mol and that of oxygen to be 15.99 g/mol that gives a concentration of Fe_2O_3 of 53.73mg/l

6.3 Experimental

6.3.1 Experimental Setup

The experimental setup was the same as that used in chapter 5.

143

6.3.2 Experimental Method

The experimental method was the same as that used in chapter 5.

6.4 Results

6.4.1 The effect of pH

The ellipsoidal hematite particles show similar aggregation behaviour to that of the spherical particles in chapter 5. Both systems are sensitive to the suspension pH which can prevent (or promote) aggregation. While there was some growth at pH 7, which was close to the particles' isoelectric point, resulting in the formation of small aggregates, there was no development of the large structures seen in chapter 4 with magnetite.

The ellipsoidal particles are also separated from suspension, as were the spherical particles. The Guinier scattering for the ellipsoidal particles at different pH and with and without a magnetic field are shown in figure 6.4. The continuous decrease in scattered intensity is due to the particles being separated from suspension, effectively decreasing the concentration over time.
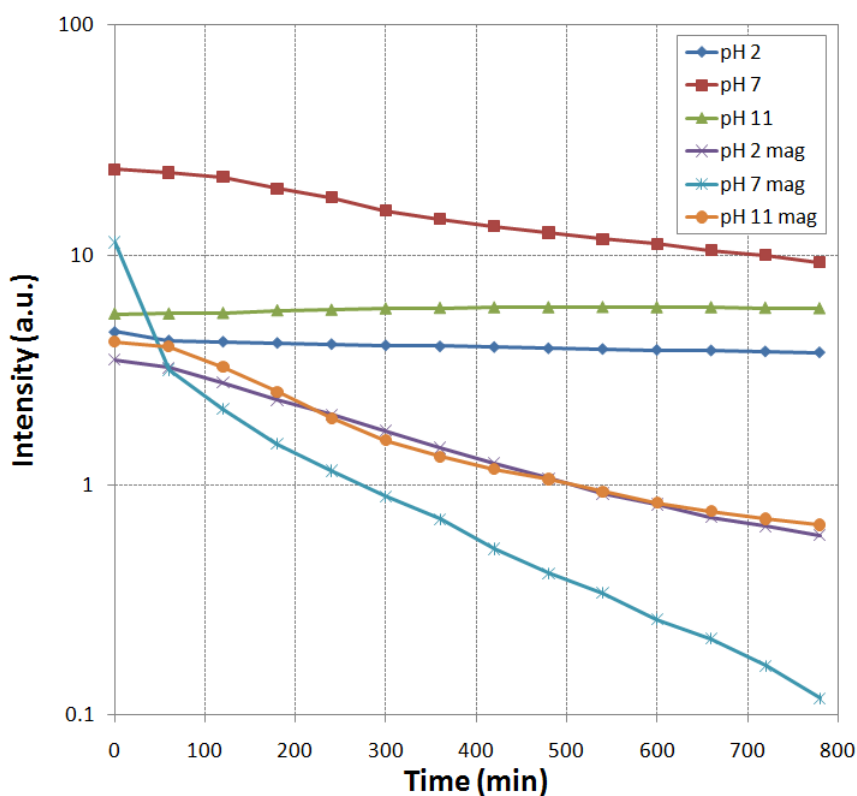
Figure 6.4: Evolution of the scattered intensity in the Guinier regime for the ellipsoidal particles.

The separation occurs more rapidly at pH 7, close to the isoelectric point, and the same was found of the spherical particles in chapter 5.

6.4.2 The effect of electrolyte

The destabilising effect of the added electrolyte causes the growth of large aggregate structures, as was seen in chapter 5. The size distributions for the ellipsoidal particles with and without a magnetic field are shown in figures 6.5 and 6.6.
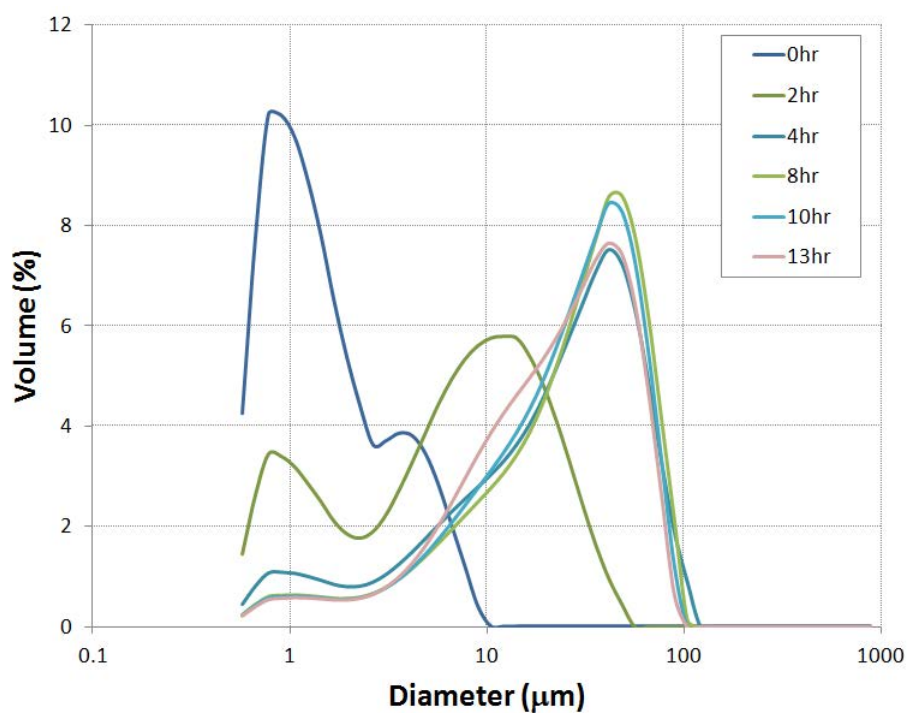
Figure 6.5: Size distributions of the ellipsoidal particles in 100mM KNO_3 over 13 hours **<u>without</u>** a magnetic field.

Similar behaviour can be seen here as was observed with the spherical hematite particles in chapter 5. The particles form much larger aggregates without the magnetic field, as can be seen from the evolution of the size distributions in figure 6.5. With the magnetic field the aggregates formed are much smaller as can be seen from the evolution of the size distributions in figure 6.6.
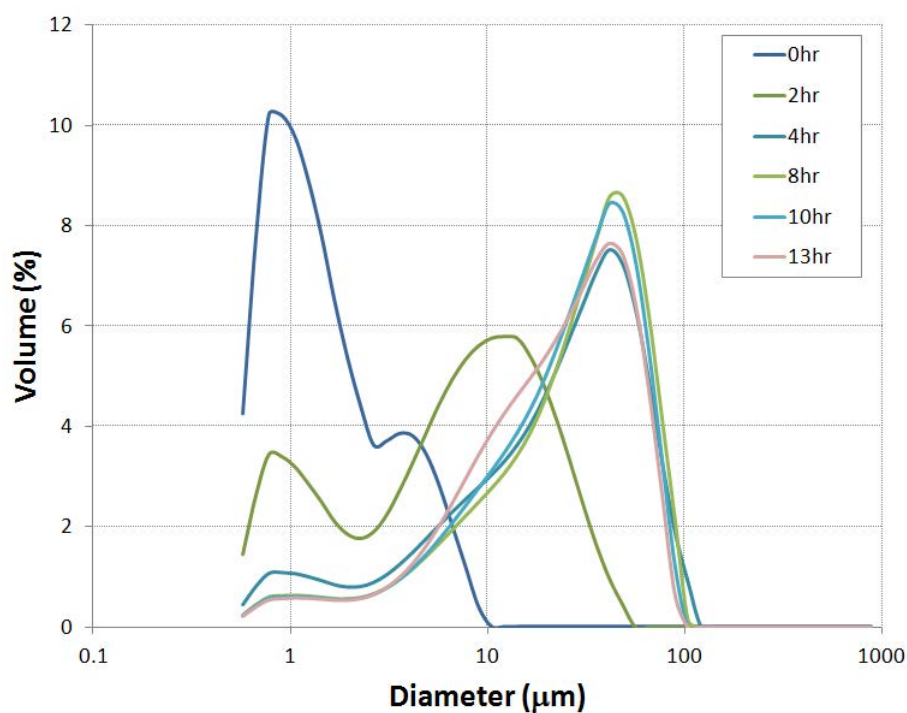
Figure 6.6: Size distributions of the ellipsoidal particles in 100mM KNO_3 over 13 hours **with** a magnetic field.

This can once again be explained by the phase separation that occurs in the presence of a magnetic field, which was confirmed visually at the end of the experiment. Although this results in size differences similar to that seen in the previous chapter, there is very little difference in structure. This can be seen in figure 6.7. The values of the scattering exponents themselves are also different from those of the spherical particles, due to the difference in the particle shape.
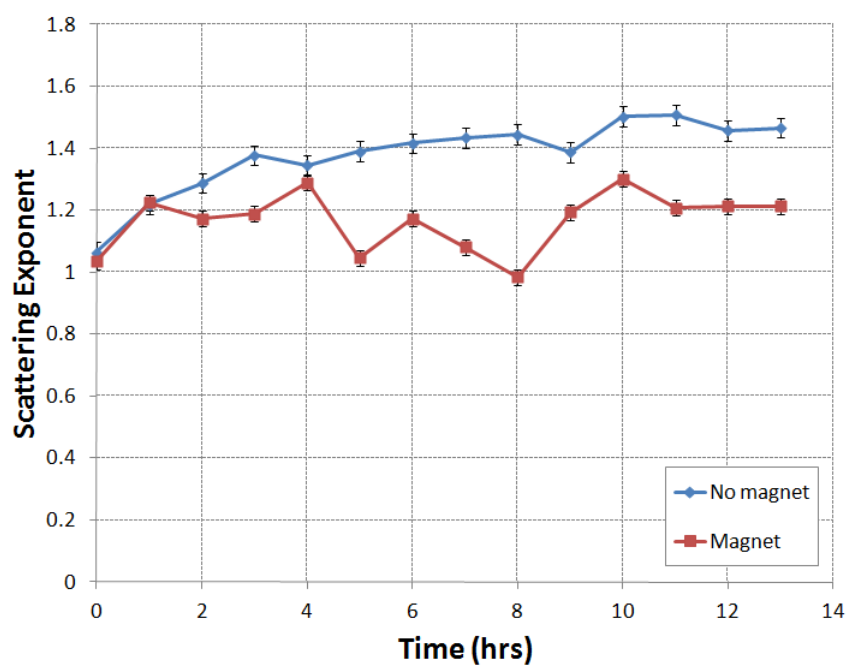
Figure 6.7: The evolution of the scattering exponent for the ellipsoidal hematite particles in 100mM KNO_3. (Combined results from 3 sets of measurements).

TEM images of the aggregates, shown in figure 6.8, also show little difference between the particles aggregated in the presence of a magnetic field and those aggregated without.

148
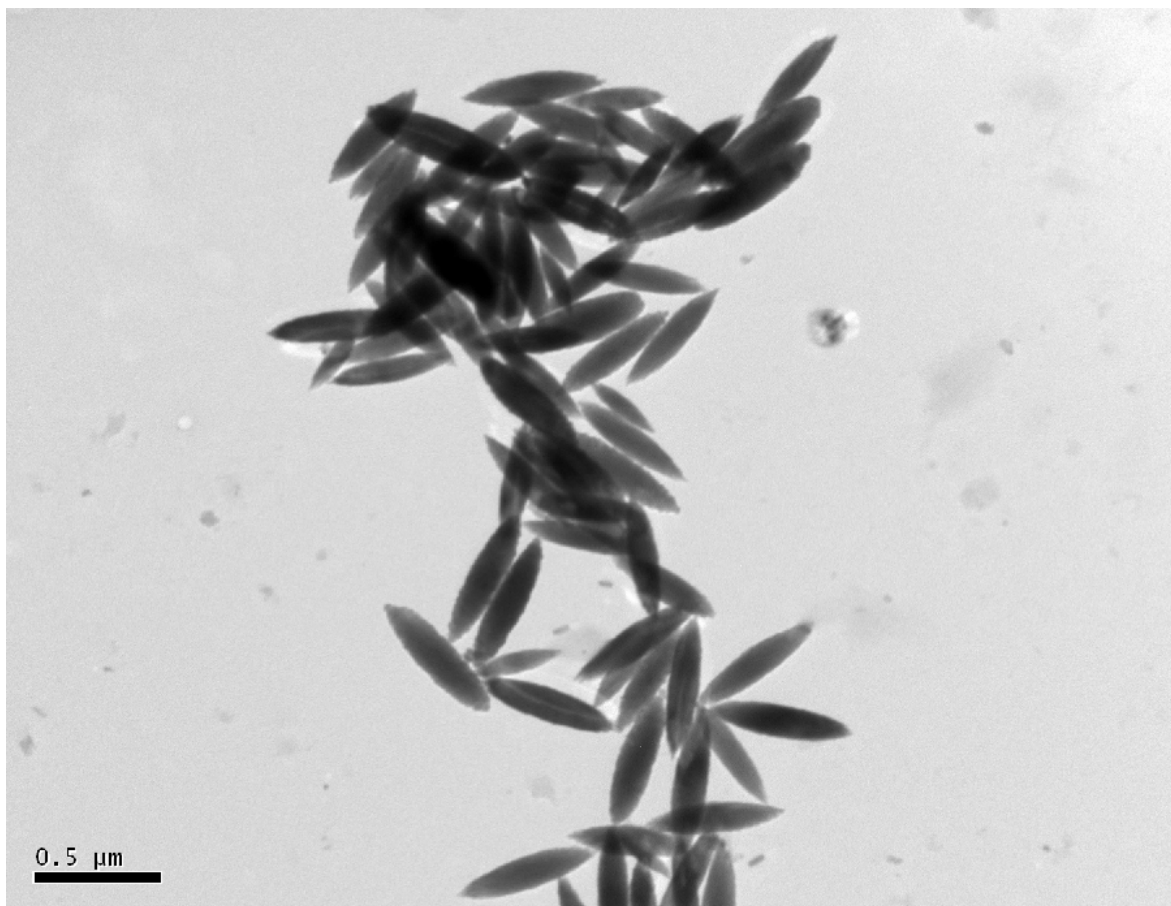
Figure 6.8: TEM images of ellipsoidal particles in 100mM KNO₃ **<u>without</u>** a magnetic field.
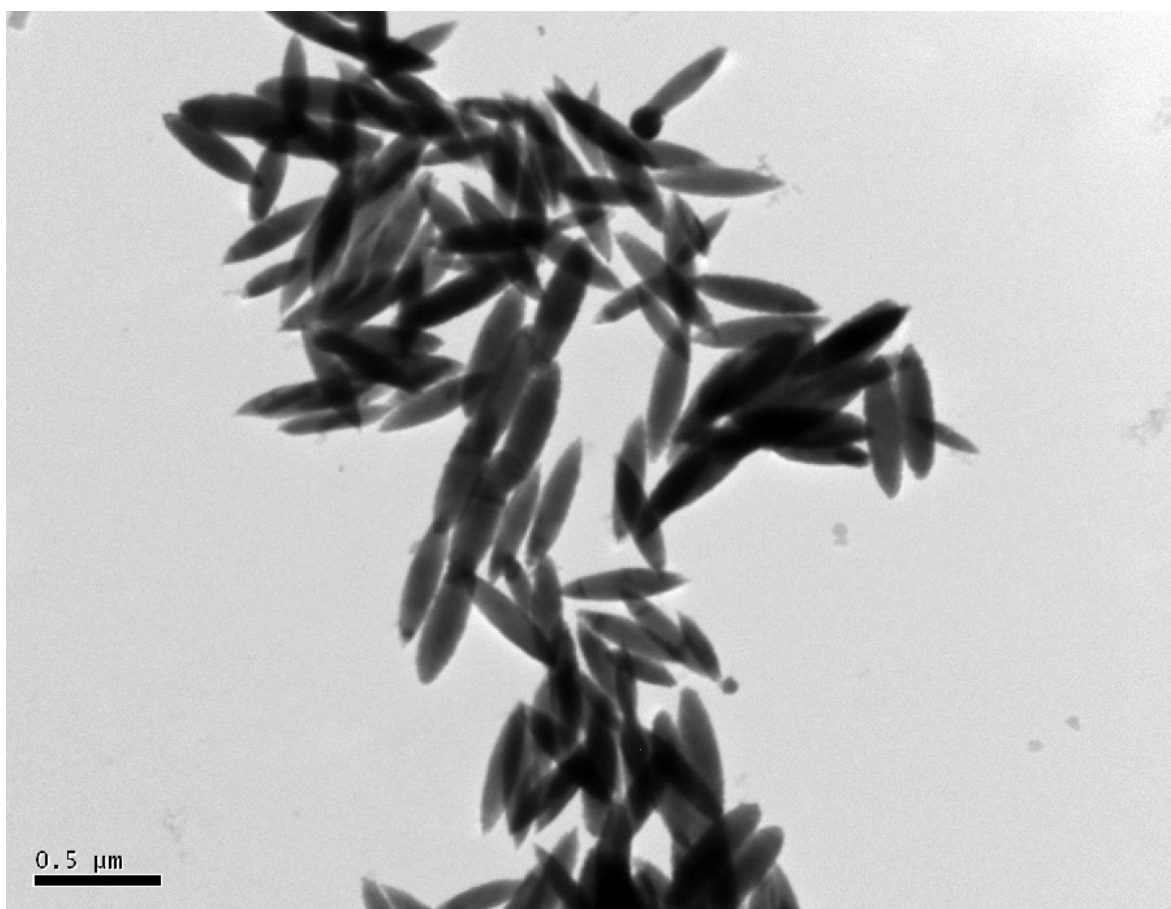
Figure 6.9: TEM images of ellipsoidal particles in 100mM KNO₃ **with** a magnetic field.

Thus the aggregation of the ellipsoidal particles in a magnetic field is similar to that of the spherical particles observed in the previous chapter.

6.5 Discussion

As in chapter 5, a method was followed for the synthesis of hematite particles but XRD measurements could not be performed. Thus, once again the particles exhibit the expected characteristics of hematite (colour and shape) but the crystal structure could not be confirmed. An important limitation here is that VSM measurements could not be performed on these particles. The magnetic behaviour is, however, more comparable to

that of the hematite particles in chapter 5 than those of the magnetite particles in chapter 4. The particles were not easily separated by a magnetic field, but as in chapter 5 the particles were separated over a longer timescale.

The particles in this chapter, as can clearly be seen in TEM images (see figure 6.1), are both a different shape and also larger than the particles in the previous chapter. The shape of the particle makes it interesting as, in theory, both the magnetic axes and the charge distribution are non-uniform, unlike in a spherical particle.

The particles had a major axis of 521.76nm $\pm$44.56 and a minor axis of 113.58nm $\pm$13.22 which gave an aspect ratio of 4.62 $\pm$0.38. These particles are comparable to those used by Ozaki et al. (1988) which had a similar aspect ratio but were several times larger, with a length of $\approx$2.5μm.

The particles' shape also means that their motion will differ from that of spheres. The ellipsoidal shape of the particles is not isotropic, unlike spheres. This gives rise to different types of diffusion, both rotational and translational.

The particles' shape also means that they can aggregate in more than one way. There are two principal ways in which the particles can aggregate - tip to tip and side to side (much like a raft). The type of aggregation also affects the density of the aggregate. Aggregates formed from particles arranged tip to tip are more linear and have a fractal dimension closer to 1 whereas when the particles aggregate side by side the aggregate formed is more closely packed and thus has a higher fractal dimension.

The aggregation of the ellipsoidal particles shows similarities to the aggregation of the spherical particles in chapter 5. The pH has a marked effect on the aggregation of the particles, a greater amount of growth occurring when the pH is nearer to the isoelectic point, and a phase separation also occurs with the applied magnetic field at all pH values measured, as seen with the spherical particles. This phase separation also takes place most effectively at pH 7, close to the isoelectric point, as was found in chapter 5.

The addition of electrolyte causes the formation of large aggregate structures, as would be expected from destabilising the suspension and it is in these conditions that differences in the aggregates can be seen. In this respect, the aggregation of the ellipsoidal particles is consistent with previous work in the literature. The structures formed exhibit lower fractal dimensions (scattering exponents in the fractal range) than that of the spherical particles which is similar to the findings of Mohraz and Solomon (2006).

However, while the aggregation of the ellipsoidal particles differs from that of the spherical particles by the formation of structures with lower fractal dimensions, the differences in aggregation with an applied magnetic field are similar. The particles form smaller aggregates in the presence of the magnetic field, in a similar manner to that observed with the spherical particles. This difference can once again be explained by the phase separation that takes place with the magnetic field. The particles aggregate in the same way as those without a magnetic field forming similar, but smaller structures (as confirmed by the scattering exponents in figure 6.7 and TEM images in figure 6.8). As was discussed with the spherical hematite particles in chapter 5, this would imply that the interactions between the particles are not altered sufficiently by the magnetic field that the aggregation of the particles changes, but the magnetic field is sufficient to overcome the Brownian motion of the particles to separate it from suspension. Again, a sort of dynamic equilibrium appears to be established whereby the particles aggregate a certain amount before being separated from suspension.

Thus, the magnetic field has the same effect on the ellipsoidal hematite particles as on the spherical hematite particles. While the aggregation of the ellipsoidal particles forms structures with lower scattering exponents with the addition of electrolyte, the effect of the magnetic field is the same. Without added electrolyte the particles are separated from suspension, most effectively when the pH is close to the isoelectric point. With added electrolyte the particles aggregate a certain amount due to the influence of the electrolyte

but are separated from suspension by the magnetic field before further aggregation can take place.

CHAPTER 7

AGGREGATION OF MAGNETITE NANOPARTICLES IN A STIRRED SYSTEM

7.1 Previous work

The orthokinetic aggregation of particles generally leads to the formation of larger, more compact aggregate structures, and indeed orthokinetic flocculation is used as a separation process in the minerals industry. The aggregates formed in orthokinetic aggregation have been shown to undergo breakage and restructuring, caused by the hydrodynamic forces from the shear, and also to show a dependence on the shear rate (Selomulya et al., 2001, 2004).

No literature could be found at the time of writing on the aggregation of bare magnetite particles in a sheared system. However, a study by Chin et al. (1998) used colloidal polystyrene and paramagnetic particles consisting of mixtures of polystyrene and magnetite to experimentally investigate flocculation kinetics in a stirred tank under turbulent shear flow. The results suggested that the flocculation rate was enhanced by increasing the agitation speed, even though the collision efficiency was decreased at a higher agitation speed. It was also found that the collision rate increased and the collision efficiency

decreased as the particle size ratio was increased.

There are also several studies on the microstructures formed in ferrofluids and their effects on rheological behaviour. Simulations of ferromagnetic colloids by Satoh et al. (1996, 1999, 2000) have shown the formation of thick chain-like clusters which are significantly influenced by an oscillatory shear flow, even if the amplitude was relatively small. Yamada and Enomoto (2006) used a molecular dynamics simulation to investigate the type of structures formed in a ferrofluid in an oscillatory shear flow. It was found that the shear rate affected how the particles aggregated, starting from chains, which were then broken into clusters at a low shear rate, to larger networks at a higher shear rate. Pop et al. (2005); Pop and Odenbach (2006) investigated the magnetoviscous effect in ferrofluids using small angle neutron scattering (SANS) and found that the microstructure produced the changes in viscosity. The viscosity increased with the strength of the applied magnetic field (magnetoviscous effect) but decreased as the shear rate increased. Brunet et al. (2005) found that a flowing suspension of superparamgnetic particles in a magnetic field formed chains, whose growth rate was proportional to the shear rate.

Small angle light scattering has been shown to be an effective method in previous investigations to monitor the aggregation process of colloidal particles, and can also yield information about changes in aggregate structure in sheared systems (Amal et al., 1990; Jung et al., 1996; Bushell and Amal, 1998; Selomulya et al., 2001).

From the literature it can be seen that shear affects the aggregation of magnetic particles, although how exactly the aggregation is altered cannot be determined based on the previous work. The purpose of this chapter is to investigate the aggregation of magnetite particles, which have a large magnetic interaction, in the presence of shear, thus increasing the collision frequency.

7.2   Synthesis and Characterisation

The same magnetite particles were used as in chapter 4. See chapter 4 for synthesis method and characterisation.

7.3   Experimental

7.3.1   Experimental Setup

A stirred beaker was used to generate shear and thus increase the frequency of collisions between the particles. The setup was very simple consisting of just a beaker and a stirrer, shown schematically in figure 7.1. The purpose of this setup was not to generate a uniform shear, but merely to use a very simple setup to observe the difference in aggregation when the system was not quiescent.

The aggregation process was again monitored by small angle static light scattering using a Malvern Instruments Mastersizer S, this time using the flow cell sample holder. The suspensions were introduced into the flow cell by using a syringe, attached by a tube to the top side of the flow cell, to draw the liquid from the beaker via another tube attached to the bottom of the flow cell with the other end placed in the beaker.
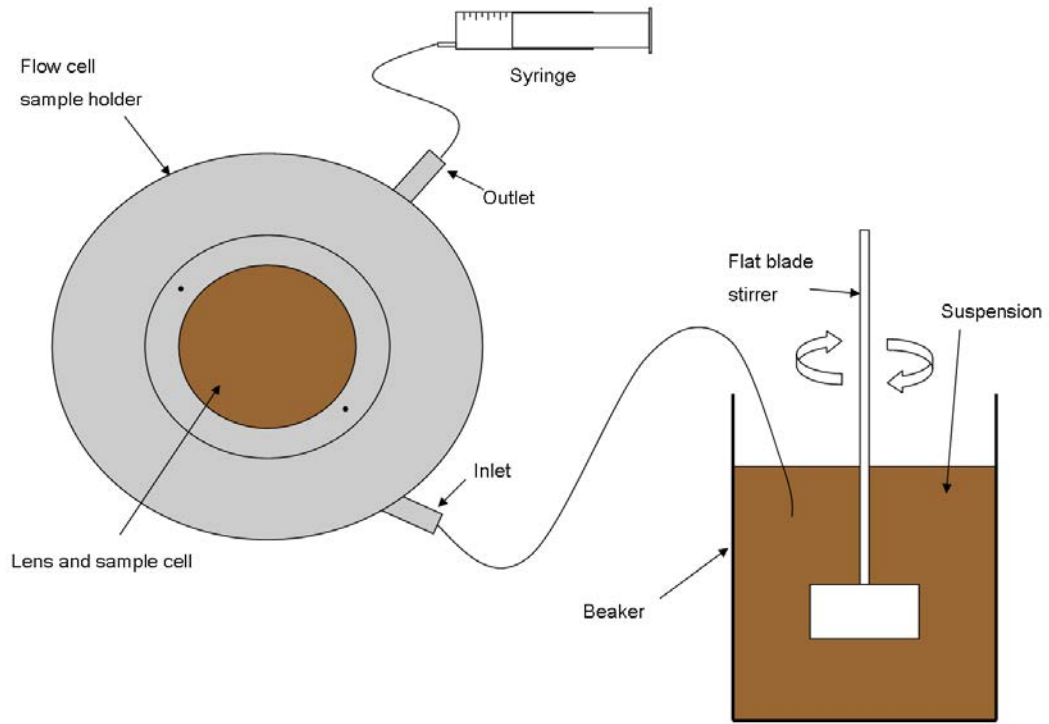
Figure 7.1: Schematic of stirred beaker and flow cell sample holder.

7.3.2 Experimental Method

0.3 ml of the stock suspension was added to 150ml of either 3.75mM HCl, distilled water or 3.75mM NaOH to give suspensions at pH 2.4, 7.0 and 11.5 respectively. The effect of added electrolyte was investigated in the same way by dispersion in 150ml of 100mM potassium nitrate KNO_3. The stirrer speeds used were 0, 60, 100 and 200rpm. The suspensions were sampled and measured every 5 minutes during half an hour by drawing the suspensions into the flow cell using a syringe (as described above).

The stirrer blade measured 4.5cm x 2.5cm (with a thickness of 0.3cm). The Reynolds number Re can be determined using the following formula (Paul et al., 2004)

$$Re = \frac{\rho N D^2}{\mu} \tag{1}$$

157

where ρ is the density of the liquid (kg m^{-3}), N is the impeller rotational speed (s^{-1}), D is the diameter of the impeller (m) and μ is the viscosity of the liquid (Pa s). The flow regime was calculated to be in the transition region ($10^2 \leqslant Re \leqslant 10^4$) for all the stirrer speeds used. This gives a Reynolds number of 2.025×10^3 at 60rpm, 3.375×10^3 at 100rpm and 6.75×10^3 at 200rpm.

The density and viscosity were taken to be that of water ($\rho = 1000$ kg m^{-3}; $\mu = 0.001$ Pa s).

7.4 Results

7.4.1 The effect of pH

The pH affected the aggregation of the magnetite suspensions in a stirred system as it did in quiescent conditions. The pH did not prevent the aggregation of the magnetite particles but did reduce the amount of aggregation the further as the pH moves away from the isoelectric point. The size distributions of the particles at different pH and a stirrer speed of 200rpm are shown in figure 7.2. The size distributions, however, do not show the difference in the degree of aggregation as well as the scattering data shown in figure 7.3.
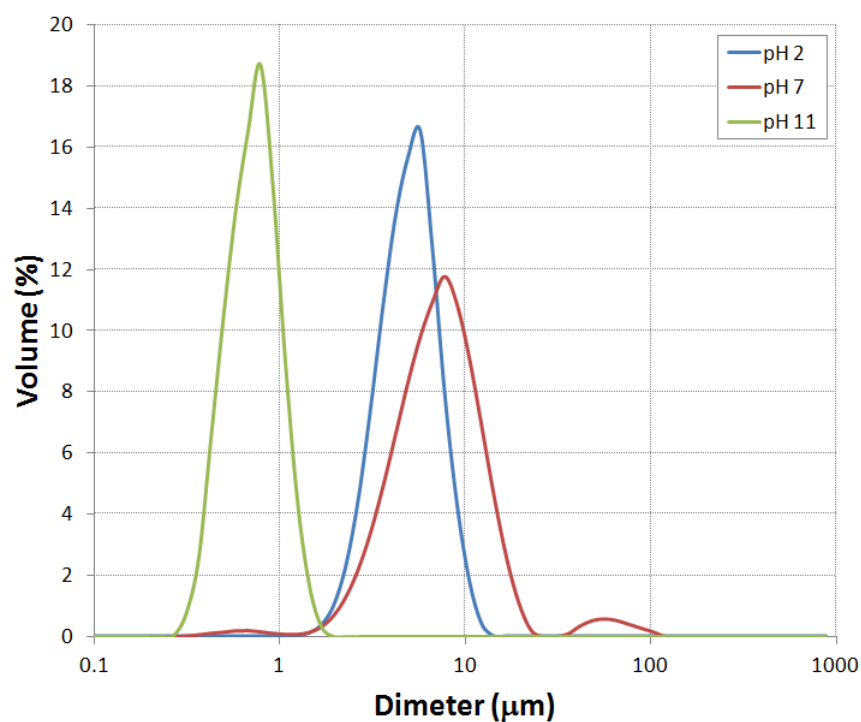
Figure 7.2: Size distributions for the magnetite particles at different pH and a stirrer speed of 200rpm after 30 minutes.

The scattering data better shows the difference in the amount of aggregation. At pH 2 and 11, far from the isoelectric point, there is still a significant amount of aggregation resulting in the formation of micron-sized aggregates.
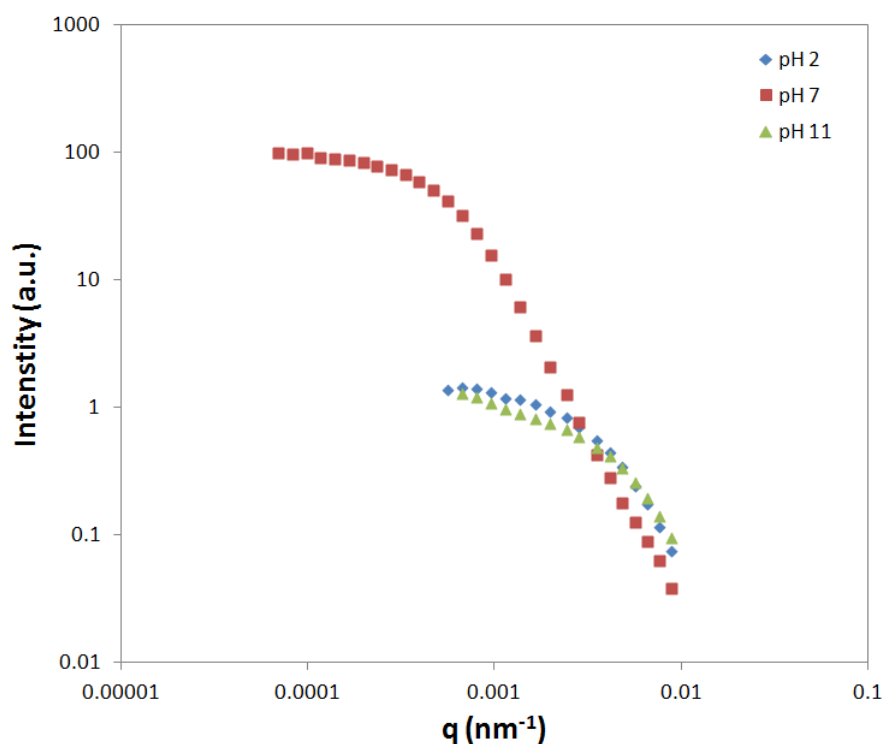
Figure 7.3: Scattering data for the magnetite particles at different pH at a stirrer speed of 200rpm.

At pH 7, which is close to the isoelectric point, there is a greater amount of aggregation, resulting in the formation of much larger aggregates. The size and structure of these aggregates was then observed to be dependent on the stirrer speed. The size distributions of the particles at pH 7 and at different stirrer speeds are shown in figure 7.4.
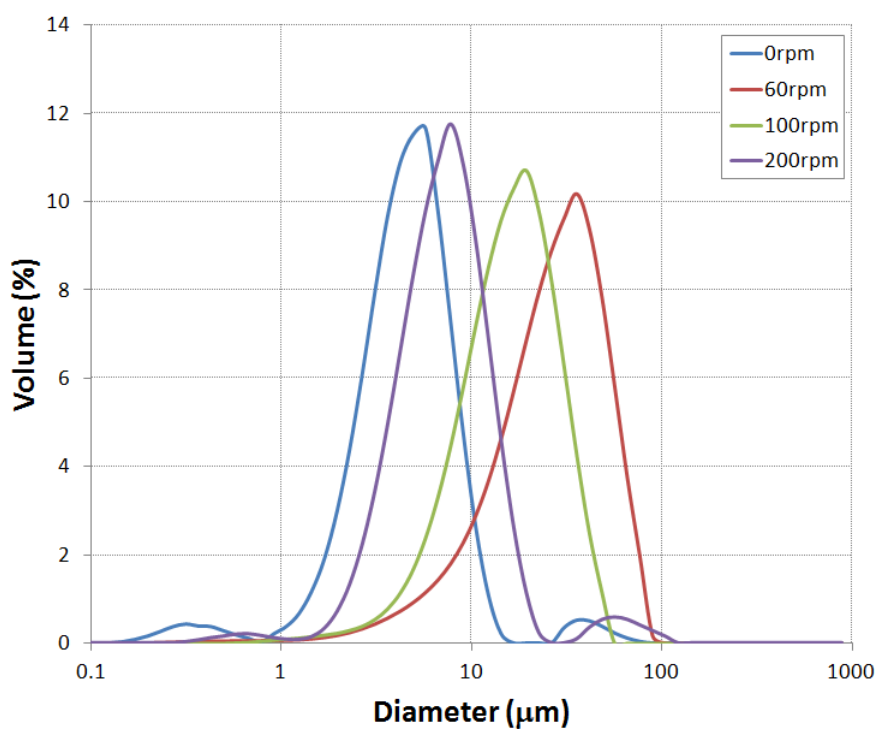
Figure 7.4: Size distributions for the magnetite particles at pH 7 at different stirrer speeds.

The aggregates initially increase in size as the system is stirred and the aggregate size then decreases as the stirrer speed increases. This is due to the structure of the aggregates changing as the stirrer speed is increased. The scattering exponents are 2.23 at 60rpm, 2.44 at 100rpm and 2.65 at 200rpm. Thus the aggregates become denser and hence smaller as the stirrer speed increases. This structural difference can also be seen in TEM images such as those shown in figures 7.5 to 7.8.
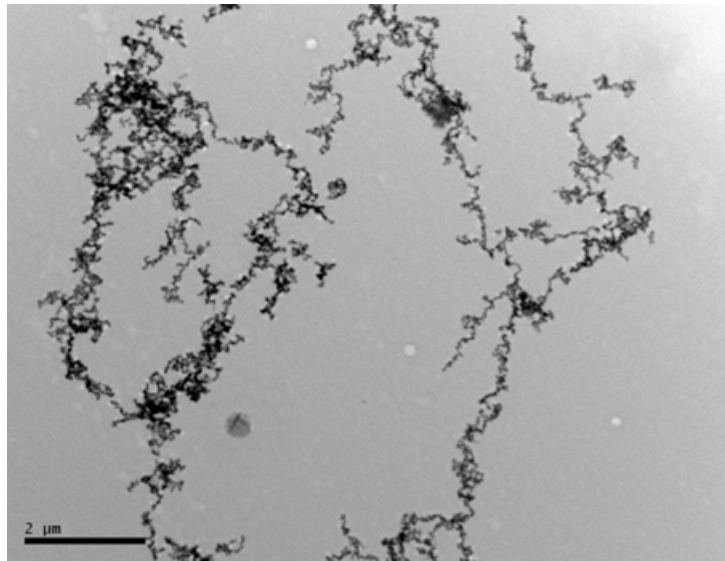
Figure 7.5: TEM images of the magnetite particles at pH 7 after 30 minutes at 0rpm.
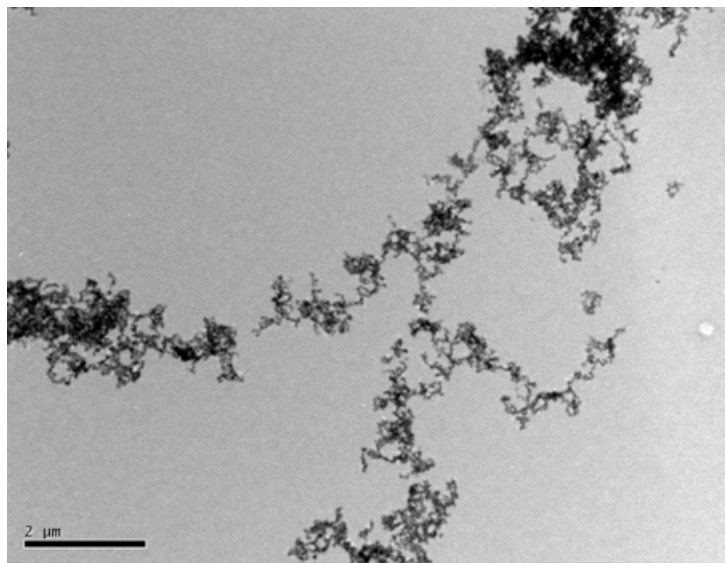
Figure 7.6: TEM images of the magnetite particles at pH 7 after 30 minutes at 60rpm.
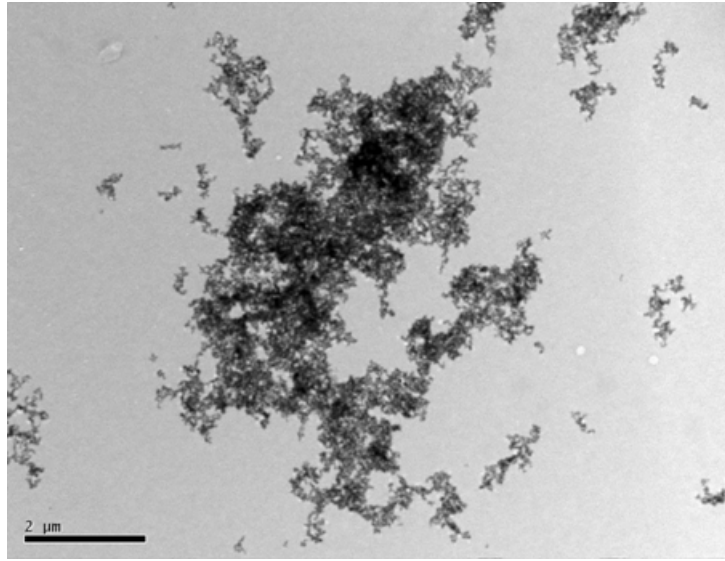
Figure 7.7: TEM images of the magnetite particles at pH 7 after 30 minutes at 100rpm.
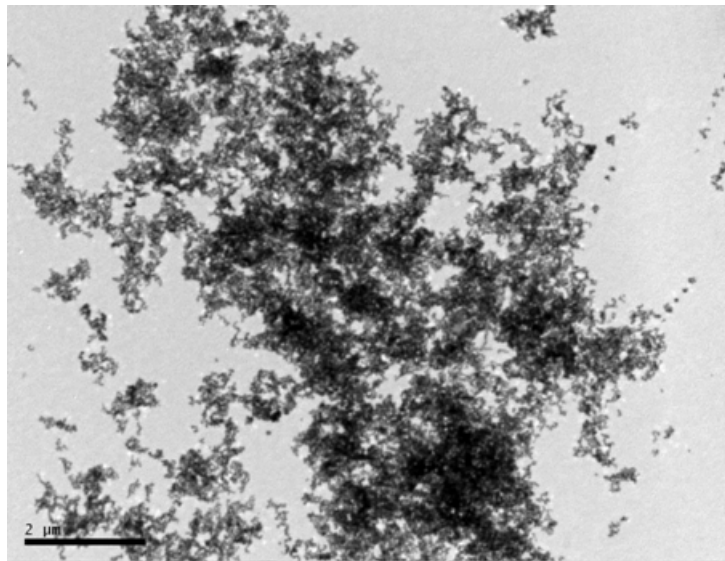
Figure 7.8: TEM images of the magnetite particles at pH 7 after 30 minutes at 200rpm.

Although the aggregation shows a dependence on the stirrer speed, there is no indication from the scattering data that the aggregates are restructuring, as has been observed in other particle systems (Jung et al., 1996; Selomulya et al., 2001). The scattering data

shows one slope as opposed to the two distinct slopes that indicate that the aggregates have undergone restructuring.

7.4.2 The effect of electrolyte

The size distributions for the suspensions at different stirrer speeds with added electrolyte (100mM KNO3 at pH 7) are shown in figure 7.9. The pattern observed without added electrolyte is not seen here, and the size distributions are more similar. The dependence of the aggregation on the stirrer speed is not observed here and the results are similar for all stirrer speeds, and this similarity can best be seen by comparing the scattering data at different stirrer speeds. This is shown in figure 7.10.
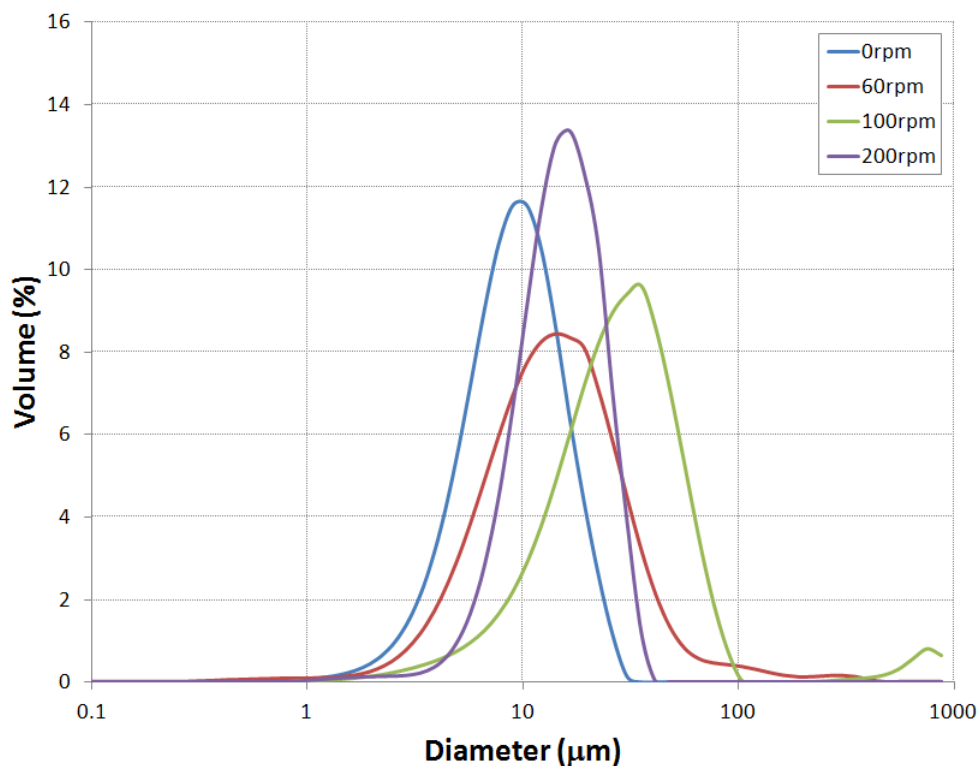
Figure 7.9: Size distributions for the magnetite particles in 100mM KNO3 at different stirrer speeds.

The scattering data also shows similar slopes at different stirrer speeds which indicate

that the structures of the aggregates at different stirrer speeds are also similar. The scattering exponents obtained for the magnetite particles are 2.46 at 60rpm, 2.39 at 100rpm and 2.55 at 200rpm. These values indicate dense aggregates with a more compact structure, as is illustrated by the TEM image in figure 7.11.
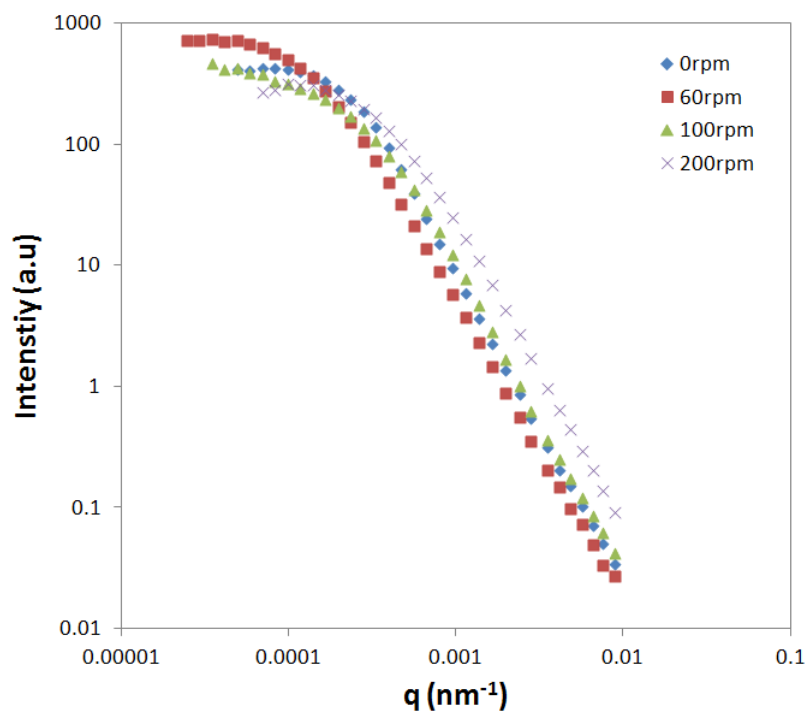
Figure 7.10: Scattering data for magnetite particles in 100mM KNO_3 at different stirrer speeds.

The scattering data shows only one distinct slope at different stirrer speeds, and therefore there is no indication of restructuring of the aggregates. This observation is the same as that made without the addition of electrolyte.
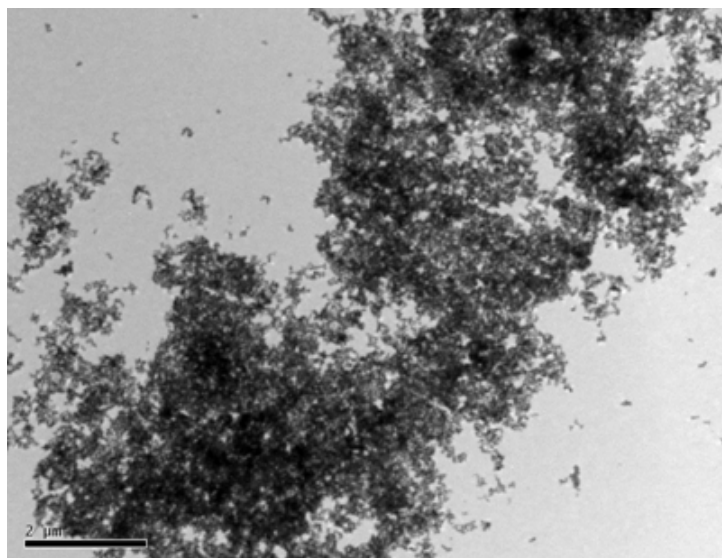
Figure 7.11: TEM image of the magnetite particles in 100mM KNO$_3$ at 200rpm after 30 minutes.

7.5 Discussion

The particles used were the same as used those used in chapter 4 and so discussion of particle characterisation can be found there.

Adding to the combination of different forces acting on the particles is now that of fluid motion. This has been observed to increase the size and density of aggregates, which is due to the increase in the frequency of collisions between particles.

The aggregates formed in these conditions are large and dense with scattering exponents greater than 2. The TEM images also show these large dense aggregates.

The aggregation of the magnetite particles in the stirred system is dependent on the stirrer speed in addition to the suspension pH and the electrolyte concentration, as was observed in chapter 3. The pH affects significantly the size of the aggregates formed, with much larger structures being formed at pH 7, which is closer to the isoelectric point. At pH 2 and 11 the structures are significantly smaller due to the much greater electrostatic repulsion between the particles, which is not, however, sufficient to stabilise

the suspension from aggregation. These structures are then dependent on the stirrer speed and the structures become more compact as the stirrer speed is increased. The size of the aggregates is also dependent on the stirrer speed, with smaller aggregates being formed at 200rpm as compared to 60rpm.

The structures also show much less evidence of the restructuring that has been observed in other systems (Jung et al., 1996; Selomulya et al., 2001). This is most likely due to the strong attraction between the particles due to their magnetic moments, which make the aggregate structures, particularly the more compact structures, more resilient to breakage or restructuring as a result of the shear forces.

The addition of electrolyte reduces the dependence of the aggregation on the stirrer speed, as can be seen from the similarity of the scattering data in figure 7.10 and comparison of VMDs in figure 7.12 below. The most compact structures are still formed at higher stirrer speeds as determined from the scattering exponents. The structures are also similar to those formed at pH 7 at 200rpm without the addition of electrolyte, as can be seen from the TEM images of the aggregates (see figures 7.8 and 7.11) and the similarity in the scattering exponents.
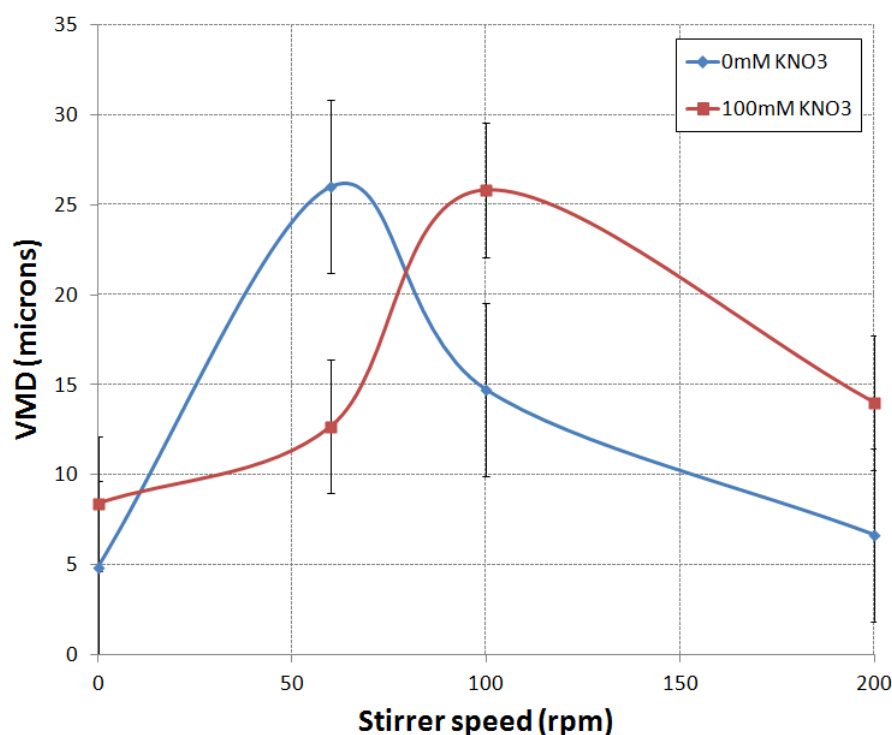
Figure 7.12: VMDs for magnetite particles at pH 7 and in 100mM KNO_3 at different stirrer speeds.

Thus the aggregation of the magnetite particles in a stirred system show differences from previous studies on non-magnetic systems. The aggregates do not seem to form in the same manner through restructuring via the breakup of aggregates, as there is no evidence of this in the scattering data. The electric double layer seems to be able to influence the aggregation without the addition of electrolyte, providing a certain amount of repulsion between the particles. However, with the addition of electrolyte and the suppression of the double layer the attractive magnetic interaction seems to dominate and there is little difference with increasing stirrer speed.

Chapter 8

Aggregation of hematite nanoparticles in a magnetic field in a stirred system

8.1 Previous work

A previous study by Jung et al. (1996) on the effect of shear on hematite aggregates showed that the aggregates restructured at low shear rates, and underwent breakup and restructuring at high shear rates. Small angle light scattering was used to monitor the formation and structure of iron hydroxide aggregates from the hydrolysation of FeCl3 solution. The freshly formed aggregates had a fractal dimension of 2.25 and as the hydrolysation proceeded the aggregates grew to larger sizes with a fractal dimension of 2.52, which was attributed to the restructuring of the aggregates. At low shear rates (stirring rate 60-200 rpm), the aggregates restructured but did not break up, while at a higher shear rate (2 min of 1500 rpm centrifugation), the aggregates broke up and restructured, showing that the iron hydroxide particles were only connected by a weak force. Subsequent studies (Selomulya et al., 2001, 2004) have also shown the dependence on shear rate

of restructuring and breakup in other sheared colloidal systems.

Tombacz et al. (1991) used dynamic light scattering to investigate the changes in the aggregation state of colloidal hematite in a flowing system with an applied magnetic field. They found an increase in average particle size when the suspension was flowing and the magnetic field was applied, but no significant change was observed for a flowing suspension without the applied field or a quiescent suspension with the applied field. Busch et al. (1996) found similar results for suspensions of colloidal latex and cholesterol and attributed the changes to magnetohydrodynamic effects, as both latex and cholesterol are diamagnetic.

Stuyven et al. (2009a,b) investigated suspensions of diamagnetic silica and alumina particles, aggregated using potassium nitrate, flowing with an applied magnetic field. Smaller average sizes were observed in a turbulent flow regime, at a Reynolds number of around 8000. In a laminar flow regime, at a Reynolds number of around 2000, the average size was observed to increase. This was attributed to Lorentz forces acting on the charged particles.

The purpose of this chapter is to study the changes in aggregation in a sheared system with an applied magnetic field using static light scattering, and thus to investigate the effects of increasing the collision efficiency on the growth and restructuring of the aggregates when the magnetic interaction is altered.

8.2   Synthesis and Characterisation

The same spheroidal hematite particles were used as in chapter 5. See chapter 5 for the synthesis method and characterisation.

8.3 Experimental

8.3.1 Experimental Setup

A magnetic field was applied to the particles by placing magnets either side of a stirred beaker. Rare earth magnets ($Ne_2Fe_{14}B$) with a magnetic flux of approximately 1 Tesla (value provided by the manufacturer, AMF Magnetics) were used. This is shown schematically in figure 8.1. This setup is simple and inexpensive, but is not effective if studying shear or mixing. However, the purpose of the setup was to alter the collision frequency of the particles by stirring, thus avoiding the separation of the particles from suspension observed in chapters 5 and 6.
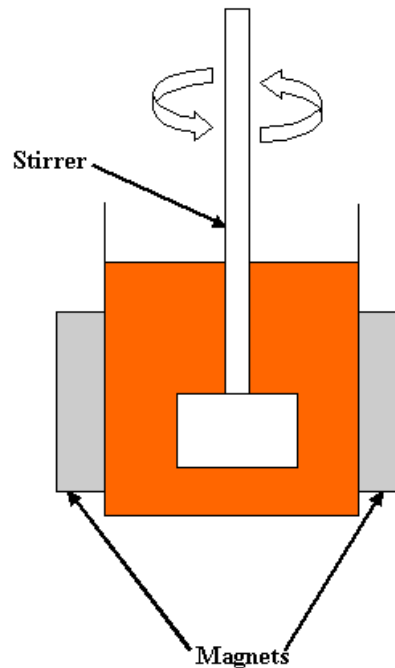
Figure 8.1: Schematic of the stirred beaker using a glass blade stirrer with an applied magnetic field.

Both the beaker and the stirrer were made from glass so that there would be no effect from the magnetic field on either during the experiment.

171

8.3.2 Experimental Method

1.5 ml of the stock suspension was added to 150ml of 3.75mM HCl, distilled water or 3.75mM NaOH to give suspensions at pH 2.4, 7.0 and 10.8 respectively. The effect of added electrolyte was investigated in the same way by dispersion in 150ml of 100mM potassium nitrate KNO_3. The stirrer speeds used were 0, 60, 100 and 200rpm. The suspensions were sampled and measured every 5 minutes during half an hour by drawing the suspensions into the flow cell using a syringe (see section 7.3.1).

8.4 Results

8.4.1 The effect of pH

The main effect of stirring is to increase the collision frequency between the particles, resulting in faster aggregation and the formation of denser aggregate structures through the breakage and restructuring of the aggregates (Selomulya et al., 2001, 2004). The pH still provides a repulsive barrier as it moves further away from the isoelectric point and thus influences the aggregation.

At a stirrer speed of 200rpm little aggregation was observed at pH 2 and 11, as was the case in chapter 5 and the aggregation was unaffected by a magnetic field. At pH 7, which is close to the isoelectric point, there was a greater degree of aggregation as the electrostatic repulsion is reduced, as was also observed in chapter 5. There is no formation of fractal aggregates as the scattering exponents obtained from the scattering data are less than 1, and thus are not in the fractal regime (between 1 and 3).

The application of the magnetic field did not alter the aggregation and similar results were obtained with and without the magnetic field. The size distributions of the particles aggregated at pH 7 with and without the magnetic field are shown in figure 8.2. The size distributions are similar, although there is a difference in intensity in the first peak.
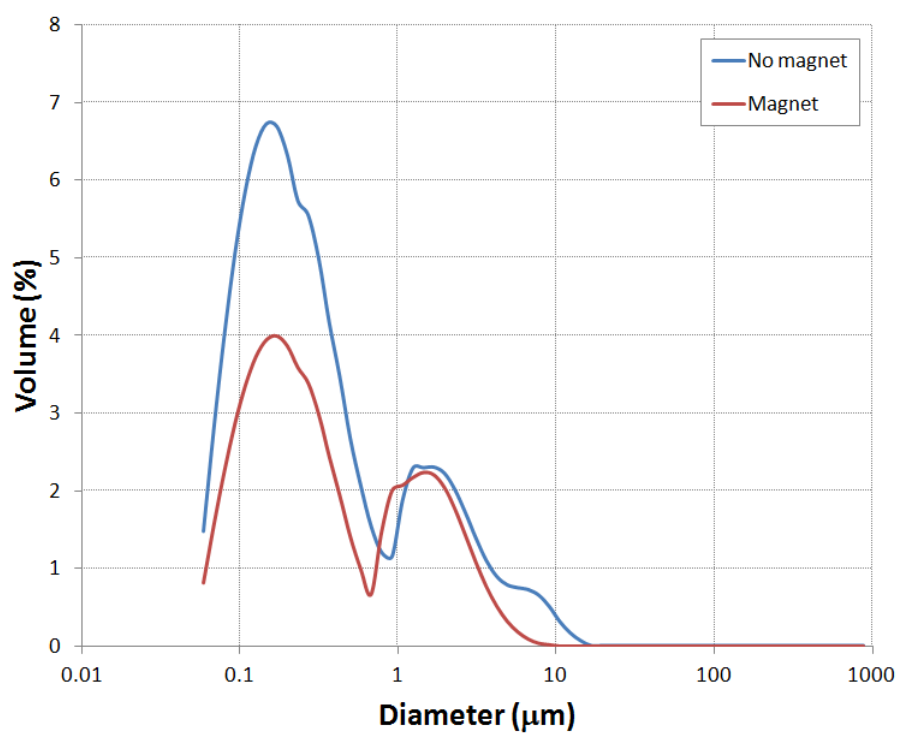
Figure 8.2: Evolution of the scattering exponents of the spherical hematite particles at pH 7 with a stirrer speed of 200rpm, **with and without** an applied magnetic field after 30 minutes.

However, the similarity can be seen even more clearly when comparing the scattering data (figure 8.3), and thus there is no observable difference with a magnetic field.
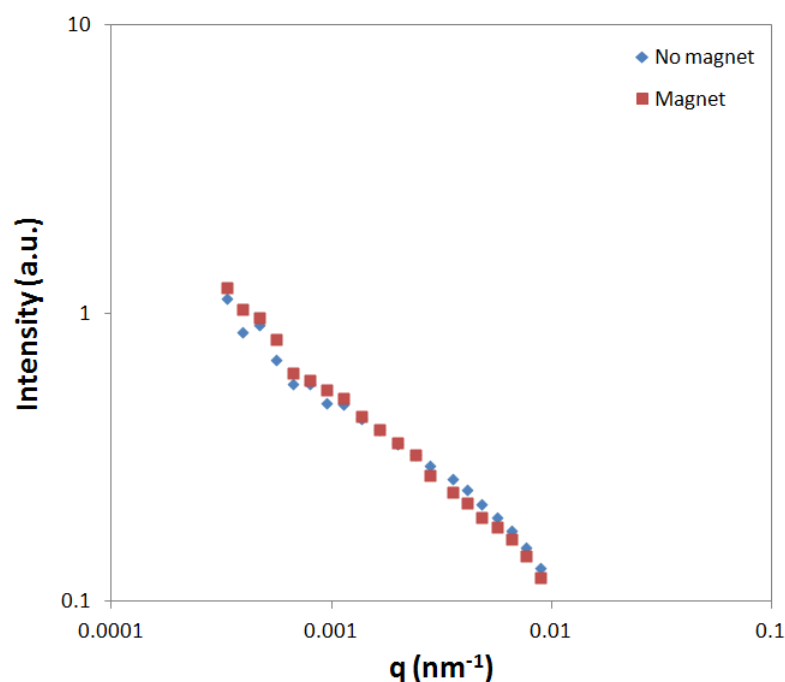
Figure 8.3: Scattering data for spherical hematite particles at pH 7 and 200rpm after 30 minutes, **with and without** a magnetic field.

Thus, without the addition of electrolyte, the pH still has the greatest influence on the aggregation, no significant difference being observed with the presence of the magnetic field.

8.4.2 The effect of electrolyte

The addition of electrolyte causes the particles to grow into large aggregate structures, and these large structures undergo breakage and restructuring, as has been observed previously (Jung et al., 1996).

The size distributions for the spherical particles in 100mM KNO_3 are shown in figure 8.4 at different stirrer speeds. As the stirrer speed increases the size distributions become narrower and the particle sizes increase. The narrowing of the peaks in the size distributions is due to the difference in structure of the aggregates, which become more compact

as the stirrer speed increases.
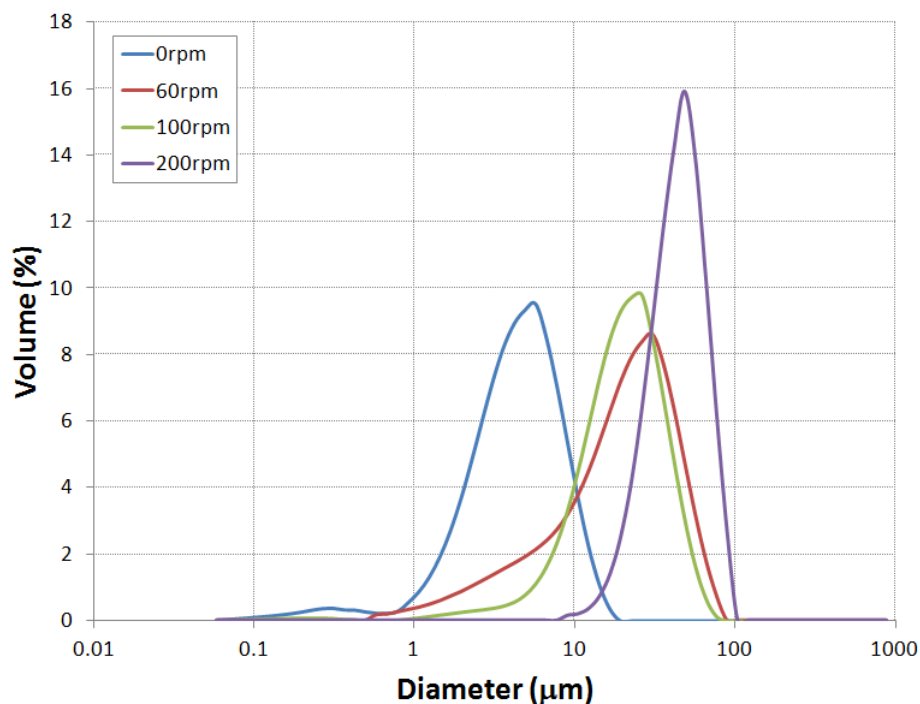
Figure 8.4: Size distributions for spherical hematite particles in 100mM KNO_3 at different stirrer speeds after 30 minutes **<u>without</u>** a magnetic field.

The size distributions for the spherical particles in 100mM KNO_3 with a magnetic field at different stirrer speeds are shown in figure 8.5. The trend is very similar to that seen without the magnetic field, and this is further confirmed by directly comparing the scattering data with and without the magnetic field. The scattering exponents are also similar with the magnetic field present, indicating that there is no change in the aggregate structure as a result of the magnetic field. The only exception to all this is at a stirrer speed of 200rpm.
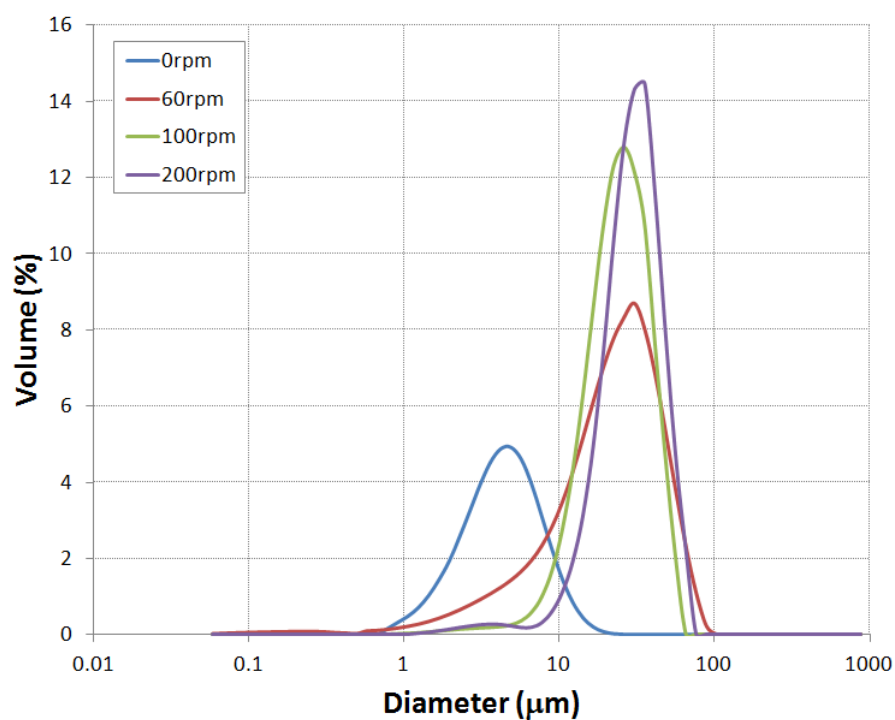
Figure 8.5: Size distributions for spherical hematite particles in 100mM KNO$_3$ **with** a magnetic field at different stirrer speeds after 30minutes.

The size distributions at a stirrer speed of 200rpm with and without a magnetic field are shown in figure 8.6. The aggregates are smaller in the presence of a magnetic field, which can be seen in the differences in the size distribution.
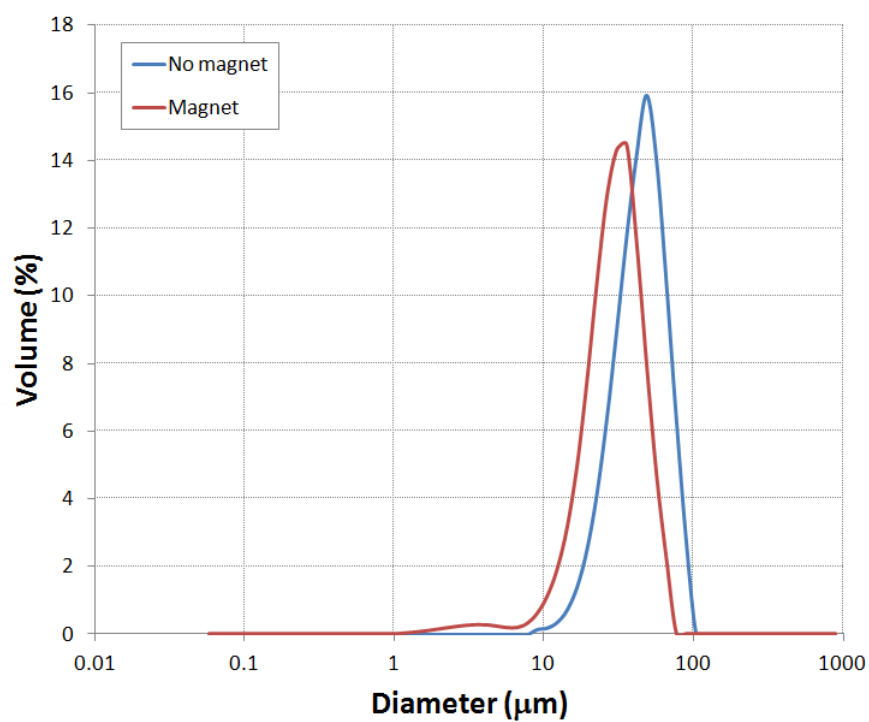
Figure 8.6: Size distribution for spherical hematite particles in 100mM KNO_3 at a stirrer speed of 200rpm after 30 minutes.

This difference at 200rpm can be seen even more clearly by directly comparing the scattering data, shown in figure 8.7.
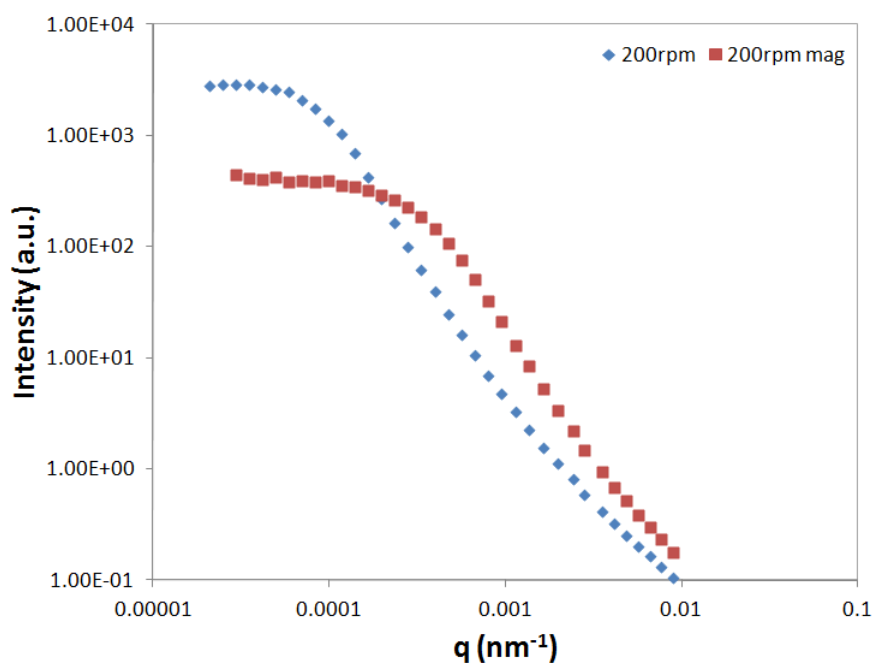
Figure 8.7: Scattering data for spherical hematite particles in 100mM KNO_3 at a stirrer speed of 200rpm after 30 minutes.

This size difference can also be seen by comparing TEM images of the aggregates with and without a magnetic field, shown in figures 8.8 to 8.13. The dense structures have similar scattering exponents of ≈ 2.5, and can be considered as fractal aggregates, but the difference in size is apparent.
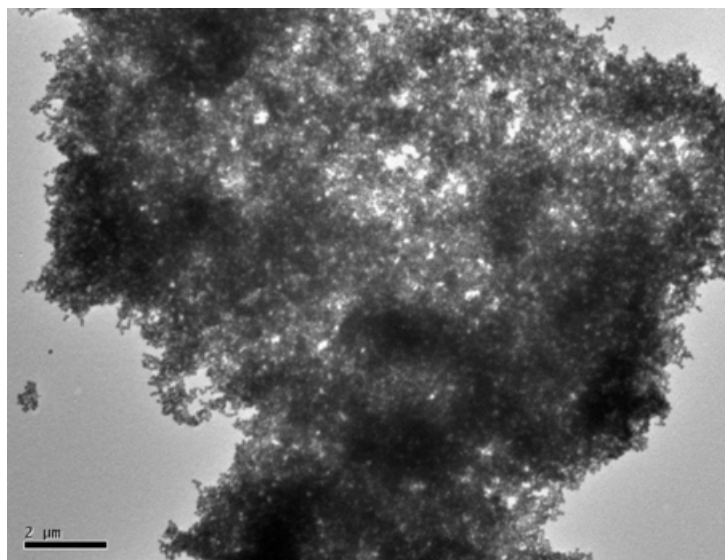
Figure 8.8: TEM image (1) of the spherical hematite particles in 100mM KNO_3 after 30 minutes at a stirrer speed of 200rpm **<u>without</u>** a magnetic field.
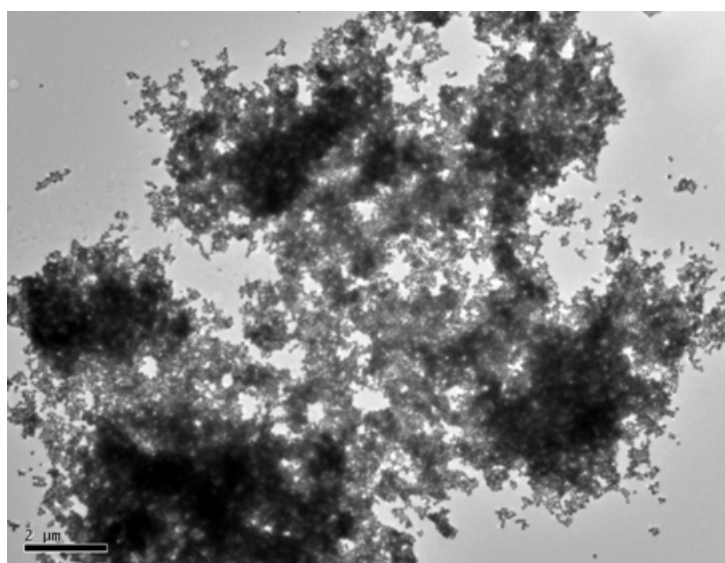
Figure 8.9: TEM image (2) of the spherical hematite particles in 100mM KNO_3 after 30 minutes at a stirrer speed of 200rpm **<u>without</u>** a magnetic field.

Figure 8.10: TEM image (3) of the spherical hematite particles in 100mM KNO_3 after 30 minutes at a stirrer speed of 200rpm **<u>without</u>** a magnetic field.
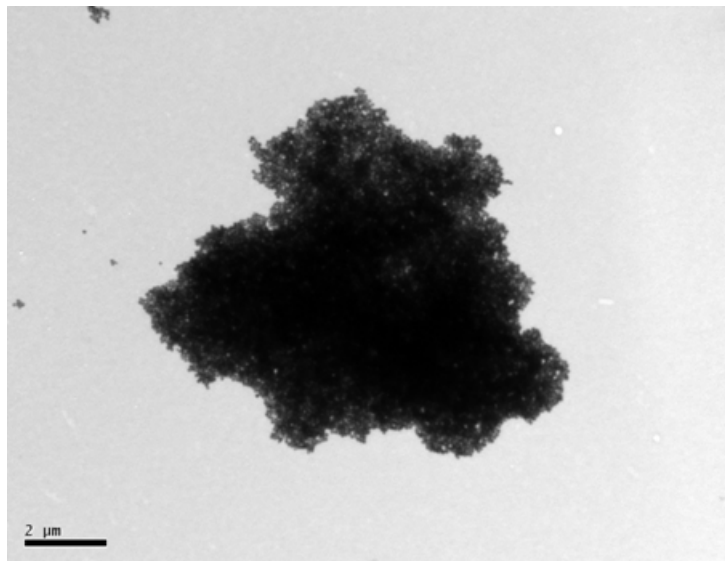
Figure 8.11: TEM image (1) of the spherical hematite particles in 100mM KNO_3 after 30 minutes at a stirrer speed of 200rpm **<u>with</u>** a magnetic field.
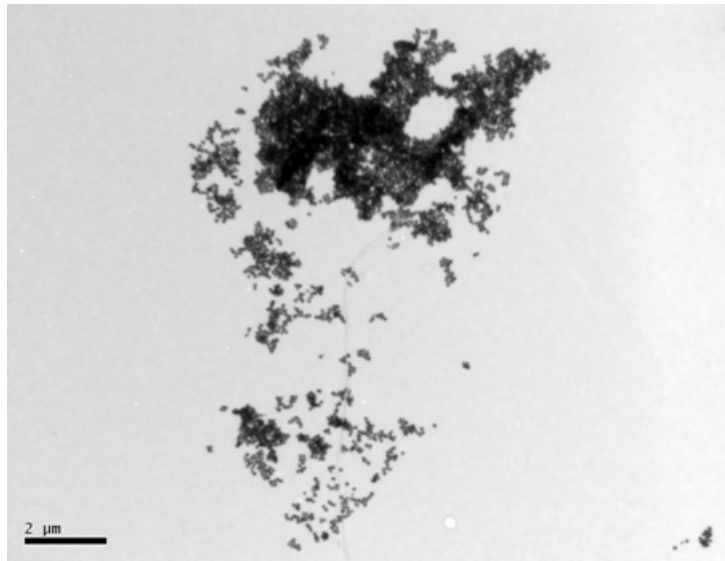
Figure 8.12: TEM image (2) of the spherical hematite particles in 100mM KNO_3 after 30 minutes at a stirrer speed of 200rpm **with** a magnetic field.
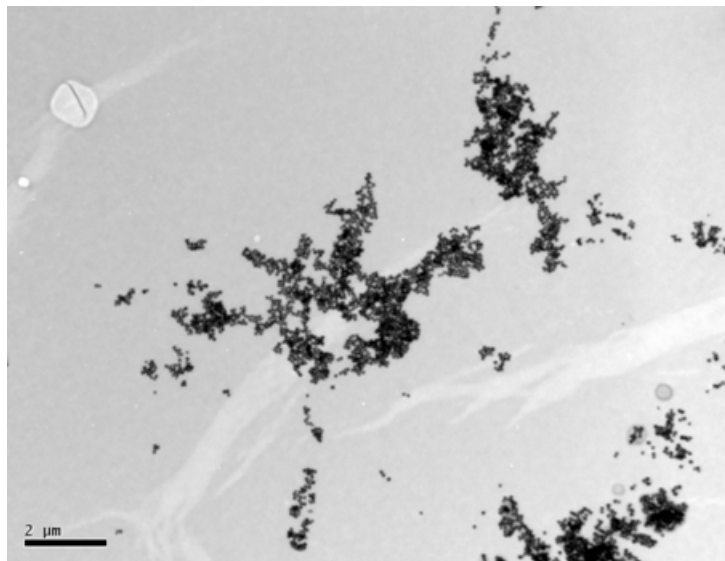
Figure 8.13: TEM image (3) of the spherical hematite particles in 100mM KNO_3 after 30 minutes at a stirrer speed of 200rpm **with** a magnetic field.

The TEM images show similar compact structures, as indicated by the scattering exponents, but the overall aggregate size is much smaller with the applied magnetic field.

8.5   Discussion

The particles used were the same as used those used in chapter 5 and so discussion of particle characterisation can be found there.

In a stirred system the frequency of collisions between particles is increased allowing the particles to come into contact more easily to form large aggregates. These large structures are then vulnerable to the shear forces which break the aggregates into smaller aggregates. These then form other aggregates and through this process of breakage and formation of other aggregates, large compact structures are formed as previously observed (Jung et al., 1996; Selomulya et al., 2001, 2004).

The stirred system does not significantly alter the aggregation of the particles without the addition of electrolyte. The surface forces are still dominant and thus the pH is the dominant factor in controlling the aggregation. At pH 7, which is close to the isoelectric point, there is some aggregation, but this is not greatly increased by stirring the system and no change is observed when the magnetic field is applied.

The addition of electrolyte to the suspension causes the particles to grow into large structures and the aggregation of the particles shows a dependence on stirrer speed, as observed previously (Jung et al., 1996). The aggregates also showed evidence of re-structuring as the stirrer speed was increased, with two distinct slopes observable in the scattering data (see figure 8.7), as has been demonstrated previously (Selomulya et al., 2001, 2004). The magnetic field did not alter the aggregation behaviour of the particles until the highest stirrer speed of 200rpm was used. The effect of the magnetic field is to cause the formation of aggregates that are smaller than without the magnetic field. This finding agrees, in part, with the findings of Stuyven et al. (2009a,b) from suspensions of silica and alumina particles, but not with the findings of Tombacz et al. (1991) and Busch et al. (1996).

In fact, the findings by Stuyven et al. (2009a,b), Tombacz et al. (1991) and Busch et al. (1996) are seemingly contradictory, stating that aggregation is both increased and decreased in turbulent flow. However, the difference in the region of turbulent flow investigated is perhaps important. Stuyven et al. (2009a,b) observed the defragmentation effect in systems with low turbulence, greatest at a Reynolds number of 8×10^3, and the effect lessened with greater turbulence, the maximum Reynolds number investigated being 6.4×10^4. Tombacz et al. (1991) and Busch et al. (1996) studied systems with much greater turbulence, with Reynolds numbers of 1.4×10^6 and 7.8×10^5 respectively, and saw increases in the average size. Also, Stuyven et al. (2009a,b) found that the average size increased in a laminar flow regime with a Reynolds number of 2×10^3.

The previous findings observed small changes using dynamic light scattering and thus focused on a length scale of less than a micron. Using static light scattering increases the length scale up to hundreds of microns and thus large changes can be observed. The smaller aggregates formed at a high stirrer speed thus agree with Stuyven et al. (2009a,b), although no increase was observed at lower stirrer speeds that would correspond to the increase in average size observed by these authors.

Thus, taking the previous work into account it would seem that the effect of the magnetic field is also dependent on the flow regime, particularly the balance between the shear forces and the Lorentz force induced by the magnetic field on the particles.

Chapter 9

Aggregation of ellipsoidal hematite nanoparticles in a magnetic field in a stirred system

9.1   Previous work

The particle shape can affect both how the particles aggregate and their magnetic properties as discussed in the previous work and chapter 6. When the suspension of particles is flowing the particle shape can also have an effect on the transport properties of the particles.

Zhang et al. (2001) studied the transport and deposition of ellipsoidal particles using direct numerical simulation (DNS) of the Navier-Stokes equation. They noted that the aspect ratio plays an important role in the deposition rate of the particles and that ellipsoidal particles tend to align themselves in the flow direction and rotate mostly around the z-axis due to the streamwise mean field with little rotation about the y-axis perpendicular to the shear field. Kim et al. (2004), using a homogeneous simple shear flow analysis, found that the initial particle size, and also the particle mass, significantly affects

particle collisions and, in turn, the extent of agglomeration or cluster formation. Gunes et al. (2008) investigated medium viscoelasticity and particle characteristics on the flow-induced orientational transitions in suspensions of spheroidal articles using microscopic and rheo-optical methods. Results showed that when elastic effects start to become significant, particle rotation slows down and the particle orbits drift toward the vorticity direction, thus producing a log-rolling state. Mortensen et al. (2008) calculated that as the aspect ratio of the particles increase the particles tend to line up more and more in the mean flow direction. Results also indicated that, in the near-wall region, prolate ellipsoids tend to orient in the mean flow direction. The effect was observed to be more pronounced as the aspect ratio increased. Cleary (2008) investigated the effects of particle shape in a shear granular flow using a discrete element method (DEM) simulation. It was found that there was a slow increase in solid fraction near the wall, and a lower central solid fraction, creating a more even distribution of particles across the shear flow. Gregorova et al. (2009) investigated the influence of particle shape on suspension rheology using different suspensions of kaolin particles. It was found that the intrinsic viscosity increased with the particle aspect ratio, such that an average aspect ratio of around 20 results in an intrinsic viscosity of about 10, as compared to 2.5 for spherical particles.

The purpose of this chapter is to investigate the aggregation of ellipsoidal hematite particles in a sheared system, given the differences in both aggregation and flow behaviour due to the particle shape, and how that aggregation is affected by the application of a magnetic field (as used in the previous chapter) and the differences apparent when compared to the spheroidal particles.

9.2   Synthesis and Characterisation

The same ellipsoidal hematite particles were used as in chapter 6. See chapter 6 for the synthesis method and characterisation.

9.3 Experimental

The experimental setup and method was the same as that used in chapter 8. See chapter 8 for details.

9.4 Results

9.4.1 The effect of pH

The size distributions for the particles at different pH and at a stirrer speed of 200rpm are shown in figure 9.1. The greatest amount of aggregation occurs at pH 7, with much smaller aggregates formed at pH 2 and pH 11. This is similar to the aggregation of the spherical particles, except there is a greater amount of aggregation with the ellipsoidal particles. The aggregation was then unaffected by the application of a magnetic field.
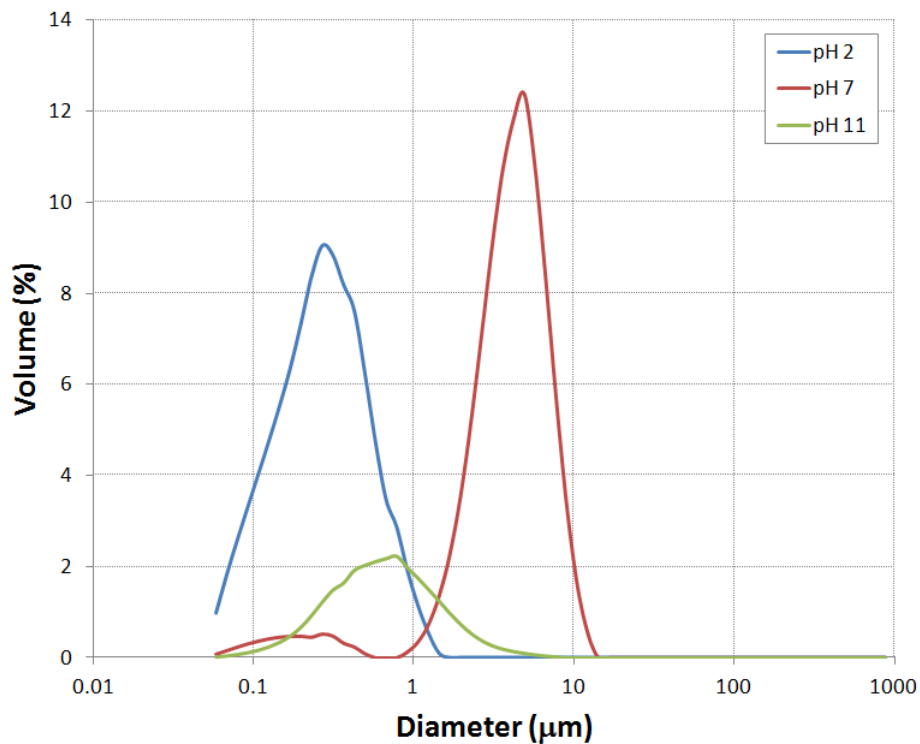
Figure 9.1: Size distributions for the ellipsoidal particles at different pH at 200rpm.

As there was a significant amount of aggregation at pH 7, the particles were also tested at different stirrer speeds with and without a magnetic field to see the effects on the growth of the aggregate structures. The size distributions for this are shown in figure 9.2 without a magnetic field and figure 9.3 with a magnetic field.
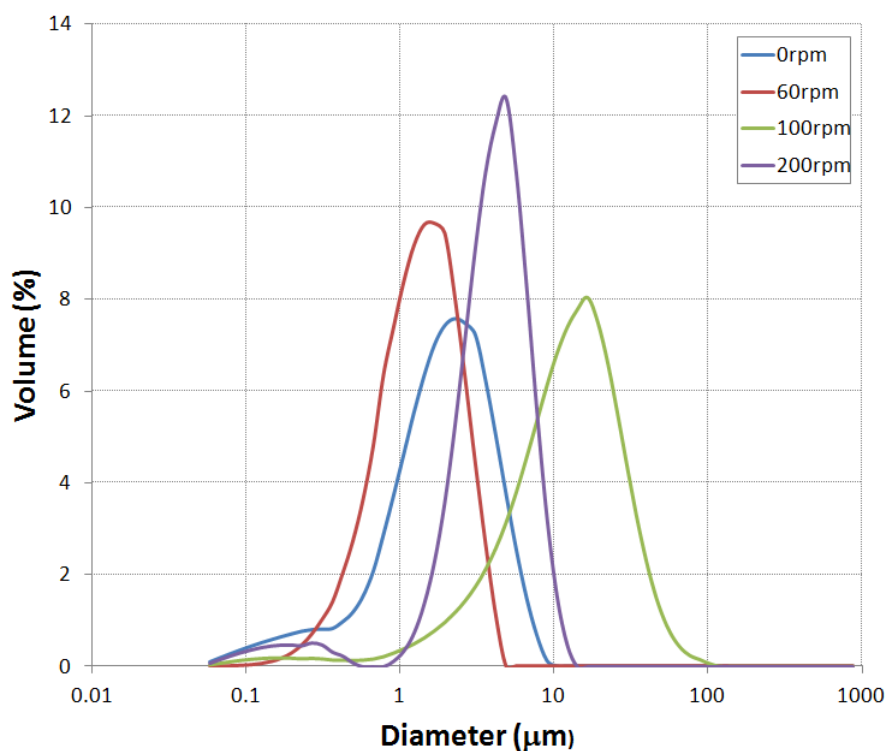
Figure 9.2: Size distributions for ellipsoidal particles at pH 7 at different stirrer speeds after 30 minutes **<u>without</u>** a magnetic field.

The aggregate structure shows some dependence on the stirrer speed, the scattering exponents increasing as the stirrer speed increased. This means the aggregates formed became denser as the stirrer speed increased. The scattering exponents are 1.77 at 60rpm, at 1.89 at 100rpm and 2.23 at 200rpm.
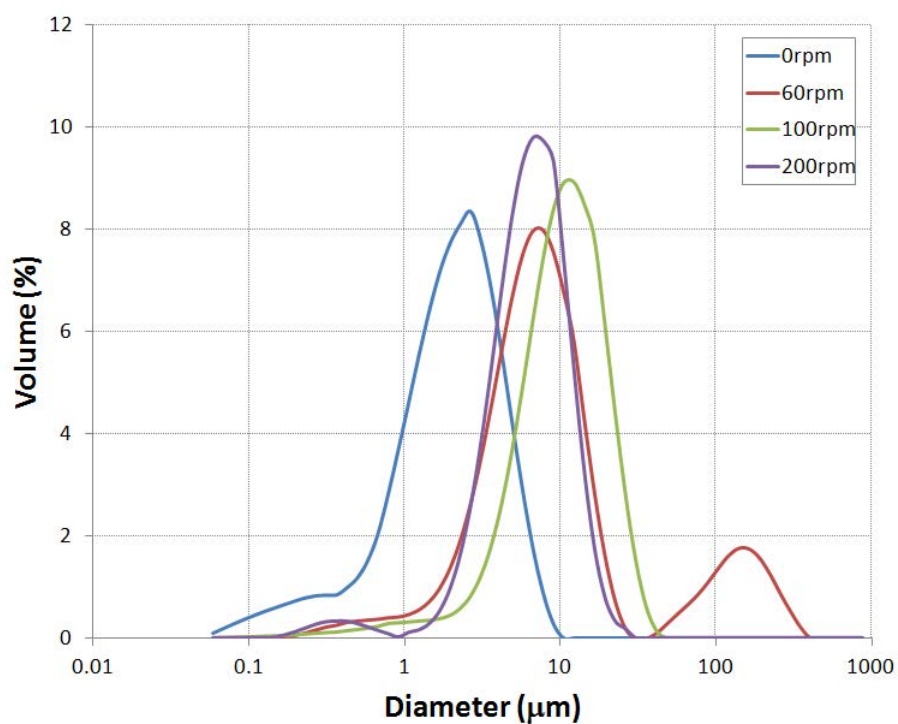
Figure 9.3: Size distributions for ellipsoidal particles at pH 7 at different stirrer speeds after 30 minutes **<u>with</u>** a magnetic field.

The size and structure of the aggregates remained unchanged by the application of a magnetic field, except at a stirrer speed of 60rpm. At 60rpm the aggregates are larger in the presence of a magnetic field as can be seen in the comparison of the size distributions in figure 9.4.
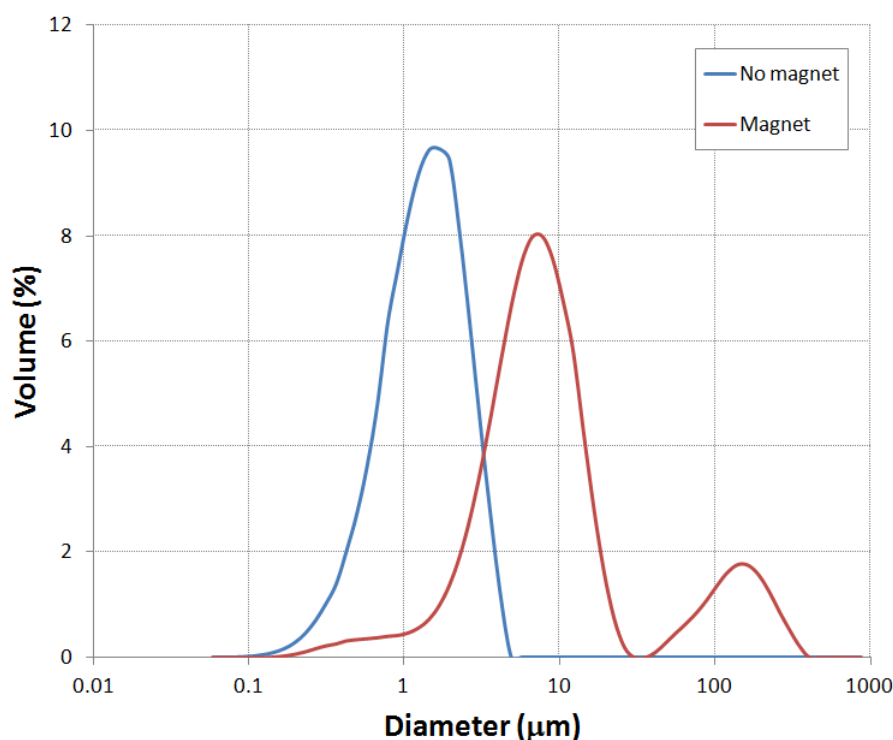
Figure 9.4: Size distributions for the ellipsoidal particles at pH 7 and at 60rpm with and without a magnetic field.

Although the aggregates are larger at 60rpm with the magnetic field, the aggregates have a similar structure to the aggregates without a magnetic field, as indicated by their scattering exponents. The magnetic field seems thus to affect the ellipsoidal particles at low stirrer speeds at pH 7, resulting in the formation of larger aggregates.

9.4.2 The effect of electrolyte

The addition of electrolyte reduces the electrostatic repulsion between particles promoting the growth of large aggregate structures. The size distributions for the suspensions with and without the applied magnetic field are shown in figures 9.5 and 9.6.

189
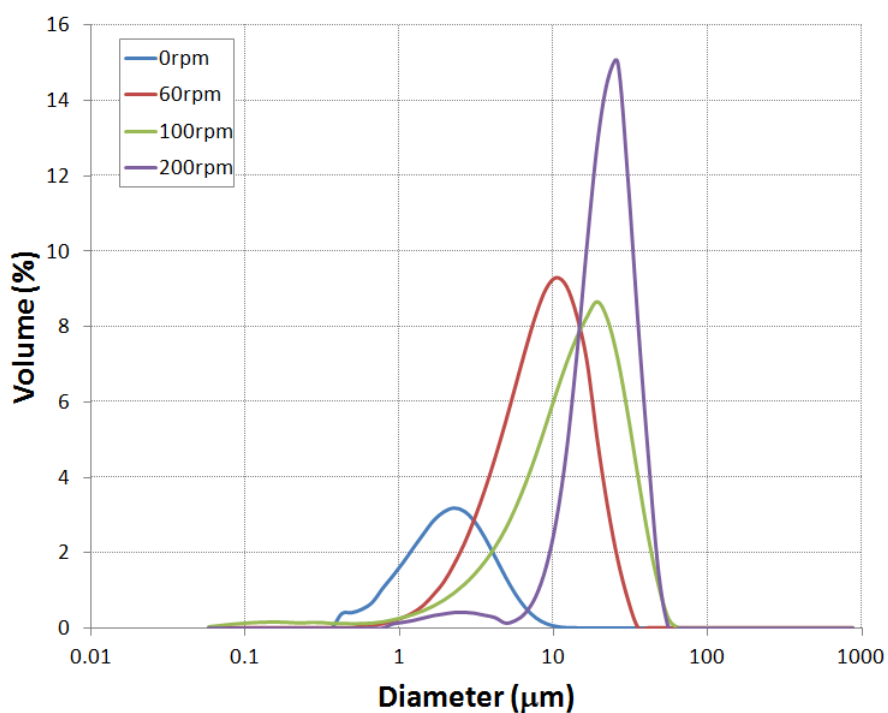
Figure 9.5: Size distributions of ellipsoidal particles in 100mM KNO_3 at different stirrer speeds **without** a magnetic field.

The aggregate size increases as the stirrer speed is increased as was seen with spherical particles. The scattering exponents also increase with the stirrer speed, indicating the formation of more dense structures. The scattering exponents are 1.88 at 60rpm, 1.96 at 100rpm and 2.56 at 200rpm.
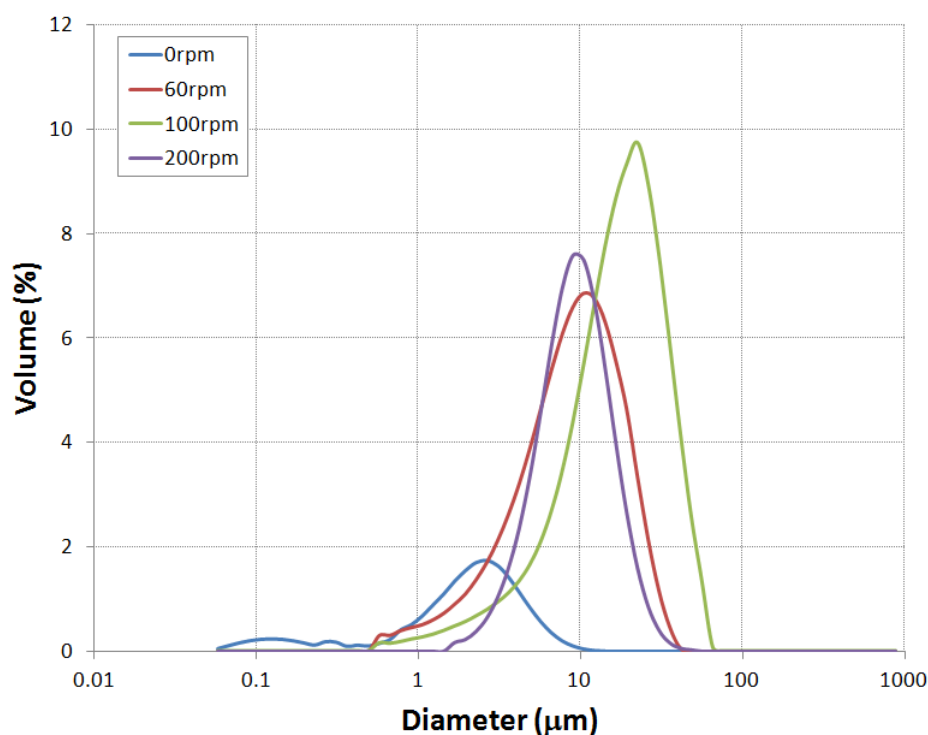
Figure 9.6: Size distributions of ellipsoidal particles in 100mM KNO_3 at different stirrer speeds **with** a magnetic field.

The application of a magnetic field does not alter the aggregation, with aggregates of similar size and structure being formed. However, at 200rpm the aggregates are smaller with the presence of the magnetic field, as was found with the spherical particles. This can be seen from the comparison of the size distributions shown in figure 9.7. The aggregates formed are smaller when the magnetic field is applied.
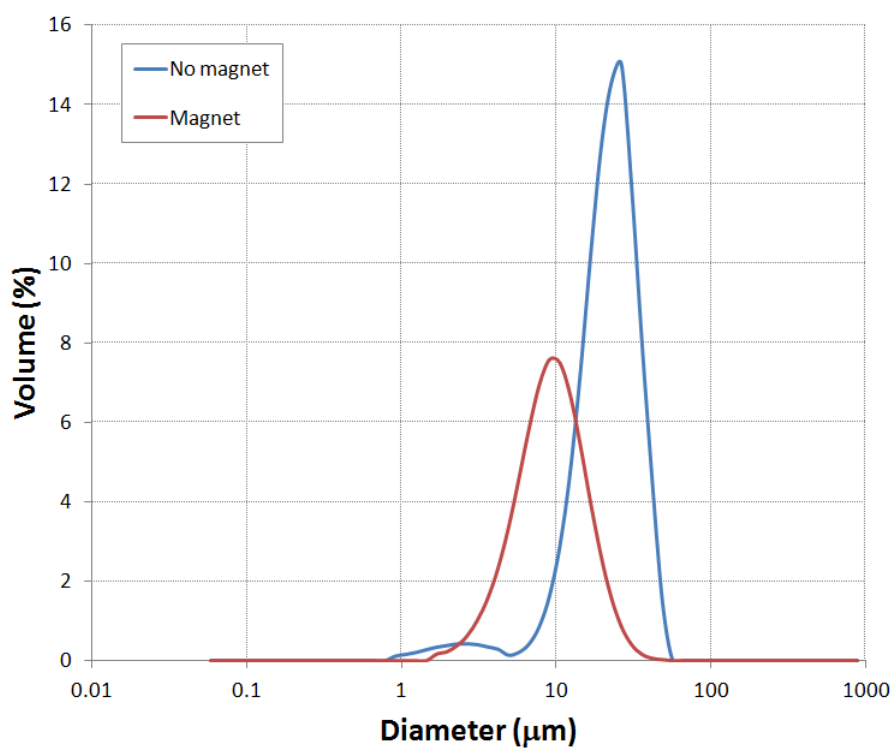
Figure 9.7: Size distributions for ellipsoidal particles in 100mM KNO$_3$ at 200rpm with and without a magnetic field.

This difference can be seen clearly in the scattering data shown in figure 9.8. In both cases there is evidence for the restructuring of the particles, as two distinct slopes can be seen in the data.
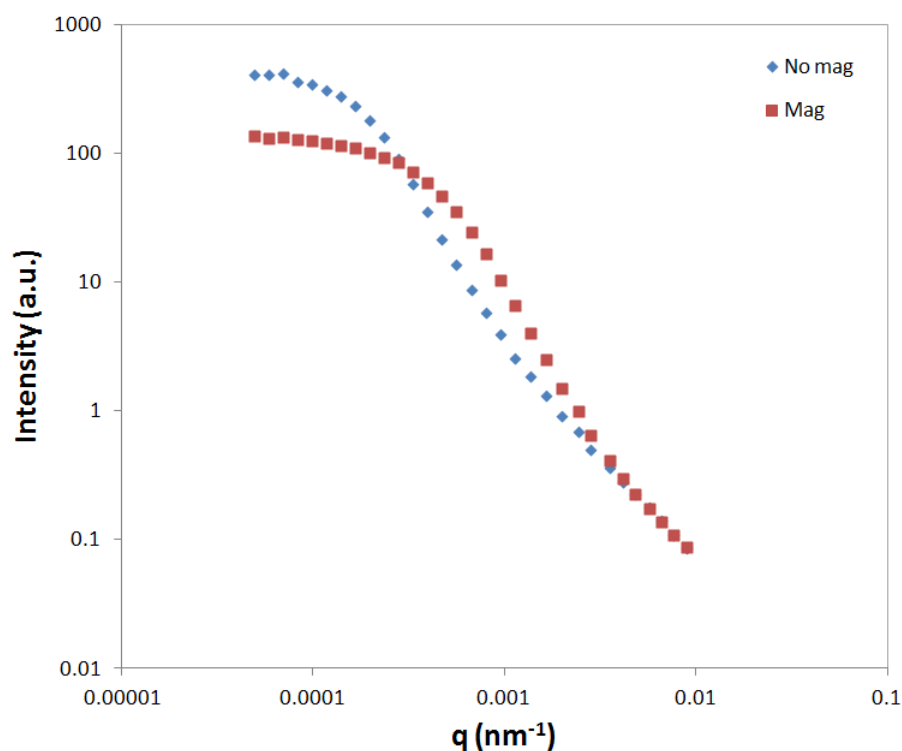
Figure 9.8: Scattering data for the ellipsoidal particles in 100mM KNO_3 and at a stirrer speed of 200rpm after 30 minutes.

TEM images of the particles at 200rpm with and without the applied field agree with the size distributions in figure 9.7. These images are shown in figures 9.9 to 9.14. The aggregates formed in the presence of the magnetic field can be seen to be smaller when compared to the aggregates formed without the applied field.
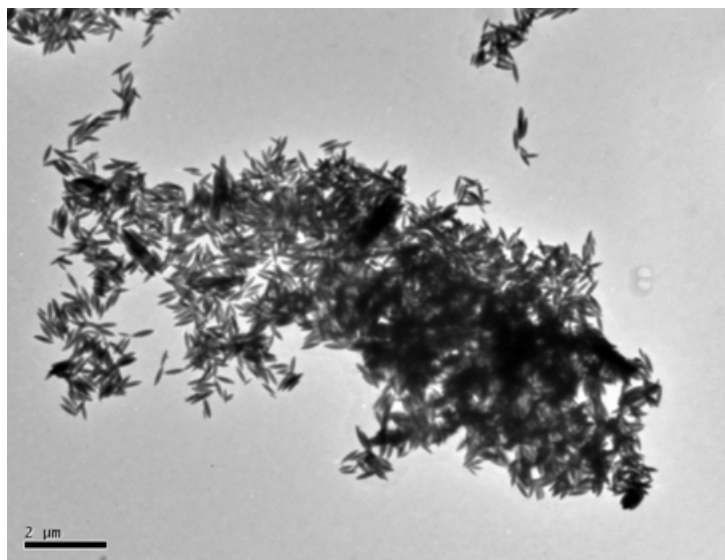
Figure 9.9: TEM image of the aggregates in 100mM KNO$_3$ and at a stirrer speed of 200rpm after 30 minutes without an applied magnetic field.
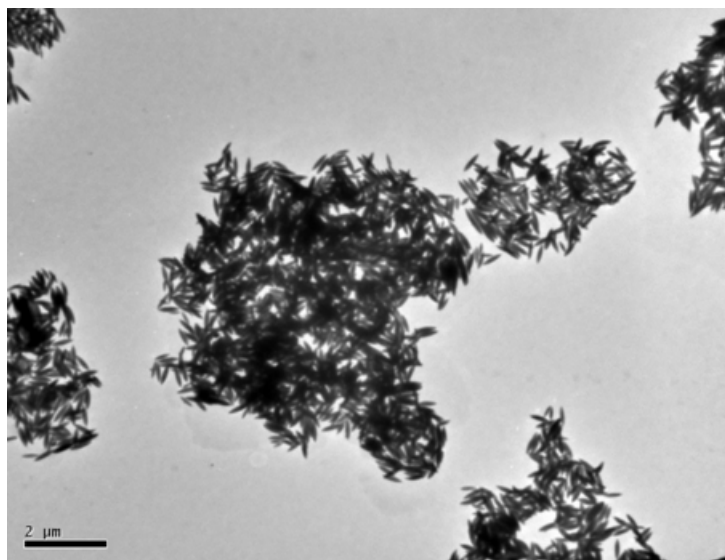
Figure 9.10: TEM image of the aggregates in 100mM KNO$_3$ and at a stirrer speed of 200rpm after 30 minutes without an applied magnetic field.
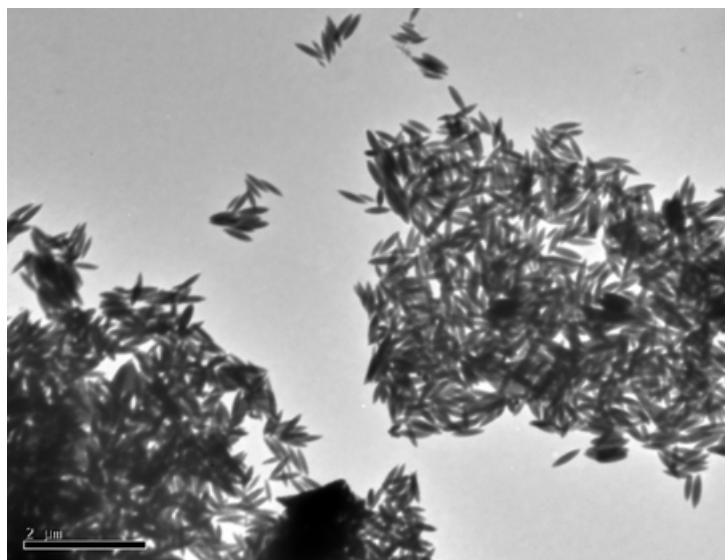
Figure 9.11: TEM image of the aggregates in 100mM KNO$_3$ and at a stirrer speed of 200rpm after 30 minutes without an applied magnetic field.
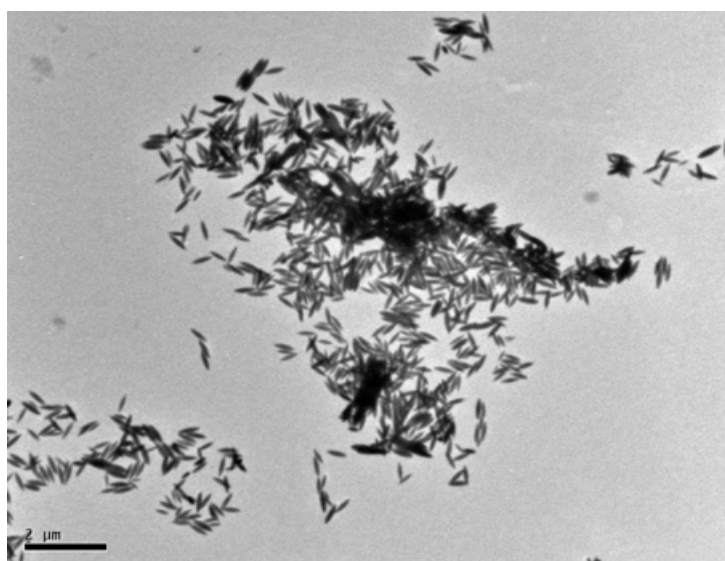
Figure 9.12: TEM image of the aggregates in 100mM KNO$_3$ and at a stirrer speed of 200rpm after 30 minutes with an applied magnetic field.
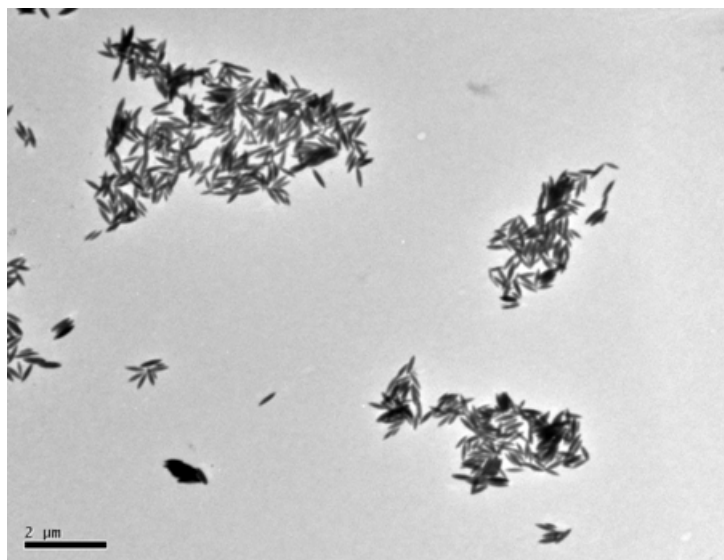
Figure 9.13: TEM image of the aggregates in 100mM KNO$_3$ and at a stirrer speed of 200rpm after 30 minutes with an applied magnetic field.
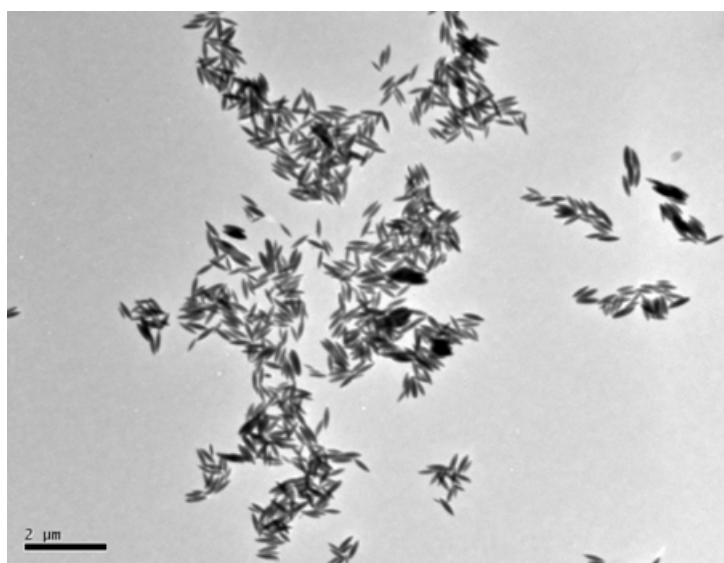
Figure 9.14: TEM image of the aggregates in 100mM KNO$_3$ and at a stirrer speed of 200rpm after 30 minutes with an applied magnetic field.

9.5 Discussion

The particles used were the same as used those used in chapter 6 and so discussion of particle characterisation can be found there.

The ellipsoidal particles exhibit somewhat different behaviour to the spherical particles. The aspects of behaviour associated with increasing the collision frequency through stirring are also evident here. With the addition of electrolyte, large, compact aggregates are formed and evidence of restructuring can be seen in the scattering data (the two slopes that can be seen figure 9.8), indicating the breakage and reformation process also occurs in the aggregation of the ellipsoidal particles.

The effect of the magnetic field is also found to be dependent on the stirrer speed, as was found with the spherical particles. At 200rpm smaller aggregates are formed with the applied magnetic field, which again partly agrees with the findings of Stuyven et al. (2009a,b) as discussed in chapter 8. The balance of the shear forces and the Lorentz forces affect the aggregation more than the particle interactions.

However, without the addition of electrolyte the behaviour of the ellipsoidal particles shows a significant difference. While aggregation is limited far from the isoelectric point at pH 2 and 11, at pH 7 there is a significant amount of aggregation when the suspension is stirred resulting in large compact aggregates. This difference is likely due to the uneven distribution of charge on the particle surface, as discussed in chapter 6. There is no evidence of restructuring in the scattering data, as only one slope is distinguishable, which would tend to indicate that the aggregates grow without being broken up by the stirring. The stirrer speed again plays an important role in the effect of the magnetic field. At 60rpm larger aggregates are formed with the application of the magnetic field, whereas at higher stirrer speeds this effect is not observed.

If the particle interactions were responsible for this increase in aggregate size then it

is likely that it would be observed at all stirrer speeds, as there is no indication that the aggregates are being broken up and undergoing restructuring, which would also imply that the aggregates are more resistant to shear when formed without the addition of electrolyte. Simulations (Mortensen et al., 2008) have indicated the importance of the flow on the alignment of ellipsoidal particles, and the tendency for the particles to line up or fall into a log-rolling state (Gunes et al., 2008). The alignment of the magnetic moment in ellipsoidal particles (Usov et al., 2002) could then induce the formation of larger aggregates.

CHAPTER 10

CONCLUSIONS AND RECOMMENDATIONS

10.1   Conclusions

One way to summarise the aim of this investigation would be as the study of the differences in aggregation behaviour due to the magnetic contribution to the overall particle interaction, specifically focusing on the iron oxide nanoparticles hematite and magnetite (for various reasons which were outlined in the introduction).

The different types of magnetic interaction produce different results. While the particles react to the chemical environment in a comparable manner (pH, electrolyte concentration) the differing magnetic behaviour of the particles leads to very different aggregation behaviour.

Near the isoelectric point more aggregation was observed for both hematite and magnetite particles. However, the aggregation of magnetite nanoparticles resulted in large aggregate structures with scale dependent aggregate densities whereas the hematite particles formed smaller aggregates with none of the nebulous features of the magnetite aggregates.

Externally applying a magnetic field to the hematite particles in these conditions resulted in the separation of the particles from suspension. This separation was also

observed at other pH values, although it took place at a significantly slower rate.

The effect of an externally applied magnetic field on the aggregation of hematite nanoparticles in various conditions was investigated and compared to the aggregation of magnetic magnetite nanoparticles in the same conditions.

The hypothesis that magnetic fields can increase the aggregation of weakly magnetic nanoparticles has been tested using iron oxide nanoparticles and static magnetic fields. The results indicate that such a general hypothesis is inappropriate to describe the behaviour of weakly magnetic nanoparticles in magnetic fields. Conditions were found in which the application of a magnetic field caused changes in the behaviour of the particles, but not those expected from the initial hypothesis and previous theoretical predictions (Svoboda, 1981; Tsouris and Scott, 1995).

In static systems the previously observed slight increases in aggregation observed using dynamic light scattering (Tombacz et al., 1991; Tsouris and Scott, 1995; Kendall and Kosseva, 2006) were not seen at the larger length scale probed by static light scattering. It was found that the magnetic field did not alter the particle interactions sufficiently to alter the aggregation between the particles, but that it was sufficient to overcome the Brownian motion of the particles resulting in their separation from the suspension.

In stirred systems the effect of the magnetic field was found to be dependent on the flow regime. Smaller aggregates were found to form at higher stirrer speeds. However, this effect is not attributed to the changes in the particle interactions but rather to the interaction of the charged particle surfaces and the magnetic field resulting in Lorentz forces. This explanation is put forward in agreement with the investigation by Stuyven et al. (2009a,b) who found similar results for diamagnetic particles. The balance of shear forces and Lorentz forces has a greater effect than the particle interactions on the aggregation. The importance of the flow regime is also highlighted by comparing previous work (Tombacz et al., 1991; Busch et al., 1996; Stuyven et al., 2009a,b) where seemingly

contradictory results are found in different flow regimes.

Thus while the initial hypothesis may be appropriate at smaller scales where small changes are observed, at larger scales this hypothesis is found to be inappropriate to describe the behaviour of the particles. Increasing the particle interactions using a magnetic field was found to be ineffective in altering the aggregation of the particles, and observed effects from the application of a magnetic field were attributed to other causes.

10.2   Recommendations

The practical and financial constraints of this project have allowed only certain issues to be explored within what is an extremely large interdisciplinary area of research extending from magnetic nanoparticles in bacteria to the underlying processes of planetary formation. However, certain questions arise that can be asked and answered with the appropriate experimental apparatus. The study of the aggregation process in fluids at could be achieved with the appropriate dedicated static light scattering setup which could then monitor aggregation as it happens.

An external magnetic field could be applied in this setup through use of an electromagnet which would allow different field strengths to be tested and ideally the effect of alternating fields as well as direct fields.

This setup would allow the evolution of the aggregation to be followed for different particle systems and information such as particle size distribution and aggregate density to be observed and the effect of chemical environment, fluid motion and possibly even temperature to be investigated.

One important factor not investigated in this study was the effect of temperature. It is already known that aggregation and magnetic behaviour are affected by temperature but how these changes affect particle aggregation when magnetic interactions become important (due to the application of an external magnetic field or because the particles

themselves are magnetic) is yet to be researched. All of this information will be useful for helping to understand the behaviour of nanoparticles in the body, in the environment and in industrial setting as well as contributing to more fundamental understanding of the role of a magnetic field in particle interactions at the nanoscale.

The construction of a dedicated experimental setup where both the flow and the magnetic field could be altered could identify conditions in which other types of behaviour are observed. This would most probably be some sort of closed loop using a pump to generate the flow, which could then be well characterised. The type of pump would also have to be carefully chosen to avoid breaking up any aggregates that form in the suspensions flowing in the system.

A setup using an electromagnet capable of generating a magnetic field of different strengths would best serve this purpose. This could then be used to produce both direct current (d.c.) and alternating current (a.c.) fields, as some commercial devices use a.c. fields claiming that this helps with the claimed benefits.

Ideally, an in-line static light scattering system could be used to monitor the aggregation and (virtually) real-time measurements. Sampling points should also be included so that samples can be taken for measuring using dynamic light scattering and also TEM. This would enable the detection of changes at the length scale not easily accessible using static light scattering.

This experimental setup could then be used to test many different types of suspensions. Of interest would be particles of differing magnetic properties including mixtures of these particles, particles with altered surfaces for stability or for functional reasons, and also non-aqueous suspensions which could provide a greater understating the role of the particle interactions in such a process.

Further understanding of the underlying processes could be garnered from computer simulations of the aggregation process. One suggestion would be a molecular dynamics

simulation that would include the particle interactions, the magnetic field and could also provide detailed information about aggregate structure by tracking the linked particles in the simulation. Graph theory (in the mathematical sense, often used in networking theories) could then provide a way of processing this detailed structural data of the aggregates, providing both size distributions and three dimensional images of aggregates.

LIST OF REFERENCES

Formation mechanism of monodisperse peanut-type -fe2o3 particles from condensed ferric hydroxide gel. *Colloids and Surfaces A: Physicochemical and Engineering Aspects*, 79 (2-3):233 – 247, 1993.

H. Ai, C. Flask, B. Weinberg, X.-T. Shuai, M. Pagel, D. Farrell, J. Duerk, and J. Gao. Magnetite-loaded polymeric micelles as ultrasensitive magnetic-resonance probes. *Advanced Materials*, 17(16):1949–1952, 2005.

C. Alexiou, W. Arnold, R. J. Klein, F. G. Parak, P. Hulin, C. Bergemann, W. Erhardt, S. Wagenpfeil, and A. S. Lubbe. Locoregional cancer treatment with magnetic drug targeting. *Cancer Research*, 60(23):6641–6648, 2000.

C. Alexiou, R. Jurgons, R. Schmid, A. Hilpert, C. Bergemann, F. Parak, and H. Iro. In vitro and in vivo investigations of targeted chemotherapy with magnetic nanoparticles. *Journal of Magnetism and Magnetic Materials*, 293(1):389–393, 2005.

R. Amal, J. A. Raper, and T. D. Waite. Fractal structure of hematite aggregates. *Journal of Colloid and Interface Science*, 140(1):158 – 168, 1990.

R. Amal, D. Gazeau, and T. Waite. Small-angle x-ray scattering of hematite aggregates. *Particle & Particle Systems Characterisation*, 11(4):315–319, 1994.

Y. Amemiya, A. Arakaki, S. S. Staniland, T. Tanaka, and T. Matsunaga. Controlled formation of magnetite crystal by partial oxidation of ferrous hydroxide in the presence of recombinant magnetotactic bacterial protein Mms6. *Biomaterials*, 28(35):5381–5389, DEC 2007.

S. Asano and G. Yamamoto. Light-scattering by a spheroidal particle. *Applied Optics*, 14 (1):29–49, 1975.

I. Avital, D. Inderbitzin, T. Aoki, D. B. Tyan, A. H. Cohen, C. Ferraresso, J. Rozga, W. S. Arnaout, and A. A. Demetriou. Isolation, characterization, and transplantation of bone marrow-derived hepatocyte stem cells. *Biochemical and Biophysical Research Communications*, 288(1):156 – 164, 2001.

M. Axelos, D. Tchoubar, and R. Jullien. X-ray scattering functions of fractal structures - comparison between simulations and experiments. *Journal de Physique*, 47(10):1843–1847, 1986.

L. Babes, B. Denizot, G. Tanguy, J. J. L. Jeune, and P. Jallet. Synthesis of iron oxide nanoparticles used as mri contrast agents: A parametric study. *Journal of Colloid and Interface Science*, 212(2):474 – 482, 1999.

J. Bandara, U. Klehm, and J. Kiwi. Raschig rings-fe2o3 composite photocatalyst activate in the degradation of 4-chlorophenol and orange ii under daylight irradiation. *Applied Catalysis B: Environmental*, 76(1-2):73 – 81, 2007.

J. Bang and L. Murr. Atmospheric nanoparticles: Preliminary studies and potential respiratory health risks for emerging nanotechnologies. *Journal of Materials Science and Letters*, 21:361366, 2002.

D. Barber and I. Freestone. An investigation of the origin of the color of the Lycurgus cup by analytical transmission electron-microscopy. *Archaeometry*, 32(Part 1):33–45, 1990.

A. Barkatt, A. L. Pulvirenti, M. Adel-Hadadi, C. Viragh, F. E. Senftle, A. N. Thorpe, and J. R. Grant. Composition and particle size of superparamagnetic corrosion products in tap water. *Water Research*, 43(13):3319 – 3325, 2009.

L. Becker, B. Popp, T. Rust, and J. Bada. The origin of organic matter in the Martian meteorite ALH84001. *Earth and Planetary Science Letters*, 167(1-2):71–79, MAR 30 1999.

B. Berne and R. Pecora. *Dynamic light scattering: with applications to chemistry, biology and physics*. Wiley-Interscience, London, 1976.

M. A. Bernstein, M. Hanson, D. Knopman, and M. Toman. An approach to assessing the technical feasibility and market potential of a new automotive device. Technical report, RAND Corporation, Santa Monica, California, 2007.

D. Bica, L. Vks, M. V. Avdeev, O. Marinica, V. Socoliuc, M. Balasoiu, and V. M. Garamus. Sterically stabilized water based magnetic fluids: Synthesis, structure and properties. *Journal of Magnetism and Magnetic Materials*, 311(1):17 – 21, 2007.

E. Blums, A. Cebers, and M. Maiorov. *Magnetic Fluids*. Walter de Gruyter, New York, 1997.

C. Bohren and D. Hufman. Absorption cross-section maxima and minima in IR absorption-bands of small ionic ellipsoidal particles. *Applied Optics*, 20(6):959–962, 1981.

B. Bonnemain. Superparamagnetic agents in magnetic resonance imaging: Physicochemical characteristics and clinical applications - A review. *Journal of Drug Targeting*, 6 (3):167–174, 1998.

P. Bradford. The effects of magnetic fields on nanoparticles in fluids. Master's thesis, University of Birmingham, January 2007.

J. Bradley, R. Harvey, and H. McSween. No 'nanofossils' in Martian meteorite. *Nature*, 390(6659):454, DEC 4 1997.

M. Brebu, M. A. Uddin, A. Muto, Y. Sakata, and C. Vasile. Catalytic degradation of AcrylonitrileButadieneStyrene into fuel oil 1. the effect of iron oxides on the distribution of Nitrogen-Containing compounds. *Energy & Fuels*, 15(3):559–564, 2001.

I. Brigger, C. Dubernet, and P. Couvreur. Nanoparticles in cancer therapy and diagnosis. *Advanced Drug Delivery Reviews*, 54(5):631 – 651, 2002.

S. Broersma. Rotational diffusion constant of a cylindrical particle. *The Journal of Chemical Physics*, 32(6):1626–1631, 1960a.

S. Broersma. Viscous force constant for a closed cylinder. *The Journal of Chemical Physics*, 32(6):1632–1635, 1960b.

R. Brown. A brief account of microscopical observations made on the particles contained in the pollen of plants. *London and Edinburgh Philosophical Magazine and Journal of Science*, 4:161–173, 1828.

E. Brunet, G. Degr, F. Okkels, and P. Tabeling. Aggregation of paramagnetic particles in the presence of a hydrodynamic shear. *Journal of Colloid and Interface Science*, 282 (1):58 – 68, 2005.

R. Brunner, S. Gall, W. Wilke, and M. Zrinyi. Formation of fractal structures by aggregation of anisometric iron (iii) hydroxide particles. *Physica A: Statistical and Theoretical Physics*, 214(2):153 – 161, 1995.

K. W. Busch, S. Gopalakrishnan, M. A. Busch, and E. Tombcz. Magnetohydrodynamic aggregation of cholesterol and polystyrene latex suspensions. *Journal of Colloid and Interface Science*, 183(2):528 – 538, 1996.

G. Bushell and R. Amal. Fractal aggregates of polydisperse particles. *Journal of Colloid and Interface Science*, 205(2):459 – 469, 1998.

J. Cai, N. Lu, and C. Sorensen. Comparison of size and morphology of soot aggregates as determined by light-scattering and electron-microscope analysis. *Langmuir*, 9(11): 2861–2867, 1993.

C. Cametti, P. Codastefano, and P. Tartaglia. Light-scattering measurements of slow aggregation in colloids - deviations from asymptotic time scaling. *Physical Review A*, 36(10):4916–4921, 1987.

C. Cametti, P. Codastefano, and P. Tartaglia. Aggregation kinetics in model colloidal systems - a light-scattering study. *Journal of Colloid and Interface Science*, 131(2): 409–422, 1989.

H. Cao, G. Wang, L. Zhang, Y. Liang, S. Zhang, and X. Zhang. Shape and magnetic properties of single-crystalline hematite (alpha-fe2o3) nanocrystals. *ChemPhysChem*, 7 (9):1897 – 1901, 2006.

D. Chan, D. Henderson, J. Barojas, and A. Homola. Thestability of a colloidal suspension of coated magetic particles in an aqueous solution. *IBM Journal of Research and Development*, 29(1):11–17, 1985.

P. Chechel and G. Annenkov. Influence of magnetic treatment on solubility of calcium sulphate. *Coke & Chemistry USSR*, (8):60–61, 1972.

C.-J. Chin, S. Yiacoumi, and C. Tsouris. Shear-induced flocculation of colloidal particles in stirred tanks. *Journal of Colloid and Interface Science*, 206(2):532 – 545, 1998.

P. W. Cleary. The effect of particle shape on simple shear flows. *Powder Technology*, 179 (3):144 – 163, 2008.

R. Cornell and U. Schwertmann. *The Iron Oxides: Structure, Properties, Reactions, Occurrence and Uses.* VCH Verlagsgesellschaft Weinheim, 1996.

L. Cumbal, J. Greenleaf, D. Leun, and A. K. SenGupta. Polymer supported inorganic nanoparticles: characterization and environmental applications. *Reactive and Functional Polymers*, 54(1-3):167 – 180, 2003.

B. Dahneke. *Measurement of Suspended Particles by Quasi-elastic Light Scattering.* Wiley, 1983.

P. de Gennes and P. Pincus. Pair correlations in a magnetic fluid. *Physik der Kondensiterten Materie*, 11(3):189–198, 1970.

P. Debye. *Polar Molecules.* Chemical Catalog Co., NY, reprinted by Dover, New York, 1929.

B. Derjaguin and L. Landau. Theory of Stability of Highly Charged Liophobic Sols and Adhesion of Highly Charged Particles in Solutions of Electrolytes. *Zhurnal Eksperimentalnoi I Teoreticheskoi Fiziki*, 15(11):663–682, 1945.

B. Devouard, M. Posfai, X. Hua, D. Bazylinski, R. Frankel, and P. Buseck. Magnetite from magnetotactic bacteria: Size distributions and twinning. *American Mineralogist*, 83(11-12, Part 2):1387–1398, 1998.

J. Donaldson and S. Grimes. Lifting the scales from our pipes. *New Scientist*, 117(1600): 43–46, 1988.

D. Dunlop and B. Schmidt. Biomagnetism i. anomalous development of the root of the narcissus tazetta. *Phytomorphology*, 14:333–342, 1964.

D. Dunlop and B. Schmidt. Biomagnetism ii. anomalies found in the root of allium cepa. *Phytomorphology*, 15:400–412, 1965.

A. Einstein. Die von der molekularkinetischen theorie der wärme geforderte bewegung von in ruhenden flüssigkeiten suspendierten teilchen. *Annalen der Physik*, 17:549–560, 1905.

D. Faivre and P. Zuddas. An integrated approach for determining the origin of magnetite nanoparticles. *Earth and Planetary Science Letters*, 243(1-2):53–60, 2006.

M. Faraday. The bakerian lecture: Experimental relations of gold (and other metals) to light. *Philosophical Transactions of the Royal Society London*, 147:145 – 181, 1857.

Federal Trade Commission, Press Release. Bogus fuel-saving device sellers settle ftc charges. `http://www.ftc.gov/opa/2005/05/fuel.shtm`, 2005. FTC File No. X05 0002.

R. Feynman. There's plenty of room at the bottom. *Engineering and Science*, XXIII(5), 1960.

L. Finegold and B. L. Flamm. Magnet therapy. *BMJ*, 332(7532):4, 2006.

P. B. Fitzgerald, S. Fountain, and Z. J. Daskalakis. A comprehensive review of the effects of rtms on motor cortical excitability and inhibition. *Clinical Neurophysiology*, 117(12): 2584 – 2596, 2006.

M. Foret, J. Pelous, R. Vacher, and J. Maignan. An investigation of the structure of colloidal aerogels. *Journal of Non-Crystalline Solids*, 147:382–385, 1992.

D. Fortin, F. Ferris, and T. Beveridge. Surface-mediated mineral development by bacteria. *Geomicrobiology: interactions between microbes and minerals*, 35:161–180, 1997. Short Course on Geomicrobiology, ALTA, UT, OCT 18-19, 1997.

X. Gao, K. M. K. Yu, K. Y. Tam, and S. C. Tsang. Colloidal stable silica encapsulated nano-magnetic composite as a novel bio-catalyst carrier. *Chemical Communications*, 24:2998–2999, 2003.

H. A. Garcia-Martinez, M. Llamas-Bueno, S. Song, and A. Lopez-Valdivieso. Magnetic flocculation of mineral fines in an external magnetic field. *Mineral Processing and Extractive Metallurgy Review*, 25(2):67 – 90, 2004.

G. Gerardi, A. De Ninno, M. Prosdocimi, V. Ferrari, F. Barbaro, S. Mazzariol, D. Bernardini, and G. Talpo. Effects of electromagnetic fields of low frequency and low intensity on rat metabolism. *BioMagnetic Research and Technology*, 6(1):3, 2008.

R. Gerber and R. R. Birss. *High Gradient Magnetic Separation.* John Wiley & Sons, Chichester, 1983.

S. A. Gómez-Lopera, R. C. Plaza, and A. V. Delgado. Synthesis and characterization of spherical magnetite/biodegradable polymer composite particles. *Journal of Colloid and Interface Science*, 240(1):40 – 47, 2001.

S. Goodwin, C. Peterson, C. Hoh, and C. Bittner. Targeting and retention of magnetic targeted carriers (mtcs) enhancing intra-arterial chemotherapy. *Journal of Magnetism and Magnetic Materials*, 194(1-3):132–139, 1999.

G. Goya, T. Berquo, and F. Fonseca. Static and dynamic magnetic properties of spherical magnetite nanoparticles. *Journal of Applied Physics*, 94:3520 3528, 2003.

E. Gregorova, W. Pabst, and J.-B. Bouchet. Influence of particle shape on the viscosity of kaolin suspensions. *Acta Geodynamica et Geomaterialia*, 6(1):101–109, 2009.

C. Grttner and J. Teller. New types of silica-fortified magnetic nanoparticles as tools for molecular biology applications. *Journal of Magnetism and Magnetic Materials*, 194 (1-3):8 – 15, 1999.

R. Gueta. *Characterization of Aragonite in Mollusk Shells.* Weizmann Institute of Science, 2003.

D. Gunes, R. Scirocco, J. Mewis, and J. Vermant. Flow-induced orientation of non-spherical particles: Effect of aspect ratio and medium rheology. *Journal of Non-Newtonian Fluid Mechanics*, 155(1-2):39 – 50, 2008.

C. Gunther. *Electro-magnetic ore separation.* Hill Publishing Company, New York, 1909.

E. M. Haacke, R. F. Brown, M. Thompson, and R. Venkatesan. *Magnetic resonance imaging: Physical principles and sequence design.* J. Wiley & Sons, New York, 1999.

S. Hamada and E. Matijevic. Fomration of monodispereds colloidal cubic hematite particles in ethanol + water solutions. *Journal of the Chemical Society - Faraday Transactions I*, 78(Part 7):2147–&, 1982.

M. Hanzlik, C. Heunemann, E. Holtkamp-Rotzler, M. Winklhofer, N. Petersen, and G. Fleissner. Superparamagnetic magnetite in the upper beak tissue of homing pigeons. *Biometals*, 13(4):325–331, 2000.

Y. Hashimoto, M. Kawasumi, and M. Saito. Effect of static magnetic field on cell migration. *Electrical Engineering in Japan*, 160(2):46–52, 2007.

Y. T. He, J. Wan, and T. Tokunaga. Kinetic stability of hematite nanoparticles: the effect of particle sizes. *Journal of Nanoparticle Research*, 10(2):321 – 332, 2007.

M. Hermawan, G. Bushell, G. Bickert, and R. Amal. Characterisation of short-range structure of silica aggregates–implication to sediment compaction. *International Journal of Mineral Processing*, 73(2-4):65 – 81, 2004.

M. Hermawan, G. Bushell, G. Bickert, and R. Amal. Relationship between floc short range structure and sediment compaction. *Particle & Particle Systems Characterization*, 20 (5):327–334, 2003.

R. Herzog, Q. Shi, J. Patil, and J. Katz. Magnetic Water Treatment - The Effect of Iron on Calcium Carbonate Nucleation and Growth. *Langmuir*, 5(3):861–867, 1989.

T. Hill. Thermodynamics of small systems. *Journal of Chemical Physics*, 36(12):3182 – 3197, 1962.

T. Hill. A different approach to nanothermodynamics. *Nano Letters*, 1(5):273–275, 2001.

T. Hill and R. Chamberlin. Fluctuations in energy in completely open small systems. *Nano Letters*, 2(6):609–613, 2002.

C. C. Ho and R. H. Ottewill. Investigation of the charge distribution of ellipsoidal particles. *Colloids and Surfaces A: Physicochemical and Engineering Aspects*, 141(1):29 – 35, 1998.

R. Hogg, T. Healy, and D. Fuersten. Mutual coagulation of colloidal dispersions. *Transactions of the Faraday Society*, 62(522P):1638–1651, 1966.

C. Holm and J.-J. Weis. The structure of ferrofluids: A status report. *Current Opinion in Colloid & Interface Science*, 10(3-4):133 – 140, 2005.

G. L. Hornyak, J. Dutta, H. F. Tibbals, and A. K. Rao. *Introduction to Nanoscience*. Taylor & Francis, Boca Raton, 2008.

G. J. Hutchings, M. S. Hall, A. F. Carley, P. Landon, B. E. Solsona, C. J. Kiely, A. Herzing, M. Makkee, J. A. Moulijn, A. Overweg, J. C. Fierro-Gonzalez, J. Guzman, and B. C. Gates. Role of gold cations in the oxidation of carbon monoxide catalyzed by iron oxide-supported gold. *Journal of Catalysis*, 242(1):71 – 81, 2006.

E. Illes and E. Tombacz. The effect of humic acid adsorption on ph-dependent surface charging and aggregation of magnetite nanoparticles. *Journal of Colloid and Interface Science*, 295(1):115 – 123, 2006.

J. Israelachvili. *Intermolecular & Surface Forces*. Elsevier Academic Press, London, 1991.

A. Ito, M. Shinkai, H. Honda, and T. Kobayashi. Medical application of functionalized magnetic nanoparticles. *Journal of Bioscience and Bioengineering*, 100(1):1 – 11, 2005.

Z. Jing and S. Wu. Preparation and magnetic properties of spherical alpha-Fe2O3 nanoparticles via a non-aqueous medium. *Materials Chemistry and Physics*, 92(2-3): 600–603, 2005.

C. J. Johnson and D. Gabriel. *Laser Light Scattering.* Dover Publications, Inc., New York, 1981.

J. D. Jorgenson. U.s. geological survey minerals yearbook 2006: Iron ore. Technical report, U.S. Geological Survey, U.S. Department of the Interior, 2008.

T. L. Jrgensen, H. Livbjerg, and P. Glarborg. Homogeneous and heterogeneously catalyzed oxidation of so2. *Chemical Engineering Science*, 62(16):4496 – 4499, 2007.

R. Jullien and P. Meakin. Simple-Models for the restructuring of 3-dimensional ballistic aggregates. *Journal of Colloid and Interface Science*, 127(1):265–272, 1989.

S. Jung, R. Amal, and J. Raper. The use of small angle light scattering to study structure of flocs. *Particle & Particle Systems Characterization*, 12(6):274–278, 1995.

S. J. Jung, R. Amal, and J. A. Raper. Monitoring effects of shearing on floc structure using small-angle light scattering. *Powder Technology*, 88(1):51 – 54, 1996. Research of Powder Technology in Australia.

N. Kallay and S. Žalac. Stability of nanodispersions: A model for kinetics of aggregation of nanoparticles. *Journal of Colloid and Interface Science*, 253(1):70 – 76, 2002.

A. K. Kandalam, B. Chatterjee, S. Khanna, B. Rao, P. Jena, and B. Reddy. Oxidation of co on fe_2o_3 model surfaces. *Surface Science*, 601(21):4873 – 4880, 2007.

K. Kendall and M. R. Kosseva. Nanoparticle aggregation influenced by magnetic fields. *Colloids and Surfaces A:Phyiscochemical and Engineering Aspects*, 286(1-3):112–116, 2006.

K. Kendall, R. Amal, X. Jiang, and A. Yu. Effect of adhesion on aggregation in nanoparticle dispersions. *Journal of Adhesion*, 83(6):573–585, 2007.

S. Khalafalla and G. Reimers. Preparation of dilution-stable aqueous magnetic fluids. *IEEE Transactions on Magnetics*, 16(2):178–183, 1980.

D. K. Kim, M. Mikhaylova, F. H. Wang, J. Kehr, B. Bjelke, Y. Zhang, T. Tsakalakos, and M. Muhammed. Starch-Coated superparamagnetic nanoparticles as MR contrast agents. *Chemistry of Materials*, 15(23):4343–4351, 2003.

H. Kim, M. Seo, and J. Song. Effect of particle size and mass on nano to micron particle agglomeration. In *SICE 2004 Annual Conference*, volume 3, pages 1923–1926 vol. 3, Aug. 2004.

J. Kirschvink. Magnetite Biomineralization and geomagnetic sensitivity in higher animals - an update and recommendations for future study. *Bioelectromagnetics*, 10(3):239–259, 1989.

J. Kirschvink, D. Jones, and B. MacFadden. *Magnetite Biomineralization and Magnetoreception in Organisms - A New Biomagnetism.* Plenum Press, New York, 1985.

J. Kirschvink, A. Kobayashi-Kirschvink, and B. Woodfrod. Magnetite biomineralization in the himan brainN. *Proceedings of the National Academy of Sciences of the United States of America*, 89(16):7683–7687, 1992.

J. Kirschvink, A. Maine, and H. Vali. Paleomagnetic evidence of a low-temperature origin of carbonate in the Martian meteorite ALH84001. *Science*, 275(5306):1629–1633, 1997.

J. Kjems, T. Freltoft, D. Richter, and S. Sinha. Neutron-scattering from fractals. *Physica B & C*, 136(1-3):285–290, 1986.

M. Kosmulski. The ph-dependent surface charging and the points of zero charge. *Journal of Colloid and Interface Science*, 253(1):77 – 87, 2002.

M. Kosmulski. ph-dependent surface charging and points of zero charge ii. update. *Journal of Colloid and Interface Science*, 275(1):214 – 224, 2004.

M. Kosmulski. ph-dependent surface charging and points of zero charge: Iii. update. *Journal of Colloid and Interface Science*, 298(2):730 – 741, 2006.

A. P. Kozlova, S. Sugiyama, A. I. Kozlov, K. Asakura, and Y. Iwasawa. Iron-oxide supported gold catalysts derived from gold-phosphine complex au(pph3)(no3): State and structure of the support. *Journal of Catalysis*, 176(2):426 – 438, 1998.

K. Kronenberg. Experimental evidence for effects of magnetic fields on moving water. *IEEE Transactions on Magnetics*, 21(5):2059–2061, 1985.

U. T. Lam, R. Mammucari, K. Suzuki, and N. R. Foster. Processing of iron oxide nanoparticles by supercritical fluids. *Industrial & Engineering Chemistry Research*, 47(3):599–614, 2008.

S. Laurent, S. Dutz, U. O. Hafeli, and M. Mahmoudi. Magnetic fluid hyperthermia: Focus on superparamagnetic iron oxide nanoparticles. *Advances in Colloid and Interface Science*, 166(1-2):8–23, 2011.

C. Li, Y. Shen, M. Jia, S. Sheng, M. O. Adebajo, and H. Zhu. Catalytic combustion of formaldehyde on gold/iron-oxide catalysts. *Catalysis Communications*, 9(3):355 – 361, 2008.

J. Li, Y. Pan, Q. Liu, K. Yu-Zhang, N. Menguy, R. Che, H. Qin, W. Lin, W. Wu, N. Petersen, and X. Yang. Biomineralization, crystallography and magnetic properties of bullet-shaped magnetite magnetosomes in giant rod magnetotactic bacteria. *Earth and Planetary Science Letters*, 293(34):368 – 376, 2010.

V. Liburkin, B. Kondratev, and T. Pavlyukova. Action of magnetic treatment of water on the structure formation of gypsum. *Glass and Ceramics (English Translation of Steklo I Keramika)*, 43(3-4):116–119, 1986.

M. Lin, H. Lindsay, D. Weitz, R. Ball, R. Klein, and P. Meakin. Universality of fractal aggregates as probed by light-scattering. *Proceedings Royal Society London Series A-Mathematical Phys. Eng. Sci. Physical and Engineering Sciences*, 423(1864):71–87, 1989.

F. London. Some characteristics and uses of molecular force. *Zeitschrift Fur Physikalische Chemie-Abteilung B-Chemie Der Elementarprozesse Aufbau Der Materie*, 11(2/3):222–251, 1930.

Magnetic Materials Group, University of Birmingham. Magnetic materials. `http://www.magnets.bham.ac.uk/magneticmaterials/index.shtml`.

P. Majewski and B. Thierry. Functionalized Magnetite NanoparticlesSynthesis, Properties, and Bio-Applications. *Critical Reviews in Solid State and Materials Sciences*, 32 (3):1040–8436, 2007.

B. Mandelbrot. *Les objets fractals, forme, hasard et dimension*. Flammarion, Paris, 1975.

S. Mann, J. Webb, , and R. Williams. *Biomineralization - Chemical and Biochemical Perspectives*. VCH Publishers, Weinheim, 1989.

F. Martinez-Pedrero, M. Tirado-Miranda, A. Schmitt, and J. Callejas-Fernandez. Aggregation of magnetic polystyrene particles: A light scattering study. *Colloids and Surfaces A: Physicochemical and Engineering Aspects*, 270-271:317–322, 2005.

O. Martynova, E. Tebenekhin, and B. Gusev. Conditions and mechanism of deposition of the solid calcium carbonate phase from aqeuous solutions under the influence of a magnetic field. *Colloid J. USSR*, 29:512–514, 1967.

E. Matijevic and R. Partch. *Fine Particles: Synthesis, Characterization and Mechanisms of Growth*, chapter 1.5 Metal Oxides: Synthesis of Monodispersed Colloids by Chemical Reactions in Aerosols, pages 97–113. Marcel Dekker, 2000.

E. Matijevic and R. Sapieszko. *Fine Particles: Synthesis, Characterization and Mechanisms of Growth*, chapter 1.1 Metal Oxides: Forced Hydrolysis in Homogeneous Solutions, pages 2–34. Marcel Dekker, 2000.

E. Matijevic and P. Scheiner. Ferric hydrous oxide sols: Iii. preparation of uniform particles by hydrolysis of fe(iii)-chloride, -nitrate, and -perchlorate solutions. *Journal of Colloid and Interface Science*, 63(3):509 – 524, 1978.

R. M. Mazo. *Brownian motion : fluctuations, dynamics and applications.* Oxford University Press, Oxford, UK, 2002.

D. McKay, E. Gibson, K. ThomasKeprta, H. Vali, C. Romanek, S. Clemett, X. Chillier, C. Maechling, and R. Zare. Search for past life on Mars: Possible relic biogenic activity in Martian meteorite ALH84001. *Science*, 273(5277):924–930, 1996.

P. Meakin. Diffusion-controlled flocculation - the effects of attractive and repulsive interactions. *Journal of Chemical Physics*, 79(5):2426–2429, 1983.

P. Meakin. Models for colloidal aggregation. *Annual Review of Physical Chemistry*, 39: 237–267, 1988.

P. Meakin. A historical introduction to computer models for fractal aggregates. *Journal of Sol-Gel Science and Technology*, 15(2):97 – 117, 1999.

D. Melville, F. Paul, and S. Roath. Direct magnetic separation of red-cells from whole-blood. *Nature*, 255(5511):706–706, 1975.

V. Mendelev and A. Ivanov. Magnetic properties of ferrofluids: an influence of chain aggregates. *Journal of Magnetism and Magnetic Materials*, 289:211 – 214, 2005. Proceedings of the 10th International Conference on Magnetic Fluids.

G. Mie. Articles on the optical characteristics of turbid tubes, especially colloidal metal solutions. *Annalen der Physik*, 25(3):377–445, 1908.

A. Mohraz and M. J. Solomon. Gelation and internal dynamics of colloidal rod aggregates. *Journal of Colloid and Interface Science*, 300(1):155 – 162, 2006.

A. Mohraz, D. B. Moler, R. M. Ziff, and M. J. Solomon. Effect of monomer geometry on the fractal structure of colloidal rod aggregates. *Physical Review Letters*, 92(15): 155503, 2004.

J. Moonen, C. Pathmamanoharan, and A. Vrij. Small-angle x-ray scattering of silica dispersions at low particle concentrations. *Journal of Colloid and Interface Science*, 131(2):349–365, 1989.

P. Mortensen, H. Andersson, J. Gillissen, and B. Boersma. On the orientation of ellipsoidal particles in a turbulent shear flow. *International Journal of Multiphase Flow*, 34(7):678 – 683, 2008.

M. Oda. *Fine Particles: Synthesis, Characterization and Mechanisms of Growth*, chapter 1.6 Metal Oxides: Reaction in Gas Phases, pages 114–124. Marcel Dekker, 2000.

S. Odenbach. *Ferrofluids: Magnetically Controlled Fluids and their Applications*. Springer, Berlin, 2002.

S. Odenbach. Ferrofluids–magnetically controlled suspensions. *Colloids and Surfaces A: Physicochemical and Engineering Aspects*, 217(1-3):171 – 178, 2003.

C. D. O'Dowd, M. C. Facchini, F. Cavalli, D. Ceburnis, M. Mircea, S. Decesari, S. Fuzzi, Y. J. Yoon, and J.-P. Putaud. Biogenically driven organic contribution to marine aerosol. *Nature*, 431(7009):676 – 680, 2004.

M. Ozaki, S. Kratohvil, and E. Matijevic. Formation of monodispersed spindle-type hematite particles. *Journal of Colloid and Interface Science*, 102(1):146 – 151, 1984.

M. Ozaki, H. Suzuki, K. Takahashi, and E. Matijevic. Reversible ordered agglomeration of hematite particles due to weak magnetic interactions. *Journal of Colloid and Interface Science*, 113(1):76 – 80, 1986.

M. Ozaki, T. Egami, N. Sugiyama, and E. Matijevic. Agglomeration in colloidal hematite dispersions due to weak magnetic interactions : Ii. the effects of particle size and shape. *Journal of Colloid and Interface Science*, 126(1):212 – 219, 1988.

S. C. Pang, S. F. Chin, and M. A. Anderson. Redox equilibria of iron oxides in aqueous-based magnetite dispersions: Effect of ph and redox potential. *Journal of Colloid and Interface Science*, 311(1):94 – 101, 2007.

M. Parker. Physics of magnetic separation. *Contemporary Physics*, 18(3):3520 3528, 1977.

E. Paul, V. Atiemo-Obeng, and S. Kresta. *Handbook of Industrial Mixing*. John Wiley & Sons, Inc., New Jersey, 2004.

O. Perales-Perez, Y. Umetsu, and H. Sasaki. Electrokinetic characteristics of magnetite produced at ambient temperatures. *Shigen to Sozai*, 116(4):297 – 301, 2000.

J. Perrin. Mouvement brownien et réalité moléculaire. *Annales de chimie et de physique*, 8(18):1–114, 1909.

J. Perrin. *Les Atomes*. Felix Alcan, Paris, 1913.

N. Petersen, T. von Dobeneck, and H. Vali. Fossil bacterial magnetite in deep sea sediments form the south atlantic ocean. *Nature*, 320(6063):611–615, 1986.

M. L. Peterson, G. E. Brown, Jr., G. A. Parks, and C. L. Stein. Differential redox and sorption of cr (iii/vi) on natural silicate and oxide minerals: Exafs and xanes results. *Geochimica et Cosmochimica Acta*, 61(16):3399 – 3412, 1997.

A. P. Philipse and A. M. Wierenga. On the density and structure formation in gels and clusters of colloidal rods and fibers. *Langmuir*, 14(1):49–54, 1998.

L. M. Pop and S. Odenbach. Investigation of the microscopic reason for the magnetoviscous effect in ferrofluids studied by small angle neutron scattering. *Journal of Physics: Condensed Matter*, 18(38):S2785–S2802, 2006.

L. M. Pop, S. Odenbach, A. Wiedenmann, N. Matoussevitch, and H. Bnnemann. Microstructure and rheology of ferrofluids. *Journal of Magnetism and Magnetic Materials*, 289:303 – 306, 2005.

M. Powell. Magnetic fuel and water treatment: myth, magic or mainstream science. *Skeptical Inquirer*, 22(1):27 – 31, 1998.

D. Rancourt. Magnetism of earth, planetary, and environmental nanomaterials. In J. Banfield and A. Navrotsky, editors, *Nanoparticles and the Environment.* Mineralogical Society of America, 2001.

A. E. Regazzoni, M. A. Blesa, and A. J. G. Maroto. Interfacial properties of zirconium dioxide and magnetite in water. *Journal of Colloid and Interface Science*, 91(2):560 – 570, 1983.

A. Roch, R. Muller, and P. Gillis. Theory of proton relaxation induced by superparamagnetic particles. *Journal of Chemical Physics*, 110(11):5403–5411, 1999.

S. Rolli, H. Briesen, and K. Sundmacher. Discrete bivariate population balance modelling of heteroaggregation processes. *Journal of Colloid and Interface Science*, 336(2):551 – 564, 2009.

J. Rowlinson. Faraday Lecture. The molecular theory of small systems. *Chemical Society Reviews*, 12(3):251 – 265, 1983.

N. Sadeghiani, L. Barbosa, M. Guedes, S. Chaves, J. Santos, O. Silva, F. Pelegrini, R. Azevedo, P. Morais, and Z. Lacava. Magnetic resonance of polyaspartic acid-coated magnetite nanoparticles administered in mice. *Magnetics, IEEE Transactions on*, 2005.

I. Safarik and M. Safarikova. Use of magnetic techniques for the isolation of cells. *Journal of Chromatography B*, 722(1-2):33–53, 1999.

I. Safarik and M. Safarikova. Magnetic techniques for the isolation and purification of proteins and peptides. *BioMagnetic Research and Technology*, 2(1):7, 2004.

A. Satoh, R. W. Chantrell, S.-I. Kamiyama, and G. N. Coverdale. Three dimensional monte carlo simulations of thick chainlike clusters composed of ferromagnetic fine particles. *Journal of Colloid and Interface Science*, 181(2):422 – 428, 1996.

A. Satoh, R. W. Chantrell, and G. N. Coverdale. Brownian dynamics simulations of ferromagnetic colloidal dispersions in a simple shear flow. *Journal of Colloid and Interface Science*, 209(1):44 – 59, 1999.

216

A. Satoh, G. N. Coverdale, and R. W. Chantrell. Stokesian dynamics simulations of ferromagnetic colloidal dispersions subjected to a sinusoidal shear flow. *Journal of Colloid and Interface Science*, 231(2):238 – 246, 2000.

Science, Research and Statistics, Home Office. Biological effects of electromagnetic fields. `http://scienceandresearch.homeoffice.gov.uk/animal-research/publications-and-reference/001-abstracts/abstractsfrom2009/07abstractsfromjuly2009/288-09a8cf.html?view=Html`.

C. Selomulya, R. Amal, G. Bushell, and T. D. Waite. Evidence of shear rate dependence on restructuring and breakup of latex aggregates. *Journal of Colloid and Interface Science*, 236(1):67 – 77, 2001.

C. Selomulya, G. Bushell, R. Amal, and T. D. Waite. Understanding the role of restructuring in flocculation: The application of a population balance model. *Chemical Engineering Science*, 58(2):327 – 338, 2003.

C. Selomulya, G. Bushell, R. Amal, and T. D. Waite. Aggregate properties in relation to aggregation conditions under various applied shear environments. *International Journal of Mineral Processing*, 73(2-4):295 – 307, 2004. Solid Liquid Separation Systems.

F. E. Senftle, A. N. Thorpe, J. R. Grant, and A. Barkatt. Superparamagnetic nanoparticles in tap water. *Water Research*, 41(13):3005 – 3011, 2007.

D. Shaw. *Introduction to Colloid & Surface Chemistry*. Butterworth-Heinemann, Oxford, 1992.

R. R. Shearer. *The Flatland Hypothesis: Geometric structures of Artistic and Scientific Revolutions*. Springer-Verlag, 1997.

L. Shen, A. Stachowiak, S.-E. K. Fateen, P. E. Laibinis, and T. A. Hatton. Structure of alkanoic acid stabilized magnetic fluids. a small-angle neutron and light scattering analysis. *Langmuir*, 17(2):288–299, 2001.

F. Shi, M. Tse, M.-M. Pohl, A. Brckner, S. Zhang, and M. Beller. Tuning catalytic activity between homogeneous and heterogeneous catalysis: Improved activity and selectivity of free nano-fe_2o_3 in selective oxidations. *Angewandte Chemie International Edition*, 46(46):8866–8868, 2007.

J.-B. Shi, C.-W. Lee, J.-W. Guo, M.-J. Cheng, C. Wu, C.-J. Chen, Y.-C. Chen, Y.-T. Lin, and C.-C. Chang. Optical and magnetic properties of elliptical hematite (alpha-Fe2O3) nanoparticles coated with uniform continuous layers of silica of different thickness. *Materials Letters*, 61(30):5268–5270, 2007.

V. I. Shubayev, T. R. P. II, and S. Jin. Magnetic nanoparticles for theragnostics. *Advanced Drug Delivery Reviews*, 61(6):467 – 477, 2009.

J. Silver. *Chemistry of Iron*. Blackie Academic & Professional, Glasgow, UK, 1993.

M. Silver and E. Hunter. *Practical Electron Microscopy: A Beginner's Illustrated Guide*. Cambridge University Press, Cambridge, 1993.

J. N. Smith. Atmospheric nanoparticles: Formation and physicochemical properties. In J. A. Schwarz, C. I. Contescu, and K. Putyera, editors, *Dekker Encyclopedia of Nanoscience and Nanotechnology*. Taylor & Francis, second edition edition, 2009.

M. Smoluchowski. Zur kinetischen theorie der brownschen molekularbewegung und der suspensionen. *Annalen der Physik*, 21:756780, 1906.

M. Smoluchowski. Drei vortrge ber diffusion, brownsche molekularbewegung und koagulation von kolloidteilchen. *Phys. Zeit.*, 17:557–571, 1916a.

M. Smoluchowski. Drei vortrge ber diffusion, brownsche molekularbewegung und koagulation von kolloidteilchen. *Phys. Zeit.*, 17:587–599, 1916b.

H. Song, J. sil Choi, Y. Huh, S. Kim, Y. wook Jun, J. Suh, and J. Cheon. Surface modulation of magnetic nanocrystals in the development of highly efficient magnetic resonance probes for intracellular labeling. *Journal of the American Chemical Society*, 127(28):9992–9993, 2005.

C. Sorensen, J. Cai, and N. Lu. Light-scattering measurements of monomer size, monomers per aggregate, and fractal dimension for soot aggregates in flames. *Applied Optics*, 31(30):6547–6557, 1992.

C. M. Sorensen, N. Lu, and J. Cai. Fractal cluster size distribution measurement using static light scattering. *Journal of Colloid and Interface Science*, 174(2):456 – 460, 1995.

L. Spielman. Viscous Interactions is Brownian Coagulation. *Journal of Colloid an Interface Science*, 33(4):562–571, 1970.

S. Staniland, B. Ward, A. Harrison, G. van der Laan, and N. Telling. Rapid magnetosome formation shown by real-time x-ray magnetic circular dichroism. *Proceedings of the National Academy of Sciences of the the United States of America*, 104(49):19524–19528, 2007.

S. Staniland, W. Williams, N. Telling, G. Van der Laan, A. Harrison, and B. Ward. Controlled cobalt doping of magnetosomes in vivo. *Nature Nanotechnology*, 3(3):158–162, 2008.

S. S. Staniland, C. Moisescu, and L. G. Benning. Cell division in magnetotactic bacteria splits magnetosome chain in half. *Journal of Basic Microbiology*, 50(4):392–396, 2010.

I. Stokroos, L. Litinetsky, J. van der Want, and J. Ishay. Magnetic minerals - Keystone-like crystals in cells of hornet combs. *Nature*, 411(6838):654, 2001.

E. Stoner and E. Wohlfarth. A mechanism of magnetic hysteresis in heterogenous alloys. *Philosophical Transactions of the Royal Society London*, 240:599 644, 1948.

A. P. Strafella, J. H. Ko, and O. Monchi. Therapeutic application of transcranial magnetic stimulation in parkinson's disease: The contribution of expectation. *NeuroImage*, 31 (4):1666 – 1672, 2006.

B. Stuyven, Q. Chen, W. V. de Moortel, H. Lipkens, B. Caerts, A. Aerts, L. Giebeler, B. V. Eerdenbrugh, P. Augustijns, G. V. den Mooter, J. V. Humbeeck, J. Vanacken, V. V. Moshchalkov, J. Vermantc, and J. A. Martens. Magnetic field assisted nanoparticle dispersion. *Chemical Communications*, (1):47–49, 2009a.

B. Stuyven, G. Vanbutsele, J. Nuyens, J. Vermant, and J. A. Martens. Natural suspended particle fragmentation in magnetic scale prevention device. *Chemical Engineering Science*, 64(8):1904 – 1906, 2009b.

T. Sugimoto. *Fine Particles: Synthesis, Characterization and Mechanisms of Growth*, chapter 1.3 Metal Oxides: Phase Transformation from Solid Precursors, pages 58–83. Marcel Dekker, 2000.

T. Sugimoto and E. Matijevic. Formation of uniform spherical magnetite particles by crystallization from ferrous hydroxide gels. *Journal of Colloid and Interface Science*, 74(1):227 – 243, 1980.

T. Sugimoto and A. Muramatsu. Formation mechanism of monodispersed α-fe$_2$o$_3$ particles in dilute fecl$_3$solutions. *Journal of Colloid and Interface Science*, 184(2):626 – 638, 1996.

T. Sugimoto and K. Sakata. Preparation of monodisperse pseudocubic -fe2o3 particles from condensed ferric hydroxide gel. *Journal of Colloid and Interface Science*, 152(2): 587 – 590, 1992.

T. Sugimoto, M. M. Khan, and A. Muramatsu. Preparation of monodisperse peanut-type -fe2o3 particles from condensed ferric hydroxide gel. *Colloids and Surfaces A: Physicochemical and Engineering Aspects*, 70(2):167 – 169, 1993a.

T. Sugimoto, A. Muramatsu, K. Sakata, and D. Shindo. Characterization of hematite particles of different shapes. *Journal of Colloid and Interface Science*, 158(2):420 – 428, 1993b.

T. Sugimoto, K. Sakata, and A. Muramatsu. Formation mechanism of monodisperse pseudocubic -fe2o3 particles from condensed ferric hydroxide gel. *Journal of Colloid and Interface Science*, 159(2):372 – 382, 1993c.

T. Sugimoto, Y. Wang, H. Itoh, and A. Muramatsu. Systematic control of size, shape and internal structure of monodisperse -fe2o3 particles. *Colloids and Surfaces A: Physicochemical and Engineering Aspects*, 134(3):265 – 279, 1998.

219

J. Svoboda. A theoretical approachh to the magnetic flocculation of weakly magnetic minerals. *International Journal of Mineral Processing*, 8(4):377–390, 1981.

P. Taboada-Serrano, C.-J. Chin, S. Yiacoumi, and C. Tsouris. Modeling aggregation of colloidal particles. *Current Opinion in Colloid & Interface Science*, 10(3-4):123 – 132, 2005.

M. Tanaka, A. Arakaki, S. S. Staniland, and T. Matsunaga. Simultaneously Discrete Biomineralization of Magnetite and Tellurium Nanocrystals in Magnetotactic Bacteria. *Applied and Environmental Microbiology*, 76(16):5526–5532, 2010.

D. Tanyolac and A. R. Ozdural. Bsa adsorption onto magnetic polyvinylbutyral microbeads. *Journal of Applied Polymer Science*, 80(5):707–715, 2001.

R. Tao and X. Xu. Reducing the viscosity of crude oil by pulsed electric or magnetic field. *Energy & Fuels*, 20(5):2046 – 2051, 2006.

P. Tartaj, M. del Puerto Morales, S. Veintemillas-Verdaguer, T. Gonzalez-Carreno, and C. J. Serna. The preparation of magnetic nanoparticles for applications in biomedicine. *Journal of Physics D: Applied Physics*, 36(13):R182–R197, 2003.

P. Tartaj, M. Morales, T. Gonzlez-Carreno, S. Veintemillas-Verdaguer, and C. Serna. Advances in magnetic nanoparticles for biotechnology applications. *Journal of Magnetism and Magnetic Materials*, 290-291(Part 1):28–34, 2005.

The Richard E Smalley Institute, Rice University. What is nanotehcnology? `http://cohesion.rice.edu/centersandinst/cnst/nano.cfm`.

D. Thomas, S. Judd, and N. Fawcett. Flocculation modelling: A review. *Water Research*, 33(7):1579–1592, 1999.

K. Thomas-Keprta, D. Bazylinski, J. Kirschvink, S. Clemett, D. McKay, S. Wentworth, H. Vali, E. Gibson, and C. Romanek. Elongated prismatic magnetite crystals in ALH84001 carbonate globules: Potential Martian magnetofossils. *Geochimica et Cosmochimica Acta*, 64(23):4049–4081, 2000.

R. Thouy and R. Jullien. Structure factors for fractal aggregates built off-lattice with tunable fractal dimension. *Journal de Physique I*, 6(10):1365–1376, 1996.

A. F. Thunemann, D. Schutt, L. Kaufner, U. Pison, and H. Mohwald. Maghemite nanoparticles protectively coated with poly(ethylene imine) and poly(ethylene oxide)-block-poly(glutamic acid). *Langmuir*, 22(5):2351–2357, 2006.

R. Tietze, S. Lyer, S. Duerr, and C. Alexiou. Nanoparticles for cancer therapy using magnetic forces. *Nanomedicine*, 7(3):447–457, MAR 2012.

M. M. Tirado and J. G. de la Torre. Translational friction coefficients of rigid, symmetric top macromolecules. application to circular cylinders. *The Journal of Chemical Physics*, 71(6):2581–2587, 1979.

M. M. Tirado and J. G. de la Torre. Rotational dynamics of rigid, symmetric top macromolecules. application to circular cylinders. *The Journal of Chemical Physics*, 73(4): 1986–1993, 1980.

E. Tombacz, C. Ma, K. Busch, and M. Busch. Effect of a weak magnetic field on hematite sol in stationary and flowing systems. *Colloid and Polymer Science*, 269(3):278–289, 1991.

K. Towe and H. Lowenstam. Ultrastructure and development of iron mineralization in radular teeth of cryptochiton stelleri (mollusca). *Journal of Ultrastructure Research*, 17 (1-2):1–&, 1967.

M. Tracy and R. Pecora. Dynamics of rigid and semirigid rodlike polymers. *Annual Review of Physical Chemistry*, 43:525–557, 1992.

A. Treiman and C. Romanek. Bulk and stable isotopic compositions of carbonate minerals in Martian meteorite Allan Hills 84001: No proof of high formation temperature. *Meteoritics & Planetary Science*, 33(4):737–742, 1998.

C. Tsouris and T. Scott. Flocculation of Paramagentic Particles in a Magnetic Field. *Journal of Colloid and Interface Science*, 171(2):319–330, 1995.

M. A. Uddin, H. Tsuda, S. Wu, and E. Sasaoka. Catalytic decomposition of biomass tars with iron oxide catalysts. *Fuel*, 87(4-5):451 – 459, 2008.

N. A. Usov, L. G. Kurkina, and J. W. Tucker. Non-uniform micromagnetic structures in asymmetrical ellipsoidal particles. *Journal of Magnetism and Magnetic Materials*, 242-245(Part 2):1009 – 1011, 2002.

H. van de Hulst. *Light Scattering by Small Particles*. Dover Publications, New York, 1981.

R. van Kleef, H. Myron, P. Wyder, D. Fletcher, J. Glew, M. Rowley, and M. Parker. Limits of Magnetic Flocculation in Colloidal Dispersions. *IEEE Transactions on Magnetics*, 19(5):2118–2120, 1983.

E. Verwey and J. Overbeek. *Theory of the stability lyophobic colloids*. Elsevier, Amsterdam, 1948.

R. S. Wadas. *Biomagnetism*. Ellis Horwood, London, 1991.

F. Wagner, S. Haslbeck, L. Stievano, S. Calogero, Q. Pankhurst, and K.-P. Martinek. Before striking gold in gold-ruby glass. *Nature*, 407(6805):691 – 692, 2000.

G. Wang, E. Sevick, E. Mittag, D. Searles, and D. Evans. Experimental demonstration of violations of the second law of thermodynamics for small systems and short time scales. *Physical Review Letters*, 89(5), 2002.

L. Wang, A. F. Khalizov, J. Zheng, W. Xu, Y. Ma, V. Lal, and R. Zhang. Atmospheric nanoparticles formed from heterogeneous reactions of organics. *Nature Geoscience*, 2010.

J. H. P. Watson, B. A. Cressey, A. P. Roberts, D. C. Ellwood, J. M. Charnock, and A. K. Soper. Structural and magnetic studies on heavy-metal-adsorbing iron sulphide nanoparticles produced by sulphate-reducing bacteria. *Journal of Magnetism and Magnetic Materials*, 214(1-2):13 – 30, 2000.

S. Weiner. Biomineralization: A structural perspective. *Journal of Structural Biology*, 163(3):229 – 234, 2008.

R. Wiltschko and W. Wiltschko. *Magnetic orientation in animals*. Springer-Verlag, Berlin, 1995.

Y. Yamada and Y. Enomoto. A microscopic simulation for structure formation in ferrofluid in oscillatory shear flow. *AIP Conference Proceedings*, 832(1):337–340, 2006.

H.-H. Yang, S.-Q. Zhang, X.-L. Chen, Z.-X. Zhuang, J.-G. Xu, and X.-R. Wang. Magnetite-containing spherical silica nanoparticles for biocatalysis and bioseparations. *Analytical Chemistry*, 76(5):1316–1321, 2004.

T. Y. Ying, S. Yiacoumi, and C. Tsouris. High-gradient magnetically seeded filtration. *Chemical Engineering Science*, 55(6):1101 – 1113, 2000.

H. Zhang, G. Ahmadi, F.-G. Fan, and J. B. McLaughlin. Ellipsoidal particles transport and deposition in turbulent channel flows. *International Journal of Multiphase Flow*, 27(6):971 – 1009, 2001.

H. Zhang, B. Gilbert, F. Huang, and J. F. Banfield. Water-driven structure transformation in nanoparticles at room temperature. *Nature*, 424(6952):1025–1029, 2003.

J. L. Zhang, R. S. Srivastava, and R. D. K. Misra. Core-shell magnetite nanoparticles surface encapsulated with smart stimuli-responsive polymer: Synthesis, characterization, and lcst of viable drug-targeting delivery system. *Langmuir*, 23(11):6342–6351, 2007.

Y. Zhang and J. Zhang. Surface modification of monodisperse magnetite nanoparticles for improved intracellular uptake to breast cancer cells. *Journal of Colloid and Interface Science*, 283(2):352 – 357, 2005.

Z. Zhong, J. Lin, S.-P. Teh, J. Teo, and F. Dautzenberg. A rapid and efficient method to deposit gold particles onto catalyst supports and its application for co oxidation at low temperatures. *Advanced Functional Materials*, 17(8):1402–1408, 2007.

Z. Zhou and B. Chu. Light-scattering study on the fractal aggregates of polystyrene spheres: Kinetic and structural approaches. *Journal of Colloid and Interface Science*, 143(2):356 – 365, 1991.

Appendix A
Determination of scattering exponent

This set of Matlab subroutines was provided by Dr. Graeme Bushell (School of Chemical Sciences and Engineering, UNSW, Sydney, Australia) in oreder to determine the fractal dimension and cluster size distribution from static light scattering data.

A.1 Key Assumptions

- Rayleigh - Gans - Debye (RGD) scattering theory holds. This means that the primary particles are small, non-absorbing and have fairly low refractive indices.

- The scatterers are fractal, and all have the same fractal dimension (ie it does not vary with size).

- The cluster size distribution can be adequately described by a "skewed" log-normal distribution, ie two log normal functions stitched together at the vertex, with different decay constants to the left and right of the vertex.

- The aggregates are well modelled by the overlapping spheres cut-off function.

- It is OK to get the fractal dimension by fitting a straight line. This may not be the case if Df is much higher than 2.

A.2 How to use it

- your input data needs to be matlab vectors, lets call them "q" and "I"

- to run the model, type [Df, Rg, csfRg, csdRg] = model(q, I) and press enter

- a graph will appear, use the mouse to select two points (click once for each point), being a range of q in which to calculate the average radius of gyration (this is just used as an initial guess for the curve fitting)

- another graph will appear, use the mouse again to select a range of q in which to fit a linear slope. This is the value of Df. This is not used as a guess. It will be the actual value returned by the model

- the fitting procedure will work its magic Caution: the GIGO principle applies: Garbage In - Garbage Out The procedure will not work well if you have data points affected by gross experimental error such as bubbles. Data should be filtered before it goes into the procedure, that's up to you.

- The output data are:

  - Df - mass fractal dimension
  - Rg - mass squared mean radius of gyration
  - csfRg - cluster size fractions as radius of gyration
  - csdRg - cluster size distribution, mass squared weighted.

- Mass squared distributions are used because that is what the technique is sensitive to. If you want to transform the distribution, that is up to you.

A.3   How it works

A.3.0.1   Model.m

Is the overseeing file. It takes the input and returns the output. First it converts the input data to column vectors if they are not. Then it makes the data equally spaced (in a log sense) and have thirty values using splines, in case they are not. Equal log spacing is critical to how size differences are accounted for (and hence calculation speed) in merror.m.
It then calls getrg.m which takes care of the initial guess for Rg
It then calls getslopelin.m which fits Df to the linear part of the graph
It makes initial guess of 100 for s1 and s2, the cluster width parameters for the size distribution.
Normalises I so that the maximum I is 1 (makes the initial guess easier and does not affect the problem).
Makes a vector called qRg, of length 59 such that the middle value is 1. This is used to calculate (using smono.m) a basis function a, which is the scattering by a single aggregate. This is passed to merror through fmins.
It then invokes the matlab routine fmins to minimise the error returned by merror.m
At the end, the cluster size distribution is calculated from s1, s2 for output.

A.3.0.2   Getrg.m

Plots the data and asks for an input range to be used for calculating Rg. It then takes that data selection and passes it to fitguinier.m

A.3.0.3 Fitguinier.m

Invokes the matlab function fmins to minimise the error returned by guinier.m

A.3.0.4 Guinier.m

Returns the error between data and a fit to the equation

$$I = I_0 \left(1 - \frac{1}{3} (qR_g)^2 \right)$$

A.3.0.5 Getslopelin.m

Plots the data and asks for an input range. Passes this data to the matlab procedure poyfit, to fit a first order polynomial to the data (linear fit)

A.3.0.6 Merror.m

Takes data passed from fmins and uses it to calculate the scattered intensity:
k: constant of proportionality (fudge factor)
Rg: mode size of the cluster size distribution
s1: decay constant for "smaller than mode siz" side of the distribution
s2: dec ay constant for 'larger than mode size" side of the distribution
Cluster size fractions, csfRg, are calculated as 1/q where q is your spaced data. This means there will be 30 cluster size fractions.
It then makes a matrix B, each column i of which represents the (I(0)=1 normalised) scattering by an aggregate of size csfRg(i). It does this by sampling 30 points from the basis function a. So the largest size fraction will be the points 1 to 30 from the 59 basis points. The smallest size fraction will be points 30 to 59.
Using the passed values of Rg (mode size, remember), s1 and s2, calculates the cluster size distribution, csdRg.
The intensity is then calculated by $I = B \times csdRg$ (matrix multiplication) and multiplied by the constant of proportionality, k.
Finally, it calculates and returns the sum of squares error (in a log sense). Fmins tries to minimise this by manipulating the cluster size distribution parameters.

A.3.0.7 Smono.m

Given q, Df and the external radius R_e, it calculates the scattering for a single aggregate based on the incomplete gamma function expansion of the structure factor based on the overlapping spheres cut-off function.

A.3.0.8 Csd.m

Calculates the cluster size distribution. Makes a Gaussian curve with two different halves, so you better feed it log of the cluster size fractions!

A.3.0.9 Rg2Re.m

Converts radius of gyration to external radius, given the Df and the fact that we are using the overlapping spheres cut-off function.

A.4 Matlab code

A.4.0.10 Model.m

```matlab
function[Df,Rg,csfRg,csdRg]=model(qq,II);
% Determine the fractal dimension and cluster size distribution from
% scattering experiments using the overlapping spheres cutoff function
%
% [Df,Rg,csfRg,csdRg]=model(q,I);


%manipulate input data
%to make sure they are column vectors
[rows,cols]=size(qq);
nq=length(qq);
nq = 30;
if (rows<cols)
    qq = qq';
end
[rows,cols]=size(II);
if (rows<cols)
    II = II';
end

% manipulate input data to make them log spaced
% just in case they aren't already
lqmin=log10(min(qq));
lqmax=log10(max(qq));
dlq=(lqmax-lqmin);
q=logspace(lqmin,lqmax,nq)';
I=spline(qq,II,q);
I=I/max(I); %Normalise the data to make fitting easier

% Get starting guesses and basis curve for the measured Df
[Rg,I0]=getrg(q,I);
[slope,dummy]=getslopelin(log(q),log(I));  %Determine Df by linear fit
Df = -slope
s1 = 100;
s2 = 100; % initial guesses for cluster distribution width parameters
X0=[1,Rg/2,s1,s2]';

qRg = logspace(0-dlq,0+dlq,2*nq-1)';
a=Smono(qRg,Df,Rg2Re(1,Df));
```

```
fop = foptions;
fop(14) = 5000;
%X = fminsearch('merror',X0,fop,[],Df,q,I,qRg,a);
X = fminsearch(@merror,X0,fop,Df,q,I,qRg,a);


k  = X(1);
Rg = X(2);
s1 = X(3);
s2 = X(4);


csfRg=1./q;
csdRg=csd(log(csfRg),log(Rg),s1,s2);
% Rg has been used up to now as the mode size, but will now
% be output as the mass mean Rg
Rg = sum(csdRg.*csfRg)/sum(csdRg);
```

A.4.0.11   Getrg.m

```
function[R,I0]=getrg(q,I);
% Measure the radius of gyration from a loglog
% Intensity plot
%
% n is the point number you want to do
%
% [R I0]=getrg(data,q,aera,n);


loglog(q,I,'b.')
text(q(1),I(1)/4,'Please click to indicate lower and')
text(q(1),I(1)/8,'upper range for calculation of Rg')
[X,Y]=ginput(2);
x1=sum(q<X(1))+1;
x2=sum(q<X(2));
[R I0]=fitguinier(q(x1:x2),I(x1:x2));
```

A.4.0.12   Fitguinier.m

```
function[Rg,I0]=fitguinier(q,I);
% Fits guinier equation to input q and Intensity
%
% Rg = fitguinier(q,I);


In=I/I(2);
%X = fminsearch('guinier',[30 1],optimset,[],q,In);
X = fminsearch(@guinier,[30 1],optimset,q,In);
Rg = X(1);
```

```
I0 = X(2)*I(2);
```

A.4.0.13   Guinier.m

```
function[E]=guinier(X,q,I);
% Error function to fit the guinier regime
%
%

Rg = X(1);
I0 = X(2);


Icalc = I0*(1-1/3*((q*Rg).^2));
E = sum((I-Icalc).^2);
```

A.4.0.14   Getslopelin.m

```
function[slope,intercept]=getslopelin(x,y);

plot(x,y,'b.')
hold on
text(x(1),y(1)-.2,'Please click to indicate lower and')
text(x(1),y(1)-.4,'upper range for fitting linear slope')
[X,Y]=ginput(2);
x1=sum(x<X(1))+1;
x2=sum(x<X(2));
[out]=polyfit(x(x1:x2),y(x1:x2),1);
intercept=out(2);
slope=out(1);
ymodel=intercept + slope*x;
plot(x(x1:x2),ymodel(x1:x2),'r-');
hold off
```

A.4.0.15   Merror.m

```
function[E]=merror(X,Df,q,I,qRg,a);
% Error function for the model
%
% returns the sum of squares error between the intensity
% and the current calculated intensity
% E = merror(X,Df,q,I,qRg,a);


nq = length(q);

% Unpack the variables
k  = X(1);
```

```
Rg = X(2);
s1 = X(3);
s2 = X(4);

% Calculate the size distribution
csfRg=1./q;
csdRg=csd(log(csfRg),log(Rg),s1,s2);
% Calculate the matrix 'B'

for i=1:nq
   B(:,i)= a(nq+1-i:2*nq-i);%.*(csfRg(i)^(Df));
   % Scattering pattern of an aggregate per unit mass squared,
   % in order to use a mass squared distribution
end

% Calculate intensity
Icalc= B*csdRg;
Icalc= k*Icalc/max(Icalc);

% Plot graphics
if (rand<0.1)
   subplot(2,1,1)
   loglog(q,I,'b.',q,Icalc,'r-');
text(q(1),I(1)/2,['Df = ' num2str(Df)])
text(q(1),I(1)/3,['Rg = ' num2str(Rg)])
text(q(1),I(1)/4.5,['s1 = ' num2str(s1)])
   text(q(1),I(1)/6.75,['s2 = ' num2str(s2)])
   xlabel('q, /nm');
   ylabel('Intensity');
   subplot(2,1,2)
   semilogx(csfRg,csdRg,'k-')
   xlabel('Rg, nm');
   ylabel('Mass ^2');
   drawnow;
end

% Calculate the error
E = sum((log(I)-log(Icalc)).^2);
```

A.4.0.16   Smono.m

```
function[S] = Smono(q,Df,Re);
% Returns the structure factor for a monodisperse
% fractal aggregate with external radius Re
```

```
%
% S = smono(q,Df,Re);

B1 = (i/2*(i*q).^(1-Df)).*(gammainc2(2*i*q*Re,Df-1).*gamma(Df-1))...
 - (i/2*(-i*q).^(1-Df)).*(gammainc2(-2*i*q*Re,Df-1).*gamma(Df-1));
B2 = (i/2*(i*q).^(-Df)).*(gammainc2(2*i*q*Re,Df).*gamma(Df))...
 - (i/2*(-i*q).^(-Df)).*(gammainc2(-2*i*q*Re,Df).*gamma(Df));
B3 = (i/2*(i*q).^(-Df-2)).*(gammainc2(2*i*q*Re,Df+2).*gamma(Df+2))...
 - (i/2*(-i*q).^(-Df-2)).*(gammainc2(-2*i*q*Re,Df+2).*gamma(Df+2));

S = ((B1) - 3/(4*Re)*(B2) + 1/(16*Re^3)*(B3))./q *Re^Df  ;
S = S/max(S);
```

A.4.0.17   Csd.m

```
function[n]=csd(N,No,s1,s2);
% Gaussian type cluster size distribution
% with different parameters either side of the mode
%
%
% n = csd(N,No,s1,s2)

n = exp(-s1*(N-No).^2).*(N<No) + exp(-s2*(N-No).^2).*(N>=No);
```

A.4.0.18   Rg2Re.m

```
function[Re]=Rg2Re(Rg,Df);
%This is cutoff specific, convert Rg to Re
%Re = rg2re(Rg,Df);

Re=Rg/sqrt(2*Df*(Df+1)/((Df+2)*(Df+5)));
```

Appendix B
Population balance MATLAB code

B.1 Main.m

```
% Main m-file
%----------------------------------------------------------------
function [time,number,Totalvol,VMD,dF] = popbaldF
% ODE23 (low order non-stiff equation)
% N=Ncurrent+dN/dt*dt
% dF=dFcurrent+ddF/dt*dt

% Input Variables
G=64; % Shear rate s-1
B=1; % fitting parameter for breakage function,cm-3a/s
do=100; % primary particle diameter, nm

phi0 = 0.035; % Surafce potential (V)
I = 0.001; % Ionic strength

Bmag = 0.1; % Magnetic field strength (T)
chi = 0.002; % Magnetic susceptibility
magflag = 0; % Include magnetic interaction (= 1)or not (= 0)

imax=25; % maximum size interval

% Original number distribution
% no concentration, no/cm3
% B#6 (404nm) or 380nm (TEM)
a=[1.099E9 1.87e5 3.08e4];
%a = [1.099e9 1.87e5];
sizea=size(a,2);
sizeb=imax-sizea;
b=zeros(1,sizeb);
```

```
no=[a,b]; % size(no)=1 x imax
Totalvol1=solvol(no,do); % Reference for total volume of solid
dFo=1.05; % dF at t=0
dcurrent=do;

% Time Span
t=0;
tmax=30; % min

% Output printout
time(1)=t;
number(1,:)=no;
VMD(1)=do*1e-3; % VMD in micron
dF(1)=dFo;

% Generate collision efficiency matrix
%[Alpha] = test(dFo,do,imax,Bmag,chi,phi0,I,magflag);

i=1;

% Loop
while t<tmax,
   ti= t + 1;
   tspan= t:1:ti;
   Yo=[no dFo]; % size(Yo)=1 x (imax+1)

   % Generate collision efficiency matrix
   [Alpha] = test(dFo,do,imax,Bmag,chi,phi0,I,magflag);

   %options=odeset('AbsTol',1e-4,'OutputFcn','odeprint');
   options=odeset('AbsTol',1e-4);
   [tf,Yf]=ode23('aggregationdF',tspan,Yo,options,imax,
   Alpha,B,G,dcurrent,do);
   tfrow=size(tf,1);
   [Yfrow,Yfcol]=size(Yf); % Yfrow=tfrow, Yfcol=imax+1
   j=1;
   while j<=(Yfcol-1),
      if Yf(Yfrow,j)<0
         Yf(Yfrow,j)=0;
      else
         Yf(Yfrow,j)=Yf(Yfrow,j);
      end
      j=j+1;
```

```
    end
    Totalvol2=solvol(Yf(Yfrow,1:(Yfcol-1)),do);
    dTotalvol=((abs(Totalvol2-Totalvol1))/(Totalvol1))*100;
    if dTotalvol>1
        save final.m time number VMD dF -ascii -double -tabs;
        error('calculation terminated');
    else
        no=Yf(Yfrow,1:(Yfcol-1));
        t=tf(tfrow);
        dFo=Yf(Yfrow,Yfcol);
        dcurrent=convertVMDsingle(no,dFo,do); % dcurrent in nm
        i=i+1;
        time(i)=t;
        number(i,:)=no;
        dF(i)=dFo;
        VMD(i)=dcurrent*1e-3; % VMD in micron
    end
end
[Totalvol]=solvol(number,do);
figure
plot(time,VMD,'b*-');
title('VMD versus time');
xlabel('Time (min)');
ylabel('VMD,micron');
title('100nm');
timeprint=time';
VMDprint=VMD';
dFprint=dF';

figure
plot(time,dF,'b*-');
title('dF versus time');
xlabel('Time (min)');
ylabel('dF');
title('100nm');

save dF38064.m timeprint number VMDprint
dFprint -ascii -double -tabs;
```

B.2 aggregationdF.m

```
% Calculate dN/dt
%-------------------------------------------------------------
```

```
function [dYdt]=aggregationdF(t,Y,flag,imax,Alpha,B,G,dcurrent,do)
%function [dYdt]=aggregationdF(t,Y,flag,Alpha,B,G,dcurrent,do);
% full term
% dF effect (using Rc)
% Accounting for Brownian motion
% Breakage using exponential model (Kuster, 1991)
% Y=[N dF]is a row vector
% dYdt=[dNdt;ddFdt] return a column vector
% dNdt

%k=1;
dYdt=zeros(imax+1,1); % a column vector of size (imax+1)x1

% dNdt
v=1.07e-2; % kinematic viscosity for latex/salt,cm2/s
e=G^2*v; % energy dissipation rate, cm2/s3
m=2;
temp=298; % absolute temperature, K
kb=1.380622e-23; % Boltzman's constant,J/K
miu=1e-3; % Viscosity of surrounding medium,Pas
N=Y(1:imax,1); % size(N)=imax x 1
dFcurrent=Y(imax+1,1);

[V,r,Np,Rc]=volspicer(do,imax,dFcurrent);


dNdt=zeros(imax,1);
for k=1:imax,

    % First term: birth in interval i due to collision
    % between particles in intervals i-1 and 1 to i-2
    % j=1 to j=i-2: 2^(j-1+1)*Alpha*Beta[i-1,j]*N[i-1]*N[j]
    i=k;
    if (i-2)>=1
        first=zeros(i,1);
        j=1;
        for j=1:(i-2),
            %Fuchs = quad(@efficiency, 2, 10, [], [], Rc, do, i, j);
            Beta1a=1.294*G*(Rc(i-1)+Rc(j))^3; % shear kernel, cm3/s
            Beta1b=((2*kb*temp)/(3*miu)*((1/(Rc(i-1)*1e-2))...
                 +(1/(Rc(j)*1e-2)))*((Rc(i-1)*1e-2...
                 +(Rc(j)*1e-2)))*1e6; % Brownian kernel, cm3/s
            Beta1=Beta1a+Beta1b;
```

```matlab
            first(j)=2^(j-i+1)*Alpha(i-1,j)*Beta1*N(i-1)*N(j);
            j=j+1;
        end
        sumfirst=sum(first);
else
        sumfirst=0;
end

% 2nd term: birth in interval i due to collisions between particles in
    % intervals i-1 and i-1 (the no of particles available is Ni-1)
% 1/2*Alpha*Beta[i-1,i-1]*N[i-1]^2
i=k;
    if (i-1)==0
        second=0;
    else
        Beta2a=1.294*G*(Rc(i-1)+Rc(i-1))^3; % Shear kernel, cm3/s
        Beta2b=((2*kb*temp)/(3*miu))*((1/(Rc(i-1)*1e-2))...
            +(1/(Rc(i-1)*1e-2)))*((Rc(i-1)*1e-2)+...
            (Rc(i-1)*1e-2)))*1e6; % Brownian kernel, cm3/s
        Beta2=Beta2a+Beta2b;
        second=(1/2)*Alpha(i-1,i-1)*Beta2*((N(i-1))^2);
end

% 3rd term: death by aggregation in interval i due to collision of
    % particles in intervals i and 1 to i-1
% j=1 to j=i-1: Ni*sum(Alpha*Beta[i,j]*N[j])
i=k;
    if (i-1)>=1
        third=zeros(i,1);
        j=1;
        for j=1:(i-1),
            Beta3a=1.294*G*(Rc(i)+Rc(j))^3; % shear kernel, cm3/s
            Beta3b=((2*kb*temp)/(3*miu)*((1/(Rc(i)*1e-2))+...
                (1/(Rc(j)*1e-2)))*((Rc(i)*1e-2)+...
                (Rc(j)*1e-2)))*1e6; % Brownian kernel, cm3/s
            Beta3=Beta3a+Beta3b;
        third(j)=2^(j-i)*Alpha(i,j)*Beta3*N(j);
            j=j+1;
        end
        sumthird=(sum(third))*N(i);
else
        sumthird=0;
end
```

236

```
   % 4th term: death by aggregation of particles in intervals i and i to
      % imax j=i to j=imax: Ni*sum(Alpha*Beta[i,j]*N[j])
   i=k;
   fourth=zeros(imax,1);
   j=i;
   p=1;
   if j<imax
    for j=i:imax,
       Beta4a=1.294*G*(Rc(i)+Rc(j))^3; % shear kernel, cm3/s
       Beta4b=((2*kb*temp)/(3*miu))*((1/(Rc(i)*1e-2))+...
                 (1/(Rc(j)*1e-2)))*((Rc(i)*1e-2)+...
                 (Rc(j)*1e-2)))*1e6; % Brownian kernel, cm3/s
       Beta4=Beta4a+Beta4b;
       fourth(p)=Alpha(i,j)*Beta4*N(j);
       j=j+1;
       p=p+1;
end
     sumfourth=sum(fourth)*N(i);
   else
       sumfourth=0;
   end

   % 5th term: death by fragmentation of flocs in interval i
% Si*Ni
   i=k;
   if i>1
       ebi=B*(Rc(i))^(-2/m);
       Si=(4/(15*pi))^(1/2)*G*exp(-ebi/e);
       fifth=Si*N(i);
   else
       fifth=0;
   end

% 6th term: breakage of flocs greater than i into flocs of size i
% binary breakage: R(i,j)=V(j)/V(i) for j=i+1, and R(i,j)=0 otherwise
   i=k;
   if i<imax
       R=2; % V(i+1)/V(i)
       ebi=B*(Rc(i+1))^(-2/m);
       Si=(4/(15*pi))^(1/2)*G*exp(-ebi/(e));
       sixth=R*Si*N(i+1);
   else
```

```
      sixth=0;
   end

   agg(k)=sumfirst+second-sumthird-sumfourth;
   frag(k)=-fifth+sixth;
dNdt(k,1)=(agg(k)+frag(k))*60;
   k=k+1;
end
dYdt(1:imax,1)=dNdt;

% ddFdt=[(constant1*(dcurrent/do))+(constant2*AB)]*(dFmax-dFcurrent)
constant1=0.100; % constant for dcurrent/do
constant2=1e-10; % constant for AB

dFmax=2.55; % Maximum fractal dimension

aggsum=sum(abs(agg));
fragsum=sum(abs(frag));
ABcurrent=aggsum*fragsum; % (sum of aggregation i=1 to imax)*
                          % (sum of fragmentation i=1 to imax) at time t
ddo=(dcurrent/do)^(1/5);
ddFdt=((constant1*ddo)+(constant2*ABcurrent))*(dFmax-dFcurrent);
dYdt(imax+1,1)=ddFdt;
```

B.3   test.m

```
function [Alpha] = test(dFo,do,imax,Bmag,chi,phi0,I,magflag)

%dFo = 1;

Rc = zeros(imax,1);
for i = 1:imax
      %Rc(i) = 0.5*(2^((i-1)/dFo))*do*1e-9; % Charateristic floc radius
      Rc(i) = 0.5*(2^((i-1)/1))*do*1e-9;
end

Fuchs = zeros(imax,imax);
Alpha = zeros(imax,imax);

for i = 1:imax
  for j = 1:imax
      if j <= i
        rmin = 2;
```

```
        rmax = 1e4*rmin;
        Fuchs(i,j) = quad(@efficiency, rmin, rmax, [], [], ...
             Rc,chi,phi0,I,Bmag,magflag,i,j);
        Alpha(i,j) = 1/Fuchs(i,j);
      end
   end
end

for i = 1:imax
  for j = 1:imax
    if j > i
        Alpha(i,j) = Alpha(j,i);
    end
 end
end

%i = 1:imax;
%j = 1:imax;
%figure
%mesh(i,j,Alpha(i,j));
%title('Collision efficiency');
%xlabel('Size interval (i)');
%ylabel('Size interval (j)');
%zlabel('Alpha');
%grid on
%axis square
%hold on
```

B.4   efficiency.m

```
% Calculate collision efficiencies
%-------------------------------
function [Fuchs] = efficiency(s,Rc,chi,phi0,I,Bmag,magflag,i,j)

% Physical constants
A = 5e-20; % Hamaker constant
kb = 1.380622e-23; % Boltzman constant(J/K)
T = 298; %Temperature (K)
mu0 = 8.8541878176e-12; % Permitivitty free space (F/m)
muv = 1e-3; % Viscosity, water (Pa s)
epsilon = 6.9417e-10; % Permittivity (C V-1 cm-1)
%epsilon = 89e-10; % Dielectric constant for water (C V-1 m-1)
e = 1.6e-19; % Elementary charge (C)
```

```matlab
z = 1; % Valence of dissociated electrolyte
%phi0 = 0.015; % Surface potential (V)
%I = 0.001; % Ionic strength


% Dervied constants
r1 = Rc(i); % Particle 1 radius (m)
r2 = Rc(j); % Particle 2 radius (m)
r = s*Rc(i);
phii = (z*e*phi0)/(kb*T);
Y = 4*tanh(phii/4);
kappa = 1/(2.8e-6*(I^0.5)); % Debye-Huckel length



% Interaction Potentials
%-------------------------------------
% Van der Waals Potential, actually Vvdw/kT
Vvdw = (-A/(6*kb*T))*...
       (((2*r1*r2))./((r.^2) - (r1 + r2)^2)+...
       ((2*r1*r2))./((r.^2) - (r1 - r2)^2)+...
       log(((r.^2) - (r1 + r2)^2)./((r.^2) - (r1 + r2)^2)));

% Electrostatic Potential
l = r - r1 - r2; % Separation
Vel1 = epsilon*(((kb*T)/e)^2)*(Y^2)*((r1*r2)./r).*exp(-kappa.*l);
Vel = Vel1/(kb*T);

%Magnetic Potential, actually Vmag/kT
di = 2*r1;
dj = 2*r2;
x = (1/(kb*T))*(pi()*(di^3)*(dj^3)*chi*chi*(Bmag^2))./(144*mu0*(r.^3));
sx = exp(-log(2).*((x/2.4).^8));

Vmag = sx.*(-((x.^2)/3).*(1./(1 + ((7.*(x.^2))./150)))) +...
    (1 - sx).*(-2.*x + log(6*(x.^2)) - (2./(3.*x)) - (7./(9.*(x.^2)))));

% Total potential, actually VA/kT
%----------------------------
if magflag == 1
    VA = Vvdw + Vel + Vmag;
else
    VA = Vvdw + Vel;
end
```

```
Dhyd = 1; %1/0.1064;

Fuchs = (1 + (r1/r2))*Dhyd*exp(VA).*(1./(s.^2));
```

B.5   solvol.m

```
% Calculate total solid volume of aggregates
%----------------------------------------------------------------
function [TotalVol]=solvol(Y,do);
% calculate total solid volume for
% lumped discrete population balance (minimum limit)
% lower limit, ie. 4 for i=3,8 for i=4 etc
% vi=2^(i-1)*vo

ro=(do/2)*1e-9; % in m
u1=4/3*pi*ro^3; % in m^3
[m,jmax]=size(Y);
j=1;
for j=1:jmax,
    u=u1*(2^(j-1)); % in m^3
    vo(j)=u;
    j=j+1;
end
vi(:,1)=vo';
Vol=[vi];

i=1;
Y=Y';
Totalvoli=zeros(jmax,m);

for i=1:m,
    Totalvoli(:,i)=Y(:,i).*Vol;
    Sumvoli(i,1)=sum(Totalvoli(:,i));
    i=i+1;
end
TotalVol=[Sumvoli];
```

B.6   volspicer.m

```
% Calculate collision radius of aggregates
%----------------------------------------------------------------
function [V,r,Np,Rc]=volspicer(do,jmax,dF);

% do: diameter of primary particle, nm
```

```
% Vi: characteristic solid volume=u1*2^(i-1),cm3
% ri: characteristic solid floc radius=(Vi/(4/3*pi))^(1/3),cm
% ro: primary particle radius,cm
% u1: primary particle volume,cm3
% Np: number of primary particle comprising a floc of size i=2^(i-1)
% (Flesch, Spicer, & Pratsinis, 1999)
% Rc: maximum collision radius=ro*(Np/k)^(1/dF)
% dF: fractal dimension

ro=do/2*1e-7; % in cm
u1=4/3*pi*ro^3; % in cm^3
kc=1; % lacunarity
j=1;
for j=1:jmax,
   u=u1*2^(j-1); % in cm^3
   rm=((u/(4/3*pi))^(1/3))*1e4; % radius of i in micron
vo(j)=u;
   rn(j)=rm;
   npo(j)=(2^(j-1)); % characteristic number of particles in section i
   if j<=2
      rco(j)=rn(j)/1e4;
   else
      rco(j)=ro*((npo(j)/kc)^(1/dF));
   end
   j=j+1;
end
vi(:,1)=vo';
ri(:,1)=rn';
npi(:,1)=npo';
rci(:,1)=rco';

% print characteristic volume (cm^3)
V=[vi];
% print radius of particle i (micron)
r=[ri];
% print Np (number of primary particles comprising
% a single floc i: 2^(i-1))
Np=[npi];
% print Rc (maximum collision radius, cm)
Rc=[rci];
```

B.7 convertVMDsingle.m

```
% Calculate volume mean diameter of aggregates
```

```
%----------------------------------------------------------------
function [VMDm]=convertVMDsingle(N,dF,do);

% Calculating volume mean diameter (VMD) from number
% concentration of flocs of size i (Ni)
% and characteristic floc diameter (Di)
% Kuster,1991
% input dF
% single calculation
% size N = 1xn

d1=do*1e-7; % primary particle diameter,cm
i=1;
[m,n]=size(N);

% Di:characteristic floc diameter
% Di=2^((i-1)/dF)*d1
% VMD=sum(Ni*Di^4)/sum(Ni*Di^3)
for i=1:n,
    if dF >= 1
   Di(i)=(2^((i-1)/dF))*d1;
   i=i+1;
    else
   dF = 1;
   Di(i)=(2^((i-1)/dF))*d1;
   %Di(i)=i*d1;
   i=i+1;
    end
end
D=[Di];

% col=n (section i)
col=1;
for col=1:n,
   TopVMDi(col)=N(1,col)*D(col)^4;
   BotVMDi(col)=N(1,col)*D(col)^3;
   col=col+1;
end
TopVMD=sum(TopVMDi);
BotVMD=sum(BotVMDi);
VMD=TopVMD/BotVMD;
VMDm=VMD*1e7; % in nm
```

B.8   convnumberdF.m

```
% Plot number distributions of aggregates
-----------------------------------------------------------------
function [D,Numcalc]=convnumberdF(t,do,N,dF);

% Plot number fraction versus characteristic floc diameter
% Kusters, 1991
% Spicer and Pratsinis, 1996
% do: primary particle diameter, nm
% dF variation
[m,n]=size(N);
v1=(4/3)*pi*(do/2*1e-7)^3; % volume of primary particle, cm3
d1=do*1e-7; % diameter of primary particle, cm
i=1;

Di=zeros(m,n);
% Di:characteristic floc collision diameter
% Di=(2^((i-1)/dF))*d1
% row=m (time)
% col=n (section i)
row=1;
Nest=zeros(m,n);
TotalN=zeros(m,1);
for row=1:m,
   col=1;
   for col=1:n,
      Nest(row,col)=N(row,col)*2^(col-1);
      col=col+1;
   end
   TotalN(row)=sum(Nest(row,:));
   row=row+1;
end

row=1;
Ni=zeros(m,n);
for row=1:m,
   col=1;
   dFrow=dF(row);
   for col=1:n,
      Ni(row,col)=Nest(row,col)./TotalN(row);
      Di(row,col)=(2^((col-1)/dFrow))*d1;
      col=col+1;
```

```
        end
    row=row+1;
end
```